Development of an absolute quantitation method for genetically modified cell therapy

Bugallo Blanco, Eva

Awarding institution:
King's College London

Development of an absolute quantitation method for genetically modified cell therapy

Eva Bugallo Blanco

Supervisors: Dr. Sophie Papa

Prof. Jane Sosabowski

This dissertation is submitted for the degree of

Doctor of Philosophy

January 2024

"We ourselves feel that what we are doing is just a drop in the ocean.

But the ocean would be less because of that missing drop."

Mother Theresa

Acknowledgements

First and foremost, I extend my heartfelt gratitude to my primary supervisor, Sophie Papa. Her support, insightful input into my research, and unwavering belief in my abilities have been the cornerstones of my success. Sophie, thank you for not only being an exceptional supervisor but also a genuine mentor, both within and beyond the laboratory. I want to express my gratitude to my second supervisor, Jane Sosabowski, for consistently providing support, encouragement, and valuable feedback. Jane, your warm welcome into the team has been truly appreciated.

I would also like to thank the members of the Immunoengineering and CAR mechanics groups, who have provided their support and encouragement throughout my doctoral journey. Special recognition goes to Rob Page and Olivier Martinez, whose commitment to engaging in scientific discussions and providing support during challenging times has been invaluable. I am equally thankful to Karen Larios for the camaraderie we shared during countless late lunches.

I would also like to extend my thanks to my secondary team at Barts Cancer Institute for introducing me to the field of molecular imaging. I am particularly grateful to Juliette Chupin for her consistent support and her delightful snack drawer stocked with chocolates.

Thank you CRUK City of London Center for choosing and providing me with scholarship funding and support in various forms during the last four years.

To my friends in London and Madrid, I appreciate your reminders that life extends beyond the lab. Thank you for the coffee outings, dinners, and hiking adventures that added balance

Abstract

CAR T cell therapies for solid tumours face additional challenges, resulting in limited efficacy compared to haematological malignancies. Overcoming obstacles such as trafficking to the tumour site, extravasation and proliferation within an immunosuppressive microenvironment remain challenging. The dynamics of these processes, the whole-body biodistribution and the minimum cell number required for tumour remission, are still not fully understood.

Here, a compartmental model was established to characterise the dynamics of $^{99m}TcO_4^-$ uptake by CAR T cells, enabling serial and non-invasive monitoring and quantitation of CAR T cell infiltration in a prostate cancer mouse model using single-photon emission computed tomography-computerised tomography (SPECT/CT).

An indirect labelling strategy was implemented by co-expressing the reporter gene hNIS with a second-generation PSMA targeting CAR. These CAR T cells can internalise the clinically relevant tracer technetium pertechnetate ($^{99m}TcO_4^-$), facilitating the visualisation of CAR T cell biodistribution in cancer-bearing mice via SPECT/CT. The SPECT/CT images provided valuable insights into CAR T cell infiltration patterns and allowed the serial and real-time monitoring of CAR T cell proliferation *in vivo* non-invasively. *Ex vivo* immunohistochemistry analysis confirmed the observed infiltration patterns *in vivo*, revealing CAR T cells predominantly accumulating around tumour vasculature while absent from the tumour core. Tumour uptake, quantified from SPECT/CT images, correlated with the number of cells quantified by flow cytometry. To better comprehend the dynamics surrounding CAR T cell infiltration and proliferation, a two-compartment model was defined to characterise

tracer behaviour *in vivo*, demonstrating a strong correlation between tracer flow from the bloodstream into the tumour and the number of infiltrating CAR T cells. This work serves as a proof of concept, laying the foundations for the further development of compartmental models as a tool for the non-invasive and *in vivo* quantitation of genetically modified cell therapies.

Table of contents

8

List of figures

13

14

15

16

List of tables

List of abbreviations

ACT	Adoptive Cell Transfer
AIC	Akaike information criterion
APCs	Antigen Presenting Cells
ATP	Adenosine Triphosphate
Axi-cel	Axicabtagene Ciloleucel
B-ALL	B Cell Acute Lymphoblastic Leukaemia
BCMA	B-Cell Maturation Antigen
BiTEs	Bispecific T Cell Engagers
BLI	Bioluminescence
BSA	Bovine Serum Albumin
CAR	Chimeric Antigen Receptor
CCRs	Chemokine Receptors
CR	Complete Response
CT	Computed Tomography
CTL	Cytotoxic T Lymphocyte
CTLA-4	Cytotoxic T Lymphocyte-Associated Antigen 4
DFO	Desferrioxamine
DLBCL	Diffuse Large B-Cell Lymphoma (Dlbcl)
DMEM	Dulbecco's Modified Eagle Medium
DMSO	Dimethyl Sulfoxide

DNA	Deoxyribonucleic Acid
E:T	Effector-To-Target
ELISA	Enzyme-Linked Immunosorbent Assay
F:P	Fluorochrome To Protein
FACS	Fluorescence-Activated Cell Sorting
FAP	Fibroblast Activation Protein
FBS	Foetal Bovine Serum
FDA	US Food and Drug Administration
FDG	Fluorodeoxyglucose
FET	Fluoroethyl-l-tyrosine
fmol	femtomolar
FOV	Field Of View
GP-RM	General Purpose Rat and Mouse
h	hour
HEK 293T	Human Embryonic Kidney 293T
HIER	Heat Induced Epitope Retrieval
HLA	Human Leukocyte Antigens
hNET	human Norepinephrine Transporter
hNIS	human Sodium Iodide Symporter
HSV1tk	herpes Simplex Virus Type 1 Thymidine Kinase
ICAM 1	Intracellular Adhesion Molecule 1
ICOS	inducible costimulator
IFNγ	Interferon Gamma
IHC	Immunohistochemistry
IL-15	Interleukin 15
IL-2	Interleukin 2
IL-4	Interleukin 4

IL2R	Interleukin-2 Receptor
i.p.	intraperitoneal
Iono	Ionomycin
ITAMS	Immunoreceptor Tyrosine-Based Activation Motifs
i.v.	intravenous
kBq	kilobecquerel
L/D	Live Dead
Lag 3	Lymphocyte Activating 3
LB	Luria-Bertani Broth
LOD	Limit Of Detection
MAGE-A	Melanoma-Associated Antigen
MBq	Megabecquerel
MCL	Mantle Cell Lymphoma
MDSCs	Myeloid-Derived Suppressor Cells
MESF	Molecules Of Soluble Fluorochrome
mg	miligram
min	minutes
MIP	Maximum Intensity Projection
MTT	3-(4,5-dimethylthiazol-2-yl)-2,5-diphenyltetrazolium bromide
NIR	Zombie Near Infrared
NSG	NOD SCID Gamma
NSCLC	Non-Small Cell Lung Cancer
NY-ESO-1	New York Esophageal Squamous Cell Carcinoma-1
PBMC	Peripheral Blood Mononuclear Cells
PBS	Phosphate-Buffered Saline
PBSA	PBS Supplemented With 1% BSA
PCR	Polymerase Chain Reaction

PD-1	Programmed Death 1
PD-L1	Programmed Death Ligand-1
PE	Phycoerythrin
PET	Positron Emission Tomography
PL	PC3-LN3
PL-LT	PC3-LN3 Luciferase Tdtomato
PLP	PSMA-PC3-LN3
PLP-LT	PSMA-PC3-LN3 Luciferase Tdtomato
PMA	phorbol 12-myristate 13-acetate
PSMA	Prostate Specific Membrane Antigen
qPCR	Quantitative Polymerase Chain Reaction
r/r	relapsed/ Refractory
ROI	Region Of Interest
RPMI	Roswell Park Memorial Institute
RT	Room Temperature
S.E.M	Standard Error of The Mean
s.c.	subcutaneous
scFv	single chain variable fragment
SD	Standard Deviation
SOC	Super Optimal Broth With Catabolite Repression
SPECT	Single-Photon Emission Computerised Tomography
SROSEM	Similarity regulated ordered subsets expectation maximization
SSTR2	Human Somatostatin Receptor 2
TAA	Tumour-Associated Antigens
TAC	Time Activity Curve
TAMs	Tumour -Associated Macrophage
T_{cm}	Central Memory T Cell

TCR	T Cell Receptor
T_e	Effector T Cell
T_{em}	Effector Memory T cell
T_{emra}	Effector Memory T cell expressing CD45RA
TILs	Tumour Infiltrating T Cells
TIM-3	T Cell Immunoglobulin And Mucin-Domain Containing-3
TMB	Tetramethylbenzidine
TME	Tumour Microenvironment
Tregs	T Regulatory Cells
VCAM 1	Vasculature Cell Adhesion Molecule 1
V_H	Variable Heavy Chain
V_L	Variable Light Chain
VQ	Visipaque™
V_T	Volume of distribution
XXUHS-M	Extra-Extra Ultra-High Sensitivity Mouse
$[^{18}F]BF_4^-$	[18F]tetrafluoroborate
%ID	% Injected Dose
%ID/g	% Injected Dose per gram
%ID/mm^3	% Injected Dose per cubic millimetre
^{123}I-MIBG	[123I]Metaiodobenzylguanidine
^{68}Ga	Gallium-68
^{89}Zr	Zirconium-89
$^{99m}TcO_4^-$	Tc-99m Pertechnetate

Chapter 1

Introduction

1.1 Cancer immunotherapy

Over the past few decades, immunotherapy has provided solutions for the treatment of malignancies with poor prognosis, arising as a promising alternative to traditional treatments and offering enhanced therapeutic effect and survival. The first record of the use of immunotherapy dates back to 1891, when William Coley treated soft tissue sarcoma patients with streptococcal species, achieving tumour regression[1]. In 1950, the concept of immunosurveillance was proposed, in which the immune system can recognise tumour-associated antigens (TAA) and eliminate tumours. Since then, the concept of immunosurveillance has further developed, describing the elimination of tumour cells by the immune system, the equilibrium between the remodelling of the tumours while under attack by immune cells, and lastly the escape of tumour cells from the immune cells leading to continuous tumour growth[2].

The first immunotherapy approved by the US Food and Drug Administration (FDA) in 1992 was the use of the cytokine interleukin 2 (IL-2) for the treatment of metastatic renal cell carcinoma[3]. IL-2 is produced by activated CD4 and CD8 T cells, playing a role in T cell proliferation, differentiation, and maintenance of regulatory T cells. A few years later,

the development of monoclonal antibody technology revolutionised the field. Monoclonal antibodies against CD20 (rituximab)[4,5] and human epidermal growth factor receptor 2 (HER2) (trastuzumab)[5] received FDA approval for the treatment of non-Hodgkin's lymphoma and breast cancer, respectively. Another significant breakthrough was the discovery of cytotoxic T lymphocyte-associated antigen 4 (CTLA-4) and programmed death-1 (PD-1) receptors, paving the way for the development of immunocheckpoint inhibitors. CTLA-4, a homologue of CD28 on T cell receptors (TCRs), binds to B7 in antigen presenting cells (APCs), blocking the interaction between the TCR and APCs, resulting in T cell anergy. Similarly, T cells can be deactivated by the binding of PD-1 on the T cell surface to programmed death ligand-1 (PD-L1) overexpressed on the cell surface of tumours[6]. In 2011, the FDA approved the anti-CTLA-4 monoclonal antibody ipilimumab for the treatment of metastatic melanoma. Several anti-PD1 checkpoint inhibitors, such as nivolumab, have been developed to block the inhibitory pathways associated with PD-1/PD-L1 binding. The concomitant use of ipilimumab (anti-CTLA-4) and nivolumab (anti-PD-1) demonstrated greater effectiveness than monotherapy with each agent when treating non-small cell lung cancer (NSCLC)[7] and melanoma[8] among other malignancies. Alternative immunotherapy strategies are based on the *ex vivo* modification of T cells followed by adoptive T cell transfer into the patients. Adoptive T cell immunotherapies include tumour infiltrating T cells (TILs), T cell receptor-engineered T cells (TCR-T) and chimeric antigen receptor T cells (CAR T cells). TILs are isolated from biopsied tumour, cultured *ex vivo* with high-doses of IL-2 and reinfused back into lymphodepleted patients, accompanied by systematic IL-2 infusions[9,10]. TILs can maintain their specificity, recognise, and engage with peptides presented on MHC-I molecules. Patients with metastatic melanoma treated with TIL immunotherapy combined with IL-2 between 1988 and 2016 had an objective response rate of 41% and a complete response rate of 12%[11,12]. More recently, objective tumour responses of around 50% have been reported with neoantigen-specific T cells being detected in peripheral blood for up to

3 years post treatment[13]. TILs are currently being investigated as a second-line treatment for melanoma patients[10], and modest responses have been observed in the treatment of metastatic human papilloma virus-associated cancers[14]. Most recently, preliminary results have shown efficacy after the combined use of anti-PD-1 inhibitor and TILs for the treatment of NSCLC[15]. However, despite these positive results, the broader application of TIL therapy has been limited due to the challenges associated with the isolation and expansion of TILs, as they are often presented in limited numbers in the resected tumours. Additionally, to achieve durable responses, the isolated T cells must retain their anti-tumour activity[10, 14]. To overcome these limitations, antitumoral TCRs identified from TILs can be sequenced and engineered into T cells to recognise multiple peptides. These engineered TCR-T cells can effectively recognise human leukocyte antigens (HLA)-peptide complexes on the tumour cells, leading to tumour regression. TCR-T production has evolved over time, optimizing TCRs to increase their affinity for tumour cells and the targeting of neoantigens, ie. antigens generated by the tumour cells and absent in normal tissues, improving patient safety[16]. Most clinical trials involving TCR-T therapies have focused on targeting germline antigens such as New York esophageal squamous cell carcinoma-1 (NY-ESO-1) and melanoma-associated antigen (MAGE-A). TCR-T therapy targeting NY-ESO-1 showed an average response rate of 47% in patients suffering from melanoma and synovial sarcoma, without significant toxicities[17, 18]. TCR-T therapy targeting MAGE-A3 in patients with metastatic melanoma resulted in 4 out of 7 patients showing partial responses, but the other three patients developed severe neurotoxicity leading to the death of two of them[19]. In a separate trial, two patients infused with TCR-T targeting MAGE-A3 developed lethal cardiovascular toxicities[20]. To mitigate on-target off-tissue toxicities, numerous trials are investigating targeting neoantigens that are exclusively expressed in tumour tissues[21].

A significant limitation of TCR-T therapy is the requirement for HLA matching. Patients must express the targeted antigen with the specific HLA haplotype. Currently, the majority

of clinical trials are restricted to prevalent HLA alleles, such as HLA-A*02:01, present in 47% of Caucasians and 17% of African Americans[22].

1.2 CAR T cell therapy

Chimeric antigen receptor T cell therapies are based on the genetic modification of T cells to express an antigen receptor capable of recognising a specific surface antigen expressed on the patient's tumour cells. Following *ex vivo* expansion, these CAR T cells are reinfused into the patient with the expectation that they will selectively recognise the target antigen and kill the tumour cells more effectively.

1.2.1 Evolution of CAR design

CAR T cells are generally designed in a modular manner, typically comprising an extracellular antigen-binding domain, a hinge domain, a transmembrane domain, and one or more intracellular domains[23–25]. The most common extracellular antigen-binding domain utilises a single-chain variable fragment (scFv) derived from an antibody. The typical scFv format is composed of variable light (V_L) and variable heavy (V_H) domains from a monoclonal antibody, linked by a flexible peptide sequence. The scFv is expressed as part of the CAR on the T cell surface and it recognises tumour antigens expressed on the tumour cell surface. In contrast to TCR-T cells, which bind to intracellular or extracellular peptides presented by the MHC complex, CAR T cell activation is triggered by the direct interaction of the scFv with the surface tumour antigen, making the process MHC-independent[23]. The strength of the CAR T cell activation depends on the scFv affinity, which can lead to high T cell potency but also premature exhaustion and on-target off-tumour toxicities. Decreasing the scFv's affinity by mutagenesis has been used to diminish reactivity against normal tissues[23]. The extracellular scFv domain is connected to the transmembrane domain via a flexible hinge

sequence. The main purpose of the hinge sequence is to provide flexibility to access the targeted antigen and achieve optimal immunological synapse formation. The choice of hinge length is then dependent on the targeted antigen, with longer hinge sequences used when targeting membrane-proximal epitopes and shorter hinges for membrane-distal epitopes[23]. The hinge domains are usually designed using immunoglobulin-like domains, such as IgG1 and IgG4, and CD28 or CD8 alpha domains. The transmembrane domain anchors the CAR to the T cell membrane and connects the scFv with the intracellular domains, providing stability to the receptor CAR. The most widely use transmembrane domains are CD28 and CD8 alpha. Notably, the transmembrane domain can influence CAR T cell stability and synapse formation[23]. The intracellular domains, also known as endodomains, consist of costimulatory and signalling domains responsible for initiating T cell activation following antigen encounter. Significant research efforts have concentrated on the identification of optimal endodomains to enhance CAR T cell function, resulting in the development of four distinct generations of CAR T cells[23,25,26].

The first CAR T cells to be designed, known as first generation CAR T cells, consisted of an scFv linked to the CD3ζ signalling domain, which can deliver a potent signal 1. Upon antigen recognition by the scFv component, CAR T cells undergo activation, initiating an anti-tumoral response characterised by the release of various cytokines, including interferon gamma, tumor necrosis factor alpha, and interleukins. This activation not only promotes the proliferation of CAR T cells but also facilitates the recruitment of other immune cells to the tumor microenvironment, enhancing overall immune activity. Moreover, CAR T cells execute precise tumor killing through the expression of membrane-bound tumor necrosis factor family ligands and the secretion of granules containing perforin and granzymes. Perforin creates pores on the target cell membrane, allowing pro-apoptotic granzymes to enter the cytoplasm of tumor cells and induce their apoptosis, effectively eliminating the tumor cells upon antigen engagement[27]. These first-generation CAR T cells induce cytolysis *in vitro*, but they

rapidly became anergic, with reduced IL-2 cytokine production and proliferation upon antigen exposure. In clinical trials, they failed to demonstrate robust cytotoxicity and persistence[28–30]. The incorporation of an intracellular costimulatory domain upstream the CD3ζ signalling domain created the second generation CAR T cells, resulting in improved cytolysis, clonal expansion, IL-2 secretion, and persistence[25, 28]. This endodomain is usually derived from the CD28 family (CD28[31] and inducible costimulator (ICOS)[32, 33]) or the tumour necrosis factor receptor family of genes (4-1BB[34], OX40[33] or CD127[35]) and mimics the co-stimulation (signal 2) usually provided during TCR recognition by antigen presenting cells[36]. Clinical studies have shown that CD28ζ-CAR T cells exhibited rapid T cell activation and terminal differentiation, whereas 4-1BBζ-CAR T cells displayed reduced effector differentiation and tonic signalling leading to prolonged persistence[23, 25, 37]. The next generation of CAR T cells were designed to express two costimulatory domains simultaneously aligned in cis to enhance tumour toxicity and increase persistence[23, 25, 28] (Figure 1.1). A phase I clinical trial demonstrated better performance by a third generation CD19 targeting CD28-BBζ-CAR compared to the second generation CD28ζ-CAR[31] . Other ongoing trials have shown promising safety profiles and will provide information on persistence[38, 39]. However, several other studies have reported mixed results, showing no striking advantages over the use of second generation CARs[37].

Fourth generation CAR T cells, referred to as TRUKs (T cells redirected for universal cytokine-mediated killing), are based on the second generation CAR T cells but incorporate a constitutive or inducible transgenic expression cassette to produce cytokines such as IL-12[40],[41]IL-18 or IL-15[42] (Figure 1.1). This generation of CARs is particularly relevant for the treatment of solid tumours since the release of cytokines can modulate the tumour microenvironment (TME)[25, 43].

Currently, the most widely adopted CAR designs follow the second generation structure, incorporating scFv-hinge-CD28/4-1BB and CD3ζ domains. In addition to CAR design, the
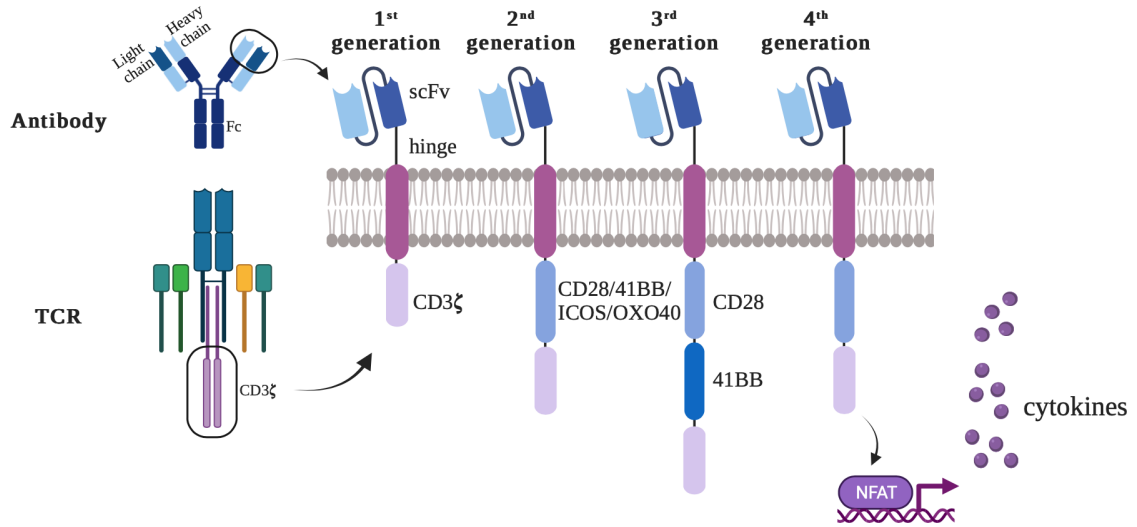
Figure 1.1: Design and evolution of chimeric antigen receptor (CAR) T cells. The single-chain variable fragment (scFv) derives from the variable heavy and light chains from an antibody and are linked to the transmembrane domain through a flexible hinge sequence. The CD3ζ domain derives from the T cell receptor intracellular domains, forming the first generation CAR T cells. Second generation CAR T cells incorporate an intracellular signalling domain, while third generation CARs incorporate two or more intracellular domains. Fourth generation CAR T cells are generally designed as a second generation CAR with the capacity to produce cytokines.

promoter also plays a key role in defining CAR T cell fate. High CAR expression levels are known to affect cell proliferation and anti-tumour activity through tonic signalling, a constitutive antigen-independent activation signal[26,37]. The tonic signal of CAR T cells containing the CD28 intracellular domain may lead to exhaustion and rapid differentiation, whereas 4-1BB tonic signalling can also induce exhaustion to a lesser extent, and T cell apoptosis[26,34,44]. By contrast, weaker promoters can reduce CAR T cell expression, resulting in increased *in vivo* anti-tumour activity[26,34,45].

1.2.2   Manufacturing of CAR T cells

CAR T cell manufacture requires the isolation of pure T cells from the patient's blood, expression of the CAR gene and *ex vivo* expansion of the CAR T cells to adequate numbers

prior to reinfusion into the patient. Usually, leukapheresis is the chosen method for collecting leukocytes, and enrichment of T cells is usually achieved through magnetic separation using CD8 and CD4 beads. The cellular composition of the collected cells is crucial for successful product manufacture. Several technologies, using viral and non-viral genetic engineering tools, have been developed to integrate the CAR gene into the purified T cells. Viral transduction is a consolidated method for genetically engineering CAR T cells. Lentiviral vectors have been used to produce the FDA-approved CAR therapies Abecma, Breyanzy, Carvikty and Kymriah, whereas gammaretroviral vectors were used for Tecartus and Yescarta[23,37]. These vectors offer large packing capacity enabling the delivery of multicistronic CAR constructs while achieving high titters. However, GMP-compliant manufacturing of these vectors is associated with high costs, and safety concerns arise regarding the persistence of residual viral vectors after transduction and potential genotoxicity associated with biased integration of retroviral vectors within the promoter and growth control genes[43]. In clinical settings, manufacturing processes are often carried out in semi-automated or automated systems. Non-viral integration can be achieved using the Sleeping Beauty or piggyBac transposon systems, which enable stable integration of the CAR gene while reducing immunogeneicity and production costs. However, electroporation of the transposon-based vectors can decrease cell viability, and the longer expansion protocols may lead to T cell differentiation and impaired activity[37]. RNA transfection has been used for the transient transfection of CAR genes for up to 1 week to study associated cytotoxicities and minimize side effects, however, the short expression time limits its clinical application. Most recently, CRISPR/Cas9 has been used to replace the natural TCR with the CAR gene, favouring a more physiological CAR expression. The substitution of the TCR with the CAR decreased the tonic signalling or antigen-independent activation, which led to reduced differentiation and exhaustion of the cells[37]. New protocols are being tested to shorten

manufacturing and expansion times to promote more memory and stem cell-like phenotypes in the infused product, which has been associated with improved treatment outcome[46, 47].

1.2.3 Clinical outcomes of CAR T cells for haematological malignancies

CAR T cell immunotherapy has shown promising results in the treatment of haematological tumours with the majority of FDA-approved products targeting CD19, an antigen restricted to the B cell lineage. CD19 is uniformly expressed in most B cell malignancies including relapsed/refractory (r/r) B-cell acute lymphoblastic leukaemia (B-ALL)[48], large B cell lymphoma (LBCL)[49], mantle cell lymphoma (MCL)[50] and follicular lymphoma[51]. Treatment with anti-CD19 or anti-B-cell maturation antigen (BCMA) CAR T cells results in the depletion of non-malignant B cells and plasma cells expressing these target antigens, leading to B cell aplasia. This toxicity is not lethal in humans and can be managed with the intravenous infusion of immunoglobulin[52]. The first FDA-approved CAR T cell therapy, granted in 2017 for the treatment of diffuse large B-cell lymphoma (DLBCL), was tisagenlecleucel, branded in the US as Kymriah. Autologous enriched T cells were transduced with a lentiviral vector encoding for a CD19 CAR. The CD19 CAR was designed as a a second generation CAR comprising of the anti-CD19 scFv derived from the monoclonal antibody FMC63, along with the intracellular domains 4-1BB and CD3ζ. The first clinical trial administering tisagenlecleucel in patients with DLCBL reported response rates of 64%, with 43% of the participants achieving complete response (CR) at 6 months. Sustained remissions at 28.6 months were achieved in 86% of responders[49]. A second, larger study in patients with DLCBL who had received two to three lines of treatment prior to CAR T cell infusion, reported a response rate of 52%, with 40% achieving CR and 12% experiencing partial responses. These results led to the FDA approval of tisagenlecleucel for DLCBL patients[53]. The second FDA-approved CAR T cell therapy, also granted in 2017 for the treatment of r/r LBCL, was Axicabtagene ciloleucel (Axi-cel), marketed in the US as

Yescarta. Autologous T cells were transduced with a gammaretrovial vector encoding a second generation anti-CD19 CAR, featuring the FMC63 scFv and the intracellular domains CD28 and CD3ζ. A trial administering Axi-cel to patients with refractory LBCL reported an 82% response rate, with 54% of the patients achieving CR[54]. Since then, two more anti-CD19 CAR T cell products have been approved for clinical use, Tecartus approved in 2020 for the treatment of r/r MCL and ALL[55], and Breyanzi approved in 2021 for the treatment of LBCL[54]. More recently, two CAR T cell products targeting BCMA were approved for the treatment of multiple myeloma under the names Abecma[56] and Carvykti[57]. Despite the success of these treatments, relapse and toxicity are common issues in the treatment of B cell malignancies with anti-CD19 CAR T cells. Relapses can be classified as CD19-positive or CD19-negative. The minority of cases are CD19$^-$ relapses, caused by antigen scape modulated by the mutation or alternative splicing of CD19 leading to loss of the targeted epitope or by myeloid lineage switch leading to the complete downregulation of the CD19 expression[47,58]. Bispecific anti-CD19, anti-CD20 CAR T cells have been shown to overcome CD19$^-$ relapse in preclinical models[59].

In contrast, CD19$^+$ relapses are associated with poor proliferation and persistence of the CAR T cells, leading to restricted anti-tumour activity and transient B cell aplasia. Several factors may influence CAR T cell persistence, including the potential immunogenicity of murine scFvs, the choice of intracellular costimulatory domains, with 4-1BBζ CAR T cells showing improved *in vivo* persistence[58]. However,the most important factor affecting T cell persistence is thought to be the differentiation status of T cells in the infused CAR T cell product.

T cell differentiation models propose that upon activation, naïve human T cells (T_n) differentiate into various memory and effector cells types, with proliferation and self-renewal capacity decreasing as differentiation progresses. T_n can differentiate into stem-like memory (T_{scm}) and central memory T cells (T_{cm}), which have limited effector function but long-lasting

persistence. These cells further differentiate into effector memory (T_{em}) and lastly into terminally differentiate effector memory expressing CD45RA (T_{emra}), which exhibit enhanced effector capacity but limited persistence[60]. In parallel to differentiation, chronic T cell activation can lead to T cell exhaustion, characterised by the expression of inhibitory receptors such as PD-1, LAG-3 and TIM-3. Although exhaustion can be induced at any stage of differentiation, exhaustion in terminally differentiation subsets is correlated with a lack of proliferation and effector functions[61]. In patients, the presence of T_{scm} clones in the infused product has been correlated with early anti-leukemic responses and long-term responses[46]. In addition, reduced expression of exhaustion markers on the cell surface of the pre-infused CAR T cells has also been linked to durable remission[62]. Therefore, there is a growing interest in producing CAR T cell products with stem-like characteristics, which have stronger self-renewal capacity and anti-tumour ability, while exhibiting less exhausted phenotypes[47]. Several strategies are being developed to produce less differentiated and exhausted CAR T cell products, including the *ex vivo* expansion in IL-15/IL-17 as opposed to IL-2[60, 63], and the mutation of immunoreceptor tyrosine-based activation motif (ITAMs) to fine-tune premature T cell differentiation and exhaustion[64].

1.2.4   Challenges for targeting solid tumours

The positive outcomes achieved in the clinical trials using the CD19 targeting CAR T cell products have established CAR T cell therapy as a mainstream treatment for managing aggressive lymphomas, but these results have not been translated to solid tumours. CAR T cell trials in solid tumours targeting a variety of TAA in various cancer types have reported results ranging from no efficacy to complete remission. For instance, partial remissions have been reported following treatment with EGFR targeting CAR T cells in patients suffering from non-small lung cancer[65], whereas no response was observed in glioblastoma tumours[66]. Interleukin 13 receptor alpha2 (IL13Rα2) targeting CAR T cells administered intracranially

to glioblastoma patients, led to complete responses, but these responses were short-lived resulting in tumour relapse[67]. Anti-GD2 CAR T cells administered to glioblastoma patients achieved a complete response in 3 out of the 11 treated patients[68] and stable disease in 6 out of 11 neuroblastoma patients[69]. Human epidermal growth factor receptor 2 (HER2) targeting CAR T cells achieved stable disease in 4 of the 17 patients suffering from sarcoma[70]. The poorer results in solid tumours can be attributed to the many challenges associated with the solid TME, including tumour heterogeneity, difficulties in CAR T cell trafficking and extravasation to the tumour site, the presence of immunosuppressive cells and cytokines within the TME, as well as the depletion of nutrients and oxygen. The first impediment is on-target off-tumour toxicity caused by the recognition of TAA in normal tissue by the CAR T cells. Ideally, a suitable target would be tumour-restricted, however, this is rare. TAAs are typically overexpressed heterogeneously in tumour cells, with lower expression in non-malignant tissues leading to on-target off-tumour toxicities that are harder to control compared to haematological malignancies, where B cells are dispensable[37]. This was exemplified by the death of a patient suffering from metastatic colon cancer after the administration of anti-HER2 CAR T cells, which were sequestered to the lungs expressing low levels of HER2 causing lethal pulmonary toxicity[71]. Careful monitoring of CAR T cell is crucial to strike the balance between effective anti-tumour efficacy without excessive toxicity. Despite the expression of TAA in normal tissues, TAA expression heterogeneity poses a significant challenge. For example, EGFRV III is mutated in about 30% of the glioblastoma tumours, leading to antigen escape and tumour recurrence after CAR T cell treatment[72]. Strategies have been developed to overcome antigen escape, including the use of dual and tandem CARs targeting multiple TAAs and CAR T cells capable of secreting bispecific T cell engagers (BiTEs) to attenuate off-target toxicities[24]. Another limitation is the impaired trafficking and infiltration of CAR T cells into solid tumours. Tumours often present aberrant vasculature with high levels of pro-angiogenic factors associated with leaky vessels, disrupted

blood flow, increased tumour pressure and dysregulated oxygen supply. Additionally, tumour endothelial cells may downregulate adhesion molecules, such as intracellular adhesion molecule 1 (ICAM1) and vasculature cell adhesion molecule 1 (VCAM1), impairing T cell extravasation from blood vessels into the tumour[73]. After T cell extravasate, they may not encounter the target TAA due to the dense tumour stroma. T cell infiltration is hampered by the presence of hyaluronan and collagen deposits within the tumour stroma, creating a physical barrier against T cell infiltration and affecting their anti-tumour efficacy and proliferation capacity[74]. Indeed, ectopic expression of heparinase, an extracellular matrix degrading enzyme, in anti-GD2 CAR T cells have enhanced infiltration and survival rates in preclinical models[75], as have fibroblast activation protein (FAP)-targeting CAR T cells, which deplete FAP-expressing tumour associated fibroblasts[76]. Besides the physical barriers, inefficient infiltration is partly attributed to the mismatched migratory signals between the chemokine ligands expressed in the tumours and the chemokine receptors (CCRs) present on CAR T cells. The ectopic expression of CCR4 and CCR2 has proven effective in enhancing CAR T migration and infiltration in preclinical models[28,77].

Once CAR T cells have successfully infiltrated the tumour stroma, they face the challenges of an immunosuppressive TME. The TME can be populated by immunosuppressive cells such as T regulatory cells (Tregs), myeloid-derived suppressor cells (MDSCs) and M2 tumour-associated macrophages (TAMs). These cells facilitate tumour growth by secreting cytokines and chemokines, including VEGF, IL-4, IL-10 and TGF-β[78]. To address CAR T cell inhibition by these cells, TRUCKs have been designed to enhance the secretion of pro-inflammatory cytokines, such as IL-12[79] or IL-18[41], to reshape the tumour TME. The expression of a TGF-β dominant receptor in prostate-specific membrane antigen (PSMA) targeting CAR T cells has also shown increasing proliferation and persistence[80].
A final barrier is the scarcity of nutrients and oxygen within the TME. Hypoxia boosts tumour proliferation and increases the acidity of the TME. In a nutrient-deprived TME, metabolic

stress occurs, resulting in the upregulation of inhibitory receptors, such as PD-1, and the recruitment of immunosuppressive cells by the tumour, ultimately decreasing the anti-tumour activity of CAR T cells[81]. Ongoing research is now focusing on understanding the tumour immunometabolism for the development of improved immunotherapies.

1.3 Critical role of imaging in advancing cancer immunotherapy

The effectiveness of CAR T cell therapy in treating solid tumours has proven to be unsatisfactory compared to the success in treating haematological malignancies. This disparity can be attributed to the unique challenges faced by the CAR T cells in solid tumours, including trafficking and extravasation to the tumour site, proliferation, and persistence within hostile microenvironments. Given that CAR T cells are "living drugs", they undergo intricate dynamic processes. Thus, understanding their kinetics and biodistribution is paramount to developing more efficacious treatments. A considerable research gap persists concerning the comprehensive whole-body biodistribution of the infused cells, their capacity to relocate within the body, the dynamics of this migration, their ability to penetrate and expand at the tumour site, the underlying causes of on-target off-tissue toxicities, as well as the critical cell numbers required to induce tumour remission[82–84]. Current research efforts primarily focus on monitoring disease progression, evaluating CAR T cell expansion and persistence in peripheral blood, and measuring cytokines in serum to assess CAR T cell functionality and associated toxicities. However, these approaches do not provide real-time insights into the spatial biodistribution, viability, and kinetics of the infused CAR T cells at the tumour site[83]. Therefore, there is a pressing need to develop non-invasive imaging tools capable of instantaneously assessing key parameters, such as the spatial localization of the infused CAR T cells, their ability to penetrate tumours, their viability,

functionality, quantity and persistence over time at the tumour site. By monitoring CAR T cell biodistribution and functionality in clinical trials, these imaging tools could emerge as a valuable tool to distinguish responders from non-responders and manage treatment-related adverse effects[55,82]. Numerous imaging methods have been developed for non-invasive monitoring of CAR T cells, with nuclear imaging providing higher sensitivity, excellent tissue penetrance, and potential for clinical translation.

1.4 Imaging techniques

1.4.1 Optical imaging

Optical imaging stands out for its affordability, sensitivity, and ease of execution. Bioluminescence (BLI) is based on the detection of photons emitted by the oxidation of luciferin by the luciferase reporter protein in the presence of ATP and oxygen[85–87]. Luciferase is integrated into the target cells, allowing for the tracking of cells upon exogenous administration of luciferin at the desired imaging time point. While BLI provides spatial and temporal localization of live cells only since the reaction depends on ATP and functional enzymes[85], it offers poor resolution and quantitation is unreliable due to the scattering of light in the body[87]. Despite these limitations, preclinical research widely employs BLI owing to its high sensitivity, cost-effectiveness and swift imaging capabilities. BLI is widely used to monitor tumorigenesis and metastasis by quantifying relative changes in light emission over time[87]. It has also been used to monitor the biodistribution of hypoxia-sensing CAR T cells in a head and neck squamous cell carcinoma mouse model[88] and of human-mesothelin targeting CAR T cells in pleural mesothelial mouse models[89]. However, its application remains confined to preclinical studies due to the limited tissue penetrance of light and the non-mammalian origin of the reporter protein[85–87]. In contrast, radionuclide-based imaging offers a powerful alternative.
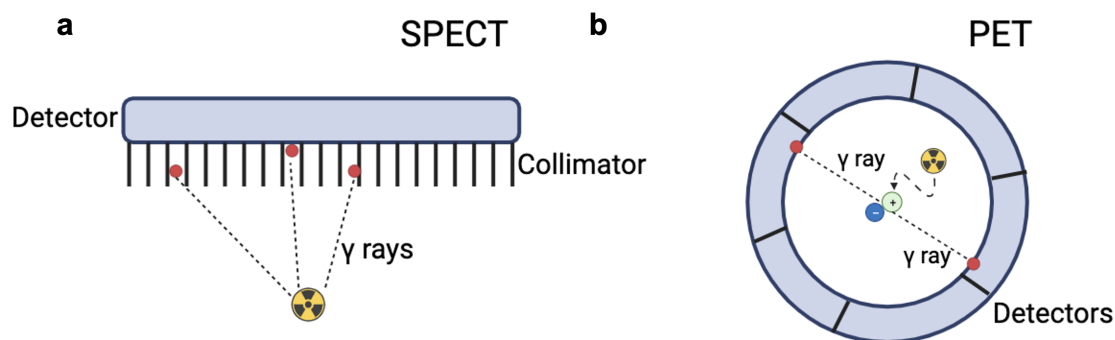
Figure 1.2: Schematic illustrating the principles of SPECT and PET detection . a) In single photon emission computer tomography (SPECT), gamma-ray photons emitted from a radiotracer are detected by a rotating gamma counter. Diagonal gamma rays collide with the collimator and are not detected , increasing the resolution. b) In positron emmission tomography (PET), positrons from the radiotracer, annihilite with electrons, releasing two gamma-ray photos in opposite directions that are detected simultaneously by a ring of detectors.

1.4.2 Radionuclide-based imaging

Positron emitted tomography (PET) and single-photon emitted tomography (SPECT) enable real-time, non-invasive tracking of radiolabelled particles within living organisms. Both techniques provide 3D images with high sensitivity, no tissue penetration constraints and excellent translational potential. Besides they can provide accurate quantitation due to the constant decay of radionuclides[84]. SPECT imaging can be used to image γ ray-emitting radionuclides. The use of collimators prevents the detection of diagonal γ ray-photons, ensuring accurate detection of the photon's origin. This yields high spatial resolution but decreases sensitivity. In preclinical studies, SPECT imaging offers submillimetre resolution, while clinical scanners offer resolutions between 5-12 mm. Among γ emitting radionuclides, technetium-99m (^{99m}Tc) is the most commonly used due to its favourable characteristics, including a short 6-hour half-life, widespread availability through generator production, and good emission properties, with over 89% gamma radiation at 140 keV[90,91] (Figure 1.2 a).

Multiplex imaging can be performed by combining multiple radionuclides with distinct energy emissions, facilitating the imaging of multiple radioactive compounds within a single subject[90]. PET imaging is tailored for positron (β^+)-emitting radionuclides. In contrast to SPECT, where individual photons passing through the collimator are measured, PET imaging relies on the coincidental detection of two gamma photons by a ring of detectors. PET radionuclides undergo decay, emitting positrons from the nucleus in random directions. Upon encountering electrons, positron/electron pairs mutually annihilate, emitting two gamma photons at an angle of approximately 180 degrees from each other, each with an energy of 511 keV. The annihilation's location is detected by the ring of detectors, which approximates the location of the PET radionuclide. The extent of positron travel before annihilation hinges on the radionuclide-specific positron energy, resulting in reduced resolution compared to SPECT[90,91]. Nevertheless, PET offers better sensitivity since it does not require collimators. Depending on the radionucleide, PET offers comparable resolution to SPECT in preclinical settings, while in clinical settings it offers resolutions of 3-6 mm. Quantitative accuracy of PET is higher than SPECT. Common PET radiotracers include ^{11}C, ^{18}F widely used in the clinic, and the generator-based ^{68}Ga for preclinical studies[90,91] (Figure 1.2 b). Despite the lower sensitivity and spatial resolution of clinical SPECT compared to PET, SPECT remains widely used in the clinic due to its cost-effectiveness and the widespread availability of tracers. However, the advent of total-body PET has rendered it highly appealing for *in vivo* cell tracking, offering vastly improved sensitivity and lower radiation doses[90,91].

1.4.3   Anatomical imaging

SPECT and PET imaging are often used in combination with high-resolution anatomical imaging like computed tomography (CT). CT relies on the distinct X-ray attenuation exhibited by tissues of varying density, yielding tissue contrast and anatomical information. CT produces high-resolution 3D images (0.5 mm clinically and 0.1 mm preclinically) and is

usually integrated with SPECT and PET imaging to provide anatomical context. In cases where tumour density significantly differs from the surrounding tissues, CT can be used to assess tumour size and growth[82,90]. However, the disadvantage of CT lies in the radiation dose as a result of the ionising X-ray radiation.

1.5   Non-invasive *in vivo* imaging of CAR T cells

Non-invasive *in vivo* imaging of cell-based immunotherapies using radionuclides can be accomplished through two primary approaches: direct cell labelling, involving the introduction of a labelling agent directly into the cells (Figure 1.3 a); or indirect cell labelling, achieved by introducing a reporter gene allowing the cells to be imaged upon addition of a contrast agent (Figure 1.3 b). Both methods provide spatial and temporal information on cell dynamics.
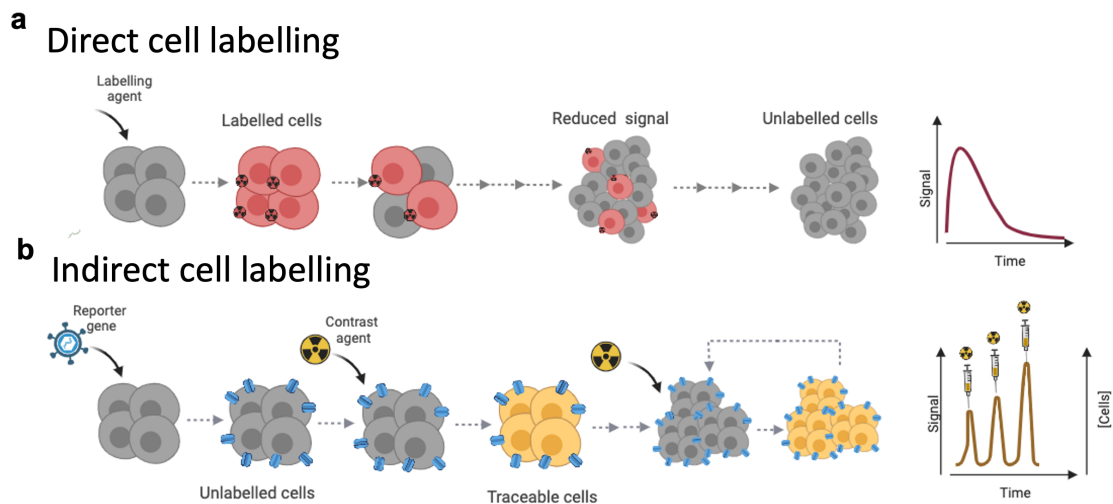
Figure 1.3: Cell labelling strategies for nuclear imaging. a) Direct labelling of cells allows for the short-term imaging of labelled cells. However, as cells proliferate the signal dilutes and the radionuclide undergoes decay until the cells are untraceable. b) Indirect labelling can be achieved with the incorporation of a reporter gene within the cells' genome, allowing for repetitive imaging over time. Upon injection of the reporter probe, the cells become traceable cells and can be imaged for as long as their lifespan. This type of labelling reports on cell proliferation as the signal is proportional to the number of traceable cells.

1.5.1 Direct labelling

Direct cell labelling involves the *ex vivo* radiolabelling of the target cells, followed by their subsequent infusion into the subject. Through *in vivo* imaging, the biodistribution of the cells can be assessed over time[82,92]. Among the various imaging modalities, radionuclide imaging is the most sensitive modality to visualize directly labelled cells in mammals[82]. Direct labelling with radioisotopes can be accomplished using different methods[82,90,93]. Radiotracers can be directly bound to the cell membrane or a specific receptor[94]; alternatively, radiotracers may penetrate the cell membrane passively and become trapped within the cells[95]. Lastly, uptake of the radiotracer can be achieved through active pumps or ion channels located on cell membranes[96].

In clinical settings, direct labelling of T cells has been widely used over the last decades. For instance, ^{111}In-oxine, a higlhy lipophilic molecule able to penetrate the cell membrane, has been utilised to label leucocytes for detecting hidden infections in patients[95], to trace tumour-infiltrating lymphocytes in patients with metastatic melanoma[97], and to monitor HER2-specific T cells in a patient with metastasised ovarian cancer[98]. Parent-Pereira et al. (2011), demonstrated the challenge of tumour infiltration by administering ^{111}In-tropolone labelled anti-MUC1 and anti-ErbB CAR T cells through different routes. Intravenous administration of the CAR T cells led to infiltration of low number of cells in the tumours compared to regional administration[99].

However, given that SPECT imaging has shown insufficient sensitivity for monitoring CAR T cells in clinical practice, the focus has shifted towards the development of imaging tools for PET imaging[84].

To overcome sensitivity limitations, [89]Zr-oxine, the PET counterpart of ^{111}In-oxine, was developed and rapidly implemented preclinically due to its similar safety profile to ^{111}In-oxine[100]. PET offers better spatial resolution and sensitivity in clinical instruments, along with the capability for absolute quantitation. [89]Zr-oxine has been employed for

tracking CAR T cells preclinically thanks to its moderate long half-life (78.4 hours), enabling the monitoring and evaluation of CAR T cells efficacy for over a week[90,92]. Weist at al. (2018), demonstrated the robust and compatible labelling of CAR T cells in preclinical models of glioblastoma (IL13Rα2-targeted CAR T cells) and prostate cancer (PSCA-targeted CAR) using ^{89}Zr-oxine[100]. More recently, ^{89}Zr-oxine has also been used to label T cells without compromising cell proliferation or anti-tumour cytotoxicity[101]. Nonetheless, the accumulation of positron emitting cells poses a safety concern for its clinical translational since CAR T cells tend to accumulate in the liver and spleen for several days. This issue can potentially be mitigated by using radiotracers with shorter half-lives[102,103]. For example, Wang et al. (2021), showed the correlation between the biodistribution patterns of CD19-CAR T cells labelled with ^{68}Ga (half-life of 68 min), and ^{89}Zr (half-life of 78.4 hours). While ^{68}Ga-labelled CAR T cells could be tracked for only 6 hours, the absorbed dose was reduced by 124-fold, resulting in increased cell viability. This illustrates the potential application of ^{68}Ga for tracking cells in humans through PET imaging[103]. However, passive diffusion of radionuclides across the membrane via lipophilic carriers, like tropolone and oxine, may lead to chemotoxicity and reduced sensitivity in the event of radionuclide efflux. As an alternative, Bansal et al. (2011), developed ^{89}Zr-desferrioxamine (DFO), which can covalently bind to the cell membrane proteins reducing the risk of chemotaxis toxicities and radiotracer efflux[104]. This method was later tested by Lee et al. (2020), on Jurkat- and PBMC-derived CAR T cells, showing indeed decreased accumulation of free ^{89}Zr in bone and liver, after labelling the CAR T cells with ^{89}Zr-DFO instead of ^{89}Zr-oxine. However, proliferation of the labelled cells was reduced over time[105]. A third alternative for the direct labelling of CAR T cells involves the use of radiolabelled nanoparticles, which are incorporated inside the cells via endocytosis or electroporation[84]. Examples include the conjugation of Copper-64 to gold nanoparticles, and the use of superparamagnetic iron oxide nanoparticles for tracking CD19-CAR T cells biodistribution through PET imaging[106]. The advantage

of using nanoparticles lies in the reduce radionuclide efflux while also preserving the cell membrane proteins[84].

Direct labelling stands as a simple method, circumventing the need for genetic modification of the target cells and enabling the integration of the probe at any stage during the CAR T cell production, thus facilitating clinical application[102]. Additionally, it allows for the incorporation of high numbers of radionuclides per cell. However, certain limitations exist, including the inability to assess cell proliferation as the signal gradually dilutes with cell division. Furthermore, the potential for repeated imaging over time is constrained by the radiotracers' half-life. Challenges also arise in determining the spatial location of the targeted cells due to potential radiotracer efflux, unbinding from the cells, and phagocytosis of dead cells[84, 85, 90].

1.5.2   Indirect labelling

Indirect cell labelling requires the incorporation of a reporter gene into the cell of interest through cell engineering. These reporter genes are typically proteins that facilitate uptake (transporter),trapping, or binding (receptors) of radiotracers[85, 90]. Following administration of the tracer, cells become detectable as distinctive hotspots, and repeated tracer injections allow for longitudinal imaging[90, 107]. The permanent integration of the reporter gene enables real-time, *in vivo* monitoring of viable cell populations and their expansion over the lifetime of the cells[85, 90]. However, exogenous tracer administration has a major drawback: it can result in detectable signals in organs responsible for excretion and clearance, potentially leading to a misinterpretation of these signals as indicative of the presence of targeted cells. Additionally, sensitivity can be constrained by the lower amount of radiotracer internalised per cell compared to direct cell labelling[90]. Several reporter genes have been utilised to image CAR T cells via SPECT or PET, the latter being more clinically desirable due to its higher sensitivity in humans. One of the first reporter genes to be developed was herpes simplex

virus type 1 thymidine kinase (HSV1tk), an enzyme-based reporter gene[84,92]. In preclinical studies, HSV1tk has been co-expressed alongside a CAR targeting human PSMA to monitor the biodistribution of CAR T cells *in vivo* using ^{18}F–FEAU and PET imaging. This approach did not only monitor biodistribution and persistence of the cells but could also predict therapeutic outcomes, as a correlation was observed between the PET signal accumulation in tumours and survival time[108]. In 2009, HSV1tk was used for the first time to monitor CD8$^+$ cytotoxic T lymphocytes (CTL) co-expressing HSV1tk and interleukin 13 zetakine gene in a patient diagnosed with glioblastoma multiforme. ^{18}F–FHBG PET imaging was used to monitor CTLs revealing activity at the tumour region and in an unknown secondary tumour site[109]. Similarly, in 2017, this strategy was employed for patients with recurrent glioma[110]. These two studies, however, encountered high background ^{18}F–FHBG signal in the brain before treatment[109,110]. Importantly, HSV1tk acts as a suicide gene, triggering programmed cell death when exposed to ganciclovir. The co-expression of the mutated HSV1-sr39tk with a B7H3 targeting CAR displayed higher specificity for ^{18}F–FHBG and ganciclovir in a human osteosarcoma mouse model, compared to the wild-type reporter gene, showcasing its potential for clinical application[111]. Despite demonstrating feasibility for non-invasive CAR-T cell using HSV1tk, the high background signal and safety concerns related to its viral origin and immunogenicity in humans prompted the development of human-derived reporter genes, such as the human somatostatin receptor 2 (SSTR2) and human norepinephrine transporter (hNET)[92]. SSTR2, a G-protein coupled receptor, can internalise the clinically approved PET radiotracer ^{68}Ga-DOTATOC[84,92].CAR T cells targeting intracellular adhesion molecule 1 were engineered to express the SSTR2 reporter gene. CAR T cells' biodistribution and anti-tumour cytotoxicity were monitored using ^{68}Ga-DOTATOC PET imaging in a metastatic thyroid mouse model. The presence of the reporter gene and PET probe did not affect CAR T cell cytotoxicity, enabling the tracking of T cell expansion. The relatively short half-life of the ^{68}Ga-DOTATOC allowed for the acquisition of high-quality images

within an hour[107]. However, SSTR2 expression in regions like the cerebellum, kidneys, and intestinal tract can result in a significant nonspecific background signal. The sensitivity may also be compromised by the internalisation upon interaction with the substrate. More importantly, SSTR2 is expressed in other immune cells and may repress their function and proliferation[84, 92, 112].

hNET has demonstrated its utility as a reporter gene for long-term imaging of Epstein-Barr virus-specific T cells, using SPECT with the probe ^{123}I-metaiodobenzylguanidine (^{123}I-MIBG) in a murine model of human lymphoma[113]. More recently, donor T cells were engineered to co-express hNET and GFP to establish the limit of detection in a murine model using PET imaging. 3×10^4 to 4×10^4 T cells were detected at the injection site, two hours after administration of the PET tracer ^{18}F-meta-fluorobenzylguanidine[114]. Nonetheless, the elevated nonspecific background signal could limit the practicality of this labelling method depending on the tumour's location, as observed in a study by Badar et al. (2011),where hNET-expressing SupT1 T cells were only discernible 24 hours post administration of the radiotracer probe ^{123}I-MIBG due to the substantial high background[115]. This renders the symporter inappropriate for real-time tracking of adoptive cell transfer (ACT) therapies.

1.5.2.1 The human sodium iodide symporter

To address these challenges, the ideal reporter gene needs to be non-immunogenic and have limited expression in normal tissue to minimise nonspecific background. The human sodium-iodide symporter (hNIS), also known as SLC5A5, is a member of the solute carrier family 5A and fits this criteria. hNIS is a 643-amino acid glycoprotein with a molecular mass ranging from 50-100 kDa depending on its glycosylation status[116]. Sequencing of the hNIS was first completed by Smanik et al. in 1996[117], pioneering its potential use as a reporter or target for imaging and therapy. The hNIS is an intrinsic membrane spanning protein with 13 putative transmembrane helices, an extracellular amino-terminus, and an intracellular
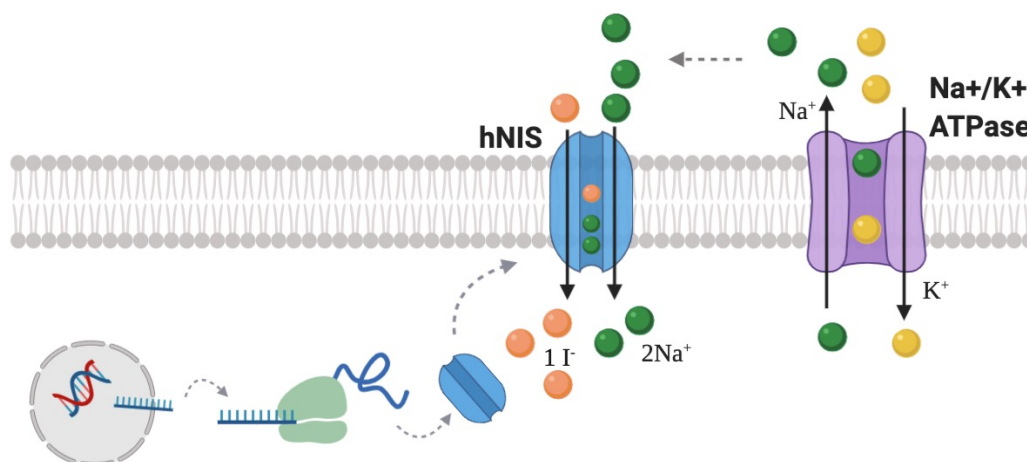
Figure 1.4: Schematic illustrating hNIS expression and mechanism of action . The hNIS needs to be expressed on the cell membrane to be functional. It transports two sodium ions down its electrochemical gradient and one iodide anion against its gradient. The sodium gradient generated by the sodium/potassium ATPase pump is the driving force.

carboxyl-terminus. It efficiently accumulates iodide (I^-) inside the cells using the sodium (Na^+) gradient generated by the Na^+/K^+ ATPase. This energy is used to simultaneously transport one I^- against its electrochemical gradient for every two Na^+ transported down its electrochemical gradient[116, 118] (Figure 1.4). The NIS-mediated transport of I^- can be blocked by competitive inhibitors, such as nitrate and perchlorate[119, 120]. hNIS is naturally expressed in the thyroid and at lower levels in the salivary and lactating mammary glands, as well as in the gastric mucosa[116, 118–121].

The hNIS is widely used therapeutically in clinical medicine due to its ability to concentrate both imaging and therapeutic radionuclides in target cells, an example being the use for almost 70 years of ^{131}I radionuclide therapy for the treatment of metastatic thyroid carcinoma and hyperthyroidism. To enhance radionucleide therapy there is a growing interest in increasing hNIS expression. This can be achieved by using disrupting chemicals or the overexpression of transcription factors, which in turn could improve radioiodide therapy outcomes in cancers that downregulate or lack expression of hNIS, such as de-differentiated and anaplastic thyroid cancers[121–124]. Ectopic expression of hNIS for the treatment of

non-thyroidal cancers has also shown promising results in pre-clinical models[125–127] but this has not yet been translated to the clinic. The hNIS has also been used as a reporter gene for clinical imaging due to its ability to transport a variety of monovalent anions coupled with the short retention time of the radionuclide, limiting radiation dose and toxicity in the targeted cells. Monovalent anions that can be transported by hNIS include the well-studied technetium pertechnetate ($^{99m}TcO_4^-$) and the novel ^{18}F-tetrafluoroborate ($[^{18}F]BF_4^-$), with the transport being significantly enhanced as the size of the monovalent anion approaches that of iodide[120]. $[^{18}F]TFB$ has recently been used to image the thyroid and NIS expression in humans using PET[127,128]. A biodistribution study carried out in five thyroid cancer patients has shown its safety and potential for diagnosis and treatment planning in thyroid disease[128]. $^{99m}TcO_4^-$ has been widely used in the clinic since 1965. It is efficiently transported into NIS-expressing cells due to its similar size and charge to I^- and it has a convenient half-life of 6 hours[129–132]. In addition, $^{99m}TcO_4^-$ is a cheap radiotracer that can be detected with widely available SPECT scanners, which makes it a good candidate for imaging NIS-expressing CAR T cells. Emami et al. (2016) demonstrated the utility of this approach for CAR T cell imaging by co-expressing a PSMA single-chain variable fragment with the hNIS imaging reporter gene in a retroviral vector. They showed the spatial accumulation of $^{99m}TcO_4^-$ radiolabelled CAR T cells in a xenograft prostate cancer preclinical model using SPECT/CT, demonstrating the correlation between CAR T cell accumulation at the tumour site and tumour rejection[133]. Similarly, Kurtys et al. (2018) and later Volpe et al. (2020), co-expressed the hNIS with an anti-ErbB CAR-T to quantify tumour retention in triple-negative human breast cancer preclinical models. CAR T cell infiltration was monitored longitudinally by PET imaging using $[^{18}F]BF_4^-$. Similar intracellular uptake was measured when exposed to $[^{18}F]BF_4^-$ and $^{99m}TcO_4^-$, these CAR T cells remained functional and detectable at the tumour site for over two weeks, proving the feasibility of using $[^{18}F]BF_4^-$ to image the hNIS reporter by PET imaging[134,135]. This was further confirmed by another study where hNIS was co-expressed

with a CAR T cell targeting anti-B-cell maturation antigen to monitor tumour infiltration in a multiple myeloma mouse model. As a control they used K562 to establish negative control tumours. $[^{18}F]BF_4^-$ PET imaging showed accumulation of CAR T cells at the tumour site but not in control tumours which correlated with the survival difference[136].

1.5.3 Non-invasive quantification of CAR T cells

Currently, the surveillance of adoptively transferred CAR T cells relies on monitoring disease progression, assessing levels of cytokines and immune markers in serum, and monitoring CAR T cell expansion and persistence in peripheral blood or in biopsy specimens. However, these measurements do not provide information about spatial biodistribution of the CAR T cells. Additionally, in the case of solid tumours, quantitation of CAR T cells in peripheral blood may not represent the extent of tumour infiltration. While tumour biopsies offer insights into CAR T cell infiltration, they only provide a snapshot of the entire tumour[65, 83, 89]. As a result, there is growing interest in the development of non-invasive methods to enable real-time and non-invasive monitoring of CAR T cell kinetics, infiltration and expansion, to manufacture more effective immunotherapeutic products. CAR T cell expansion and persistence are considered crucial determinants of long-term efficacy[137]. Despite their importance, standardised protocols for monitoring CAR T cells post-infusion are still lacking in clinical practice. Although, several detection methods have been employed in clinical trials to monitor cell kinetics, with varying time points and testing frequency, the two main technologies utilised for the detection of CAR T cells in peripheral blood, bone marrow, and spinal fluid are quantitative polymerase chain reaction (qPCR) assays and multiparametric flow cytometry[138]. qPCR uses target-specific primers to measure vector copy number in gDNA from patients' blood over the course of the CAR T cell treatment[139]. They require a positive control for relative quantitation[140]. While it is a rapid method, it does not provide real time data, and is often used in combination with flow cytometry in clinical settings.

qPCR effectively measures CAR transgene copy numbers, monitoring concentration of CAR transgene copies over time[138, 139]. Despite its robustness, it tends to overestimate the number of functional CAR T cells, as it does not measure cell surface CAR T cell expression, which not only depends on vector copy number but also the viral promoter and post-transcriptional modifications[139]. Conversely, flow cytometry enables quantitation and phenotyping of T cells expressing the CAR protein. Multiparametric flow cytometry is routinely used for identifying CAR T cell abundance in peripheral blood or bone marrow aspirates. Utilizing CAR-specific reagents, absolute CAR T cells numbers can be quantified with high sensitivity. It can also provide information on the different T cells sub populations (helper or cytotoxic) and status of the T functionality of the cell product (activation, exhaustion)[138, 141]. These two approaches have offered valuable insights into CAR T cell expansion and persistence in clinical trials for haematological malignancies. However, for solid tumours, monitoring of CAR T cells in peripheral blood may not accurately represent infiltration at the tumour site[65, 83]. Tumour biopsies can provide information on the biodistribution of infiltrating CAR T cells, as well as the antigen expression levels in tumour cells through immunohistochemistry[65, 89, 142, 143]. Apart from being a highly invasive procedure, tumour biopsies may be limited by the anatomical tumour location[65]. Serial and multiple biopsies may not be feasible, especially in metastatic sites[89]. Besides, biopsies may not capture the true tumour heterogeneity, making quantitation of infiltrating CAR T cells challenging. Thus, there is a need to develop non-invasive dynamic methods to quantify CAR T cell infiltration and expansion in solid tumours. Non-invasive nuclear imaging methods for relative quantitation of infiltrating CAR T cells has been developed in preclinical models[92, 107, 113]. The quantitation relies on establishing a standard curve correlating labelled T cells doses with the imaging signal. The linear relationship between imaging signal and T cell dose is then leveraged to estimate the amount of T cells infiltrating the tumours. Doubrovin et al. (2007), employed this strategy to estimate the number of cytotoxic T cells co-expressing hNET and GPF (CTL-hNETiGFP),

that could infiltrate EBV$^+$ xenografts[113]. They first established the standard curve by intratumorally injecting different doses of CTL-hNETiGFP cells, followed by intravenous injection of ^{124}I-MIBG for PET imaging. A strong, linear correlation between the PET signal and the injected cell dose was observed. They subsequently treated another group with intravenous injection of CTL-hNETiGFP, using the standard curve and the quantified PET signal to non-invasively estimate the number of T cells accumulating in the tumours over time. A robust correlation was found between their estimated infiltrating CAR T cell count, *ex vivo* PET signal quantitation on the isolated tumours, and the quantified number of GFP$^+$ cells by FACs, demonstrating the feasibility of estimating T cell numbers non-invasively[113]. Similarly, Minn et al. (2019), incorporated a mutated PSMA tag into a CD19-CAR construct to detect T cells using the clinically relevant ^{18}F-DCFPyL PET probe[92]. In this study, they establish the standard curve using an *in vitro* phantom study, revealing strong linear correlation between the quantified PET signal and the cell number per well. This standard curve was then used to extrapolate the number of infiltrating CD19-tPSMA CAR T cells in Nalm6 tumour xenografts. However, they did not validate their estimation with *ex vivo* quantitation. Interestingly, they observed no correlation between the estimated total number of CAR T cells at the tumour site and the number of cells quantified by flow cytometry from peripheral blood and bone marrow, highlighting the importance of directly imaging the CAR T cells when treating solid tumours[94]. The described approaches only provide relative quantitation, relying on a pre-established standard curve for estimating the amount of infiltrating CAR T cells, limiting their translational applicability into the clinic.

1.6 Mathematical models

Several quantitation methods can be employed to derived physiologically relevant information from PET and SPECT images, from simple semi-quantitative indexes to complex compartment analysis. A widely used semi-quantitative index for measuring static PET scans in clinical

practice is the standard uptake value. It provides a macro-description of radiotracer uptake based on the quantitation of radiotracer uptake within an ROI and normalising to the injected dose and the patient's body mass, weight or lean mass. Although a simple and effective method, several factors can affect its calculation, thus, extensive pre-validation is always needed. For the analysis of dynamic data, graphical analysis are the simplest method for the visualisation and quantitation of certain parameters, but only compartmental models allow for the full quantitation of radiotracer kinetics behaviour[144].

Compartmental models originated from pharmacology and biochemistry. They are widely used to study the pharmacokinetics of absorption, biodistribution and elimination of radiopharmaceuticals used in nuclear medicine. These models mathematically explain, through differential equations, the changes in radiotracer concentration as a function of time in defined compartments. By solving the differential equations describing the influx and efflux from each compartment, the rate constants K can be estimated, providing absolute quantitation of biologically relevant parameters[145–148]. Radiotracer concentrations in the different compartments are visualised and quantified through dynamic PET or SPECT imaging. These compartments are defined by the different states of the radiotracer molecule, i.e., free radiotracer, non-specifically or specifically bound to receptors and metabolites, and they do not necessarily correspond to distinct anatomical locations. They are connected based on knowledge or assumptions of the radiotracer movement. The input function for compartmental models is the measured concentration of radiotracer in the blood as a function of time, which is often referred to as the central compartment (Cp(t)). The number of status of the radiotracer defines the number of peripheral compartments, leading to two-, three- or multi-compartmental models. Two-compartment models are suitable for radiotracers that are not metabolised. A three-compartment model is suitable for tracers that enter the tissues and then are metabolised or bind to specific receptors.

a Central compartment / Tissue compartment

$C_p(t)$ $\xrightarrow{K_1}$ $C_1(t)$ $\xrightarrow{K_2}$

Nonspecific + specific binding

$$\frac{dC_1(t)}{dt} = K_1 C_P(t) - k_2 C_1(t)$$

b

$C_p(t)$ $\xrightarrow{K_1}$ $C_1(t)$ $\xrightarrow{K_3}$ $C_2(t)$ $\quad K_2 \quad K_4$

Free + Nonspecific binding   *Specific binding*

$$\frac{dC_1(t)}{dt} = K_1 C_P(t) - (k_2 + k_3) C_1(t) + k_4 C_2(t)$$
$$\frac{dC_2(t)}{dt} = k_3 C_1(t) - k_4 C_2(t)$$

c

$C_p(t)$ $\xrightarrow{K_1}$ $C_1(t)$ $\xrightarrow{K_3}$ $C_2(t)$ $\quad K_2 \quad K_4$

Free   *Specific binding*

K_5 K_6

$C_3(t)$

Nonspecific binding

$$\frac{dC_1(t)}{dt} = K_1 C_P(t) - (k_2 + k_3 + k_5) C_1(t) + k_4 C_2(t) + k_6 C_3(t)$$
$$\frac{dC_2(t)}{dt} = k_3 C_1(t) - k_4 C_2(t)$$
$$\frac{dC_3(t)}{dt} = k_5 C_1(t) - k_6 C_3(t)$$

Figure 1.5: Schematic presentation of compartmental models. Structure of two-(a), three-(b) or multi-(c) compartmental models. C_p represents the radiotracer concentration in plasma or blood and its the input driving the models. C_i represents the radiotracer concentration in the different compartments. K_i represents the transfer coefficient of radiotracer between the different compartments. The flow of tracer between compartments can be expressed with ordinary differential equations.

Four-compartment models are appropriate to model receptor-ligand interactions where the radiotracer enters the tissue and can bind to the receptor but also non-specifically to other structures[147] (Figure 1.5).

Compartmental models assume no concentration gradients within a compartment and instant mixture of the radioligand when it passes from one compartment to the other. It is also assumed that the flow between compartments is linear and follows first-order kinetics, only the tracer concentration is allowed to change over time and an input is needed to drive the system[146, 148]. As mentioned, the input function is defined by the radiotracer time activity curve in blood. Arterial sampling is the gold standard to define the input function, but it is a highly invasive method[146]. Alternatives have been developed to reduce or eliminate the number of blood samples collected, including population-based and image-derived approaches. Population-based approaches are built by establishing the blood time-activity curve (TAC) with continuous blood sampling in several subjects and averaging the concentrations. Two blood samples are then collected from the rest of the subjects to individually scale this population-derived TAC[149]. This approach has been used in FDG-PET brain studies and ^{18}F-fluoride skeletal studies. However, this method still requires a few blood samples to scale the population-based TAC and may not be accurate if individual blood TAC differ substantially from the population-based TAC shape. A non-invasive method consists of deriving the input function directly from dynamic SPECT/PET imaging. For this, the blood compartment (cardiac blood pool, descending aorta, carotid artery) must be in the same field of view (FOV) as the target tissue. Short frames are acquired for the first few minutes after tracer bolus injection to capture the peak of the input function. Although non-invasive, this approach presents several disadvantages. Dynamic imaging is needed to capture early tracer dynamics resulting in long scanning times. Partial volume and spill over effects, can affect the accuracy of the image-derived input function derived from small areas such as the carotid artery, while this is not necessary for bigger blood pools like the heart.

However, these disadvantages are less important with the introduction of whole-body PET scanners, which allow the fast dynamic imaging of full subjects and thus the blood TAC can be derived from different blood compartments[149]. In a comparative study by Zhang et al. (2011), little differences were observed between input functions derived from five blood regions, with the aorta being the ideal blood region[112].

Compartmental models are widely used in nuclear medicine to calculate internal dosimetry from radiopharmaceuticals used for diagnostics and therapy, permitting the planning of more personalised treatments. Multiple compartmental models have been developed to improve patient dosimetry[150, 151]. In the oncology field, [^{18}F]FDG PET scanning is a standard procedure to estimate tumour glucose consumption. It is used for clinical diagnosis, staging, treatment planning and treatment outcome monitoring[152, 153]. Several compartmental models have been developed to study the kinetics of [^{18}F]FDG[154, 155]. Clinical studies of CAR T cell therapy for haematological malignancies have highlighted the prognostic value of [^{18}F]FDG PET imaging to measure metabolic tumour volume (tumour volume with increased glucose consumption), associating lower metabolic tumour volume with positive treatment responses[156]. Besides, [^{18}F]FDG PET brain imaging may allow the detection of neurotoxicity linked to the treatment[96, 147, 156]. The implementation of dynamic PET imaging is improving the quantitative characterisation of tumour glucose metabolism, and the introduction of whole-body PET scanners, with bigger FOV and faster acquisition times, is expected to further spread the application of compartmental modelling.

A simpler approach for quantifying dynamic data is the use of graphical analysis, since they do not account for blood volume or provide values for the individual rate constants. The two most employed graphical methods are Logan and Patlak plots. They offer a streamlined means of extracting the relevant parameters after transforming the dynamic data, which would exhibit a linear trend after reaching equilibrium.

The Logan plot, designed for reversible tracer uptake in two- or three-compartment models, allows the estimation of the volume of distribution (V_T) from the slope of the linear trend. The Logan plot is expresed as:

$$\frac{\int_0^t C_{tissue}(T)\, d(T)}{C_{tissue}(t)} = V_T \frac{\int_0^t C_{blood}(T)\, d(T)}{C_{tissue}(t)} + q \qquad (1.1)$$

Here, the integral of tissue activity from the time of injection is divided by the instantaneous tissue activity. The input curve (C_{blood}) is also integrated and divided by the instantaneous tissue activity. In cases where the system is defined by reversible compartments, the resulting plot will exhibit a straight line. The slope of this line (V_T) represents the ratio of tracer concentration between tissue and blood at equilibrium. In a two-compartment model, V_T equals the ratio between K_1/K_2, whereas in a three-compartment model, it equals $K_1/K_2(1+K_3/K_4)$[157].

The Patlak plot was designed for systems with irreversible tracer trapping, such as FDG studies. The Patlak plots is given by the expression:

$$\frac{C_{tissue}(t)}{C_{blood}(t)} = K_i \frac{\int_0^t C_{blood}(T)\, d(T)}{C_{blood}(t)} + V \qquad (1.2)$$

Here, K_i is derived from the slope and represents the irreversible uptake rate in tissue once the reversible compartments have reached equilibrium[158].

Apart from tracer kinetic compartmental models, several non radiotracer mathematical models have been developed to explore the complex multiphasic CAR T cell kinetics, dynamics, the effect on CAR T cell differentiation[159–161] as well as to predict cytokine mediated efficacy and toxicity[159, 162, 163]. Despite the challenge in comparing data from clinical trials due to the variability in antigen targeted, CAR T cell design, preconditioning regimen and restricted sample number, modelling has improved our understanding on CAR T cell kinetics. Liu et al. (2021), developed a cellular kinetic model by evaluating

clinical outcomes across diverse trials, focusing mainly on haematological malignancies. CAR T cell kinetics follow four distinct phases: early biodistribution (2-3 days post infusion), expansion, contraction, and persistence. Patient response was closely tied to CAR T cell kinetics, with responders exhibiting higher peak concentrations and lower contraction rate than non-responders. However, CAR T cell dosing weakly correlated with the cellular kinetics and treatment outcome[160]. This was also observed in a multiscale pharmacokinetic-pharmacodynamic modelling approach for anti-BCMA CAR T cells, indicating that CAR T cell kinetics may be more influenced by initial tumour burden than by CAR T cell dosing[164]. Despite the ongoing advancements on understanding CAR T cell kinetics and dynamics, the current models do not directly quantify CAR T cell infiltration and proliferation at the tumour site.

1.7   Summary and aims

Despite the recent advances in cell-based immunotherapies, CAR T cells therapies for the treatment of solid tumours has shown limited effectiveness in clinical trials. This can be attributed to the inadequate homing to the tumour site, the hostile tumour microenvironment, and insufficient CAR T cell persistence. Notably, CAR T cell expansion and persistence are pivotal for sustained anti-tumour cytotoxicity, however, there is a lack of standardised protocols for monitoring CAR T cell kinetics post-infusion. While modelling analysis has shed light on CAR T cell kinetics, there is still a need for a more comprehensive understanding of their *in vivo* biodistribution, behaviour, persistence in solid tumours, and its correlation with treatment response. The work undertaken in this thesis aims to non-invasively monitor CAR T cell kinetics *in vivo* and study the feasibility of achieving direct quantitation of CAR T cells *in vivo* through mathematical modelling. To this purpose, four specific aims have been outlined:

- The development of a traceable PSMA-targeting CAR by co-expressing the reporter gene hNIS.
- The characterisation of the reporter gene and its effect on the CAR T cell immunotherapy treatment.
- Non-invasive monitoring of CAR T cell infiltration and proliferation via SPECT/CT imaging.
- Establishment of a compartmental model for image-derived quantitation of infiltrating CAR T cells non-invasively.

Chapter 2

Materials and Methods

2.1 Molecular Biology

2.1.1 Packaging plasmids

All recombinant DNA constructs were expressed via the retroviral vector SFG. The tricistronic retroviral SFG vectors containing the $4\alpha\beta$, P28ζ CAR and hNIS genes (4P28ζN) and the truncated version $4\alpha\beta$, PTr CAR and hNIS (4PTrN), were produced by Dr. Nia Emami (King's College London)[133]. The PSMA targeting CAR was designed from the J591 antibody provided by Neil Bander (Cornell University). The furin T2A cleavage sites were used to ensure stoichiometric expressions of $4\alpha\beta$, P28ζ and hNIS genes. Retroviral packaging plasmids PEQ-PAM and RD114 were donations from Dr. John Maher's laboratory (King's College London). A lentiviral vector containing the myc tagged-P28ζ CAR (pU_P28ζ) was provided by Dr. Robert Page (King's College London).

2.1.2 Cloning of lentiviral transfer plasmids

NEBuilder Hifi DNA Assembly (New England Bioscience (NEB), UK) was used to clone the hNIS gene into the myc-tagged PSMA targeting CAR lentiviral vector as shown in
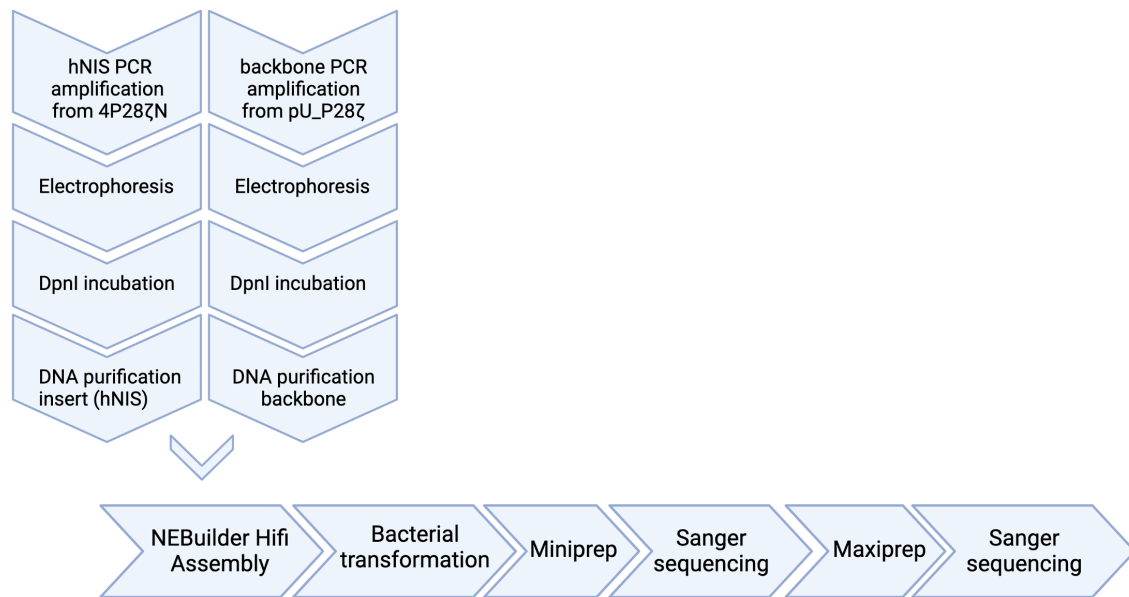
Figure 2.1: Workflow for cloning the hNIS insert into the lentiviral constructs encoding for the PSMA targeting CAR. The hNIS insert and the lentiviral vector backbone were amplified by PCR, the size of the amplified fragments was confirmed by gel electrophoresis. The PCR reaction was incubated with DpnI to eliminate the template DNA and the amplified PCR fragments were purified. Insert and backbone were assemble using NEBuilder Hifi Assambly. The assembled DNA was transformed into competent bacteria and the resulting colonies were miniprepped to confirm correct DNA assembly via Sanger sequencing. The bacterial culture was then scaled up, DNA was maxiprepped and DNA sequence confirmed by Sanger sequencing.

(Figure 2.1). The resulting lentiviral plasmids were used as a template to clone the myc-tagged

CAR into the tricistronic retroviral SFG vectors.

2.1.2.1 PCR amplification

The vector backbone from the pU_P28ζ lentiviral plasmid and the hNIS gene from the

4P28ζN retroviral vectors (Figure 2.2) were amplified by PCR using the Q5 Hot start

High-Fidelity DNA Polymerase (NEB, UK). PCR primers were designed to amplify the

vector backbone while adding a T2A sequence after the CAR gene. To amplify the hNIS

insert, PCR primers were specifically designed to amplify the insert while adding at least
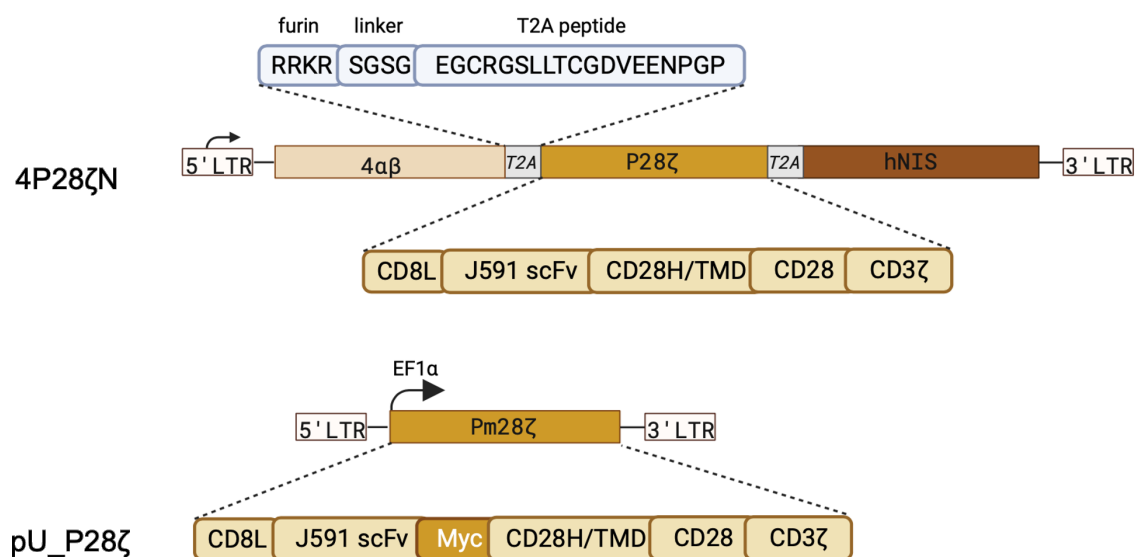
Figure 2.2: Structure of template DNA constructs. The 4 $\alpha\beta$ cytokine chimeric receptor is upstream of the CAR P28ζ, which is formed by the J591 scFv downstream of the CD8 leader sequence (CD8L). Downstream of the CAR is the CD28 hinge and transmembrane domains (CD28H/TMD), followed by the intracellular signalling CD28 and CD3ζ domains. Downstream of the CAR is the reporter gene (hNIS). Genes were separated by furin T2A cleavage sites. The pU_P28ζ contains the P28ζ CAR with an extracellular myc tag downstream the scFv, and is expressed under the control of the promoter EF1α in the pULtra lentiviral vector.

20 base pairs (bp) of sequence homologous to the digested backbone to facilitate assembly. Standard PCR reaction and conditions are described in Table 2.1 and Table 2.2. The annealing temperature was calculated using NEB Tm calculator. A list of all primers used, and template DNA is displayed in Table 2.3.

2.1.2.2 Agarose gel electrophoresis

5 μl of the PCR reactions were mixed with 6x DNA loading dye (NEB, USA) and visualized by electrophoresis in an agarose gel. The gel was run for approximately 1 hour (h) at 100V and visualized using a UV light device. After confirming the right amplicon size from the PCR reactions, the rest of the PCR mixture was incubated at 37°C for 15 minutes (min) with

Table 2.1: **Standard PCR reagents**

Reagent	Volume (μl)	Final concentration
5X Reaction buffer	5	1X
5X Q5 High GC enhance	5	1X
10 mM dNTPs	0.5	200 μM
Forward Primer	1.25	0.5 μM
Reverse Primer	1.25	0.5 μM
Q5 Hot start polymerase	0.25	0.02 U/ μl
Nuclease-Free water	Up to 25 μl	-

Table 2.2: **Standard PCR reaction conditions**

Step	Temperature (°C)	Time (seconds)
Initial denaturation	98	30
Denaturation	98	15
Annealing	50-71	15
Amplification	72	30/kb amplicon
Final extension	72	120
Hold	10	indefinite

0.25 μl of FastDigest DpnI (Thermo Fisher Scientific, USA) to remove the remaining DNA template, and the PCR product was purified using E.Z.N.A Cycle Pure DNA Clean Up Kit (Omega Bio-Tek, USA) following the manufacturer instructions.

2.1.2.3 DNA Assembly

The concentration of the purified vector backbone and PCR insert was measured using a Nanodrop TM 1000 Spectrophotometer (Thermo Fisher Scientific). NEB Builder Calculator was used to calculate the amount of insert needed to achieve 1:1 molar ratio with the vector

Table 2.3: **List of primers used to clone hNIS into lentiviral plasmids**

Insert	Primer sequence (5' - 3')	Template
Backbone	F: cagcaggaaacaaacctgtaatgacaaccactcgagagtcgtcgactcgacaatcaacc R: gccctccccggatccacttctcttcctcctgcgaggggcaggg	pU_P28ζ
Backbone	F: cagcaggaaacaaacctgtaatgacaaccactcgagagtcgtcgactcgacaatcaacc R: gccctccccggatccacttctcttcctcctgatgatgaaggccacggtcaccag	pU_P28ζ
hNIS	F: aggaggaggaagagaagtggatccgggggag R: ctcgagtggttgtcattacaggtttgtttcctgctg	4P28ζN

backbone. 50 ng of vector backbone and the appropriate amount of insert were mixed 1:1 with 2X NEBuilder Hifi DNA Assembly Mix (NEB) and incubated for 1 h at 50°C.

2.1.3 Bacterial transformation

2.1.3.1 Agar plates

Agar plates were prepared by melting LB-agar (Fisher Scientific, UK) using a microwave oven for 30 min. Melted agar was left to cool and ampicillin (100 µg/ml) (Alfa Aesar, USA) was thoroughly mixed. 25 ml of the solution was poured per Petri dish and left to cool at room temperature.

2.1.3.2 Bacterial Transformation

5 µl of the NEBuilder Hifi Assembly reactions were transformed into 25 µl of NEB 5-alpha competent E.Coli (NEB). The mixture was kept on ice for 30 min, followed by a heat shock for 30 seconds at 42°C and returned to ice for 5 min. 250 µl of SOC media (NEB) was added to the transformed bacteria and vials were incubated at 37°C for 1 h with shaking. The bacteria were plated on agar plates containing ampicillin and incubated at 37°C overnight.

The resulting ampicillin resistant colonies were miniprepped and isolated DNA was screened by restriction digestion and Sanger sequencing (Figure 2.3)
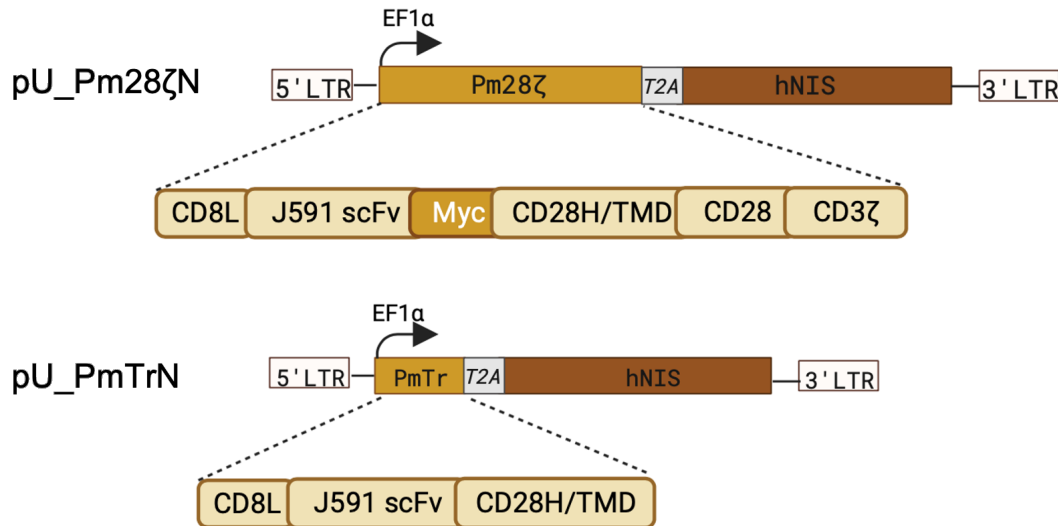
Figure 2.3: Structure of the lentiviral PSMA-targeting CAR constructs. The CAR Pm28ζ, is formed by the J591 scFv downstream of the CD8 leader sequence (CD8L) followed by a myc tag. Downstream of the CAR are the CD28 hinge and transmembrane domains (CD28H/TMD), followed by the intracellular signalling CD28 and CD3ζ domains. The hNIS was inserted downstream of the CAR separated by a furin T2A cleavage site. The truncated CAR, pU_PmTrN, is identical to pU_Pm28ζN except it does not contain the intracellular domains. These CARs were expressed under the control of the promoter EF1α in the pUltra lentiviral vector.

2.1.4   Isolation of plasmid DNA

Miniprep: The resulting colonies were grown in 15 ml of LB broth containing ampicillin (100 µg/ml) in a shaking incubator for 18 h at 37°C. Bacteria was centrifuged at 4000g for 5 min, the supernatant was discarded, and the plasmid DNA was extracted from the pellet using E.Z.N.A Plasmid DNA mini Kit II (Omega Bio-Tek) following the manufacturer's instructions. Briefly, the bacterial pellet was resuspended in 500 µl of buffer 1 and lysed by adding 500 µl of buffer 2. The lysis was stopped by adding 700 µl of buffer 3. The

falcons were then centrifuged at 16000 g for 5 min. The supernatant was transferred to a silica spin column to purify the DNA plasmid by centrifugation at 16000 g for 1 min. The flowthrough was discarded, and the column was washed twice with 500 μl of DNA wash buffer. The flowthrough was discarded, and the empty column was centrifuged again to remove any excess wash buffer. To elute the DNA from the column, 100 μl of water was added, the column was allowed to rest for 1 minute before centrifugating at 16000 g for 2 min. The concentration of the elute DNA was quantified using a Nanodrop TM 1000 Spectrophotometer (Thermo Fisher Scientific). Plasmid DNA was stored at -20°C.

Maxiprep: To scale up the production of DNA, the resulting colonies were grown in 2 ml of LB broth containing ampicillin (100 μg/ml) in a shaking incubator for 8 h at 37°C. 500 μl of this starter culture were then transferred to 250 ml of LB broth containing ampicillin (100 μg/ml) and grown in a shaking incubator for 18 h at 37°C. Bacteria was centrifuged at 4000g for 10 min, the supernatant was discarded, and the plasmid DNA was extracted from the pellet using E.Z.N.A Plasmid Maxi Kit (Omega Bio-Tek) following the manufacturer's instructions. Briefly, the bacterial pellet was resuspended in 10 ml of buffer 1 and lysed by adding 10 ml of buffer 2. The lysis was neutralised by adding 12 ml of buffer 3. The falcons were then centrifuged at 20000 g for 10 min. The supernatant was transferred to a maxi column to purify the DNA by centrifugation at 4000 g for 2 min. The flowthrough was discarded, and the column was washed twice with 15ml of DNA wash buffer. The flowthrough was discarded, and the empty column was centrifuged again to remove any excess wash buffer. To elute the DNA from the column, 2 ml of water was added, and the column was allowed to rest for 1 minute before centrifugating at 4000 g for 5 min. The concentration of the elute DNA was quantified using a Nanodrop TM 1000 Spectrophotometer (Thermo Fisher Scientific). Plasmid DNA was stored at -20°C.

2.1.5 Restriction digestion and Sanger sequencing

To confirm the correct assembly of the insert into the vector backbone, restriction digestion was performed on the purified DNA. The enzymes were chosen to generate distinct digestion patterns. The plasmid was digested following the standard protocol in Table 2.4 and digested products were visualized by electrophoresis in an agarose gel. If the bands corresponded to the expected patterns, the DNA was sent for Sanger sequencing. The Sanger sequences were then compared to the reference plasmid maps using Snapgene (Insightful Science, Australia).

Table 2.4: **Restriction digestion reagents**

Reagent	Quantity
10x NEB Buffer	2.5 µl
DNA	0.5 µg
Enzymes	10 units/ enzyme
Nuclease-Free water	Up to 25 µl

2.1.6 Cloning of retroviral transfer plasmids

To clone the myc-tagged CAR into the tricistronic retroviral plasmids the lentiviral plasmids pU_Pm28ζN, pU_PmTrN Figure 2.3 and the template retroviral plasmid 4P28ζN (Figure 2.2) were digested and ligated following the workflow depicted in Figure 2.4.

2.1.6.1 Digestion of plasmids

The vectors were digested with SphI-HF and BstBI-HF restriction enzymes (NEB) for 1 h at 37°C, following the standard protocol described in Table 2.4. The digested plasmids were mixed with 6x DNA loading dye and separated in an agarose gel by electrophoresis. The 9 kb band from the digested 4P28ζN backbone, the 2.4 kb band from the digested pU_Pm28ζN and the 2 kb band from the digested pU_PmTrN were excised using a sterile
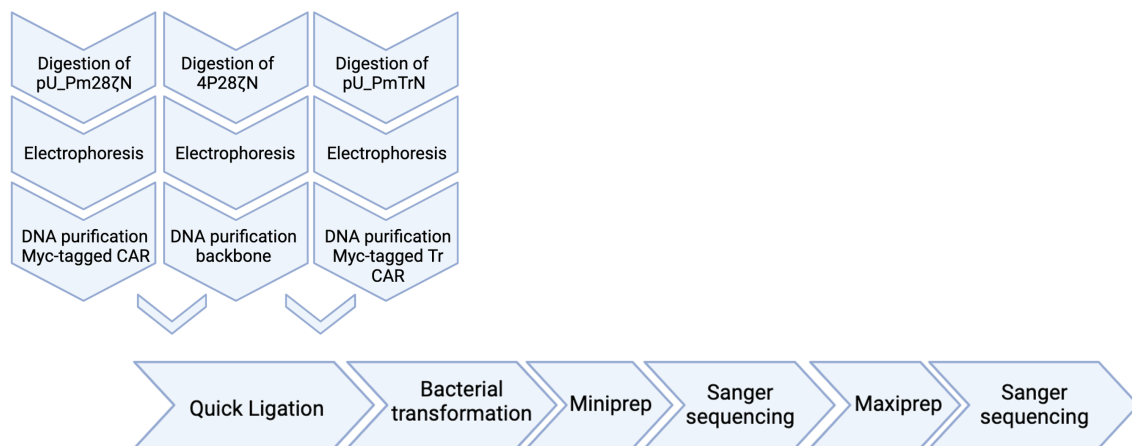
Figure 2.4: Workflow for cloning the myc-tagged CAR into the retroviral construct
The template plasmids were double digested, and the digested products were visualized by gel electrophoresis. The correct band size was excised from the gel and purified. Insert and vector backbone were assembled using a quick ligation. The assembled DNA was transformed into competent bacteria and the resulting colonies were miniprepped to confirm correct DNA assembly via Sanger sequencing. The bacterial culture was then scaled up, DNA was maxiprepped and DNA sequence confirmed by Sanger sequencing.

razor and purified using E.Z.N.A Cycle Pure DNA Clean Up Kit (Omega Bio-Tek) following the manufacturer instructions.

2.1.6.2 Quick ligase

The concentration of the purified vector backbone and PCR insert was measured using a Nanodrop TM 1000 Spectrophotometer (Thermo Fisher Scientific). NEB Builder Calculator was used to calculate the amount of insert needed to achieve 3:1 insert:backbone molar ratio. 50 ng of vector backbone and the appropriate amount of insert were mixed 1:1 with 2X Quick Ligase (NEB) reaction buffer and 0.25 μl of Quick Ligase (NEB). The ligation was incubated for 15 min at RT. 5 μl of each reaction was transformed into competent bacteria, colonies were miniprepped and isolated DNA sent for sequencing as described above. The resulting retroviral plasmids 4Pm28ζN and 4PmTrN are depicted in Figure 2.5.

Lastly, NEBuilder Hifi DNA Assembly was used to clone the myc-tagged CAR Pm28ζ into the SFG retroviral vector to create a control CAR not expressing the hNIS reporter gene.

The Pm28ζ CAR gene was amplified by PCR using the following primers: cttcccctagcgcttctcct gcatgcagaggtgcagctgcagcagtcaggacc & ggactaatccggatccctcgagtggttgtcagcgaggggggcagggcctgc atgtgaaggg. The 4Pm28ζN plasmid was digested with SphI and XhoI (NEB). The PCR amplicon and digested DNA were purified, assemble and transformed into competent bacteria as described above. Colonies were miniprepped and isolated DNA sent for sequencing as described above. The resulting bicistronic retroviral plasmids, termed 4Pm28ζ, is depicted in Figure 2.5.
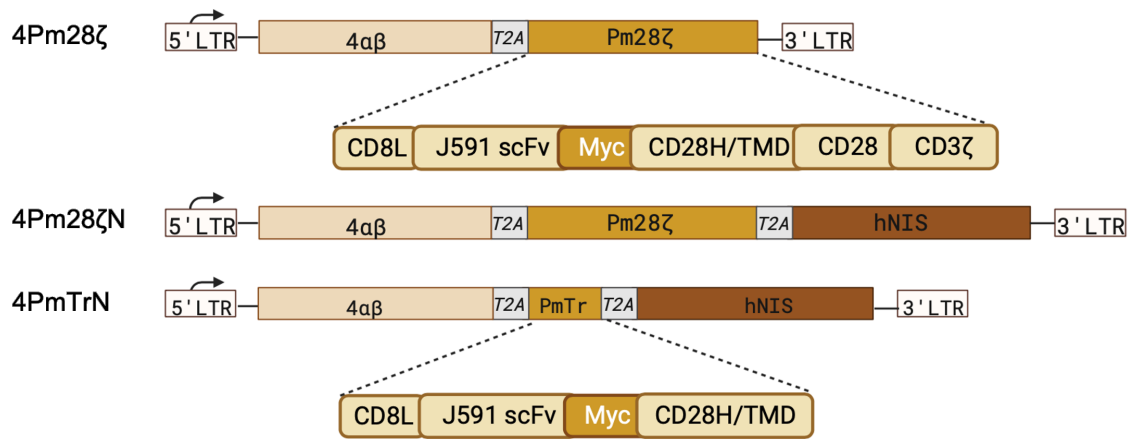
Figure 2.5: Structure of the resulting PSMA-targeting CAR constructs The 4 $\alpha\beta$ cytokine chimeric receptor is upstream of the CAR P28ζ, which is formed by the J591 scFv downstream of the CD8 leader sequence (CD8L). A Myc tag was inserted downstream of the scFv. Downstream of the CAR are the CD28 hinge and transmembrane domains (CD28H/TMD), followed by the intracellular signalling CD28 and CD3ζ domains. This CAR was termed 4Pm28ζ. If the reporter gene (hNIS) was expressed downstream of the CAR, it was termed 4Pm28ζN. The truncated CAR, 4PmTrN, is identical to 4Pm28ζN except it does not contain the intracellular domains. Genes were separated by furin T2A cleavage sites. All these CARs were expressed in a retroviral SFG construct.

2.2 Cell culture

2.2.1 Media and cell lines

Dulbecco's Modified Eagle Medium (DMEM) (Gibco, Thermo Fisher Scientific) supplemented 10% Foetal Bovine Serum (FBS)(Sigma-Aldrich, UK) and 5% L-Glutamine (Sigma-Aldrich, UK), was termed D10.

Roswell Park Memorial Institute (RPMI) 1640 (Gibco) supplemented with 5% Human serum and 5% L-Glutamine, was termed R5.

PC3-LC3 (PL), PC3-LN3-PSMA (PLP), PL-Luciferase dTomato (PL-LT) and PLP-LT, were produced by Dr. Emami[133], and HEK293T cells were cultured in D10 medium. Isolated PBMCs were cultured in R5. All cell lines were cultured at 37°C in 5% CO_2.

2.2.2 Retroviral production in HEK 293T

$1.7x10^6$ HEK 293T were plated in 10 mm dishes and allowed to adhere for 24 h. The transfection mixture was prepared by mixing 30 μl of genejuice with 470 μl of serum-free DMEM and incubating for 5 min at room temperature. Then 3.125 μg of RD144, 4.697 μg of pEQ-Pam3 and 4.697 μg of the retroviral CAR plasmid DNA were added to the transfection mix and incubated for 15 min at room temperature. The transfection mix was added dropwise to transfect the HEK 293T. HEK 293T were incubated at 37°C in 5% CO_2 and viral supernatants were collected at 48 and 72 h. Supernatants were snap-frozen in 1.5 ml aliquots and stored at -80°C.

2.2.3 Isolation, transduction, and expansion of human PBMCs

PBMCs were isolated from whole blood obtained from healthy donors recruited under the approval of the Guy's and St Thomas' Research Ethics Committee (reference 09/H0804/92). 30 ml of whole blood was carefully layered over 15 ml of Ficoll-Paque (GE Healhtcare,

USA) to isolate PBMCs by density gradient centrifugation. Tubes were centrifuged at 800 g for 35 min at room temperature with brake and acceleration set to the minimum. The PBMCs buffy coat layer was aspirated with a Pasteur pipette and transferred to a clean falcon containing 30 ml of R5 media. Cells were centrifuged at 800 g for 5 min and the supernatant was discarded. Cell pellets were washed twice with 50 ml of PBS followed by centrifugation at 800 g for 5 min. The remaining cell pellet was resuspended in R5 media to a concentration of $3x10^6$ cells/ml and activated with 5 μg/ml Phytohemagglutinin-L (Sigma-Aldrich). 24 h after activation, PBMCs were supplemented with 100 U/ml recombinant human IL-2 (IL-2) (R&D systems, USA). RetroNectin (TakaRa, Japan) plates were prepared for PBMCs transduction by coating non-tissue culture 6-well plates with 2 ml of diluted RetroNectin (11 μg/ml). Plates were stored at 4°C.

24 h after activation of the isolated PBMCs, retroNectin was aspirated from the 6-well plates and 1.5 ml of viral supernatant was added per well. Plates were incubated for 4 h at 4°C. Viral supernatants were aspirated after the incubation and $1x10^6$ viable PBMCs were added per well. 3 ml of viral supernatant was added, and each well was supplemented with 100 U/ml of IL-2.

72 h after transduction, PBMCs were harvested from each well with a Pasteur pippette and centrifuge at 800 g for 5 min. Supernanst were discarded and cell pellets were resuspended in 2 ml of fresh R5 and supplemented with 3 ng/ml recombinant human IL-4 (IL-4) (Peprotech, UK). Transduced cells were maintained at a concentration of $2x10^6$ cells/ml by adding fresh media and supplementing with IL-4 every second day. Untransduce cells were supplemented with 100U/ml IL-2.

2.2.4 PBMCs stimulation with Phorbol Myristate Acetate and Ionomycin

PBMCs were counted using the Tripan Blue exclusion method and diluted to $1x10^6$ cells/ml. Phorbol Myristate Acetate (PMA) (Sigma-Aldrich) and Ionomycin (Iono) (Sigma-Aldrich)

were added to the cells to achieve a final concentration of 50 ng/ml and 500 ng/ml, respectively. PBMCs were cultured in 24-well plates for 24 h, PBMCs were then washed and resuspended in fresh media for downstream applications.

2.2.5   PBMC co-culture with target tumour cells

For cytotoxicity assays, 1×10^4 target cells were plated in 96-well plates in 100 µl of D10 media. Target cells (PL, PLP, PL-LT or PLP-LT) were allowed to adhere for 24 h. PBMCs were counted and washed thoroughly to remove cytokines from the supernatant. PBMCs were then added to the 96-well plate according to the effector-to-target (E:T) ratios indicated. Co-cultures were incubated at 37°C for 48 h or 72 h, as indicated. If co-cultures were performed to assess phenotypic markers or perform uptake assays on the activated PBMCs, 1.8×10^5 target cells were plated in 24-well plates in 500 µl of D10 media and PBMCs were co-cultured as described above.

2.3   *In vitro* functional uptakes

2.3.1   Cytotoxicity assays

CAR T cell cytotoxicity against target cells was assessed by measuring tumour viability using 3-(4,5-dimethylthiazol-2-yl)-2,5-diphenyltetrazolium bromide (MTT) assay or by measuring real-time changes in Tdtomato fluorescence expressed by the target cells using an Incucyte®.

MTT: after co-culture of the PBMCs with PL or PLP target cells, the media was aspirated and replaced with D10 supplemented with 500 µg/ml MTT (Sigma-Aldrich). Plates were incubated at 37°C in 5% CO_2 for 90 min. Following the incubation time, media was aspirated, and the crystals formed by the remaining target cells were dissolved in 200 µl of Dimethyl sulfoxide (DMSO)(Sigma-Aldrich). The solution's absorbance was measured at 590 nm wavelength in a FLUOstar Omega plate reader (BMG LabTech, Germany). Tumour viability

was calculated by comparing the absorbance from the treated wells to the control wells, containing target cells alone, following the formula bellow:

$$\text{Target cell viability } (\%) = \frac{\text{Absorbance of treated wells}}{\text{Absorbance of target cells only}} \text{ x } 100 \qquad (2.1)$$

Incucyte®: PL-LT or PLP-LT cells were used as target cells for real-time cytotoxicity assays. CAR T cells were co-cultured as described above and plates were immediately transferred into the Incucyte® S3 Live-Cell System (Sartorius, Germany), which was placed inside a cell incubator at 37°C and 5% CO_2. Four images per well were acquired for technical repeats in the phase contrast and the red fluorescence channel every 2 h for 70 h using a 10x magnification. The red channel acquisition was 400 ms. The Incucyte® analysis software was used to quantify changes in fluorescence. A cell mask was applied to the phase contrast images to differentiate cells from background, and to the red channel to quantify the fluorescence signal. The fluorescence signal was normalised to time 0 and changes in fluorescence were plotted against time.

2.3.2   Cytokine production

IL-2 and IFNγ cytokines released by T cells were measured by enzyme-linked immunosorbent assay (ELISA) as per the manufacturer's instructions. Supernatants from co-cultures were harvested after 24 h to measure IL-2 (Invitrogen, Thermo Fisher Scientific) or 48 h to measure IFNγ (R & D systems) release. Briefly, high-affinity binding plates were coated with the capture antibody overnight. Wells were aspirated and washed three times with wash buffer. Supernatants were diluted with the appropriate diluent and standards were prepared following the manufacturer's protocol. Plates were incubated overnight at 4°C. Wells were aspirated and washed three times with wash buffer. For the detection of IL-2 cytokine, the detection antibody was added to the wells, and plates were incubated for 1 h at RT. Plates were washed three times, Avidin-HRP enzyme was added to the wells, and plates were incubated for

30 min at RT. Plates were washed five times before adding the Tetramethylbenzidine (TMB) substrate. Plates were incubated for 15 min at RT. The reaction was stopped by adding the stop solution and absorbance was measured at 450 nm. For detention of IFNγ, the detection antibody was added to the wells, and plates were incubated for 2 h at RT. Plates were washed three times, Avidin-HRP enzyme was added to the wells, and plates were incubated for 20 min at RT. Plates were washed five times before the substrate solution, containing a mixture of H_2O_2 and TMB. Plates were incubated for 20 min at RT. The reaction was stopped by adding the stop solution and absorbance was measured at 450nm. The concentration of each sample was extrapolated from the standard curve, considering the dilution factor.

2.4 Flow cytometry

2.4.1 Cell surface staining

The standard protocol to stain for surface markers consisted of washing 1×10^5 viable cells with 1 ml of staining buffer (PBS + 2% FBS) and centrifuged at 800 g for 5 min. For staining of adherent cells, cells were harvested using trypsin-EDTA 0.5% (Thermo Fisher Scientific) and washed with PBS before aliquoting 1×10^5 viable cells. Cell pellets were resuspended in 100 µl of Zombie Near Infrared (NIR) Live/Dead (L/D) dye (BioLegend, UK) at the indicated dilution for 15 min at RT in the dark. Cells were then stained with 100 µl of the primary conjugated antibody and incubated for 30 min at 4°C. Cells were then washed with 1 ml of staining buffer and resuspended in 200 µl before acquisition in the flow cytometer. The compensation matrix was obtained with single stained compensation controls prepared by adding two drops of compensation beads (positive and negative compensation beads) per tube and staining with 100 µl of the antibody at the indicated dilution. Compensation samples were incubated and washed alongside the samples. The conjugated antibodies and compensation beads used for the analysis of cell surface protein expression are shown in

Table 2.5 .

<p style="text-align: center;">Table 2.5: **List of conjugated antibodies used for cell surface staining**</p>

Conjugated antibody	Supplier, place	Dilution
Mouse anti-Myc phycoerythrin (PE) (9B11)	Cell signalling, USA	1:20
Human SLC5A5 AlexaFluor® 647	R & D systems, USA	1:10
Zombie NIR L/D	BioLegend, UK	1:1000
Mouse anti-human CD3 APC/C Cyanine 7 (SK7)	BioLegend, UK	1:40
Mouse anti-human CCR7 PE/Cyanine 7 (G043H7)	BioLegend, UK	1:40
Mouse anti-human CD45RA PE	BioLegend, UK	1:40
Mouse anti-human PD-1 FITC (EH12.2H7)	BioLegend, UK	1:40
Mouse anti-human TIM3 APC (F38-2E2)	BioLegend, UK	1:40
Mouse anti-human LAG 3 PerCP-Cyanine5.5 (11C3C65)	BioLegend, UK	1:40
Mouse anti-human CD69 APC (FN50)	BioLegend, UK	1:40
Mouse anti-human CD45 BV510 (2D1)	BioLegend, UK	1:20
Mouse anti-human CD3 BV421 (SK7)	BioLegend, UK	1:20
Mouse anti-human CD4 BV785 (OKT4)	BioLegend, UK	1:20
Mouse anti-human CD8 BV650 (OKT4)	BioLegend, UK	1:20
Mouse anti-Myc AlexaFluor® 488 (9B11)	Cell signalling, USA	1:20
Mouse anti-human PSMA AlexaFluor® 488 (FOLH1)	BioLegend, UK	1:100
Mouse IgG1, k isotype PE AlexaFluor® 488	BioLegend, UK	1:100
Anti-H2A.x Phospho PE (Ser139)	BioLegend, UK	1:100
Mouse IgG1, k isotype PE	BD Pharmigen, USA	1:100
Anti-mouse Ig, k compensation beads	BD, USA	1 drop/sample
ArCTM amine reactive compensation beads	Invitrogen, USA	1 drop/sample

2.4.2   Intracellular staining for γH2Ax

Phosphorylation of γH2Ax was measured to assess DNA damage after exposure to increasing concentrations of $^{99m}TcO_4^-$. 2×10^5 viable cells were plated per well in a 96-well plate and cells were incubated for 30 min at 37°C with the indicated radiotracer amounts. Cells were then washed with 200 µl of ice-cold PBS, centrifuged at 800 g for 5 min and resuspended in

200 µl fresh media. At the indicated time point, cells were washed, stained with Zombie NIR L/D (1:1000) for 15 min at room temperature in the dark, and washed again with ice-cold PBS. Cell pellets were resuspended in ice-cold 90% ethanol added dropwise by vortexing and samples were stored at -20°C between 24 and 72 h. 300 µl of fixed cells were added to a V-bottom 96-well plate, washed in ice-cold PBS and stained with γH2Ax-PE (1:100) (BioLegend) or Mouse IgG1k-PE isotype (BioLegend) for 30 min at RT in the dark. Cells were washed with staining buffer and resuspended in 200 µl of staining buffer for analysis by flow cytometry.

2.4.3 Cell viability Annexin L/D

Cell viability was quantified by staining with PE-conjugated Annexin V (BioLegend) and Zombie NIR L/D. Cells were washed in PBS and centrifuged at 800 g for 5 min. Cell pellets were stained in 100 µl of Annexin V Binding buffer containing Annexin V-PE antibody (1:20) and Zombie NIR L/D dye (1:1000) for 30 min at 4°C. Cells were washed twice with Annexin V binding buffer and resuspended in 200 µl for Annexin V binding buffer for analysis by flow cytometry.

2.4.4 Counting cells using CountBright Beads

CountBright Beads (Invitrogen) were used to quantify cells in suspension by flow cytometry. Cell were stained for cell surface marker proteins as stated above. Cells were then resuspended in 375 µl of staining buffer and 25 µl of counting beads were added directly to each sample before acquisition. Samples were analysed acquiring at least 1000 bead events. To calculate the concentration of the cells, the following formula was applied:

$$\text{Cell count}(\text{cells}/\mu l) = \frac{\text{cell count x 25 } \mu l}{\text{bead count x 375 } \mu l} \text{ x CountBright lot (beads}/\mu l) \qquad (2.2)$$

2.4.5 Quantifying cell surface expression

Quantum R-PE and AF647 MESF (molecules of soluble fluorochrome) beads were used to quantify the number of surface CAR and hNIS copies expressed on the cell membrane of the transduced T cells. Beads were run alongside the CAR T cell samples to create a standard curve. The number of CAR and hNIS expressed on the cell surface was then extrapolated form the standard curve, considering the effective fluorochrome to protein (F:P) ratio of the myc tag and hNIS antibodies.

Samples were acquired using a BD LSR Fortessa flow cytometer or a ThermoFisher Attune NxT Flow Cytometer.

2.5 *In vitro* uptake assays

$^{99m}TcO_4^-$ was provided by the Barts Health Radiopharmacy in the Nuclear Medicine Department, Barts Health NHS Trust, London. The generator was eluted with saline at least 24 h before delivery to reduce accumulation of the daughter radionuclide ^{99m}Tc.

2.5.1 Standard uptake assay

$3x10^5$ viable cells/eppendorf were aliquoted in triplicates per condition. Cells were washed in PBS and cell pellets were resuspended in either 300 μl of PBS or 300 μl of PBS containing 10mM sodium perchlorate (Sigma-Aldrich). Cells were incubated for 30 min at 37°C, 5% CO_2. All samples were then incubated with 0.1 MBq $^{99m}TcO_4^-$ for 30 min at 37°C, 5% CO_2. The same amount of tracer was added to scintillation tubes to create the standards. Cells were then washed once with 1 ml of ice-cold PBS and centrifuge at 800 g for 5 min. Radioactivity in samples and standards was quantified using a gamma-counter (LKB Wallac 192 Compugamma CS) and results expressed as intracellular uptake percentage.
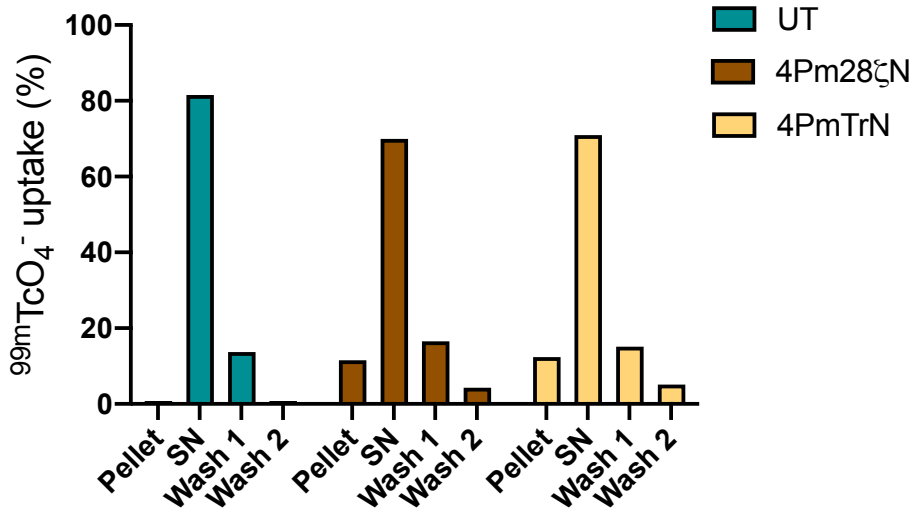
Figure 2.6: Defining the number of washes for uptake assays. T cells were incubated with 0.33 MBq/ml of $^{99m}TcO_4^-$ for 30 min followed by centrifugation. The supernatant (SN) was collected and cell pellets were washed twice, collecting the supernatant (Wash 1 or 2) after each wash. The majority of the added $^{99m}TcO_4^-$ remained in the supernatant. hNIS-expressing cell lines were able to internalize $^{99m}TcO_4^-$, but a second wash led to tracer efflux. Average of experimental triplicates.

$$\text{Intracellular uptake}(\%) = \frac{\text{Counts per minute (samples)}}{\text{Counts per minute (standards)}} \times 100 \qquad (2.3)$$

A single wash was performed as subsequent washes led to the efflux of $^{99m}TcO_4^-$ from the cell pellet (Figure 2.6).

2.5.2 Repetitive uptake assay

To investigate the effect of repetitive exposure to $^{99m}TcO_4^-$ in the level of uptake by the CAR T cells, a standard uptake assay was performed in sterile conditions. After radioactivity measurement, samples were resuspended in fresh R5 media and cultured at 37°C, 5% CO_2 for 48 h. After the culture time, cells were subjected to a second standard uptake.

2.5.3   Cell viability essential for $^{99m}TcO_4^-$ uptake

To investigate the dependence of hNIS mediated uptake on cell viability, $3x10^5$ viable cells were aliquoted in triplicates and exposed to 95°C for 15 min. In parallel, $3x10^5$ viable cells were aliquoted in triplicates and incubated at 37°C, 5% CO_2. Cell viability was measured staining for Annexin V and Zombie NIR L/D by flow cytometry as described above (section 2.4.3), and a standard uptake assay was performed.

2.5.4   Uptake of $^{99m}TcO_4^-$ as a function of time

$3x10^5$ viable cells were aliquoted in triplicates per condition. Cells were washed in PBS and cell pellets were resuspended in 300 μl of PBS containing 0.1 MBq $^{99m}TcO_4^-$ (0.33 MBq/ml) and incubated for 10, 30, 60, 120 or 180 min at 37°C, 5% CO_2. At the indicated time point, cells were washed in 1ml ice-cold PBS and sample radioactivity was counted at the last time point with a gamma counter. Maximum uptake was normalized to 100%.

2.5.5 $^{99m}TcO_4^-$ efflux as a function of time

$3x10^5$ viable cells were aliquoted in triplicates per condition. Cells were washed in 1ml of room temperature PBS and cell pellets were resuspended in 300 μl of PBS containing 0.1 MBq $^{99m}TcO_4^-$ (0.33 MBq/ml) and incubated for 30 min at 37°C, 5% CO_2. Following incubation, cells were centrifuge for 5 min at 800 g and resuspended in medium containing 88 kBq/ml of $^{99m}TcO_4^-$ for up to 180 min. At the indicated time point, cells were washed in 1 ml ice-cold PBS and cell pellet radioactivity was counted at the last time point with a gamma counter. Uptake at 0 min was normalised to 100%. The amount of $^{99m}TcO_4^-$ in media (88 kBq/ml) represents the amount of $^{99m}TcO_4^-$ circulating in blood at steady state, quantified as described in section 2.6.5.

2.5.6   Cytotoxicity assays with labelled CAR T cells

1×10^6 viable cells were incubated with 10 MBq of $^{99m}TcO_4^-$ and incubated for 30 min 37°C, 5% CO_2. After the incubation time, cells were resuspended in fresh R5 media and co-culture with the target cell lines as described above in section 2.3.1.

2.5.7   Proliferation of labelled CAR T cells

1×10^6 cells were plated in 2 ml per well in a 6-well plate and proliferation was measured for eight days. On day 1 and day 3, R5 media or 2 MBq /ml $^{99m}TcO_4^-$ was added to the wells. Cells were counted every second day using the Trypan Blue exclusion method.

2.5.8   Cell viability after exposure to $^{99m}TcO_4^-$

Radiation induced apoptosis was measured by staining with Annexin V and Zombie NIR L/D after exposure to $^{99m}TcO_4^-$. 5×10^5 cells were treated with increasing concentrations of $^{99m}TcO_4^-$ (0, 0.5, 1, 2, 5, 15 and 30 MBq /ml) for 30 min at 37°C, 5% CO_2. Following incubation, cells were centrifuge centrifuge for 5 min at 800 g and resuspended in 0.5 ml of fresh R5 media and incubated at 37°C, 5% CO_2 for 24 h or 4 days before assessing apoptosis by flow cytometry (section 2.4.3).

2.5.9   Double strand DNA damage after radiotracer exposure

DNA damage was measured by staining for phosphorylated γH2Ax after exposure to tracer. 5×10^5 cells were treated with increasing concentrations of $^{99m}TcO_4^-$ (0, 0.5, 5, 10 and 25 MBq/ml) for 30 min at 37°C, 5% CO_2. Following incubation, cells were resuspended in fresh R5 media and incubated at 37°C, 5% CO_2. DNA damage was measured following tracer incubation and at 3, 24 and 72 h post exposure. as detailed in section (section 2.4.2).

2.5.10 Detection sensitivity of labelled CAR T cells

To assess the limit of detection in the VECTor^{6}CT^{XUHR} SPECT camera (MiLabs), Cell pellets were prepared by mixing increasing amounts of CAR T cells with untransduced cells to reach a consistent cell pellet size of 1×10^6 cells/pellet. Cell pellets were exposed to 5 MBq ^{99m}TcO$_4^-$ (10 MBq/ml) for 30 min at 37°C, 5% CO$_2$, washed with 1 ml ice-cold PBS and cell pellets were sealed with 20 µl of low-density agarose. Tubes were immediately scanned in the SPECT camera as described below (section 2.6.4.1). The experiment was done in triplicates and the limit of detection (LOD) was defined as three times the standard deviation above background signal.

2.5.11 Correlation between CAR T cell number and SPECT signal

To assess the linearity of the SPECT signal, cell pellets were prepare with increasing amounts of CAR T cells. Cell pellets were exposed to 5 MBq ^{99m}TcO$_4^-$ /pellet (10 MBq/ml) for 30 min at 37°C, 5% CO$_2$, washed with 1 ml ice-cold PBS and cell pellets were sealed with 20 µl of low-density agarose. Tubes were immediately scanned in the SPECT scanner for 30 min. Reconstructed images were analysed using Vivoquant software and radioactivity was measured by drawing region of interest (ROI) over the cell pellets. The experiment was done in triplicates and the LOD was defined as three times the standard deviation above background signal. Cell pellets' radioactivity was also counted in a gamma counter to determine the agreement between both measurements, SPECT image-derived quantitation and gamma counting.

2.5.12 Saturation uptake assay

To measure specific uptake, ^{99m}TcO$_4^-$ was serially diluted in PBS containing 1% BSA (PBSA) to achieve concentrations up to 5 MBq ^{99m}TcO$_4^-$ per well (225 µl). This was done in two sets of triplicates. Standards were also performed in scintillation tubes. 2×10^5 viable

T cells/well in assay buffer (RPMI supplemented with 1% FBS and 0.1% sodium azide) were then added to each well of the 96-well plate. To normalize the radioactivity to protein level per well, 2×10^5 viable cells/well were plated in a different 96-well plate. To measure non-specific binding, 10 mM of sodium perchlorate was added to the second set of triplicates containing the cells and the radiotracer. The plate was incubated for 90 min at 37°C, 5% CO_2. In the meantime, a Multiscreen 96-well filter plate (0.45 µm Durapore) was blocked with 200 µl of PBSA per well. After the incubation time, the PBSA was aspirated from the plate using a pump and the samples were transferred to the filtered plate and aspirated. The filter plate was then washed twice with PBSA. The filters were punched out of the filtered plate and transferred to scintillation tubes. Radioactivity in samples and standards was measured in a gamma counter. To measure protein level, the plate containing the cells alone was washed twice in PBS and protein concentration was measured using a Bio-Rad protein assay. Briefly, 300 µl of Bio-Rad Protein Assay buffer A was added per well and incubated for 15 min at RT. Protein standards were performed following the manufacturer's instructions (Bio-Rad, UK). 5 µl from the lysates or standards were added to a 96-well plate and wells were treated with 25 µl of reagent A and 200 µl of reagent B. The plate was incubated for 15 min at RT and absorbance at 562 nm was measured on a plate reader. The concentration of each sample was extrapolated from the standard curve. Intracellular radioactivity was described as femtomol (fmol) of radiotracer per milligram (mg) of protein.

2.5.13 Competition assay

2×10^5 viable T cells/well were plated in RPMI supplemented with 1% FBS in 96-well plate and treated in triplicates with different concentrations of the inhibitor. The inhibitor sodium perchlorate was diluted in PBSA to make the following working solutions: 1×10^4, 1×10^3, 500, 100, 60, 30, 10, 3, 1 and 0.1 nM and 25 µl were added to the appropriate wells. 25 µl of the radiotracer $^{99m}TcO_4^-$ diluted in PBSA were added to all wells and to three standard tubes.

The plate was incubated for 2 h at 37°C, 5% CO_2. In the meantime, a Multiscreen 96-well filter plate (0.45 μm, Durapore,UK) was blocked with 200 μl of PBSA per well. After the incubation time, the PBSA was aspirated from the plate using a pump and the samples were transferred to the plate and aspirated. The filter plate was then washed twice with 1% PBSA. The filters were punched out of the filtered plate and transferred to scintillation tubes to measure the radioactivity in a gamma counter along with the standards.

2.5.14 Uptake after CAR T cell activation with Iono/PMA or PL/PLP co-cultures

Radiotracer uptake was measured after antigen-independent (Iono/PMA) or antigen-dependent (co-culture with target cells) activation of CAR T cells following the standard radiotracer uptake protocol described above (section 2.5.1).

2.6 SPECT/CT imaging

In vivo experiments involved 6 to 8 week-old male NOD scid gamma (NSG JAX strain, NOD.Cg-Prkdc^scid^ll2rg^tm1Wjl^/SzJ) or BALB/C (Charles River UK). All animals had access to water and a maintenance diet, and were housed up to 6 animals per cage. Cages incorporated wood shavings and a cardboard tube for environmental enrichment and were kept in a controlled room.

All *in vivo* experiments were performed in accordance to U.K. Home Office guidelines, as specified in project licence number PP6127261.

2.6.1 SPECT/CT imaging and analysis

Images were acquired using a multi-modal SPECT/CT scanner (VECTor^{6}CT^{XUHR}, MiLabs) fitted with a 1.5 mm multi-pinhole collimator, named general purpose rat mouse (GP-RM),

or a 3 mm pinhole collimator, named extra extra-ultrahigh sensitivity mouse (XXUHS-M). Animals were kept under approximately 2% isoflurane in air anaesthesia throughout the imaging session and received heat support from a heated pillow placed under the mice in the scanner bed. Respiratory rate and bed temperature were monitored and adjusted using BioVet sensors (m2m Imaging; Newark, NJ, USA). SPECT images were acquired as described in each chapter followed by a CT scan (50 kV tube voltage, 0.21 mA tube current and 75ms exposure time) for anatomical reference. Image reconstruction was undertaken using the integrated MiLabs Rec 11.00 software. The CT images were reconstructed at $80\,\mu m^3$. SPECT images were reconstructed using the similarity regulated OSEM (SROSEM) algorithm and a photo peak energy window centred at 140 keV with a 20% window width (background weight, 2.5). Two adjacent photo peak energy windows were used for triple-energy window scatter and crosstalk correction. SPECT images were co-registered with the CT and attenuation correction was applied. Images were visualized and analysed with VivoQuant software. A post-processing 0.4 mm FWHM Gaussian filter was applied to the SPECT images for visualization. A calibration factor was used to convert the scanner units to radioactivity concentration either manually or as part of the image post-processing in VivoQuant software. To normalise between mice and experiments, the injected activity was inputed during the image post-processing to quantify the SPECT signal, expressed as %ID (injected dose) or %ID/g (injected dose/gram) by comparison to a reference standard of the injected stock.

2.6.2 Calculation of the calibration factor

To obtain the calibration factor, a point source phantom with a known amount of radioactivity was imaged for 10 min. Following the SPECT imaging, a CT scan was also recorded. The SPECT image was reconstructed, registered to the CT, and attenuation corrected. The activity

was quantified by drawing an ROI and using the following formula (Equation 2.4):

$$\text{Calibration factor}(\text{MBq/mm}^3) = \frac{\text{Phantom activity*}}{\text{Number of voxels x summation of voxels values}} \quad (2.4)$$

*(Decay corrected to scan time).

A calibration factor was calculated per experiment using the appropriate collimator. The same imaging parameters and reconstruction algorithm were used for imaging the calibration phantom as for the *in vivo* experiments.

2.6.3   Collimator quantification range

Accurate tracer quantification was tested with different frame binning using each collimator. A point source phantom containing 20 MBq was prepared and imaged every half-life (approximately 6 hours). To mimic *in vivo* conditions, the phantom was also imaged inside a water jacket. SPECT images were acquired in list mode, recording five-second frames for 5 min at each time point. A CT scan was acquired only at the first time point. Images were reconstructed using the SROSEM algorithm (0.8 mm^3, 128 subsets and 4 iterations) and time frames were binned to achieve frame lengths of 5 seconds, 30 seconds, 1 and 5 min. Radioactivity in the phantom was measured at each time point by drawing a ROI over the source point and applying the following equation:

$$\text{Activity}(\text{MBq}) = \frac{\text{Summation of voxels values in ROI x Calibration factor x ROI volume}}{\text{Number of voxels}}$$

$$(2.5)$$

The deviation between the measured activity and the expected activity was calculated using the following formula (Equation 2.6). A 5% deviation was considered acceptable.

$$\text{Deviation}(\%) = \frac{\text{Expected activity} - \text{Measured activity}}{\text{Expected activity}} \tag{2.6}$$

2.6.4 Collimator's sensitivity limit

2.6.4.1 Phantoms studies

Phantoms containing increasing amounts of CAR T cells were prepared as described above (section 2.5.11). Phantoms were imaged using the XXUHS-M in listmode (1 frame, 30 min acquisition). Following SPECT acquisition, a whole-body CT scan was recorded for anatomical information. SPECT images were reconstructed using the SROSEM algorithm (0.8 mm^3, 128 subsets and 4 iterations), registered to the CT scan and corrected for attenuation. Images were analysed by drawing ROI over the point source and the total activity was calculated with formula (Equation 2.5).

2.6.4.2 *In vivo* sensitivity studies

To assess the sensitivity limit of traceable CAR T cells *in vivo*, T cells were inoculated subcutaneously (s.c.) in the shoulder of animals BALB/c or NSG mice followed by intravenous (i.v.) inoculation of $^{99m}\text{TcO}_4^-$. 30 min after tracer administration mice were anaesthetised with 2% isoflurane in air and transferred to the heated imaging bed. Following SPECT acquisition, a whole-body CT scan was recorded for anatomical information. SPECT images were reconstructed using the SROSEM algorithm (0.4 mm^3, 128 subsets and 3 iterations), registered to the CT scan and corrected for attenuation correction. Images were analysed as above (section 2.6.1).

Whole body SPECT imaging: T cells were resuspended in 50% matrigel and the indicated number of T cells were inoculated s.c. on each shoulder of BALB/c mice. 20 MBq of $^{99m}\text{TcO}_4^-$ was then administered i.v. 30 min prior to SPECT imaging. Mice were then anaesthetised with 2% isoflurane in air and transferred to the heated imaging

bed. SPECT images were acquired using the GP-RM collimator in spiral mode (1 frame, 30 min acquisition). Following SPECT acquisition, a whole-body CT scan was recorded for anatomical information. SPECT images were reconstructed using the SROSEM algorithm (0.4 mm^3, 128 subsets and 3 iterations), registered to the CT scan and corrected for attenuation. Images were analysed as above.

Dynamic imaging using 1-bed position: animals were placed on a heated pad and anaesthetised using isoflurane through a nose cone. T cells were resuspended in PBS and the indicated number of T cells were inoculated s.c. on each shoulder of NSG mice. 20 MBq of ^{99m}TcO$_4^-$ was then administered i.v. and animals were transferred immediately to the imaging bed. Images were acquired using the GP-RM or XXUHS-M collimators in list mode using a single SPECT bed position (10-second/frame x 540 frames) followed by an ultra-focused CT scan. SPECT images were reconstructed using the SROSEM algorithm and corrected for decay. SPECT images were registered to the CT scan and corrected for attenuation. Images were analysed as above (section 2.6.1).

2.6.5 *In vivo* tracer kinetics

Dynamic imaging using 1-bed position was used to study the feasibility of establishing an image-derived input function to drive the mathematical model. A BALB/c mouse was anaesthetised and the tail vein was cannulated. Images were acquired using the GP-RM in list mode using a single SPECT bed position (5-second/frame x 999 frames) followed by an ultra-focused CT scan. 45 μl of heparine saline was flushed before the start of the scan to prime the cannula. Two frames were recorded prior administration of 20 MBq of ^{99m}TcO$_4^-$, followed by 60 μl of heparine saline to flush the cannula tubing. 200 μl of Visipaque™(GE Healthcare) were slowly injected through the cannula before the CT scan to provide enhanced tissue contrast. SPECT images were reconstructed using the SROSEM algorithm and corrected for decay. SPECT images were registered to the CT scan and

corrected for attenuation. Images were analysed as above (section 2.6.1). To investigate the effect of using Visipaque™in the quantitation of SPECT/CT images, three phantoms were prepared containing 7.5 MBq/ml of $^{99m}TcO_4^-$ and resuspended in PBS with increasing concentrations of Visipaque™, 0, 150 or 320 μl/ml. Phantoms were imaged using the GP-RM in list mode using a single SPECT bed position (5-second/frame x 60 frames) followed by an ultra-focused CT scan. Images were reconstructed using the SROSEM algorithm (0.8 mm^3, 128 subsets and 4 iterations) and time frames were binned to achieve frame lengths of 5 seconds, 30 seconds, 1 and 5 min. Radioactivity in the phantom was measured by drawing a ROI and applying Equation 2.5. The deviation between the measured activity and the expected activity was calculated using Equation 2.6. A 5% deviation was considered acceptable.

To build a population curve of the concentration of tracer circulating in blood in relation to time, 10 NSG mice were anaesthetised and injected i.v. with 10 MBq of $^{99m}TcO_4^-$. Mice were transferred to a heat box with bed and nose cone inserts to keep the animals under anaesthesia. At the indicated time points, a cardiac puncture with a heparin coated syringe was performed under anaesthesia. Blood samples were collected in heparin coated Eppendorf tubes and kept on ice. Blood samples were processed . 100 μl of whole blood were transferred to a scintillation tube. The remaining blood was centrifuged at 2000 g for 10 min at 4°C, with the brake set to the minimum, to separate plasma from whole blood. Plasma was collected and transferred to a clean Eppendorf and 100 μl were transferred to a scintillation tube. To collect the protein-free plasma, 100% acetonitrile was added to the remaining plasma following a 2:1 ratio. Tubes were vortexed and centrifuged as above. The supernatant containing the protein-free plasma was transferred to a scintillation tube. Radioactivity in the protein pellet, the scintillation tubes, and the standards for each time point were measured in a gamma counter.

2.6.6 Tracking CAR T cells *in vivo*

2.6.6.1 PSMA xenograft mouse model

PC3-LN3-PSMA expressing luciferase and TdTomato (PLP-LT) were inoculated subcutaneously in the shoulder area. For the titration experiments, mice received 0.25×10^5, 0.5×10^5 and 1×10^6 PLP-LT cells and the chosen dose of 0.25×10^5 PLP-LT cells was used for subsequent studies. At the indicated time point, 2×10^6 T cells were administered intravenously in 200 μl of PBS. Tumour growth was monitored by caliper measurements and bioluminescence imaging (BLI) using an IVIS Lumina III *in vivo* imaging system (PerkinElmer, USA). Mice were injected intraperitonially (i.p.) with 200 μl of D-luciferin at 150 mg/kg and imaged under isoflurane anaesthesia. Firstly, animals were imaged for 30 min to assess optimal imaging time post D-luciferin i.p. injection. As depicted in Figure 2.7, maximum signal was detected 8 min post D-luciferin i.p. injection. Thus, animals were imaged at 8 min post D-luciferin administration using a 20 cm field of view, medium binning and automatic exposure. Analysis was performed drawing an ROI over each animal using Living Image 4.3.1 software (Caliper Life Sciences, USA) and the resulting signal summation was plotted.

2.6.6.2 *In vivo* SPECT/CT imaging and Image Analysis

Images were acquired using a multi-modal SPECT/CT scanner (VECTor^{6}CT^{XUHR} MiLabs) fitted with the XXUHS-M collimator. Animals were kept under 2% isoflurane anaesthesia in air throughout the imaging session and received heat support from an integrated heating source in the scanner bed. Respiratory and bed temperature were monitored and adjusted using BioVet sensors (m2m Imaging; Newark, USA). SPECT images were acquired dynamically (30 seconds/frames x 78 frames), in list mode using 13-bed positions to contain the heart and the tumour xenograft within the field of view. The first frame was acquired to measure the background counts, and animals were injected i.v. with 10 MBq of ^{99m}TcO$_4^-$ directly on the bed before resuming the scan. Following dynamic SPECT
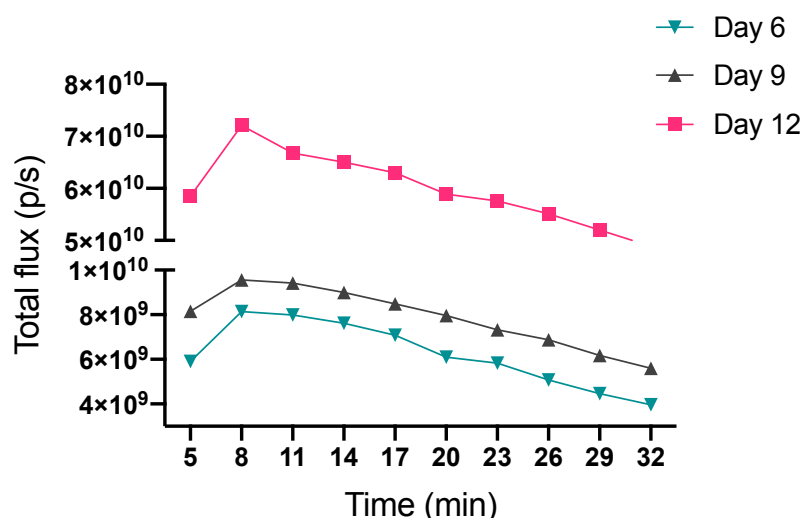
Figure 2.7: Time course of luciferase signal. Luciferase kinetic time curves after the intraperitoneal injection of luciferin at days 6, 9 and 12 post tumour inoculation. Maximum signal was recorded 8 min post injection. n=1 mouse/day.

imaging, a whole-body CT scan was acquired for anatomical reference. SPECT/CT data were reconstructed using the integrated MiLabs Rec 11.00 software. The CT images were reconstructed at 80 μm^3. SPECT images were binned into 19 frames: 10 x 1 min, 3 x 2 min, 2 x 6 min, 2 x 10 min, 2 x 15 min. Each frame was reconstructed using the SROSEM algorithm (0.8 mm^3, 128 subsets and 9 iterations), registered to the CT and corrected for attenuation, and radioactivity decay.

Images were analysed using VivoQuant software(Invicro, USA). For each scan, ROIs were delineated over the heart (to establish the input function) and tumour using the CT anatomical data as a reference for the quantitation of radioactivity. Uptake was normalised to the injected dose and expressed as percentage of the injected dose (%ID) or percentage of the injected dose per gram of tissue (%ID/g). For the compartmental modelling, the tumours were segmented using a thresholding method value of 2.5 on normalized images on 0-12 %ID/g scale or the 3x3x3 cube of voxels centred around the highest uptake voxel within the ROI.

2.7   Compartmental modelling

Two-compartment and three-compartment models were built to simulate the distribution of $^{99m}TcO_4^-$ in tissues using SAAM II software v2.3.1.1. (The Epsilon Group, USA). The central compartment, denoted as q1, represents the concentration of tracer in bloodstream as a function of time. These values were quantified by drawing an ROI over the heart and served as the basis for establishing the image-derived input function (IDIF). In the two-compartment model, q2 represents the concentration of tracer within the tumour (Figure 2.8 a). In the three-compartment model, q2 refers to the unbound tracer in the tumour tissue, while q3 refers to the concentration of tracer bound to the CAR T cells within the tumour (Figure 2.8 b). The transfer of tracer between these compartments is characterized by rate constants K_i. Specifically, K_1 reflects the rate at which the tracer is delivered from the bloodstream to the tumour space. K_2 represents the rate constant of tracer efflux from the tumour to the bloodstream. Lastly, in a three-compartment model, K_3 denotes the rate at which the tracer is internalized by the CAR T cells from the tumour tissue. To account for the missing excretion and distribution of the tracer to other organs from the central blood compartment, a forcing function (FF) was employed to describe the tracer concentration change in the bloodstream. A two-phase exponential decay equation was fitted to the blood dynamic data, which was subsequently used as the forcing function. The models were then fitted to the dynamic SPECT data provided (s1) and the rate constants were extracted.

For the graphical analysis, Logan and Patlak plots were calculated in Microsfot Excel applying equations 1.1 & 1.2. The resulting data were plotted using Prism v.9 (GraphPad).
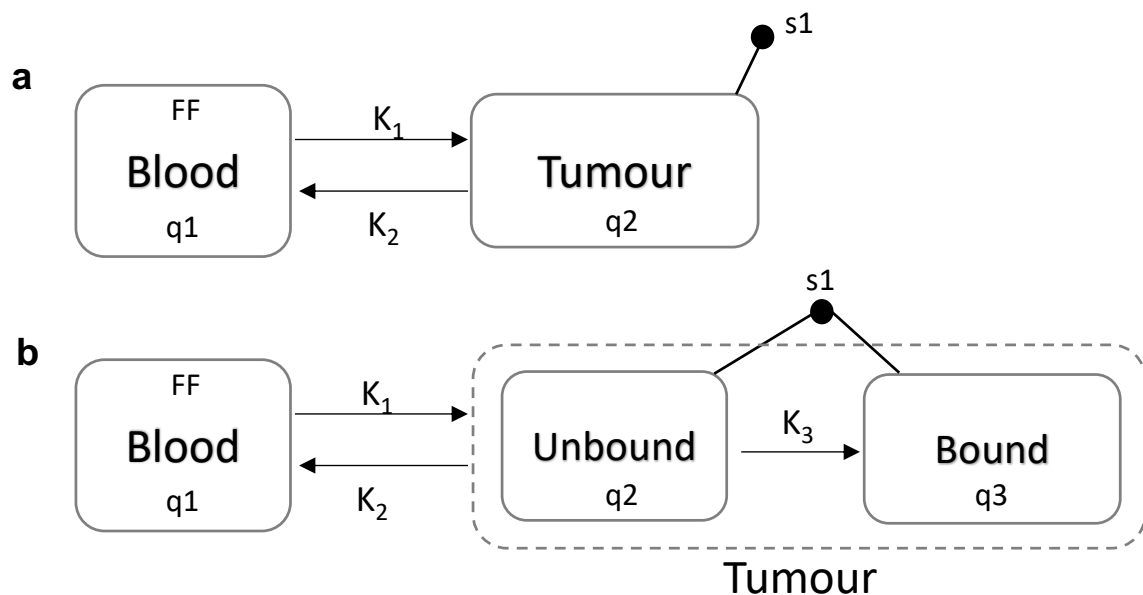
Figure 2.8: Proposed compartmental models built in SAAM II software. a) In a two-compartment model, the blood compartment, q1, exchanges tracer with the tumour compartment, q2, at the rate defined by K_1 and K_2. The blood compartment was fixed with a forcing function (FF) and the model was fitted to the quantified tumour signal, s1. b) In a three-compartment model, the tumour compartment is formed by two compartments representing the unbound tracer in tumour tissue and bound tracer to the CAR T cells, with the exchange rate defined by K_3.

2.8 Tracking CAR T cell *ex vivo*

2.8.1 *Ex vivo* Biodistribution

Following SPECT/CT imaging, animals were sacrificed, and organs of interest were immediately dissected out and transferred to pre-weighed scintillation tubes. Radioactivity was quantified using a gamma counter with calibration standards. Radioactivity obtained from the different organs and tumours was calculated as %ID or %ID/g.

2.8.2 Tumour processing

To quantify the number of infiltrating CAR T cells and obtain the ground truth to establish the mathematical model, tumours were disassociated to a single cell suspension for FACs analysis. Firstly, tumours were mechanically dissociated in 0.9 ml of RPMI, followed by enzymatic digestion with 0.35 μg/mL Liberase (Roche, Switzerland) and 0.25 μg/mL DNAse (Sigma-Aldrich) for 30 min at 37°C. After incubation, an additional 5 ml of RPMI supplemented with 5 μM of EDTA (Sigma-Aldrich) was added and the solution was filtered through a 70 μm strainer (Falcon, USA). Cells in the filtrate were washed twice with plain RPMI. Cell pellets were resuspended in 30% percoll and 70% percoll was added to the bottom carefully. Cells were centrifuged at 700 g for 25 min with minimum brake and acceleration. This step allowed for the separation of lymphocytes from tumour cells (Figure S 8.2). The ring of lymphocytes between the percoll layers was resuspended in 0.5 ml of RPMI. Cell surface staining was performed by incubating samples on 25 μl of Human Fc block (Life-Technologies) solution for 10 min at 4°C. The samples were then washed and stained as previously described (section 2.4.1). CountBrightTM Absolute Counting Beads were added to the samples just before acquisition and number of infiltrating CAR T cells was calculated following formula (Equation 2.2). T cells were defined as human CD45$^+$, human CD3$^+$ (Figure S 8.3).

The compensation matrix was obtained using Ultracomp beads and ArC reactive beads (Invitrogen) according to the manufacturer's instructions. BD FACS Fortessa Cell Analyzer (BD Biosciences) was used for sample acquisition.

To delay tumour processing, tumours were stored in 1 ml of MACS Storage buffer (Miltenyi, UK) at 4°C overnight before performing the protocol just described.

2.8.3   Immunohistochemistry

For histology, tumours were fixed in 10% neutral buffered formalin for 24 hours and then embedded in paraffin. Immunohistochemistry staining was performed by the Pathology Core at Barts Cancer Institute. Anti-CD3 and anti-CD31 staining was done by automation in a Ventana Discovery XT machine (Roche Diagnostics Ltd.). All reagents were acquired from Roche, Ventana Medical. Briefly, 4 µm tissue sections were deparafinised using Discovery wash solution at 75°C for 8 min, followed by heat induced epitope retrieval (HIER) in Tris-EDTA buffer pH 7.8 at 95°C for 44 min. Slides were then blocked with inhibitor CM at 37°C for 4 min. Anti-CD3 (abcam ab11089, 1:200) and anti-CD31 (Abcam ab28364, 1:200) were added in 100 µl of Antibody diluent buffer and incubated for 60 min, followed by one drop of the secondary antibody rabbit anti-rat Ab (Bio-Rad) at 42°C for 20 min. After the incubation with the antibodies, one drop of OmniMap anti-Rabbit HRP was applied and incubated for 16 min, followed by one drop of DAB CM and One Drop H_2O_2 CM, for 8 min, and one drop of Copper CM for 5 min. Counterstain with Haemotoxylin was incubated for 8 min followed by Bluing Reagent for a further 8 min. Slides were dehydrated in graded ethanol and xylene and coverslips were attached with mounting media. Slides were scanned in a Nanozoomer s210 slide scanner (Hamamatsu, Japan) with 40X magnification and analysed using QuPath software 297. To discriminate between positive and negative cells, part of the tissue was used to establish the adequate threshold values. Next, the images were analysed using the 'positive cell detection' command to quantify the number of cells positive for CD3 staining within the full tissue section (Figure S 8.4). All the images were analysed following the same workflow with the same settings.

2.9   Statistical analyses

Independent experiments were performed on different days with CAR T cells from different donors for all *in vitro* assays. Data were plotted using Prism v.9 (GraphPad) and statistical analysis details were added to figure legends. Graphs report mean ± SD unless otherwise noted.

Chapter 3

Characterisation of traceable CAR T cells *in vitro*

CAR T cell has shown promising results in the treatment of haematological tumours; however, the success rate drastically decreases for solid tumours. CAR T cells need to migrate to the tumour site, extravasate, proliferate and persist to elicit a response, but little is known about these dynamic processes. Non-invasive serial *in vivo* imaging of CAR T cells could improve our understanding of CAR T cell behaviour, dosing and reasons behind treatment outcomes, thus paving the way to safer and more efficacious immunotherapeutic drugs for solid tumours.

3.1 Generation of a traceable PSMA-targeted CAR T cell

The reporter gene hNIS, an indirect labelling strategy, was chosen for the *in vivo* imaging of PSMA-targeting CAR T cells, which were designed by Dr. Emami[133]. The PSMA-targeting CAR, namely P28ζ, is a second-generation CAR consisting of a single chain variable fragment (scFv) derived from the J591 human PSMA targeting antibody and the intracellular domains of CD28 and CD3ζ, which are connected to the scFv by a CD28 hinge and

transmembrane domain. A bicistronic retroviral vector was designed to co-express the P28ζ CAR downstream of the 4$\alpha\beta$ gene (coupling the IL-4 receptor alpha ectodomain to the transmembrane and endodomain of IL-2/IL-15Rbeta), which allows for the enrichment of the transduced population upon addition of IL-4. This CAR was termed 4Pm28ζ. To create the traceable CAR T cells, the reporter gene hNIS was co-expressed downstream of the 4Pm28ζ CAR. This tricistronic construct containing the 4$\alpha\beta$, P28ζ and hNIS genes was termed 4Pm28ζN. A control CAR was designed by truncating the CD28/CD3ζ intracellular signalling domains, this CAR was termed 4PmTrN. In all constructs, I cloned an extracellular myc tag between the scFv and the CD28 hinge to facilitate the detection of transduced cells by flow cytometry (Figure 3.1).
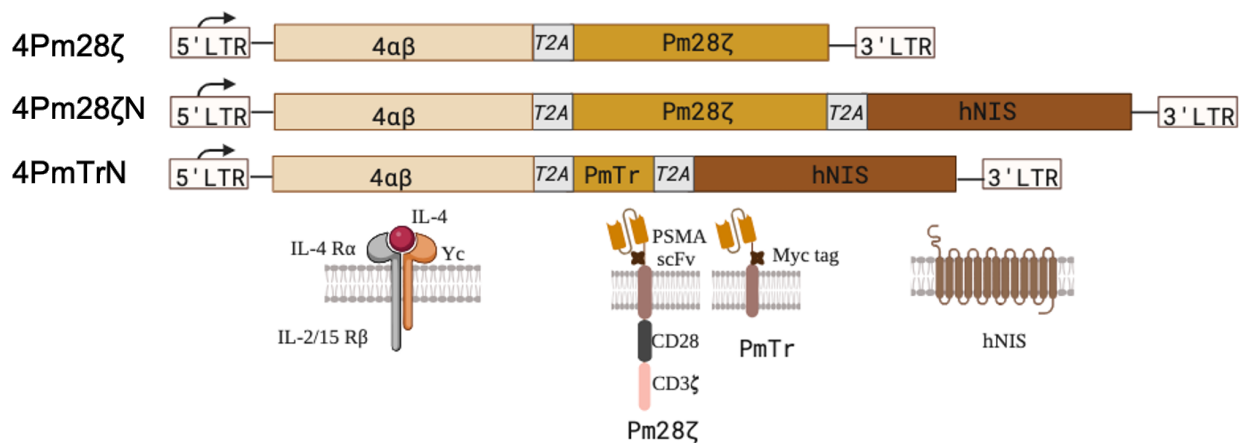
Figure 3.1: Structure of PSMA-targeted CAR constructs. The P28ζCAR consists of the J591 human PSMA targeting scFv antibody downstream the CD8 leader sequence. Downstream of the scFv there is a myc tag, CD28 hinge and transmembrane domain, followed by the CD28 and CD3 intracellular domains. The truncated CAR, PTr, was designed by removing the intracellular signalling domains. To make the CAR T cells traceable, the reporter gene hNIS, was expressed downstream the CAR separated by a T2A. All three CAR constructs expressed the 4$\alpha\beta$ gene, which allows for enrichment of the transduced population.

The PC3-LN3 (PL) prostate cancer cell line was selected as the target tumour cell line to assess the CAR T cell functionality in co-culture experiments. PL cells do not endogenously express PSMA at detectable levels by flow cytometry, so this cell line has been previously

modified in our lab to express high levels of surface PSMA, generating PC3-LN3-PSMA cells (PLP). Furthermore, luciferin and Tdtomato were also transduced to produce PL-LT and PLP-LT, respectively[133] (Figure 3.2).
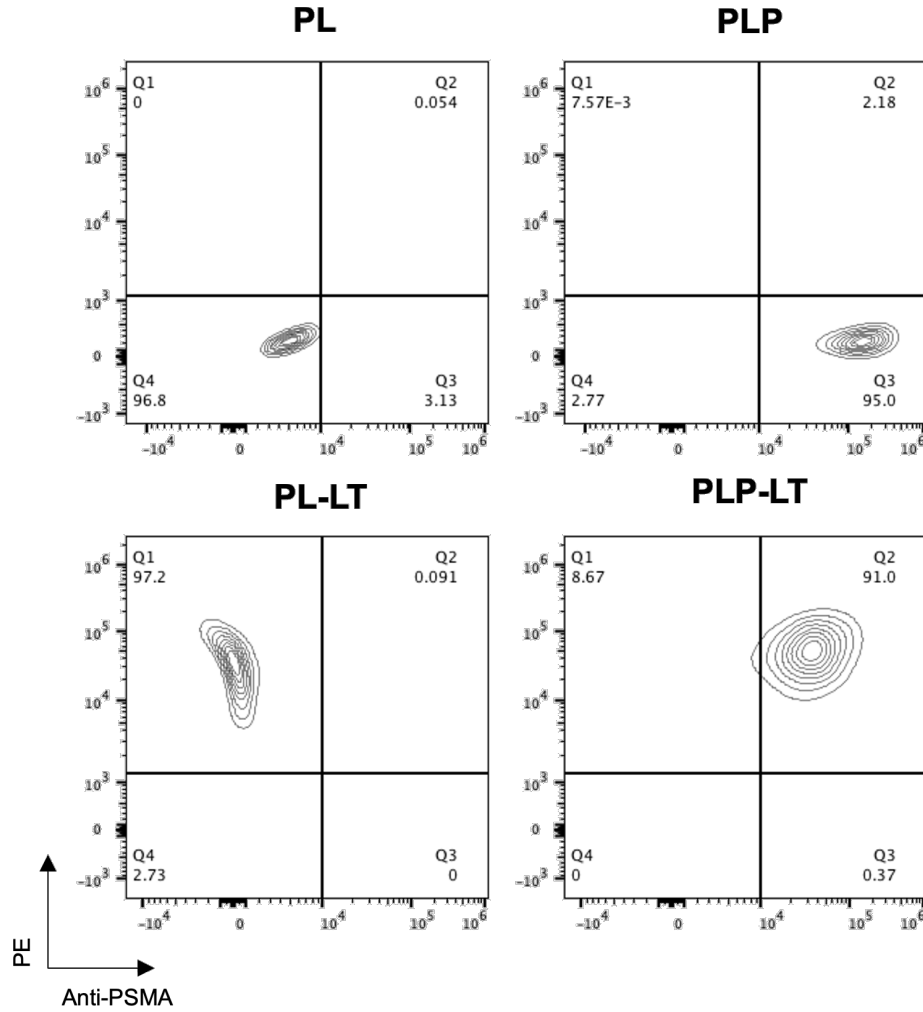
Figure 3.2: Expression of Tdtomato and PSMA on target cells. Flow cytometry contour plots of target cells depicting PSMA and Tdtomato (detected in the PE channel) cell surface expression.

To investigate the effect of the inclusion of the hNIS on CAR T cell proliferation and cytotoxicity, PBMCs were transduced with the bicistronic construct 4Pm28ζ or the tricistronic hNIS construct 4Pm28ζN (Figure 3.1). There were no significant differences in CAR T cell proliferation after the 11-day expansion period (Figure 3.3 a). Although the

transduction efficacy, based on the myc tag expression, was higher for the bicistronic construct compared to the tricistronic construct (Figure 3.3 b), myc tag cell surface expression levels were comparable as determined by the median fluorescence intensity (MFI) (Figure 3.3 c). hNIS-mediated uptake was only observed by the PBMCs expressing the tricistronic construct and uptake was blocked by the inhibitor sodium perchlorate ($NaClO_4$)(Figure 3.3 d).
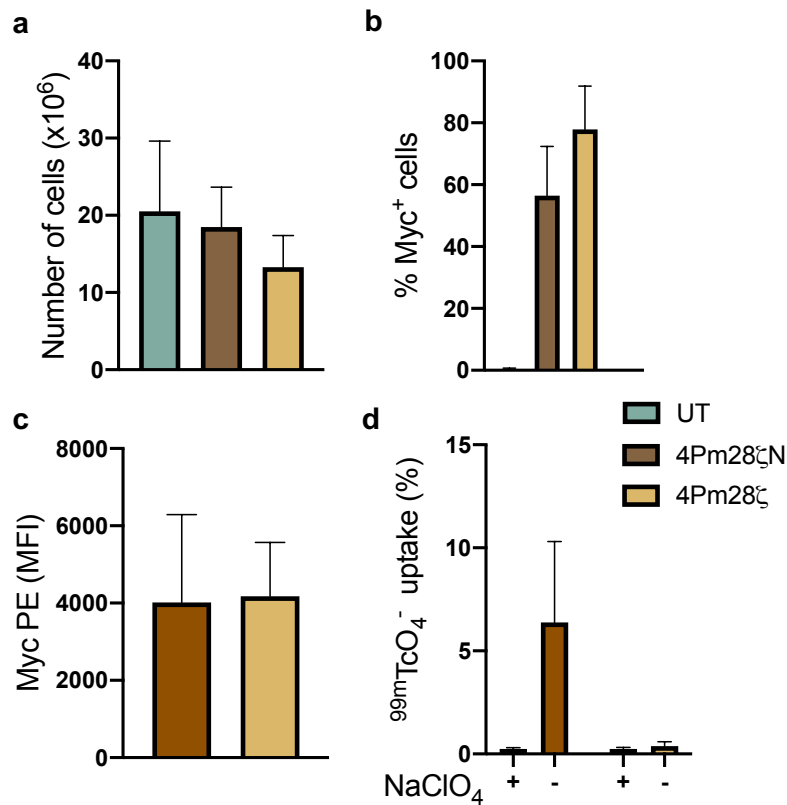
Figure 3.3: Comparing proliferation and transduction efficacy of PBMCs transduced with bicistronic and tricistronic constructs. a) Cell count 11 days post transduction. b) Transduction efficiency based on myc tag surface expression. c) MFI of myc-tagged positive cells. d) *In vitro* uptake levels of 4Pm28ζN or 4Pm28ζ CAR T cells incubated with $^{99m}TcO_4^-$ in the presence or absence of the inhibitor. n=3 donors. UT=untransduced. Graphs represent mean ± SD.

To determine the effect of the addition of the hNIS on CAR T cell cytotoxicity, PBMCs transduced with each construct were co-cultured with fluorescence target cells to monitor real-time tumour killing using an Incucyte® live cell analyser. Comparable cytotoxicity was

observed when culturing the bicistronic 4Pm28ζ or the hNIS expressing 4Pm28ζN T cells with PLP-LT cells. Cytotoxicity occurred in a dose-dependent manner (Figure 3.4 a). Tumour killing was observed at the higher effector ratios after 50 hours in co-culture with PL-LT cells, suggesting low expression of PSMA in the wild-type cancer cell line (Figure 3.4 b). Untransduced cells did not induce cytotoxicity when co-cultured with either tumour cell line (Figure 3.4 c).

3.2 Functional validation and characterisation of the traceable CAR T cells

Since the addition of hNIS had no detrimental effect on CAR T cell proliferation and cytotoxicity, PBMCs were transduced with the hNIS expressing constructs, i.e. 4Pm28ζN and 4PmTrN (Figure 3.1). Expression of all transgenes was demonstrated in retrovirus-transduced T cells by flow cytometry. Transduction efficiency was very low following transduction, however addition of IL-4 led to a rapid enrichment of CAR$^+$ cells (Figure 3.5 a). After the 11-day expansion period, there were no significant differences in CAR T cell proliferation (Figure 3.5 b). Likewise, transduction efficiency, based on myc expression, was similar between constructs with >70% of the PBMCs expressing the CAR on the cell surface (Figure 3.5 c). CAR density on the T cell surface was quantified using Quantum beads. The average CAR number expressed on the cell surface of 4Pm28ζN T cells was higher than in 4PmTrN T cells (31,231 ± 9,801 copies/cell and 16,795 ± 6,222 copies/cell, respectively) (Figure 3.5 d & e).
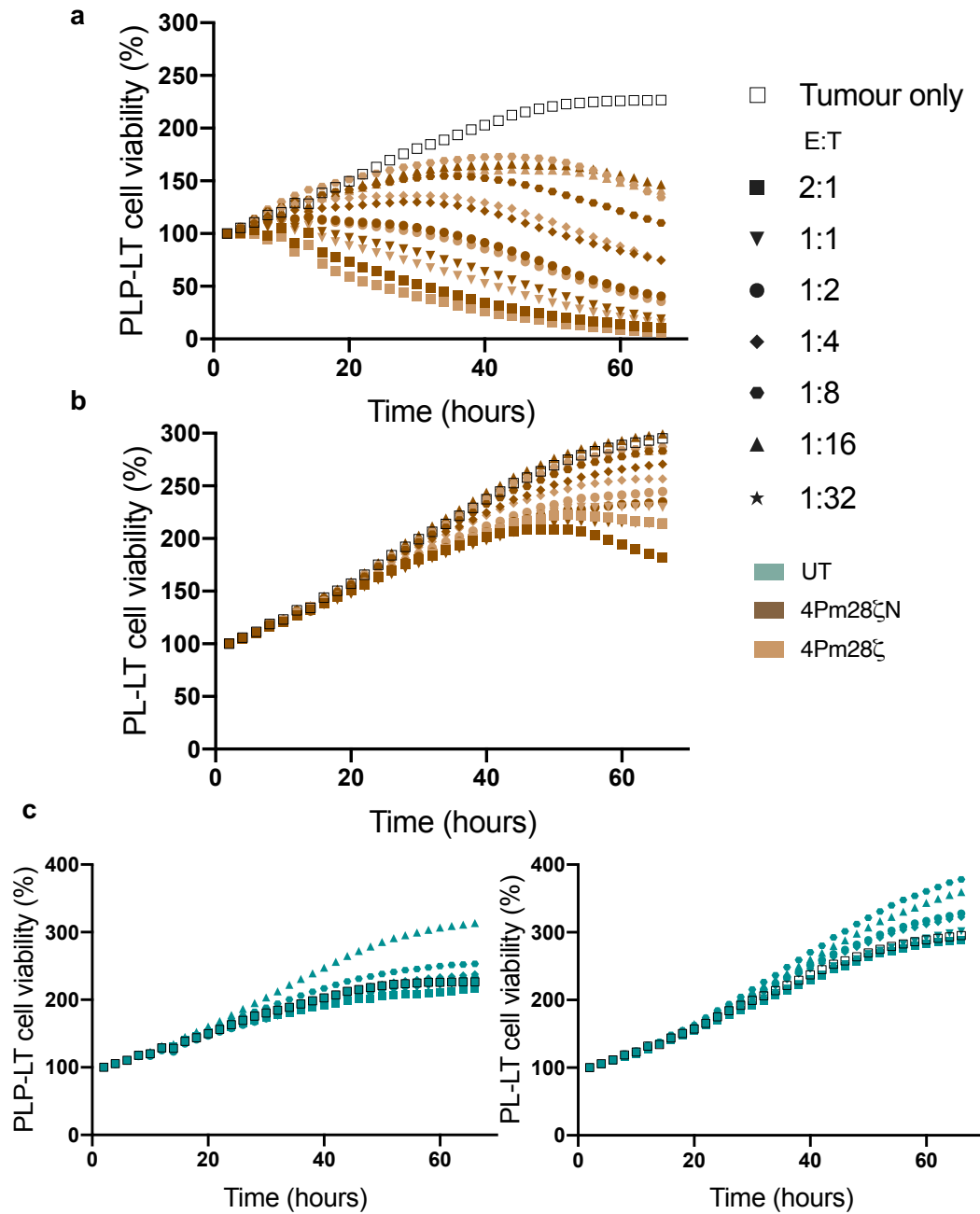
Figure 3.4: Cytotoxicity of CAR T cells when co-cultured with target cells. Real time tumour cell viability after co-culture of CAR T cells (a & b) or with untransduced T cells (c) with tumour cells at different effector-to-target (E:T) ratios. Data acquired using an Incucyte®. n=4 donors/group. Graphs represent mean citotoxicity from 4 donors.
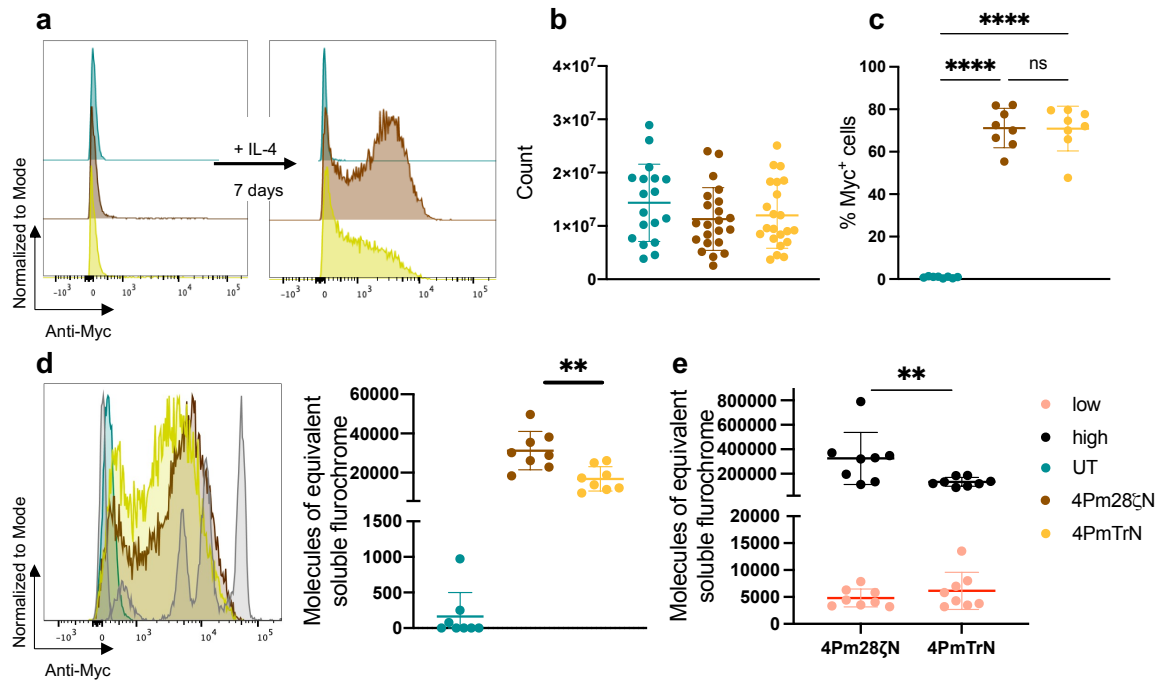
Figure 3.5: Transduction of PBMCs with tricistronic retroviral construct.
a) Representative flow cytometry histogram showing selective expansion of transduced PBMCs in the presence of IL-4. b) Cell count 11 days post transduction. n=18/UT group; n=22/CAR groups. c) Transduction efficiency based on myc tag surface expression. n=8 donors/ group. Statistical analysis performed by one-way Anova. d) Representative histogram showing surface myc tag staining in the presence of Quantum beads (grey). Average fluorescence quantification of CAR cell surface expression and e) range of expression. n=8 donors/ group. Statistical analysis performed by Student's t-test. Graphs represent mean ± SD. ns: no significant, ∗∗p ⩽ 0.01, ∗∗∗∗p ⩽ 0.0001. UT = untransduced.

PBMCs transduced with 4Pm28ζN showed a broader range of CAR surface expression levels (3,509-790,234 copies/cell) with higher variability between donors compared to PBMCs transduced with 4PmTrN (3,180-187,002 copies/cell) (Figure 3.5 d).

After the successful production of the CAR T cells, cell phenotype and activation status was assessed by flow cytometry staining for the cell surface markers CCR7 & CD45RA, and PD-1 & CD69, respectively. Figure 3.6 a, shows the gating strategy used to define the different cells subsets: $T_{n/scm}$ (CCR7$^+$ CD45$^+$),T_{cm} (CCR7$^+$ CD45RA$^-$), T_{em} (CCR7$^-$ CD45RA$^-$), and T_{emra} (CCR7$^-$ CD45RA$^+$). The phenotype was analysed before and after

co-culture with PLP at a 1:2 effector-to-target (E:T) ratio. T cell phenotype comprised a mixture of memory and effector phenotypes. Viral transduction caused a decrease in naïve populations compared to the activated untransduced cells. After exposure to antigen, there was a further decrease in the proportion of the naïve population, and enrichment of the effector memory cells, especially for 4Pm28ζN T cells (Figure 3.6 a bottom). The percentage of 4Pm28ζN T cells expressing CD69 and PD-1, as well as the MFI, significantly increased after exposure to antigen, but did not increase on untransduced or truncated controls (Figure 3.6 b).

Functional activity was demonstrated by co-culturing CAR T cells with PLP and PL tumour cells at different E:T for 48 hours before the viability of the tumour cells was measured. 4Pm28ζN T cells elicited cytotoxicity against PLP cells at all E:T ratios in a dose-dependent manner (Figure 3.7 a). Cytotoxicity was also observed against PL cells at the highest E:T ratios of 2:1 and 1:1, but at lower E:T ratios no significant cytotoxicity was observed compared to 4PmTrN or untransduced cells (Figure 3.7 a). In line with the cytotoxicity data, 4Pm28ζN T cells released IFNγ and IL-2 cytokines in a dose-dependent manner when co-cultured with PLP cells (Figure 3.7 b), but no cytokines were released when co-cultured with PL tumour cells (Figure 3.7 c). The controls, 4PmTrN and untransduced PBMCs, did not elicit cytotoxicity against the tumour cells or produce cytokines (Figure 3.7 a & c). These data demonstrate the robust antigen specific activation and cytotoxicity of 4Pm28ζN T cells.

3.3 hNIS mediated technetium pertechnetate uptake

The function of hNIS was demonstrated by *in vitro* ^{99m}TcO$_4^-$ uptake assays. There were no differences in tracer internalisation between 4Pm28ζN and 4PmTrN T cells. Uptake was blocked in the presence of the inhibitor sodium perchlorate, further confirming hNIS-specific uptake (Figure 3.8 a). hNIS-mediated transport depends on the sodium gradient generated by the ATP-consuming sodium-potassium pump. As expected, therefore, uptake was only
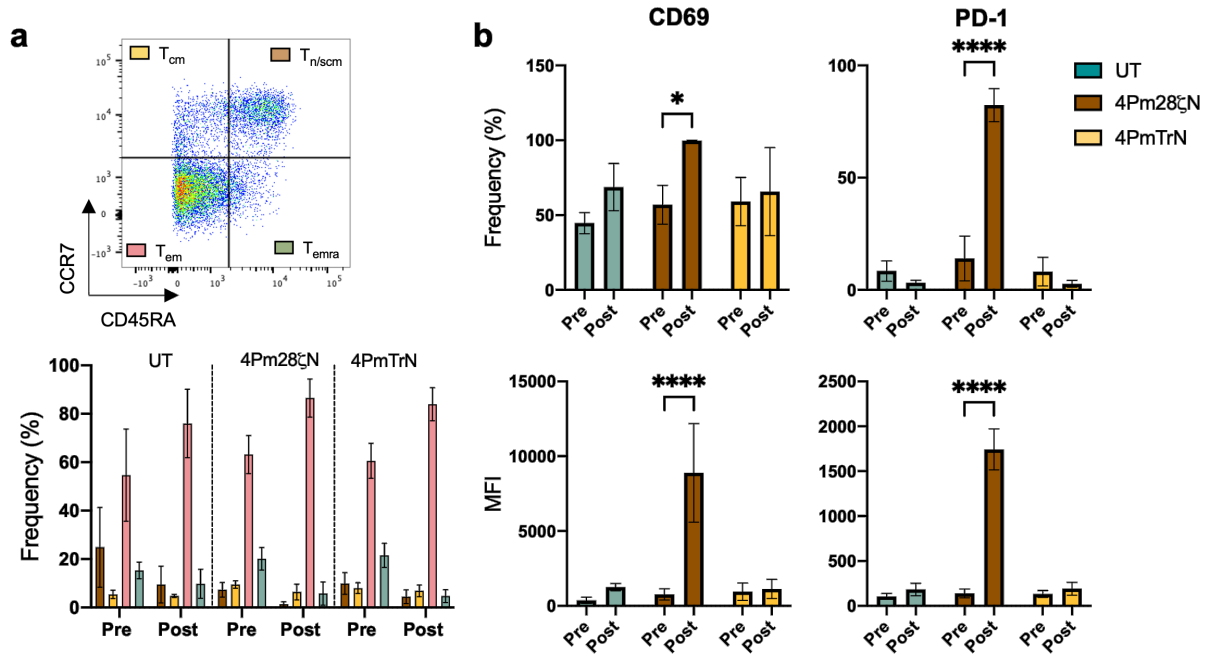
Figure 3.6: CAR T cell phenotyping. a) CAR-T cell gating strategy for phenotyping cells stained for CD45RA and CCR7 (top); (bottom) frequency of each subset before and after co-culture with PLP tumour cells. $T_{n/scm}$: naïve ; T_{cm}: central memory T cells; T_{em}: effector memory T cells; T_{emra}: effector memory T cells expressing CD45RA. b) CD69 and PD-1 surface level expression and MFI before and after co-culture with PLP cell line. n=3 donors/ group. Graphs represent mean ± SD. Statistical analysis performed by two-way ANOVA. ****$p \leqslant 0.0001$.

observed in viable cells. The frequency of viable cells was assessed before exposure to tracer by staining for Annexin V and Zombie near-infrared L/D dye (Figure 3.8 b). The $^{99m}TcO_4^-$ uptake in relation to time is depicted in (Figure 3.8 c). Rapid tracer influx was observed in the traceable CAR T cells, reaching the peak at 30 minutes with 70% of the maximal uptake being still internalised 2 hours post-exposure to the tracer. Radiotracer efflux in relation to time was assessed after the addition of $^{99m}TcO_4^-$ to the cells in culture. Decreasing the concentration of $^{99m}TcO_4^-$ in the media to mimic *in vivo* tracer kinetics in blood led to efflux of intracellular radionuclides with less than 50% of the radiotracer being retained in the cells after 30 minutes (Figure 3.8 d). $^{99m}TcO_4^-$ uptake was not detected in the target tumour cells (Figure 3.9).
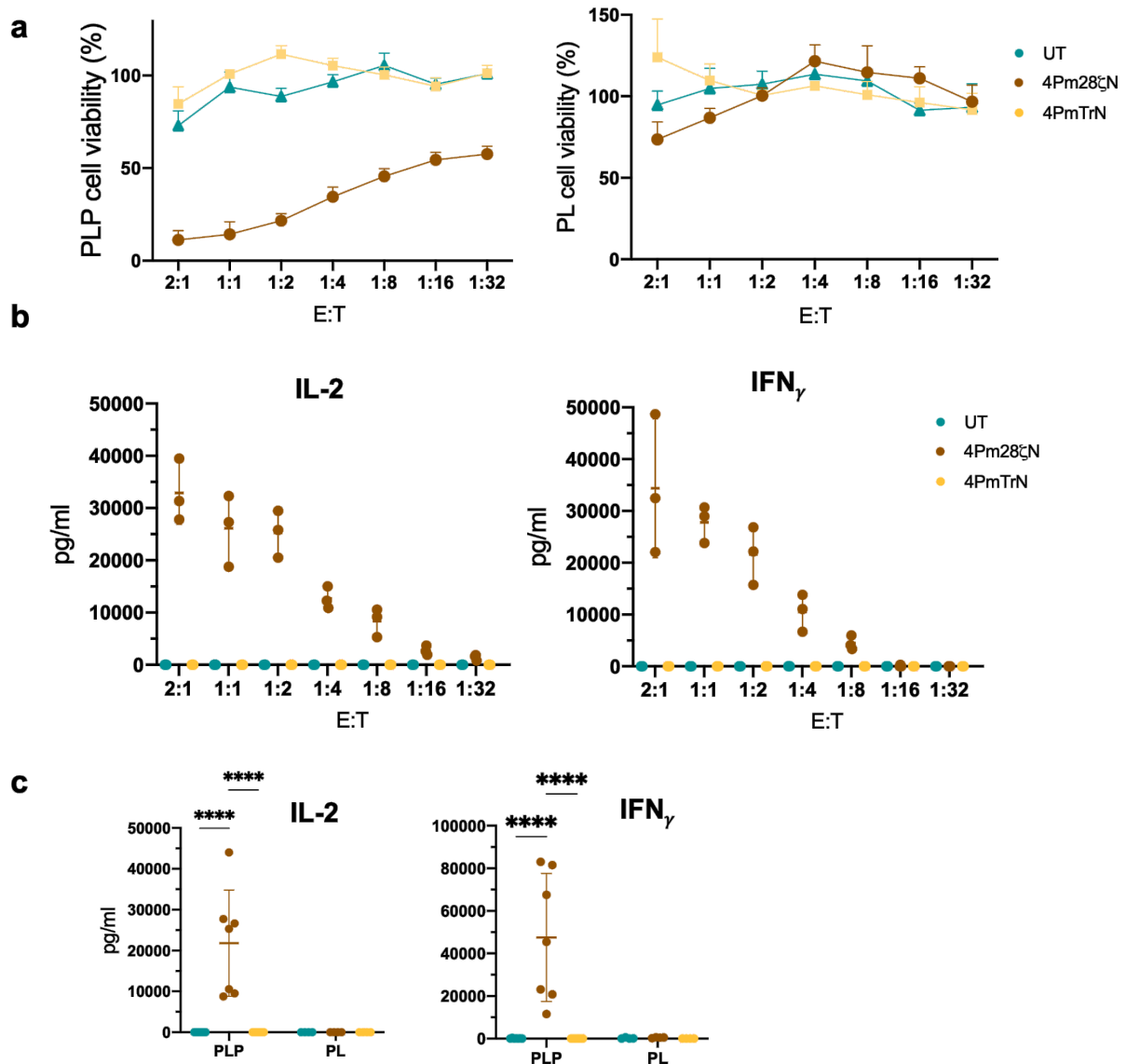
Figure 3.7: CAR T cell cytotoxicity and cytokine release. a) Percentage of tumour cell viability 48 h after co-cultured with CAR T cells determined by MTT assays. b) ELISAs were carried out on supernatants from experiments in a) to determine secretion levels of IL-2 and IFNγ by CAR T cells at different E:T when co-cultured with PLP tumour cells c) IL-2 and IFNγ release at E:T 1:1 when co-cultured with PLP or PL target cells. n=3-7 donors/group. Graphs represent mean ± SD. Statistical analysis performed by two-way ANOVA. ****p ⩽ 0.0001. PLP=PC3-LN3-PSMA ; PL= PC3-LN3.
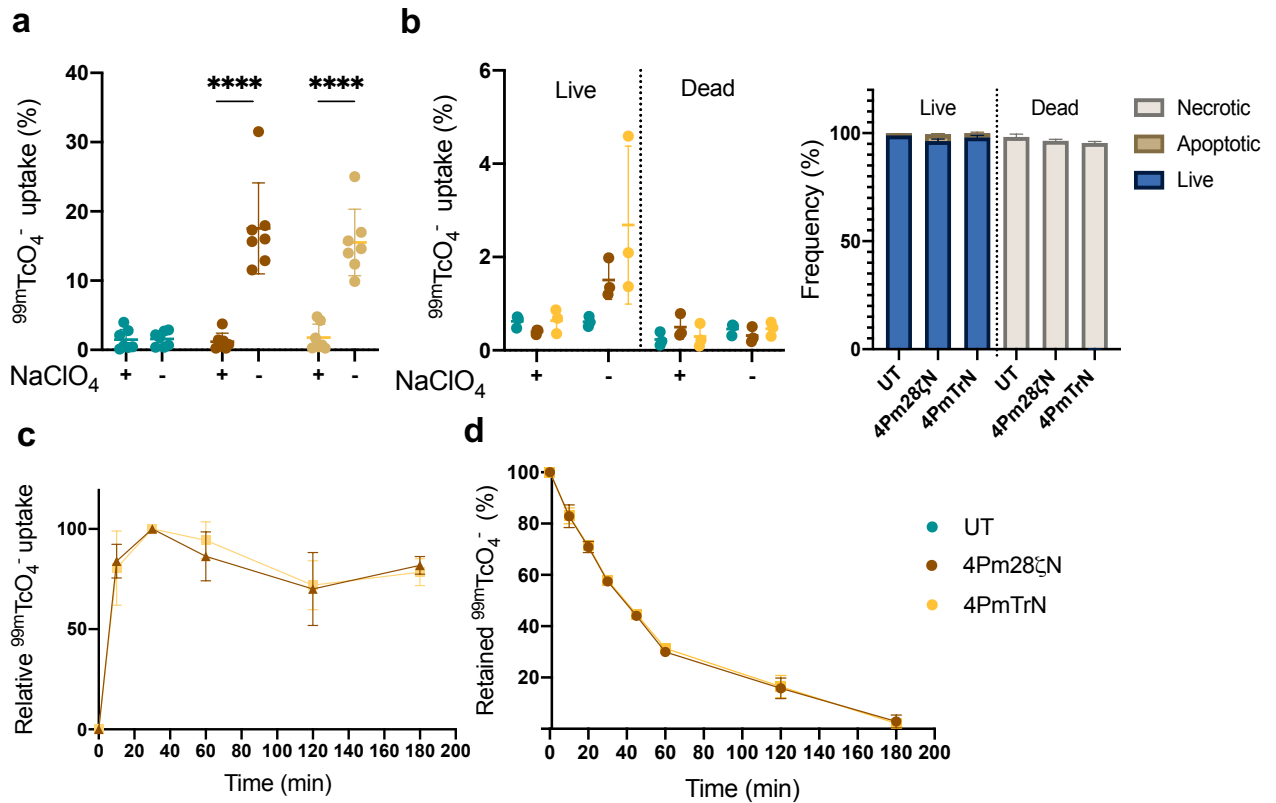
Figure 3.8: hNIS mediated $^{99m}TcO_4^-$ uptake. a) *In vitro* uptake levels of CAR T cells incubated with $^{99m}TcO_4^-$ in the presence or absence of the inhibitor. n=7 donors/group. b) *In vitro* uptake levels in viable or dead CAR T cells treated with $^{99m}TcO_4^-$ n=3 donors/group. c) Relative tracer uptake over three hours. n=3 donors/group. d) Efflux of $^{99m}TcO_4^-$ from the cells. n=3 donors/group. Graphs represent mean ± SD of assays performed in triplicates. Statistical analysis performed by two-way ANOVA. $****p \leqslant 0.0001$.

To further characterise the hNIS behaviour in the traceable CAR T cells, competition inhibition and saturation uptake assays were performed. $^{99m}TcO_4^-$ uptake was reduced by increasing the concentration of the inhibitor sodium perchlorate (Figure 3.10 a). Tracer internalisation affinity was investigated through uptake saturation assays. Saturation of the symporter was not achieved at the tested tracer amounts, but higher uptake was observed in 4Pm28ζN T cells compared to the 4PmTrN T cells (Figure 3.10 b).

The difference in the uptake level was further investigated to determine whether the activation status of the CAR T cells impacts their ability to uptake $^{99m}TcO_4^-$ as the observed
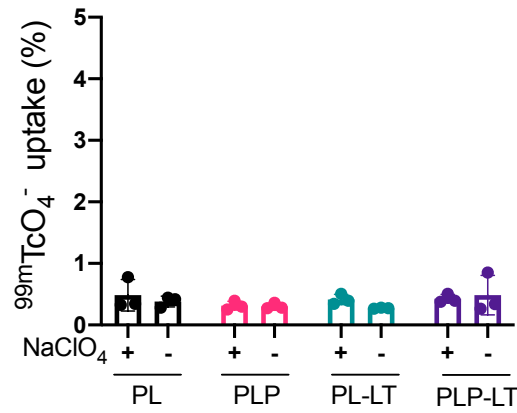
Figure 3.9: Target tumour cells lines do not take up $^{99m}TcO_4^-$. *In vitro* uptake levels of target cells incubated with $^{99m}TcO_4^-$ in the presence or absence of the inhibitor. Graphs represent mean ± SD of assays performed in triplicates.
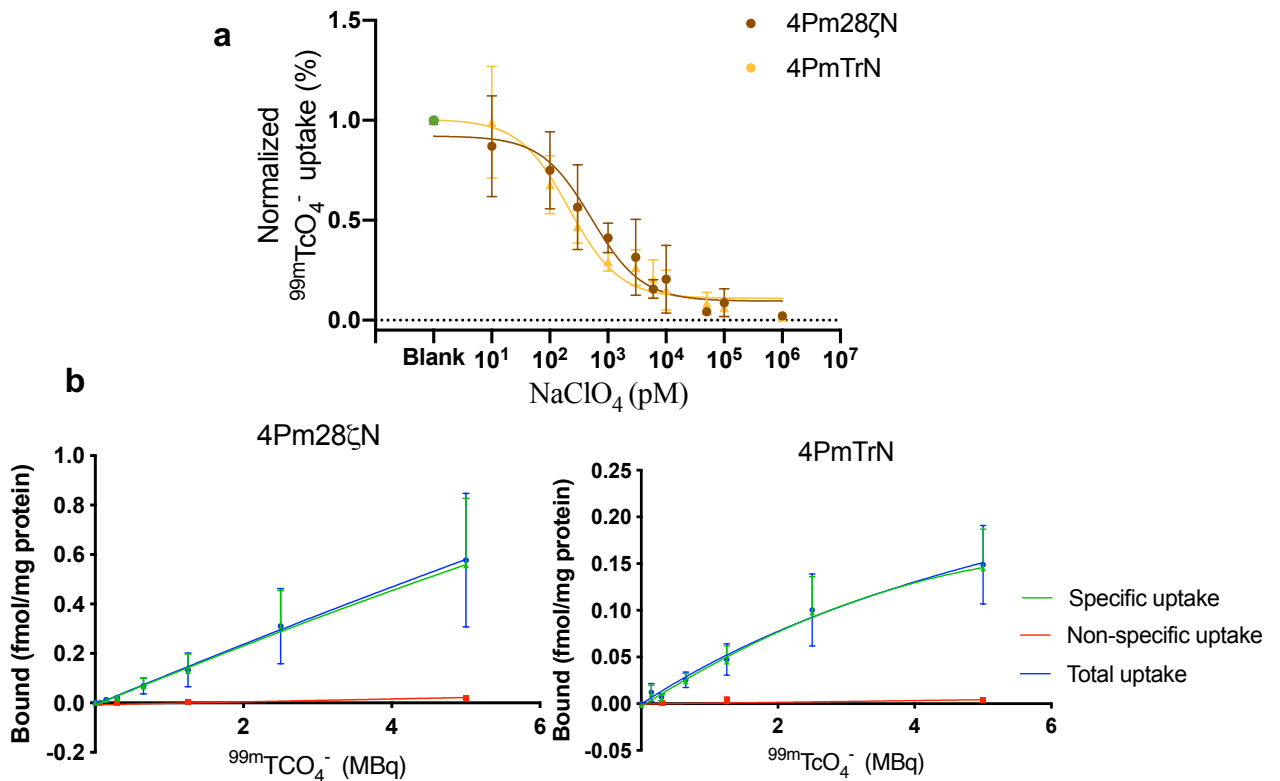
Figure 3.10: Competition and saturation assays. a) Competition inhibition curve showed the effect of increasing concentrations of inhibitor on $^{99m}TcO_4^-$ uptake by PBMCs transduced with the CAR constructs. b) Specific saturation uptake of 4Pm28ζN T cells (left) and 4PmTrN T cells (right). Each point represents mean ± SD of three assays performed in triplicate.

difference could then be attributed to tonic signalling through the CD28/CD3ζ chains of the CAR in the 4Pm28ζN T cells[26, 34, 44].

To assess the effect of T cell activation on hNIS-mediated uptake, CAR T cells were stimulated with ionomycin and phorbol 12-myristate 13-acetate (Iono/PMA) to achieve rapid activation while bypassing the CAR/TCR complex. Robust activation was achieved with Iono/PMA as demonstrated by the increase in cells expressing CD69 compared to PBMCs maintained in IL-4 (Figure 3.11 a). The number of cells expressing surface CAR was maintained after activation (Figure 3.11 b), in contrast to the decrease in cells expressing surface hNIS (Figure 3.11 c). Reduced uptake was also observed after antigen-independent activation for 4Pm28ζN and 4PmTrN transduced PBMCs (Figure 3.11 d) compared to cells cultured in IL-4. Interestingly, there were no significant differences in the uptake levels of Iono/PMA activated 4Pm28ζN and 4PmTrN T cells (Figure 3.11 d), suggesting that the activation state of the cells may influence tracer uptake.

The observed decrease in uptake levels between resting and Iono/PMA activated 4Pm28ζN T cells was further investigated as it could impact the feasibility of tracking the cells *in vivo* over time. To mimic more relevant clinical conditions, 4Pm28ζN T cells were co-cultured with PL and PLP tumour cells to induce antigen-dependent activation. After 24 hours, 4Pm28ζN T cells were subjected to uptake assays. Although there was a modest increase in the percentage of activated 4Pm28ζN T cells co-cultured with PLP compared to cells co-cultured with PL target cells (Figure 3.12 a), CD69 surface expression levels were significantly enhanced, as determined by the MFI (Figure 3.12 b). The number of CAR$^+$ cells decreased after exposure to antigen, likely due to the internalisation of the CAR following antigen engagement (Figure 3.12 a)[165, 166]. By contrast, the number of hNIS$^+$ cells and the hNIS-mediated uptake was comparable after co-culture with PL and PLP target cells (Figure 3.12 c). This data confirms the feasibility of tracking CAR T cells *in vivo* independent of their activation status.
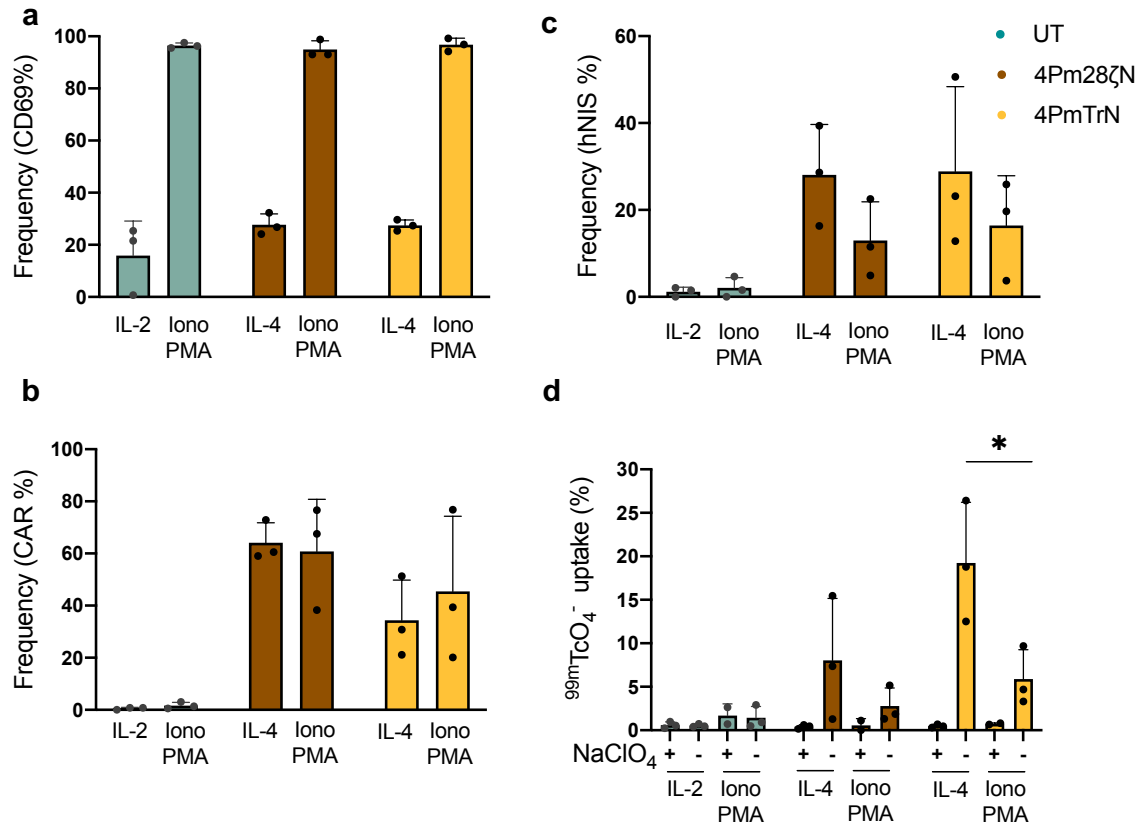
Figure 3.11: CAR T cell activation through stimulation with Ionomycin and PMA. Frequency of CD69 (a), CAR (b) and hNIS (c) measured by flow cytometry on rested cells supplemented with IL-4 or activated cells. d) *In vitro* uptake levels of CAR T cells incubated with $^{99m}TcO_4^-$ in the presence or absence of the inhibitor. n=3 donors/group. Graphs represent mean ± SD. Statistical analysis performed by Student's t-test. $^*p \leqslant 0.05$.

3.4 Quantification of CAR and hNIS surface expression

Following the finding of a commercial anti-hNIS antibody (human SLC5A5 AlexaFluor® 647), the relationship between CAR, hNIS surface expression, and the degree of tracer uptake by the cells was explored. The commercial anti-hNIS antibody was validated and transduced PBMCs were stained for both myc tag and hNIS (Figure 3.13 a & c). CAR and hNIS surface density was quantified using Quantum beads on day 11 post transduction (Figure 3.13 c & d). Transduction efficiency was variable between donors, ranging from 20%-80% of PBMCs expressing myc tag and hNIS (Figure 3.13 b). Higher CAR surface density was quantified on
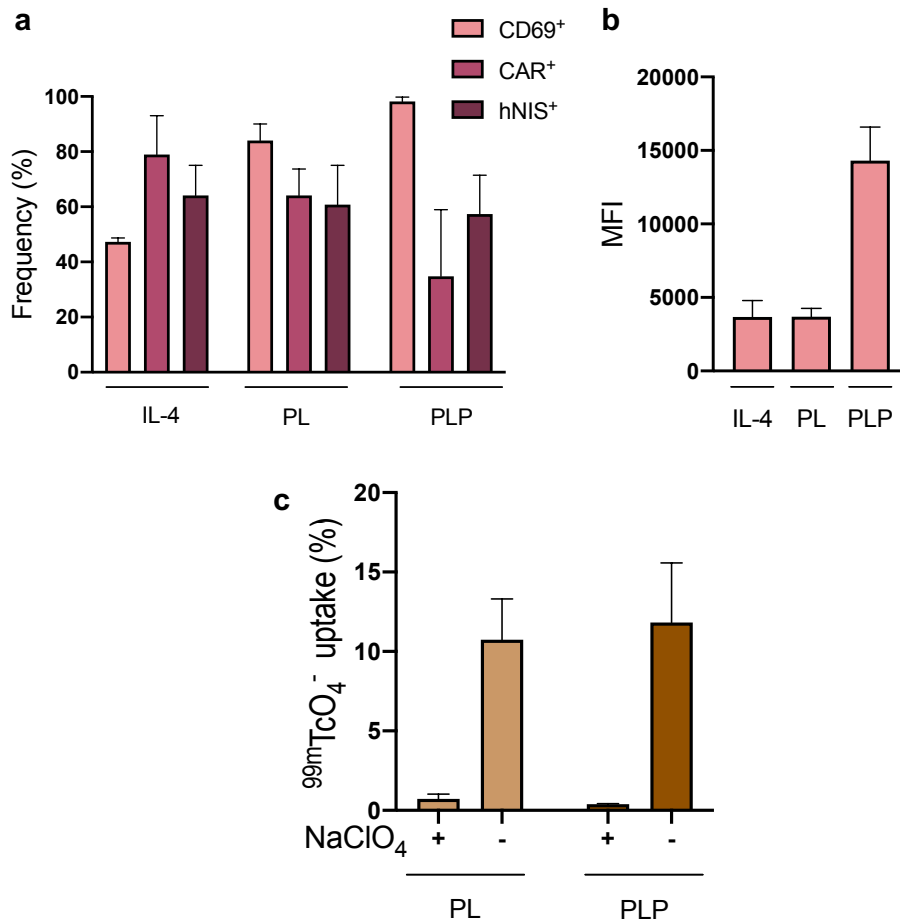
Figure 3.12: T cell activation after co-culture with PLP tumour cell line. a) Frequency of CD69, CAR and hNIS on 4Pm28ζN T cells co-culture with PL tumour cells (control) or PLP tumour cells for 24 hours. b) CD69 MFI levels. c) *In vitro* uptake levels of CAR T cells incubated with $^{99m}TcO_4^-$ in the presence or absence of the inhibitor. n=3 donors/group. Graphs represent mean ± SD.

4Pm28ζN T cells (44,822 ± 21,726 CARs/cell) compared to 4PmTrN T cells (15,757 ± 6,557 CARs/cell); variability between donors was also greater for 4Pm28ζN. In contrast, hNIS surface expression was slightly higher on 4PmTrN (15,671 ± 9,632 hNIS/cell) compared to 4Pm28ζN (11,644 ± 7,106 hNIS/cell) transduced PBMCs (Figure 3.13 c), which may be explained by the smaller construct size facilitating expression of the third downstream gene.
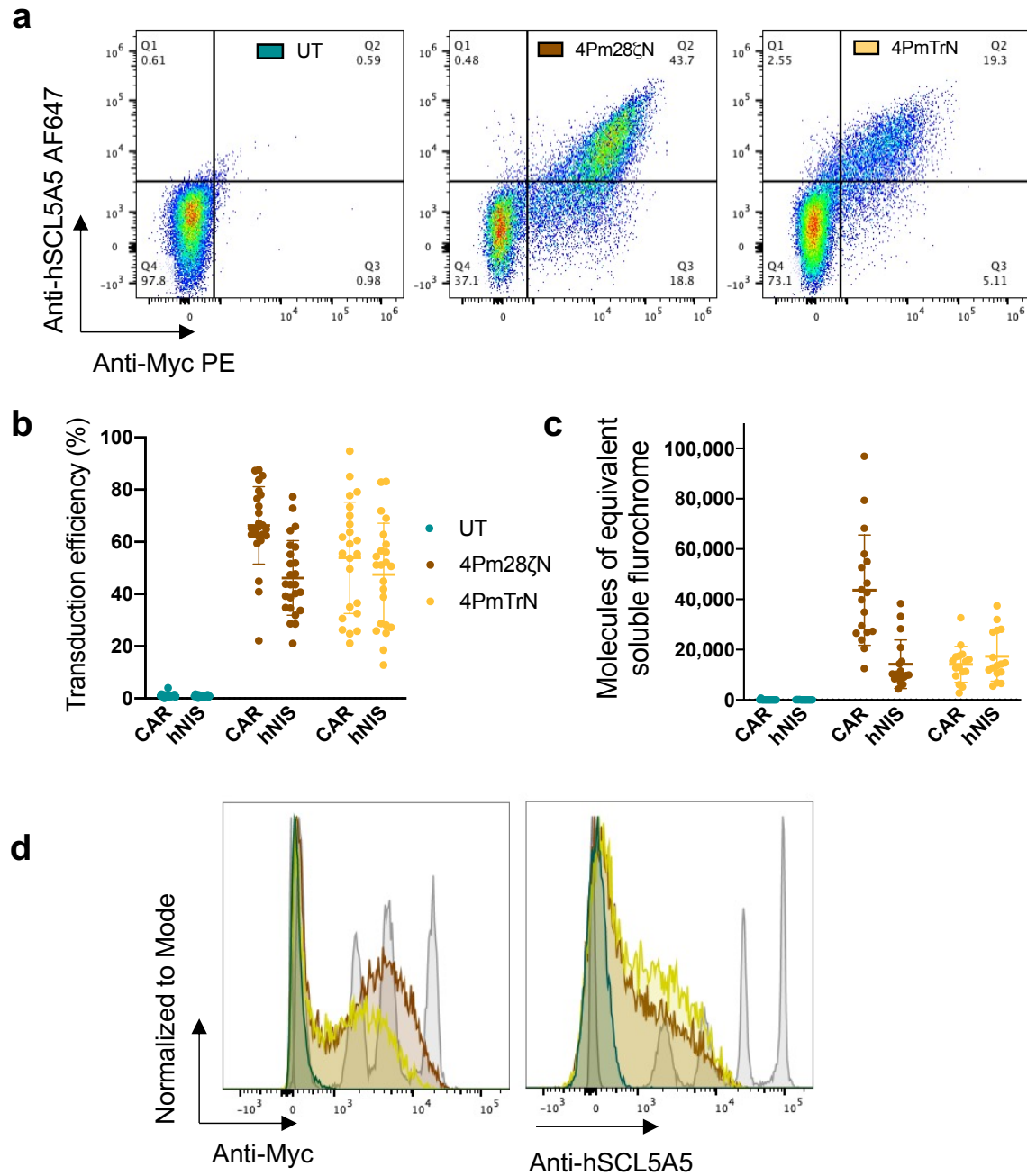
Figure 3.13: Protein surface expression. a) Representative flow cytometry dot plots, staining for myc and hNIS at day 11 post-transduction. b) Transduction efficiency at day 11. n=15 donors/group. c) Average fluorescence quantification of cell surface expression of CAR and hNIS. d) Typical histograms staining for myc tag and hNIS while using Quantum beads. n=15 donors/ group. Graphs represent mean ± SD.

Following quantitation by flow cytometry, CAR T cells were exposed to $^{99m}TcO_4^-$ and the uptake was recorded. Uptake differed across donors, 4PmTrN T cells showed slightly higher average uptake than 4Pm28ζN T cells, and uptake was revoked in the presence of the inhibitor (Figure 3.14 a). There was no positive correlation between the amount of tracer internalised and the quantified hNIS surface expression. Uptake also did not correlate with surface CAR expression levels (Figure 3.14 b). These finding suggest that the presence of other factors may influence the uptake levels, beyond the number of hNIS symporter copies expressed at the cell surface.
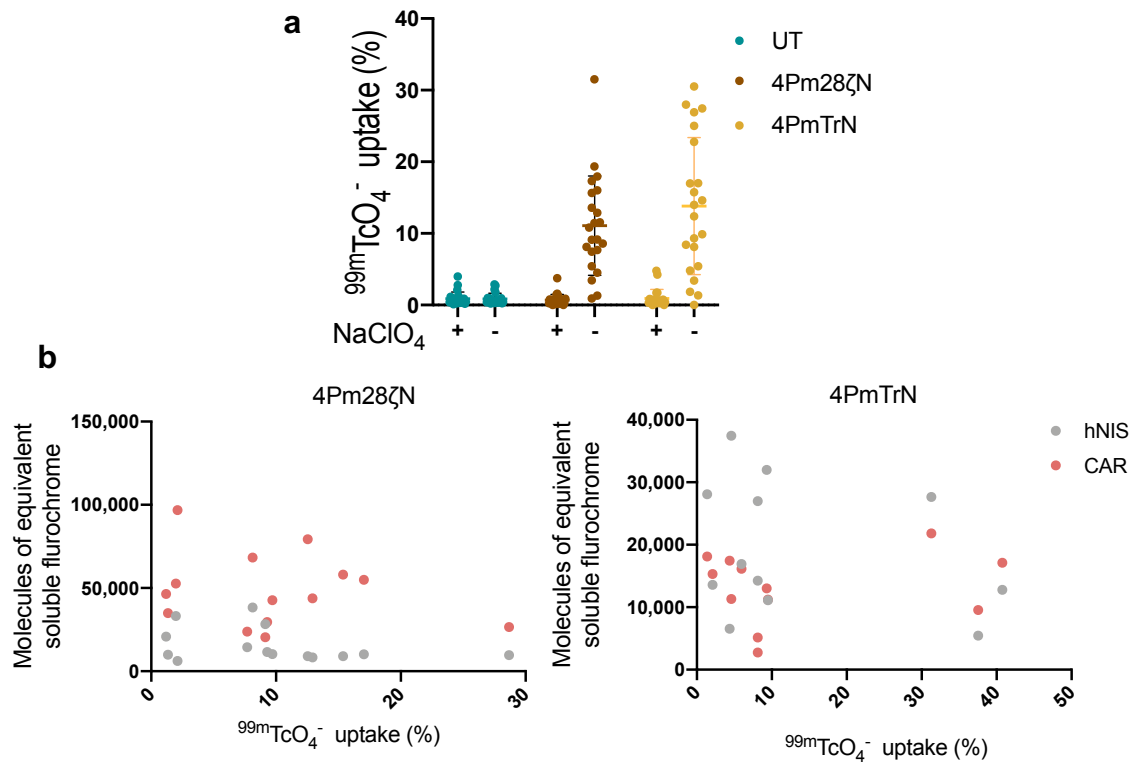
Figure 3.14: hNIS surface expression and uptake correlation. a) *In vitro* uptake levels of CAR T cells incubated with $^{99m}TcO_4^-$ in the presence or absence of the inhibitor. n=15 donors/group. b) Correlation between $^{99m}TcO_4^-$ uptake and quantified CAR and hNIS surface expression. Graphs represent mean ± SD.
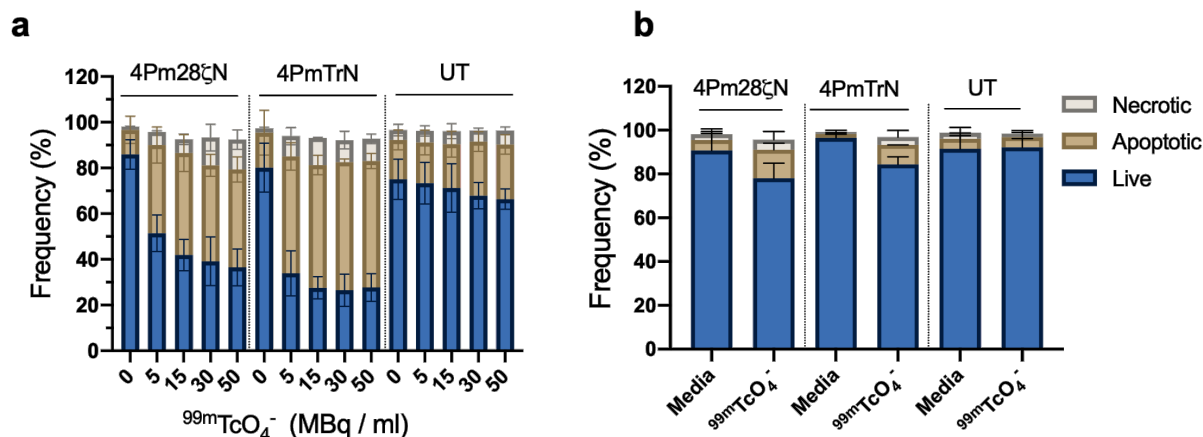
Figure 3.15: Cell viability of T cells exposed to increasing concentrations of $^{99m}TcO_4^-$. Percentage of live, necrotic, or apoptotic cells 24 hours (a) or 4 days (b) after exposure to 5 MBq/ml of $^{99m}TcO_4^-$. n=4 donors/ group. Graphs represent mean ± SD.

3.5 Impact of $^{99m}TcO_4^-$ uptake on CAR T cells

As the use of $^{99m}TcO_4^-$ to visualize the traceable CAR T cells *in vivo* could lead to radiation-mediated DNA damage, affecting the CAR T cell functionality, CAR T cells were exposed to increasing $^{99m}TcO_4^-$ concentrations and cell viability was measured 24 hours later. PBMC viability was determined by staining the cells with Annexin V and Zombie near-infrared L/D dye. Cell viability of hNIS-expressing CAR T cells decreased as the cells were exposed to higher $^{99m}TcO_4^-$ concentrations. To a lesser extent, viability was also reduced in a dose-dependent manner for untransduced cells (Figure 3.15 a). If the cells exposed to the tracer were rested in media, the radiation-induced apoptosis was no longer detectable and the frequency of viable cells was restored within four days, reaching comparable viability to cells not exposed to the tracer (Figure 3.15 b).

To determine the level of $^{99m}TcO_4^-$ exposure the CAR T cells may encounter, the radiotracer kinetics were studied *in vivo*. NSG mice were injected with 10 MBq $^{99m}TcO_4^-$ and blood samples were collected at the established time points by cardiac puncture. Blood samples and injection standards were subjected to gamma counting to assess radioactivity

113
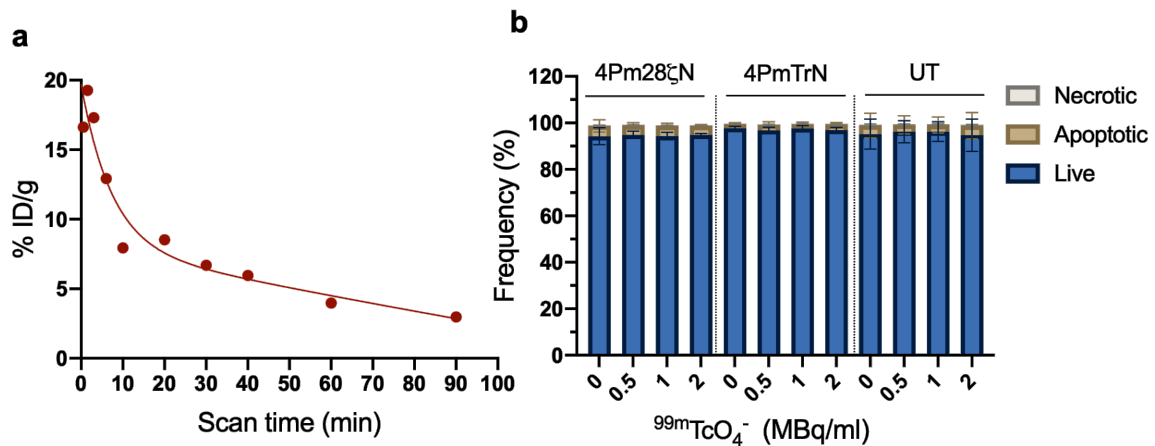
Figure 3.16: *In vivo* **tracer biodistribution.** a) $^{99m}TcO_4^-$ kinetics in blood over a 90-minute period. n=1 mice/time point. b) Viability of CAR T cells 24h after exposure to tracer determined by staining for Annexin V and Zombie near-infrared L/D dye. n=3 donors/group. Graphs represent mean ± SD.

levels. There was a rapid increase of tracer circulating in blood following the intravenous injection of $^{99m}TcO_4^-$. Peak concentration was reached at 1 min post injection followed by an exponential decay phase reaching steady state at 60 minutes. Radiotracer concentration in blood ranged from about 1.2 MBq/ml at five minutes post $^{99m}TcO_4^-$ injection to 0.7 MBq/ml at steady state (Figure 3.16 a). Based on these *in vivo* tracer concentrations, CAR T cells were exposed to lower $^{99m}TcO_4^-$ concentrations ranging from 0 to 2 MBq/ml and apoptosis was quantified as above. At these concentrations, cell viability was not affected (Figure 3.16 b).

To allow for repetitive imaging, CAR T cells must concentrate the radiotracer after each $^{99m}TcO_4^-$ injection at different time points without affecting their proliferation. To assess changes in proliferation, CAR T cells cultured in media were exposed to $^{99m}TcO_4^-$ twice in a week. Irrespective of gene transfer, there were no significant differences in CAR T cell proliferation upon exposure to the radiotracer (Figure 3.17 a). To confirm that the CAR T cells can be visualised repeatedly, 4Pm28ζN T cells were re-exposed to $^{99m}TcO_4^-$ 48 hours after the first uptake assay. Subsequent exposure to $^{99m}TcO_4^-$ did not affect the CAR T

cells' ability to concentrate the tracer again and the uptake was abolished by the inhibitor (Figure 3.17 b).
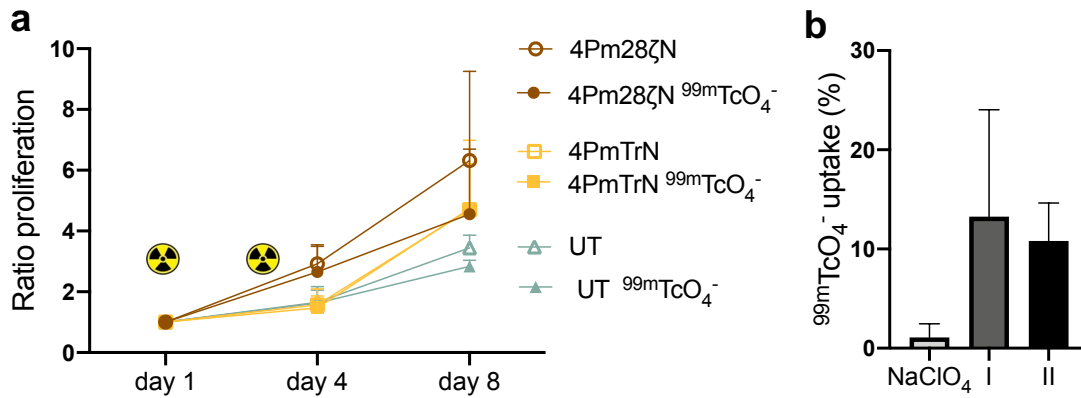
Figure 3.17: Repetitive exposure to $^{99m}TcO_4^-$. a) Proliferation of CAR T cells in the presence or absence of $^{99m}TcO_4^-$ (2 MBq/ml) measured over 8 days. b) *In vitro* uptake levels after first (I) and second exposure (II) to $^{99m}TcO_4^-$ or in the presence of the inhibitor. n=3 donors/group. Graphs represent mean ± SD.

To investigate whether CAR T cell activity was impaired in the presence of the tracer, unlabelled (media) or radiolabelled ($^{99m}TcO_4^-$) CAR T cells were co-cultured with PLP and PL monolayers. Tumour viability was measured by MTT after 48 h. There were no significant differences between the cytotoxicity elicited by the unlabelled and their counterpart traceable CARs at all E:T ratios tested. 4Pm28ζN T cells elicited cytotoxicity against PLP cells in a dose-dependent manner, with no cytotoxicity against PL cell lines. Cytotoxicity was not observed by the control untransduced and truncated cells (Figure 3.18).

Cytokine production was measured from the above co-cultures at an E:T of 1:1. Radiolabelled 4Pm28ζN T cells produced comparable levels of IL-2 and IFNγ cytokines to unlabelled 4Pm28ζN T cells (Figure 3.19). Similarly, no significant differences were observed in the immunophenotype of the radiolabelled CAR T cells. T cell phenotype comprised a mixture of memory and effector phenotypes with the most frequent population being effector memory cells, defined as CCR7$^-$ CD45RA$^-$. Activation status was also unaltered in the presence of the tracer (Figure 3.20).
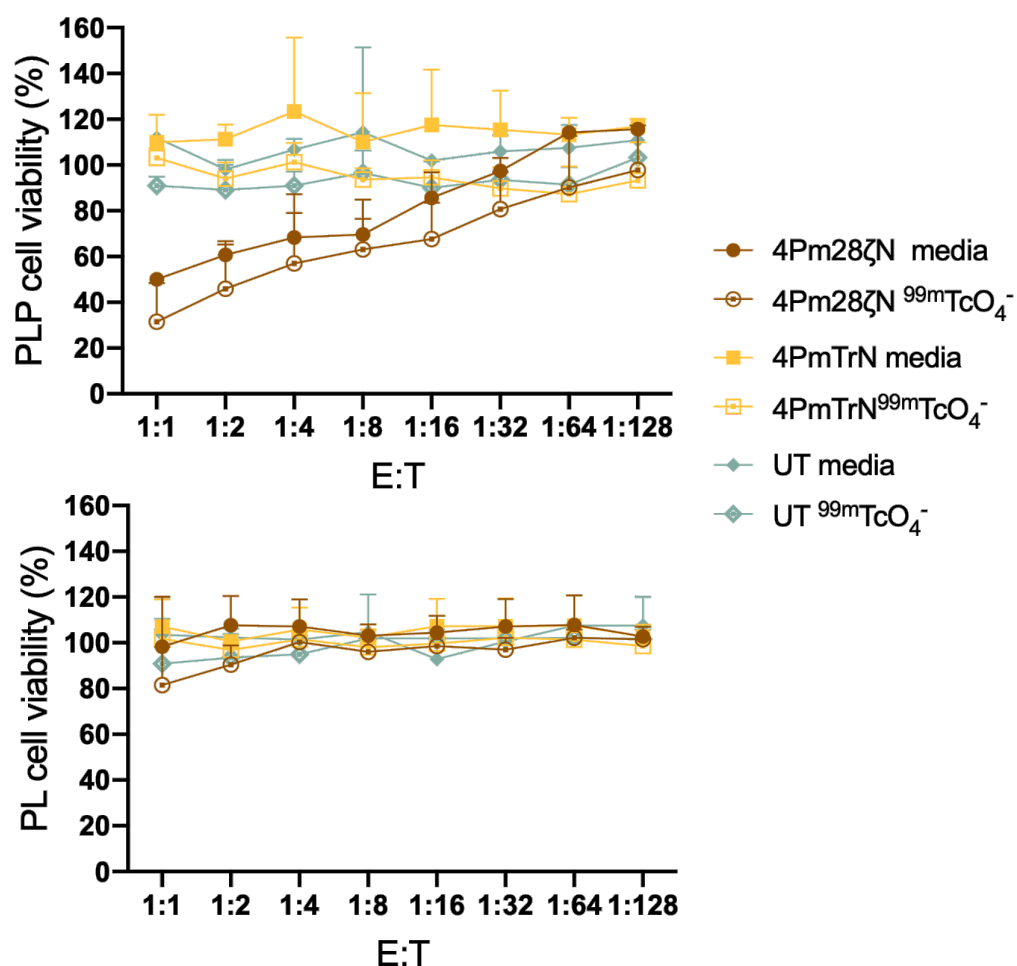
Figure 3.18: Effect of $^{99m}TcO_4^-$ on CAR T cell cytotoxicity. Percentage tumour cell viability 48 h after co-culture with unlabelled (media) or radiolabelled CAR T cells (10 MBq $^{99m}TcO_4^-$/million T cells) determined by MTT assays. UT : untransduced T cells. n=3/group. Graphs represent mean ± SD.
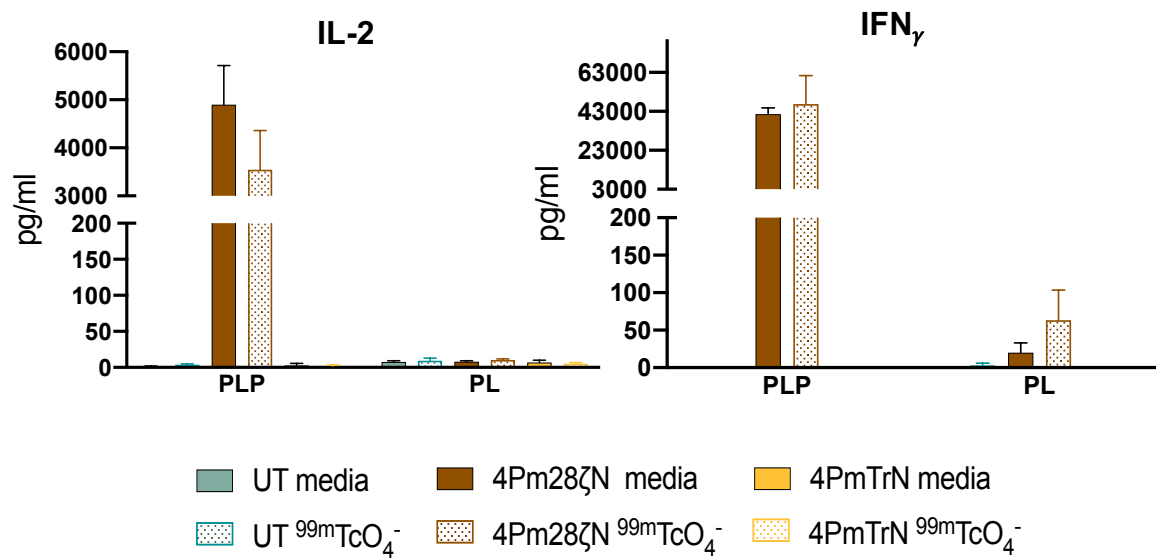
Figure 3.19: Effect of $^{99m}TcO_4^-$ on CAR T cell cytokine production. ELISAs were carried out on supernatants from experiments on Figure 3.18 to determine secretion levels of IL-2 and IFNγ. n=3/group. Graphs represent mean ± SD.
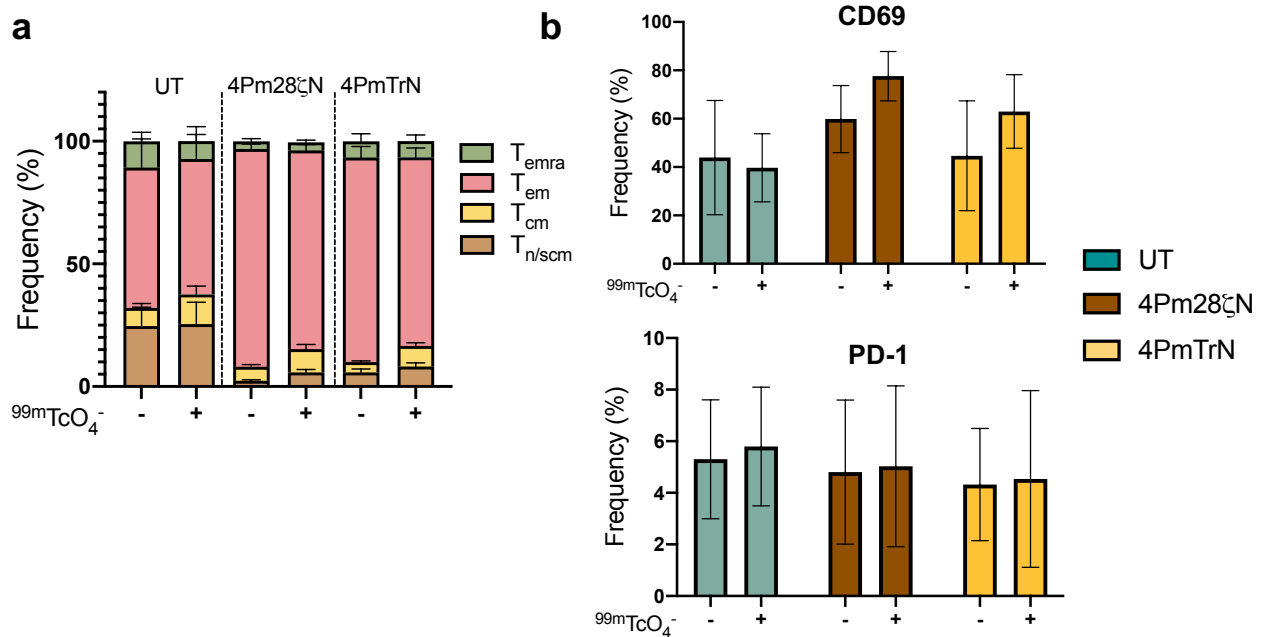
Figure 3.20: Immunophenotype of CAR T cells. a) Frequency of T cells after staining for CD45RA and CCR7. $T_{n/scm}$: naïve ; T_{cm}: central memory T cells; T_{em}: effector memory T cells; T_{emra}: effector memory T cells expressing CD45RA. b) Percentage of cells expressing surface CD69 (top) and PD-1 (bottom) before and after exposure to tracer. n=4 donors/ group. Graphs represent mean ± SD.

Lastly, tracer-induced DNA damage was assessed by measuring changes in phosphorylation of γH2Ax through flow cytometry. 4Pm28ζN and 4PmTrN T cells were exposed to increasing amounts of ^{99m}TcO$_4^-$. Exposure to over 5 MBq of ^{99m}TcO$_4^-$ caused a significant increase in the percentage of PBMCs expressing phosphorylated γH2Ax in both 4Pm28ζN (Figure 3.21 a) and 4PmTrN (Figure 3.21 b) T cells. DNA damage was repaired within 24 hours except on those cells exposed to 25 MBq of ^{99m}TcO$_4^-$, which required 72 hours.
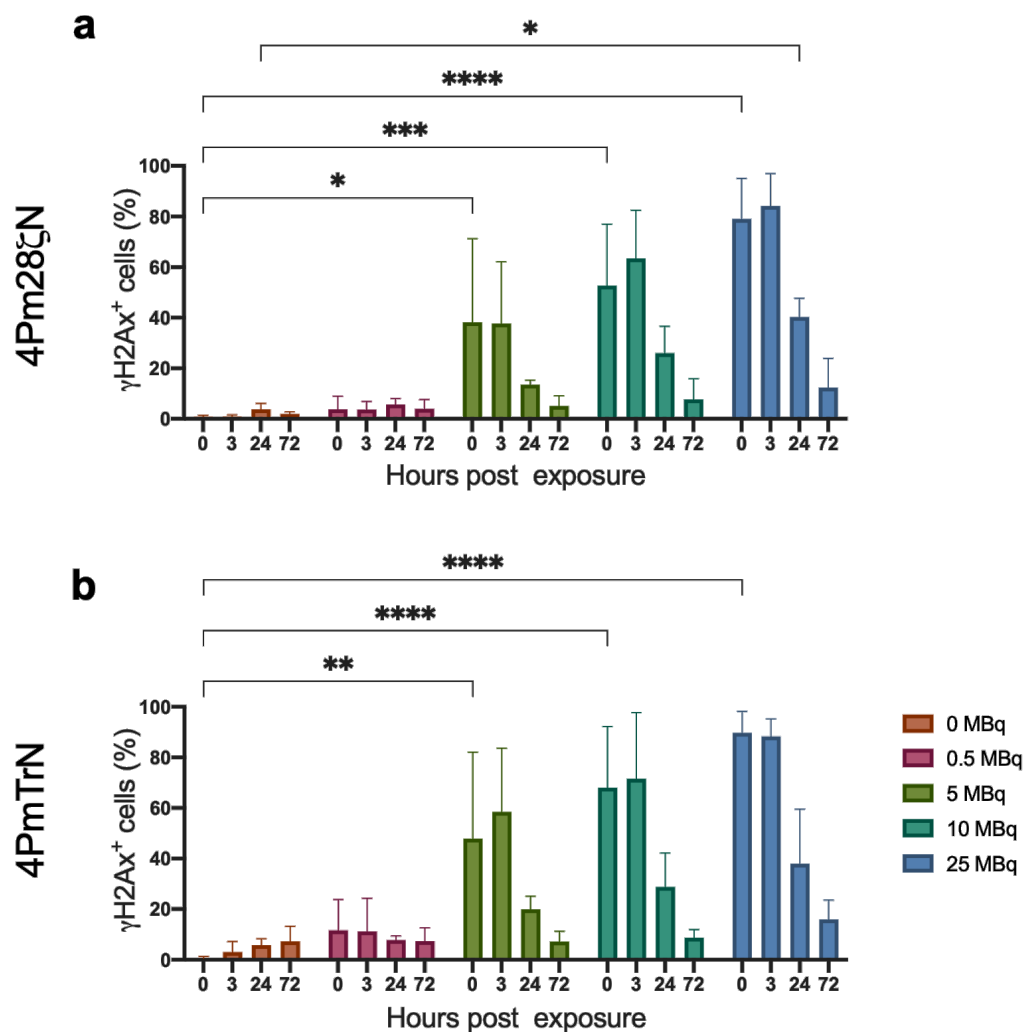
Figure 3.21: Radiation-induced DNA damage. Percentage of 4Pm28ζN T cells (a) or 4PmTrN T cells (b) expressing phosphorylated γH2Ax after incubation with different amounts of ^{99m}TcO$_4^-$ (MBq/ml). Representative flow cytometry plots shown in Figure S 8.1. n=3 donors/group. Graphs represent mean $\pm$ SD. Statistical analysis performed by two-way ANOVA. *p $\leqslant$ 0.05, **p $\leqslant$ 0.01, ***p $\leqslant$ 0.001, ****p $\leqslant$ 0.0001.

Quantification of SPEC/CT images from tumour bearing animals injected with untransduced cells, yielded a maximum concentration of 0.12 MBq of $^{99m}TcO_4^-$ per gram of tumour (Figure 5.14 & 5.22). Taking these data together, radiotracer-mediated apoptosis or DNA damage is not expected when tracking these CAR T cells in our *in vivo* model.

3.6 Summary

To image CAR T cells homing to the tumour site non-invasively, the reporter gene hNIS was expressed at the T cell surface to allow for internalisation of $^{99m}TcO_4^-$, which can be visualised by SPECT imaging. By expressing the $4\alpha\beta$ domain, transduced cells were enriched over the expansion period, reaching high transduction efficiency. The addition of the myc tag within the CAR gene facilitated the detection and quantification of CAR surface expression by flow cytometry. Importantly, the addition of the reporter gene did not negatively impact CAR T transduction, proliferation, or cytotoxicity. The hNIS-mediated internalisation of $^{99m}TcO_4^-$ did not affect CAR T cell viability, functionality or phenotype when exposed to *in vivo* relevant concentrations. Thus, these data demonstrate the successful production and in-depth characterisation of traceable CAR T cells.

Chapter 4

Imaging traceable CAR T cells *in vivo*

Following the *in vitro* characterisation of the CAR T cells, I next tested the capabilities of the VECTor^{6}CT^{XUHR} SPECT/CT instrument. The aim was to employ SPECT dynamic imaging to develop a mathematical model for tracer kinetics. By combining this model with *ex vivo* flow cytometry data, I sought to achieve non-invasive quantitation of CAR T cells homing to the tumour.

The VECTor^{6}CT^{XUHR} SPECT/CT instrument can be used with a General Purpose Rat and Mouse (GP-RM) collimator or with the newly developed Extra-Extra Ultra-High Sensitivity Mouse (XXUHS-M) collimator. This collimator has higher sensitivity and allows for imaging extra ultra-low doses but has lower resolution than the former.

To assess which of these two collimators was best suited to quantify the CAR T cells *in vivo*, quantitation accuracy, detection sensitivity and tracer doses were compared.

4.1   Quantitation accuracy during dynamic imaging

Phantoms studies using both collimators were performed to determine the accurate quantitation range of each collimator during dynamic imaging. Images were acquired in 5-second frames using a single-bed position. Time frames were binned during reconstruction to compare
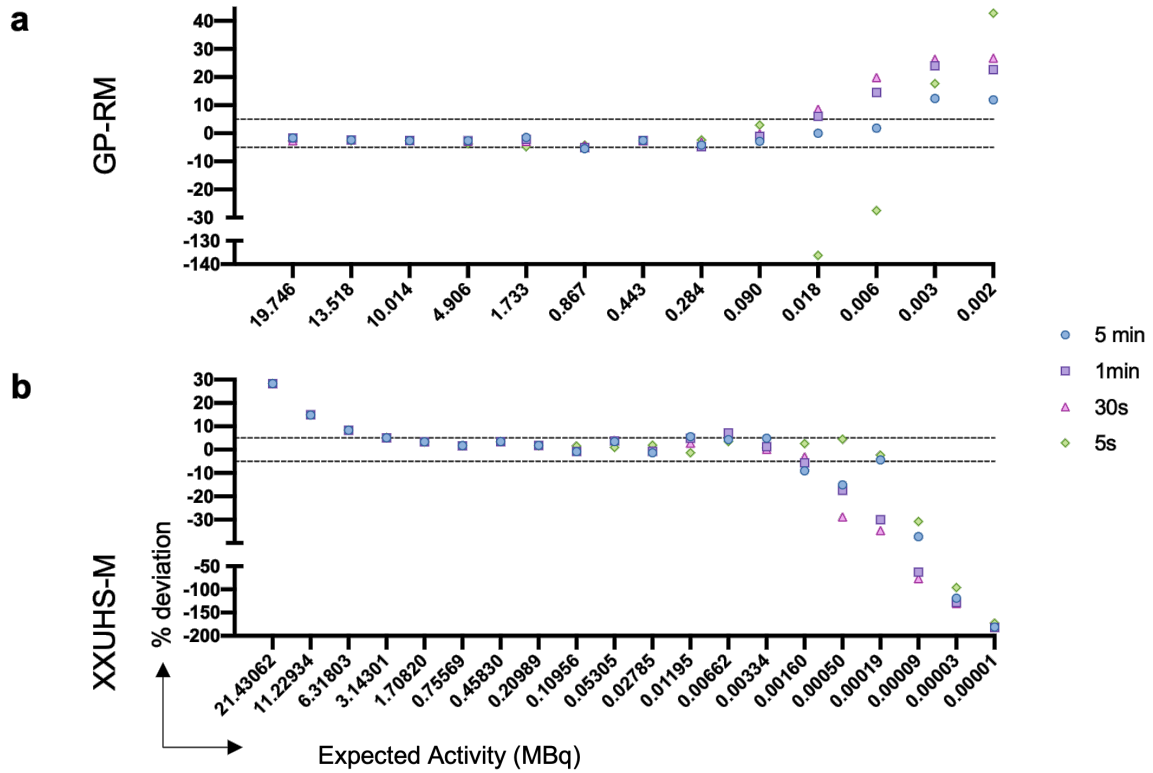
Figure 4.1: Optimal activity levels for the GP-RM and XXUHS-M collimators. Accuracy of tracer quantitation during dynamic imaging acquisition of phantoms using the a) GP-RM or b) XXUHS-M collimator. Deviation percentage defined as [(expected - measured)/expected]. Dotted line depicts the maximum deviation accepted.

quantitation accuracy between 5-second, 30-second, 1- and 5-minute frames. A 5% deviation threshold was accepted as optimal imaging range. Accurate quantitation was achieved at all time frames when imaging above 90 kBq of $^{99m}TcO_4^-$ per bed position using the GP-RM collimator. Binning the frames to five minutes, showed accurate quantitation down to 6 kBq of $^{99m}TcO_4^-$ (Figure 4.1 a). On the other hand, the higher sensitivity of the XXUHS-M collimator led to accurate quantification of as little as 3 kBq per bed position, but detectors were saturated when >3 MBq of $^{99m}TcO_4^-$ were present in the field of view (Figure 4.1 b).

To closely simulate preclinical conditions, and consider the body attenuation observed when imaging animals, these phantoms studies were replicated using a water jacket, and more time points were incorporated. The suitable range for the GP-RM collimator was determined
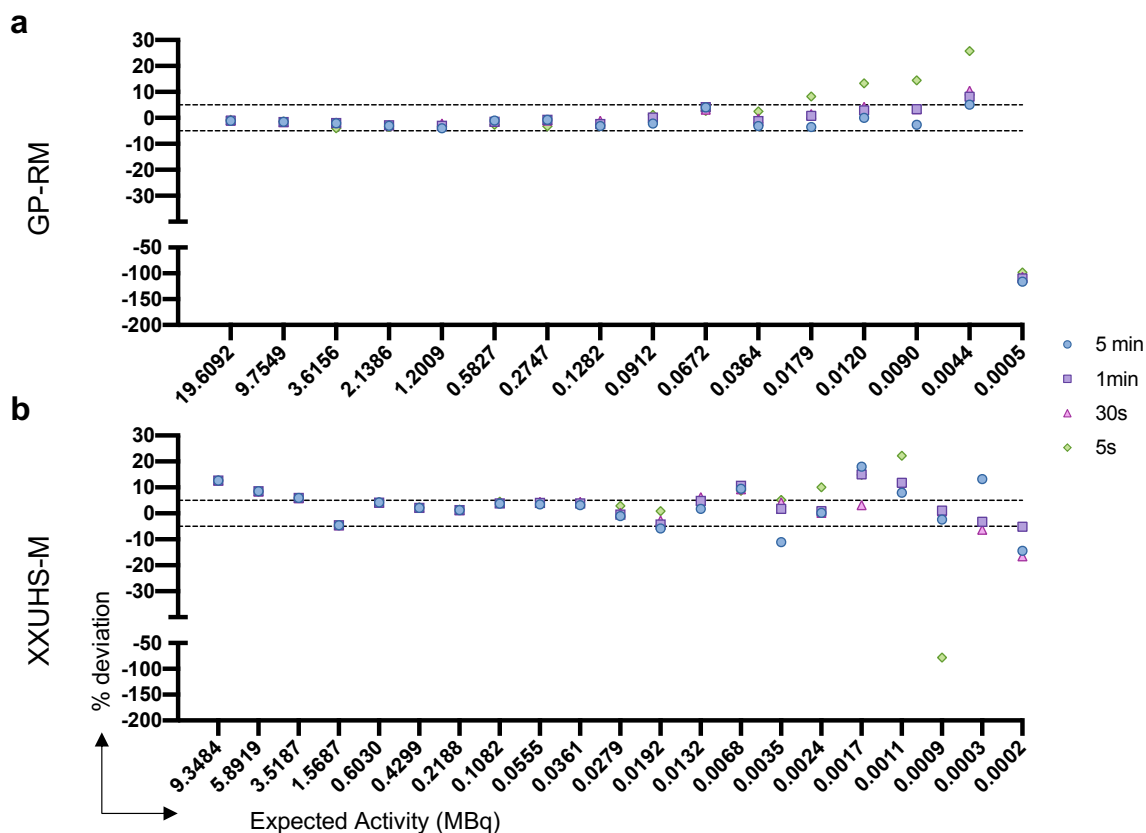
Figure 4.2: Optimal activity levels for the GP-RM and XXUHS-M collimators using water phantoms. Accuracy of tracer quantitation during dynamic imaging acquisition of phantoms in water jackets using the a) GP-RM or b) XXUHS-M collimator. Deviation percentage defined as [(expected - measured)/expected]. Dotted line depicts the maximum deviation accepted.

to be 20 MBq to 36 kBq of $^{99m}TcO_4^-$, even for frames as brief as 5 seconds. However, if longer time frames of 30 seconds were quantified, the optimal range was expanded to a minimum of 9 kBq of $^{99m}TcO_4^-$ (Figure 4.2 a). The XXUHS-M collimator had optimal activity levels between a maximum of 3MBq and a minimum of approximately 3 kBq of $^{99m}TcO_4^-$ (Figure 4.2 b).

122

4.2 CAR T cell detection sensitivity

To determine the detectability of traceable CAR T cells on the VECTor^{6}CT^{XUHR} SPECT/CT instrument, different quantities of 4Pm28ζN T cells were injected subcutaneously (s.c.) followed by intravenous (i.v.) injection of ^{99m}TcO$_4^-$. In the first instance, the limit of detection in full body scans using the GP-RM collimator was assessed. 20×10^3 and 3×10^3 4Pm28ζN T cells were injected s.c. in 50% matrigel (yellow arrows) and matrigel alone was injected in the opposite shoulder as a control (white arrow). The SPECT images showed accumulation of tracer at the CAR T cell injection sites, but tracer uptake was also observed in the control shoulder that received matrigel alone (Figure 4.3 b).
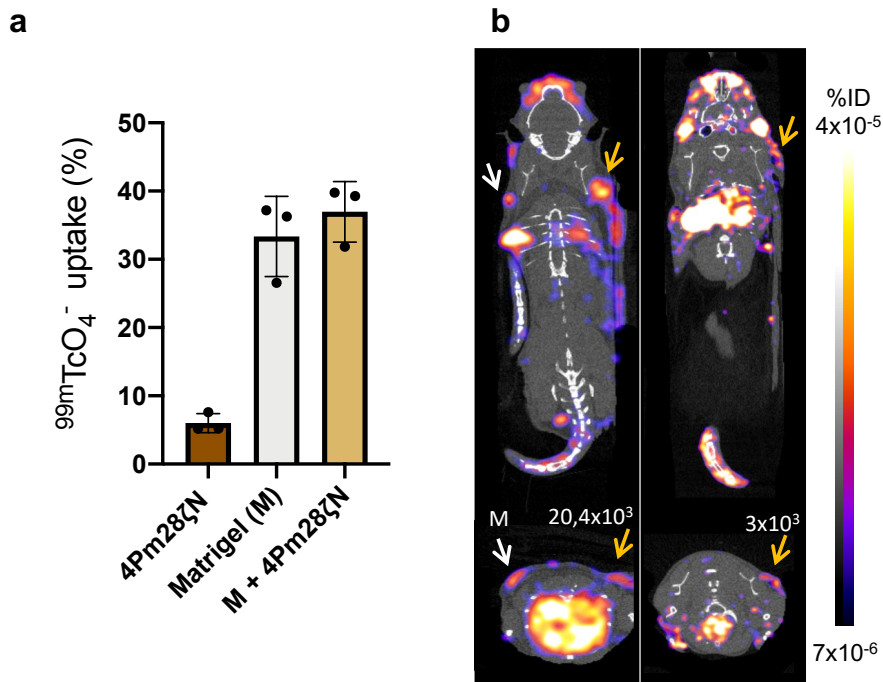
Figure 4.3: Sensitivity of 4Pm28ζN T cells injected in matrigel. a) *In vitro* ^{99m}TcO$_4^-$ uptake assay. 0.3 MBq/ml of ^{99m}TcO$_4^-$ was added to each sample and tracer uptake was quantified with a gamma counter. n=3/group. b) *In vivo* coronal and transversal views. 4Pm28ζN T cells in matrigel were injected subcutaneously in the shoulder of BALB/c mice (yellow arrows). As a control, matrigel alone was also injected (white arrow), followed by 20 MBq of ^{99m}TcO$_4^-$. M=matrigel. Graphs represent mean ± SD.

The non-specific accumulation of tracer within the matrigel matrix was confirmed by *in vitro* assays (Figure 4.3 a). 4Pm28ζN T cells in PBS, 4Pm28ζN T cells in 50% matrigel and matrigel alone samples were subjected to $^{99m}TcO_4^-$ uptake assays. The matrigel matrix retained a significant amount of tracer, posing a challenge to accurately measure the uptake by CAR T cells embedded in matrigel (Figure 4.3 a). Based on these results, the use of matrigel to establish a xenograft model was discarded.

To prevent non-specific tracer retention by the matrigel matrix, CAR T cells were injected in PBS instead. The use of PBS could lead to dispersion of the CAR T cells after injection since there is no structure holding them together. To test whether CAR T cells injected in PBS would be retained at the injection site, four different amounts of 4Pm28ζN T cells were injected in the shoulders of two animals, followed by intravenous injection of 20 MBq of $^{99m}TcO_4^-$ (Figure 4.4 a). Full body images were acquired using the GP-RM collimator and cell uptake was quantified by drawing an ROI over the injection sites and on the right thigh as a control. As shown in Figure 4.4 b), the detection threshold for CAR T cells was set at $3.5x10^3$ cells (Figure 4.4 b). Quantified tracer uptake was comparable between $7.6x10^3$ and $3.5x10^3$ 4Pm28ζN T cells, resulting in an accumulation of approximately 1.2 MBq by the CAR T cells. No tracer uptake was detected in the thigh region. (Figure 4.4 c).

In order to investigate CAR T cell kinetics following infusion and establish a mathematical model for non-invasive quantitation of these cells, dynamic SPECT imaging is required to detect rapid changes in tracer concentration over time. To assess the limit of detection for each collimator during dynamic acquisition, a single-bed position was selected, enabling the imaging of rapid 10-second frames. Prior to *in vivo* administration, CAR T cells were subjected to an uptake assay to confirm hNIS mediated internalisation of $^{99m}TcO_4^-$. About 6% of the added tracer was concentrated inside the cells. In the presence of the inhibitor, uptake was blocked (Figure 4.5).
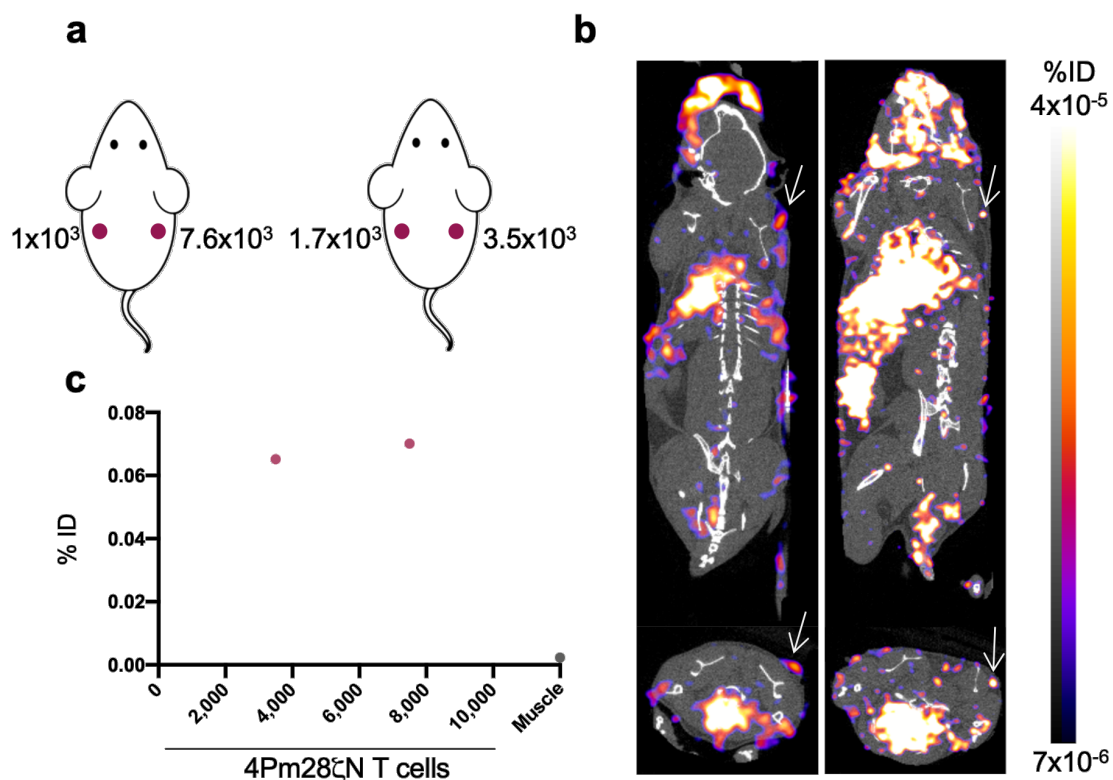
Figure 4.4: Detection sensitivity of 4Pm28ζN T cells in whole body scans. a) Schematic of CAR T cell concentration injected per animal. b) *In vivo* coronal and transversal SPECT/CT views. 4Pm28ζN T cells were injected subcutaneously in the shoulder of BALB/c mice (white arrows). c) Quantified $^{99m}TcO_4^-$ uptake from SPECT images.
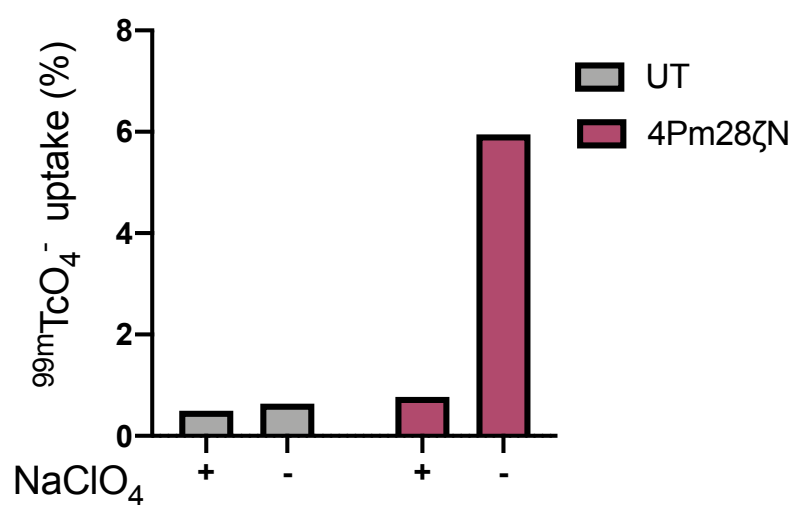
Figure 4.5: *In vitro* $^{99m}TcO_4^-$ uptake by injected 4Pm28ζNT cells. Cells were incubated with 0.3 MBq/ml $^{99m}TcO_4^-$ in the presence or absence of the inhibitor. UT = untransduced T cells.

The large field of view (FOV) of the GP-RM collimator covered the entire chest area using a single-bed position. CAR T cells were injected s.c. in each shoulder as depicted in Figure 4.6 a. The SPECT images revealed tracer internalization at all CAR T cell numbers injected, the lowest amount being $6x10^3$ 4Pm28ζN T cells (Figure 4.6 c). The experiment was repeated to acquire the SPECT images with the XXUHS-M collimator. This collimator had a smaller FOV, allowing CAR T cells injection in only one of the shoulders. There was clear accumulation of tracer at the injection sites, detecting down to $3.5x10^3$ 4Pm28ζN T cells (Figure 4.7 b & c).
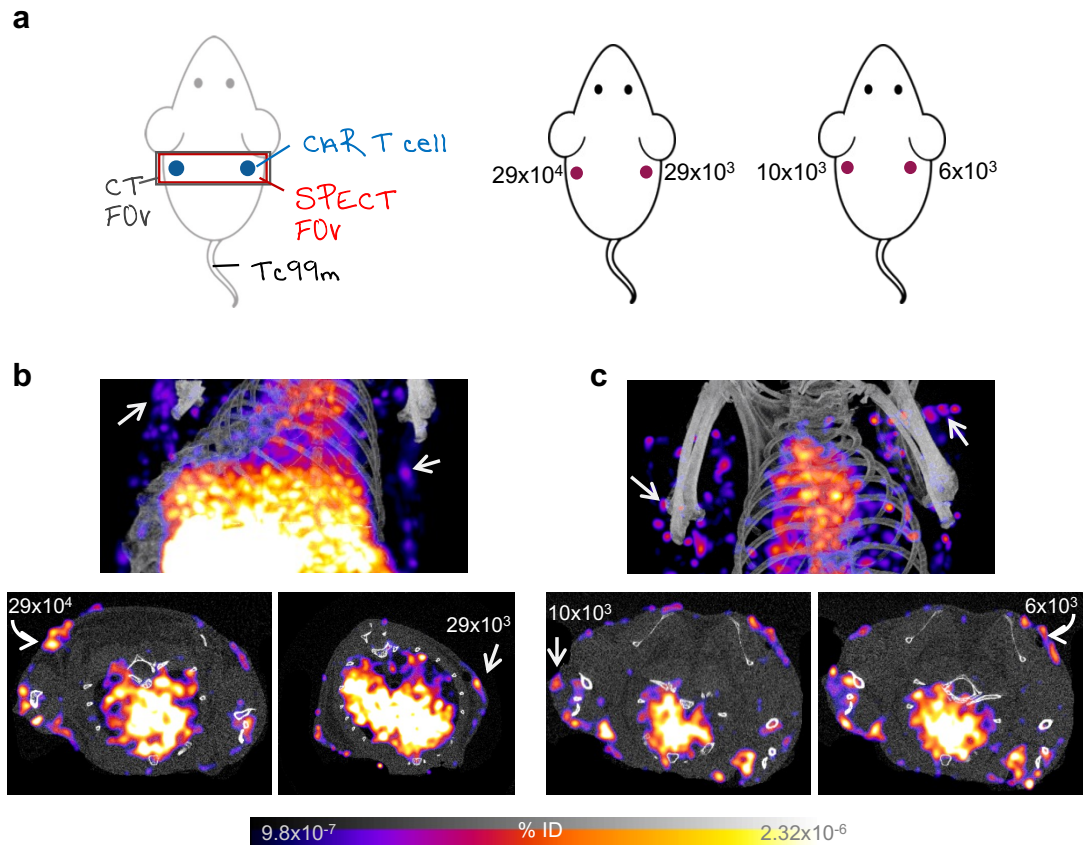
Figure 4.6: Detection sensitivity of 4Pm28ζN T cells during dynamic imaging using a single bed position and GP-RM collimator a) Schematic of the imaging strategy and amounts of CAR T cells injected. b) & c) Images binned and reconstructed as a single 70-minute frame. Top: SPECT/CT MIP view; bottom: transversal views. Arrows point to injected 4Pm28ζN T cells.
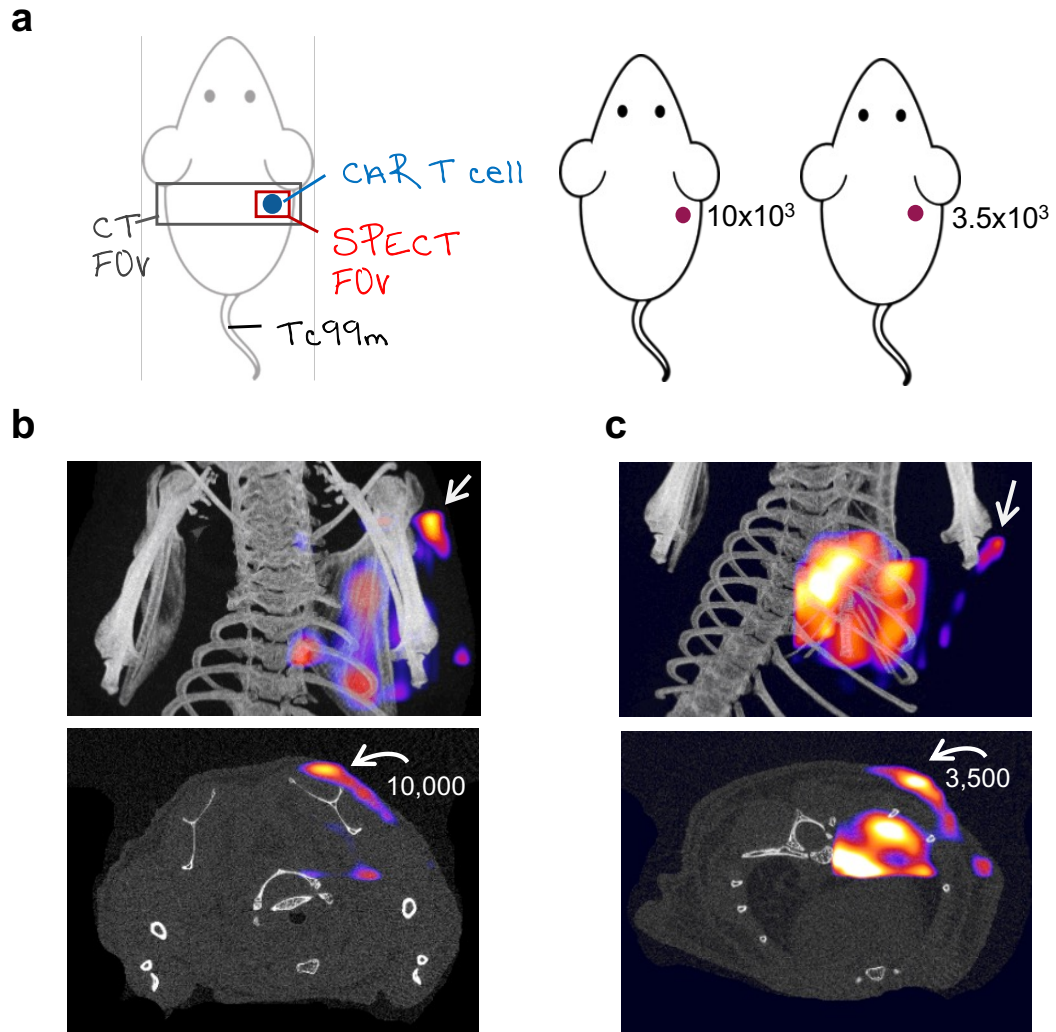
Figure 4.7: Detection sensitivity of 4Pm28ζN T cells during dynamic imaging using a single bed position and XXUHS-M collimator a) Schematic of the imaging strategy and amounts of CAR T cells injected. b) and c) Images binned and reconstructed as a single 70-minute frame. Top: SPECT/CT MIP views; bottom: transversal views. Arrows point to injected 4Pm28ζN T cells.

Following the dynamic acquisition, animals were sacrificed, and organs were collected for *ex vivo* analysis. Radioactive uptake in the samples was measured using a gamma counter. *Ex vivo* biodistribution showed radiotracer accumulation in endogenous hNIS expressing organs, i.e., stomach and salivary glands, as expected. Tracer uptake was similar among all animals (Figure 4.8).

127
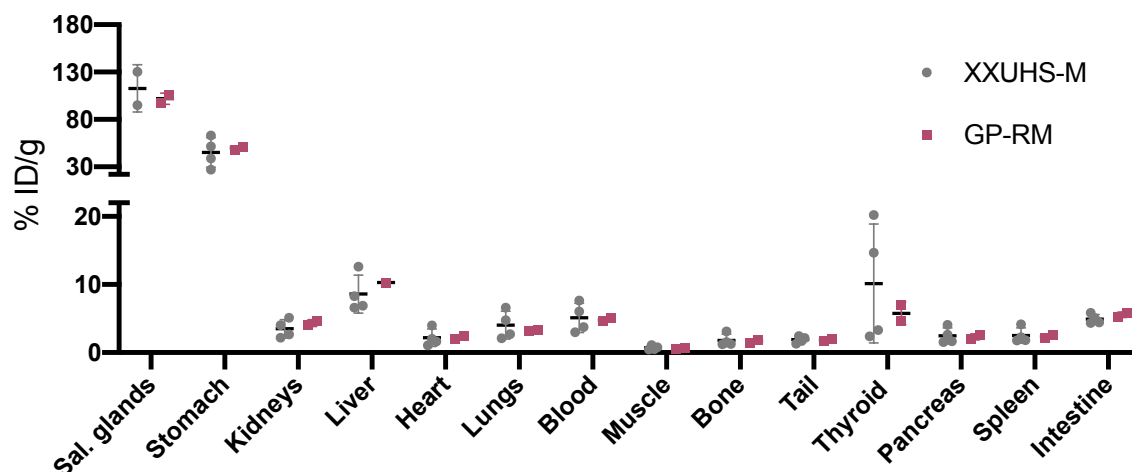
Figure 4.8: *Ex vivo* analysis of radioactivity in organs measured using a gamma counter. Radioactivity in organs harvested after SPECT imaging using the XXUHS-M (n=4) or GP-RM (n=2) collimators. Graphs represent mean ± SD or mean, respectively.

To further assess the detection sensitivity of the CAR T cells using the XXUHS-M collimator, untransduced T cells were mixed with increasing numbers of 4Pm28ζN T or 4PmTrN T cells and subjected to $^{99m}TcO_4^-$ uptake assays. One hour after exposure, SPECT/CT images were acquired. Concentration of $^{99m}TcO_4^-$ in the cell pellets was quantified from the SPECT images and the limit of detection was calculated as three times the standard deviation from the background, i.e. approximately $5x10^3$ 4Pm28ζN T cells (Figure 4.9 a).

Despite $^{99m}TcO_4^-$ uptake being donor dependent as seen in previous chapter (Figure 3.14), there was strong positive correlation between the number of traceable 4Pm28ζN T cells and the quantified SPECT signal for samples with over $20x10^4$ 4Pm28ζN T cells (Figure 4.9 b, top). However, when the number of hNIS positive cells per cell pellet was bellow $6x10^4$ cells, the correlation weakened (Figure 4.9 b, bottom). A positive and strong correlation was also observed when measuring $^{99m}TcO_4^-$ activity in the cell pellet *in vivo* (by drawing an ROI on the SPECT images) and *ex vivo* (samples measured in a gamma counter) (Figure 4.9 c), demonstrating accurate quantitation of tracer activity through a non-invasive method.
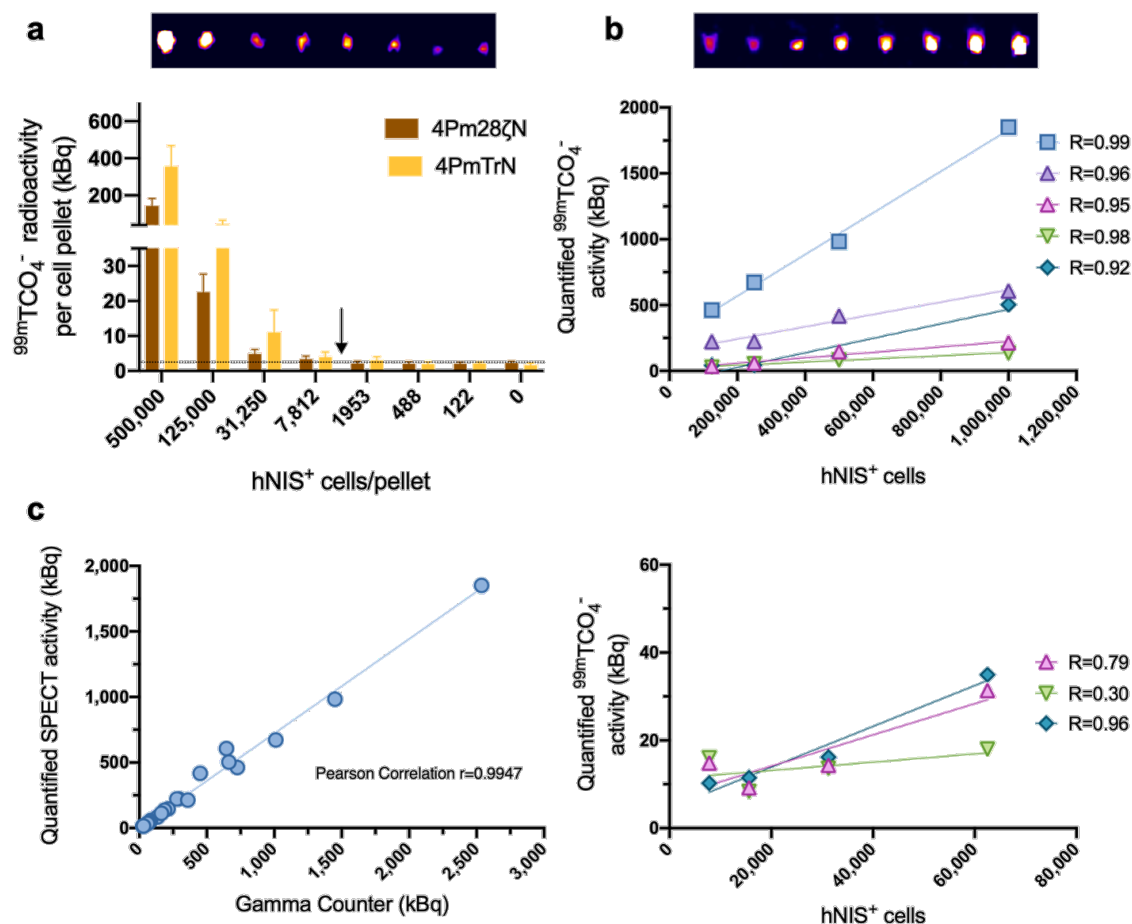
Figure 4.9: Detection sensitivity of CAR T cells using XXUHS-M collimator. a) SPECT images acquired 60 minutes after radiolabelling 4Pm28ζN and 4PmTrN T cells with 5 MBq of ^{99m}TcO$_4^-$. Typical images shown from one 4PmTrN T cell batch. Graph depicts quantified activity per pellet after imaging. n=3 donors. Error bars represent S.E.M. b) Typical image of SPECT phantom imaging from one 4Pm28ζN T cell batch. Linear regression of quantified tracer activity and number of positive hNIS cells. Each shape represents a donor. n=3-5 donors. c) Correlation of quantified activity by drawing ROIs on the SPECT images and *ex vivo* gamma counting.

4.3 Tracer dose for XXUHS-M collimator

The data above demonstrated the higher sensitivity and accuracy of the XXUHS-M collimator for the quantitation of low tracer activity, compared to the GP-RM collimator. It was hypothesised that lower tracer doses could be administered when using the XXUHS-M

collimator to avoid saturation of the detectors (above 3 MBq/ bed position) and unnecessary exposure. To build a compartmental model to quantify CAR T cell, tracer concentration in the bloodstream and target site needs to be measured simultaneously. Thus, a single-bed position would not suffice due to the small FOV covered by this collimator (Figure 4.7). To test both tracer dose and settings for the dynamic imaging, 300×10^3 and 30×10^3 4Pm28ζN T cells were injected s.c. in each shoulder followed by either 10 MBq or 5 MBq of $^{99m}TcO_4^-$ injected i.v. (Figure 4.10 a). Thirteen bed positions were used to image the CAR T cells and the heart within the FOV, increasing the frame length to one minute. As expected, higher signal was observed in the SPECT images when 10 MBq of $^{99m}TcO_4^-$ were administered compared to animals that received 5 MBq of tracer (Figure 4.10 b & c). Quantified uptake by the CAR T cells was within the accurate range of the SPECT camera for animals that received 10 MBq of tracer, however, when the injected dose was reduced to 5 MBq of tracer, the activity internalised by the 30×10^3 CAR T cells fell outside the accurate range (ranging from 3 kBq to 3 MBq of $^{99m}TcO_4^-$). Superior sensitivity of the XXUHS-M collimator was further corroborated by comparing SPECT images acquired after injection of the lower dose of tracer. SPECT image quantitation showed 2-fold increase in the quantified activity if images were acquired with the XXUHS-M collimator. Importantly, quantitation using the GP-RM collimator fell out of its accurate range even if imaging 300×10^3 4Pm28ζN T cells (Figure 4.11).

These data demonstrated the superior sensitivity of the XXUHS-M collimator, which enabled the visualisation and precise quantification of extremely low doses of tracer. This characteristic made it particularly well-suited for my longitudinal approach to quantify CAR T cells non-invasive. A dose of 10 MBq of tracer was selected for future *in vivo* experiments to prevent detector saturation and ensure that the quantitation of low activities remained within the accurate range.
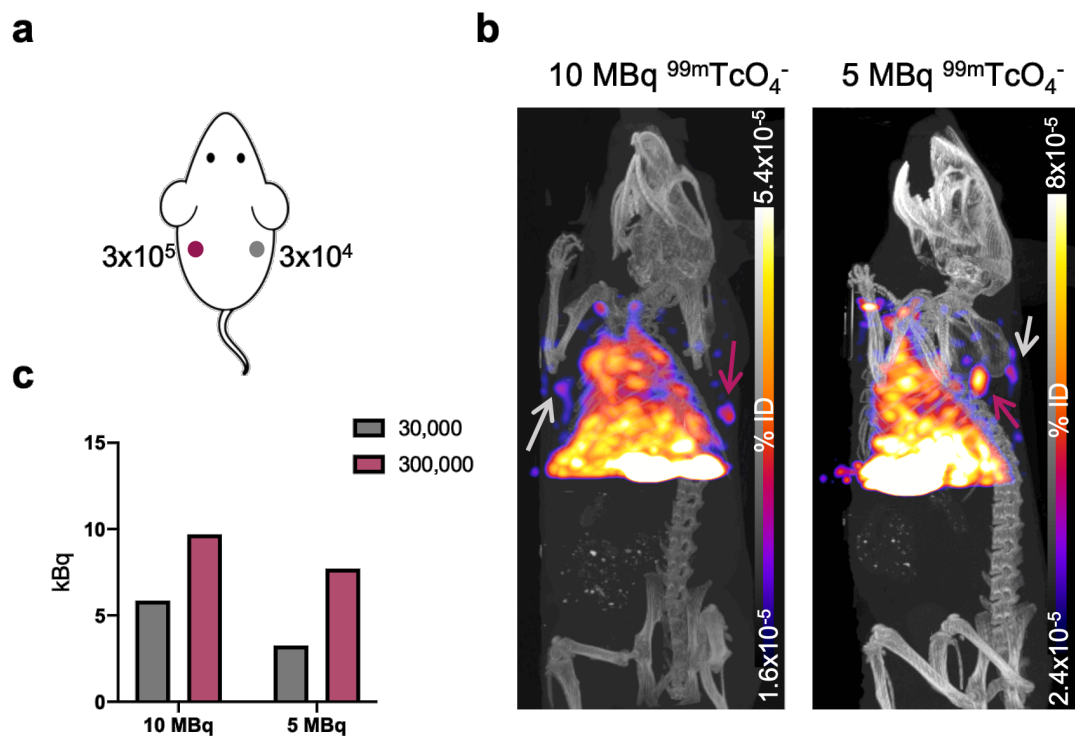
Figure 4.10: Visualisation of 4Pm28ζN T cells with varying tracer doses. a) Schematic of CAR T cell concentration injected per animal. b) SPECT/CT MIP views. Arrows point to injection sites. c) Quantified $^{99m}TcO_4^-$ activity from SPECT images.
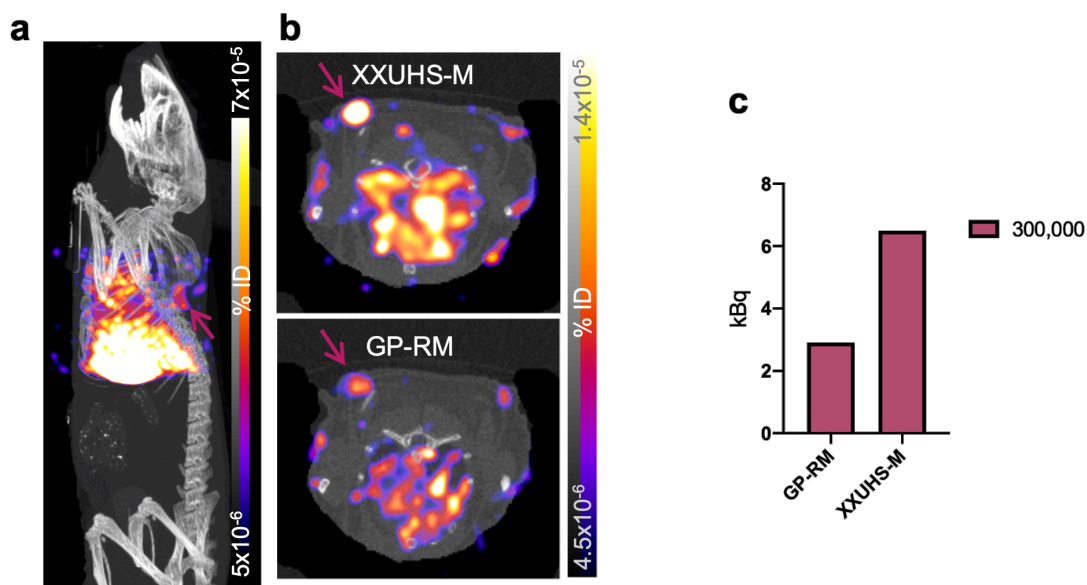
Figure 4.11: XXUHS-M collimator demonstrates superior sensitivity. a) SPECT/CT MIP view imaging with GP-RM. Arrows point to injection sites. b) Transversal views of the same animal image with XXUHS-M collimator (top) or with the GP-RM (bottom). Images reconstructed as a single 10-minute frame. c) Quantified $^{99m}TcO_4^-$ activity from SPECT images.

4.4 Compartmental model for CAR T cell quantitation

In order to model tracer kinetics and quantified number of CAR T cells homing to the tumour site non-invasively, concentration of tracer in the bloodstream and the target tissue must be concurrently measured. The suggested approach to quantify tracer kinetics involved a two-compartment model consisting of a blood compartment and a tumour compartment. Given that $^{99m}TcO_4^-$ is not metabolised or organified, no additional compartments are required within the tumour compartment. To establish a non-invasive quantitation method using this model, infiltrating CAR T cells were measured by flow cytometry to obtain the reference quantitation data. Subsequently, the kinetic constants K_1 and K_2 were ascertained and could serve as a non-invasive readout for determining the number of CAR T cells within the tumour (Figure 4.12).
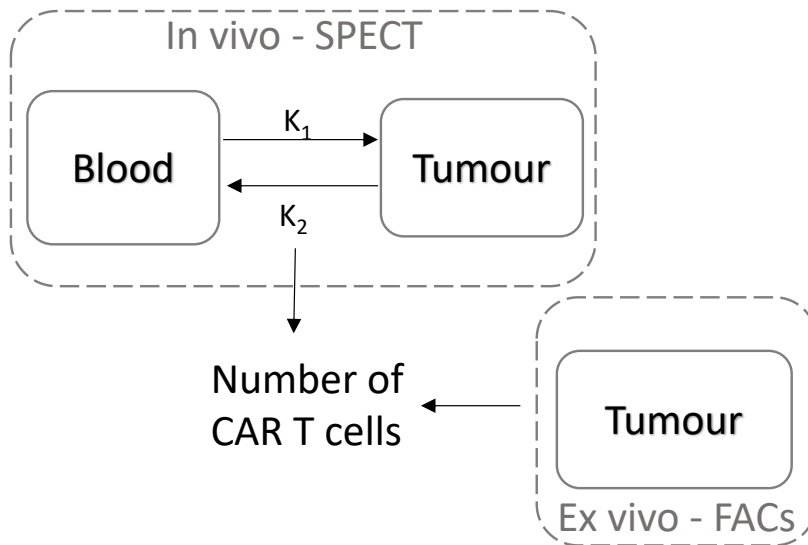
Figure 4.12: Proposed mathematical model for the non-invasive quantitation of CAR T cells through SPECT imaging. Tracer kinetics were measured by dynamic SPECT imaging. The number of infiltrating CAR T cells were measured after *ex vivo* tumour processing by flow cytometry. By combining the *in vivo* and *ex vivo* information a model can be established for the non-invasive quantitation of CAR T cells.

4.5   Image derived input function

To build a mathematical tracer kinetic model, concentration of radiotracer in the bloodstream is defined as the input function. Arterial sampling is considered the gold standard method for measuring tracer activity in the blood. However, this approach is highly invasive and there are limitations on the number of samples that can be collected[146]. As an alternative, I chose to define an image-derived input function from the SPECT dynamic data by drawing an ROI over the heart to quantify tracer concentration over time. To test the feasibility of using an image-derived input function for the mathematical model, the GP-RM collimator was used to visualise fast occurring changes after bolus injection due to its ability to record as short as 5-second frames. An animal was catheterised, and dynamic data was acquired serially using 5-second frames. Frames were then re-binned and reconstructed as 30- or 60-second frames, to match the minimum frame length that could be acquired with the XXUHS-M collimator. Recording 5-second frames allowed the visualisation of the first pass of tracer through the heart, followed by a second peak after flushing the catheter with saline solution. Similar peak height was observed if dynamic data was re-binned in 30-second frames. Quantitation of tracer concentration in the 1-minute frames followed a similar blood time activity curve. Radiotracer concentration in blood rapidly decreased after administration reaching steady state by thirty minutes post injection (Figure 4.13).

   To facilitate standardisation between studies and prevent potential partial volume effects when quantifying blood pool in the entire heart, tracer concentration is usually measured from the left ventricle[149]. Visipaque was used as a contrast agent to facilitate the delineation of the ROI over the left ventricle. As shown in Figure 4.14 a, Visipaque allowed the visualisation of both heart ventricles and the vasculature of the liver. However, since Visipaque is an iodinated contrast agent that increases tissue attenuation, it was hypothesised that its use could impact the accurate quantitation of the SPECT/CT images. Three different phantoms were tested *in vitro*. Two phantoms were prepared by mixing different amounts of Visipaque
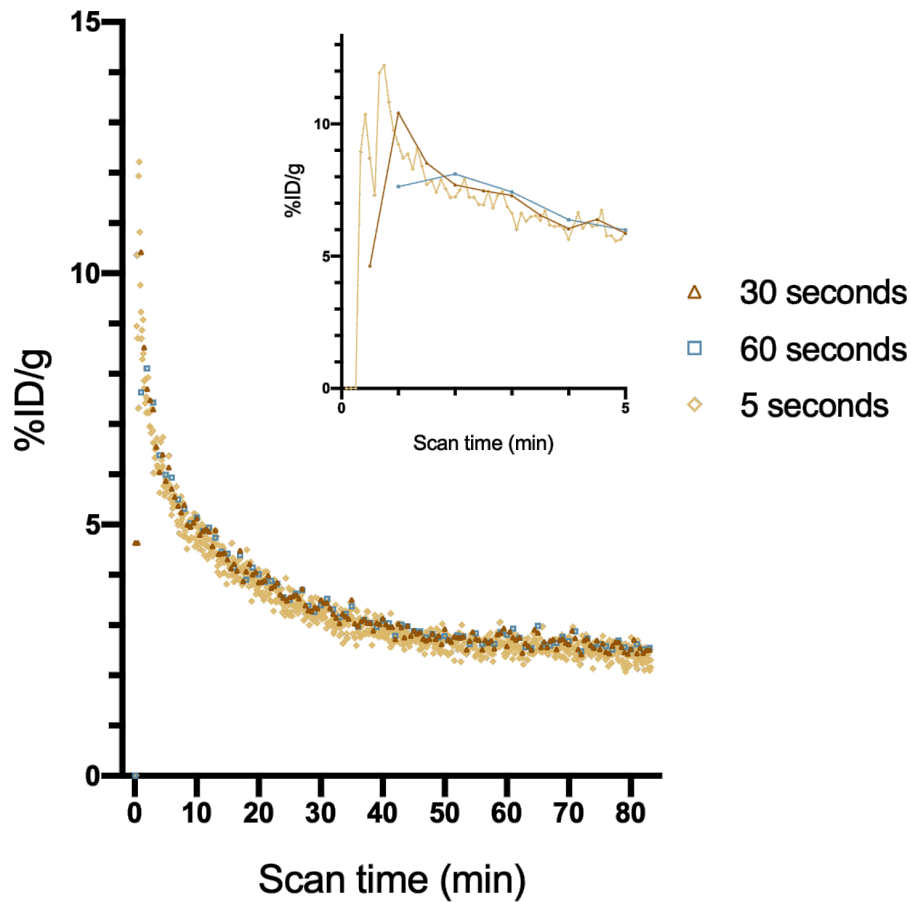
Figure 4.13: Blood pool time-activity curve. ROI drawn over the whole heart for quantitation of dynamic imaging. Frames were binned at different lengths to allow comparison. Inset shows zoom-in of the first 5 minutes of dynamic imaging.

with a known amount of radiotracer ($^{99m}TcO_4^-$). As a control, a third phantom was prepared by diluting the radiotracer in PBS. Phantoms were imaged dynamically, and radioactivity was quantified in co-registered and attenutation corrected SPECT/CT images. Addition of Visipaque led to overestimation of the measured activity in a dose dependent manner if the images were corrected for attenuation and scatter radiation (Figure 4.14 b). Shorter frames proved to be less accurate, as expected. If images were not corrected for attenuation, the addition of the contrast media did not affect quantitation compared to the PBS phantom; however, the lack of attenuation correction led to inaccurate and underestimated quantitation, even in the absence of contrast agent (Figure 4.14 c). Thus, although Visipaque facilitated

the visualisation of the left ventricle, it modified the tissue properties leading to inaccurate tracer quantitation.
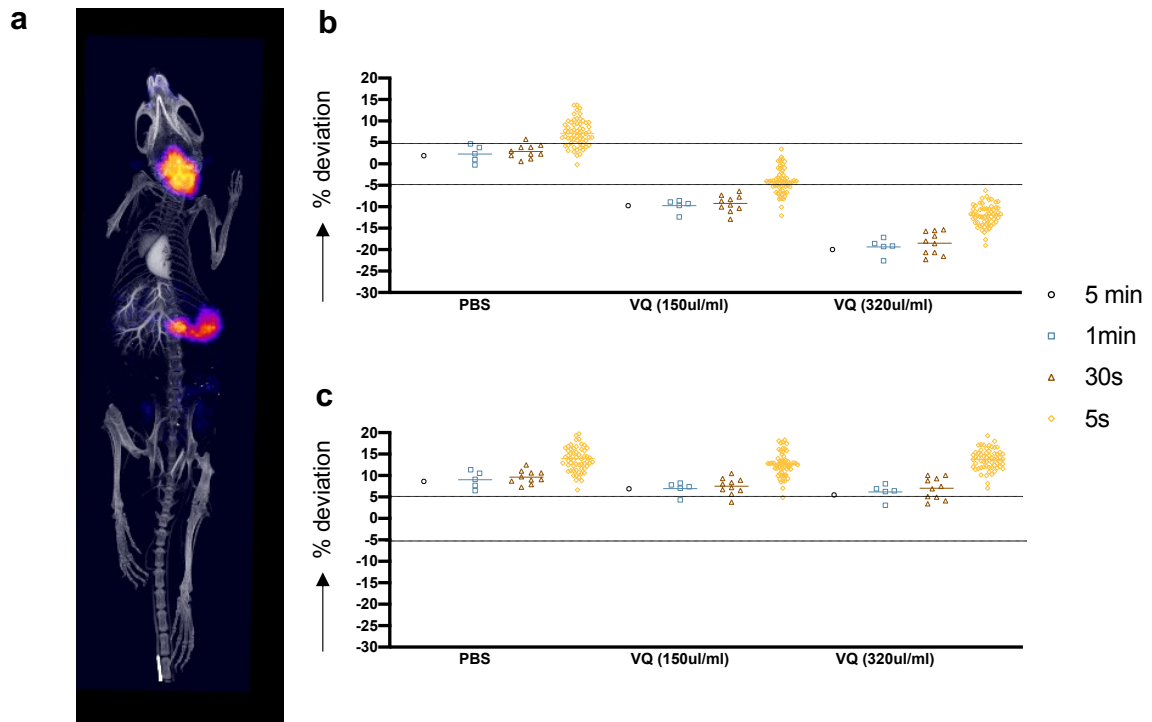
Figure 4.14: Visipaque for visualisation of the left ventricle. a) Whole body MIP view showing Visipaque contrast in heart ventricles and liver vasculature as well as endogenous $^{99m}TcO_4^-$ uptake by the stomach and salivary glands/thyroid. b) *In vitro* phantom studies quantifying tracer from corrected (top) or non-corrected (bottom) images. Deviation percentage defined as [(expected - measured)/expected]. VQ : Visipaque.

Up until now, tracer concentration in whole blood was used to describe the input function. However, it is important to note that only tracer in plasma can extravasate to the tissue. Thus, blood samples were collected, and plasma was extracted to compare tracer distribution in whole blood versus plasma. Similar concentrations were observed between whole blood and plasma samples, indicating that the blood time-activity curve does not need to be corrected to plasma (Figure 4.15).
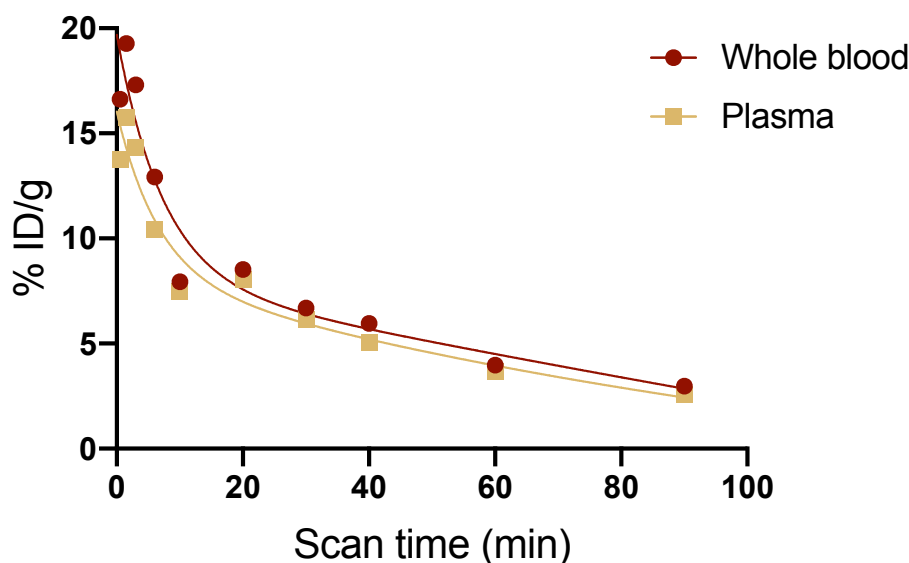
Figure 4.15: Blood and plasma time-activity curves. Population curves from blood samples collected by cardiac puncture. Blood samples were manually collected, and plasma was separated by centrifugation. n=1/time point.

4.6 Proof of concept for the mathematical modelling

The next step was to test whether uptake by the CAR T cells could be fitted by the proposed two-compartment model (Figure 4.12). As a proof of concept, 3×10^5 4Pm28ζN T cells were injected subcutaneously in the shoulder followed by i.v. injection of $^{99m}TcO_4^-$. Dynamic SPECT images were acquired from one minute post tracer injection following a 1-minute frame sequence that spanned 110 minutes. The two-compartment model, shown in Figure 4.16 a, was built in SAAMII modelling software. To account for the absence of excretion data and the tracer distribution to other organs, a forcing function (FF) was applied to the blood compartment. This forcing function, name q1.FF, was derived from a two-phase exponential decay curve fitted to the blood time activity data (Figure 4.16 b). The model was fitted to the quantified CAR T cell data (s1) showing gradual accumulation of the tracer, reaching maximum uptake 15 minutes post injection with steady state reached at approximately 30 minutes post injection (Figure 4.16 c). The rate constants were extracted from the model and are detailed in Table 4.1. The 95% confidence interval ranged from
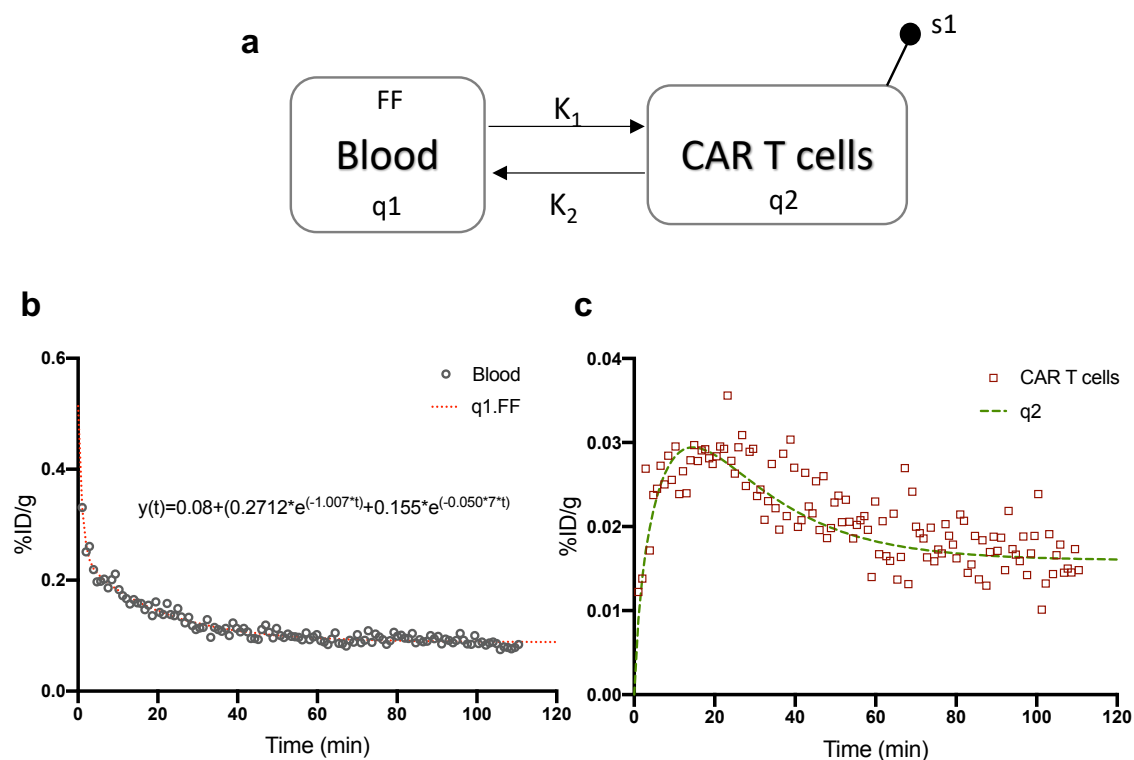
Figure 4.16: Proof of concept for the two-compartment model fit. a) Two-compartment model built in SAAMII software. The blood compartment, q1, exchanges tracer with the CAR T cell compartment, q2, at the rate defined by K_1 and K_2. The blood compartment was fixed with a forcing function (FF) and the quantified CAR T cell signal, s1, was fitted to the model. b) Blood time activity curve and derived two-phase exponential decay equation. c) Quantified CAR T cell signal with curve (q2) fitted by the model. n=1.

0.10 to 0.14 for K_1 and from 0.019 to 0.025 for K_2, indicating a good fit of the model (Table 4.1).

Table 4.1: **Rate constant values extracted from the two-compartment model.**

Rate constant	Value (SD)	95% confidence interval
K_1	0.12415 (0.0083)	0.10767-0.14062
K_2	0.02204 (0.0014)	0.01956-0.02539

This preliminary study showed that tracer distribution in blood, and uptake by CAR T cells, can be fitted to a two-compartment model by acquiring dynamic SPECT data with the heart and CAR T cells present within the field of view. This experiment was a proof of concept since CAR T cells were injected subcutaneously. Thus, the next step was to determine the feasibility of modelling CAR T cell trafficking in animals bearing shoulder xenografts.

Chapter 5

Tracking CAR T cells *in vivo* non-invasively

5.1 Establishing a xenograft mouse model

To non-invasively monitor CAR T cell trafficking and build a compartmental model to quantify the number of CAR T cells homing to the tumour, I set out to establish a mouse model with shoulder xenografts. PLP-LT tumours cells were injected s.c. in the shoulder to allow the acquisition of dynamic data containing both the heart and the tumour within a small field of view. The presence of firefly luciferase in the prostate cancer cell line (PLP-LT) allowed for the non-invasive monitoring of tumour progression using BLI.

Titration experiments were performed to evaluate the optimal tumour cell dose required to establish a mouse model in which disease progressed steadily over the course a few weeks. Three different PLP-LT doses, 0.25, 0.5 or 1 x10^5 cells, were injected s.c. above the shoulder. After eleven days, tumour engraftment was visible in all cohorts. Fast tumour growth was observed at the highest dose. In this group ulcerations (represented by a star in Figure 5.1) appeared from day 13 and animals were culled between day 15-18 due to large tumour size or ulceration (Figure 5.1 a). Interestingly, BLI signal started to decrease
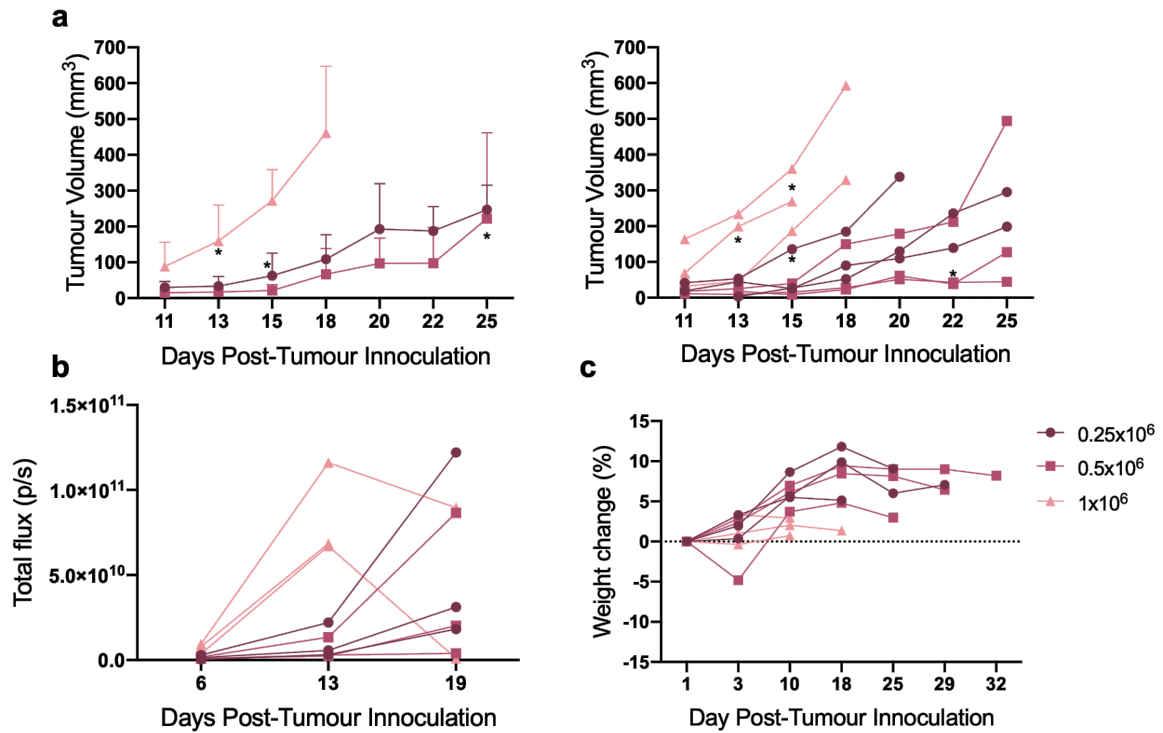
Figure 5.1: Titration of PLP-LT tumour cells for establishing a xenograft mouse model.
a) Tumour volume was monitored by callipers measurements three times per week. Average values per group are depicted on the left, individual animals are depicted on the right. Stars represent first appearance of ulceration. b) Burden of firefly-luciferase PLP-LT tumours assessed by BLI. c) Differences in body weight. n=3 animals/group. Graphs represent mean ± SD.

from day 13, which could correlate with tumour necrosis since the oxidation reaction of D-luciferin requires the presence of ATP and oxygen (Figure 5.1 b). The growth kinetics were similar for the other two cohorts. Ulcerations were observed from day 25 for the medium dose group ($0.5x10^5$ cells) and only one animal developed an ulcer in the low dose group ($0.25x10^5$ cells). Weight loss was not observed in any of the groups (Figure 5.1 c).

The lowest dose of $0.25x10^5$ cells was chosen to establish the model to allow for steady disease progression and minimise the chances of ulcerations forming.

5.2 *In vivo* non-invasive monitoring of CAR T cell trafficking

PLP-LT tumours were established in the shoulder area to allow for dynamic SPECT imaging of heart and tumour within a small field of view; approximately 13 bed positions. BLI and $^{99m}TcO_4^-$ SPECT/CT were employed serially to assess tumour burden and intra-tumoural accumulation of CAR T cells, respectively, as depicted in Figure 5.2 a. SPECT/CT baseline scans were performed the day before PBS or 4Pm28ζN T cells were injected. Injection of the tumour cells in the shoulder proved to be challenging due to location. Despite the presence of viable PLP-LT tumour cells in all animals, as shown by BLI (Figure 5.2 b), tumour growth was slower than in the titration experiment and exponential growth was observed from day 20 post-injection, instead of at 9 days post inoculation as predicted by the titration experiments. Despite the limited tumour engraftment, animals were serially administered with $^{99m}TcO_4^-$ and imaged to assess CAR T cell infiltration and establish the protocol to quantify blood time-activity curves.

The small tumour size made quantitation of SPECT images challenging since there was not a clear outline of the tumours in the CT images. Nonetheless, quantitation of *in vivo* imaging data was performed and the results showed increased uptake in tumours from treated animals as early as two days post CAR T cell treatment (Figure 5.2 c). Intra-tumoural accumulation of 4Pm28ζN T cells was visible in a treated tumour two days post CAR T cell injection, with no visible tracer accumulation in control animals (Figure 5.2 d).
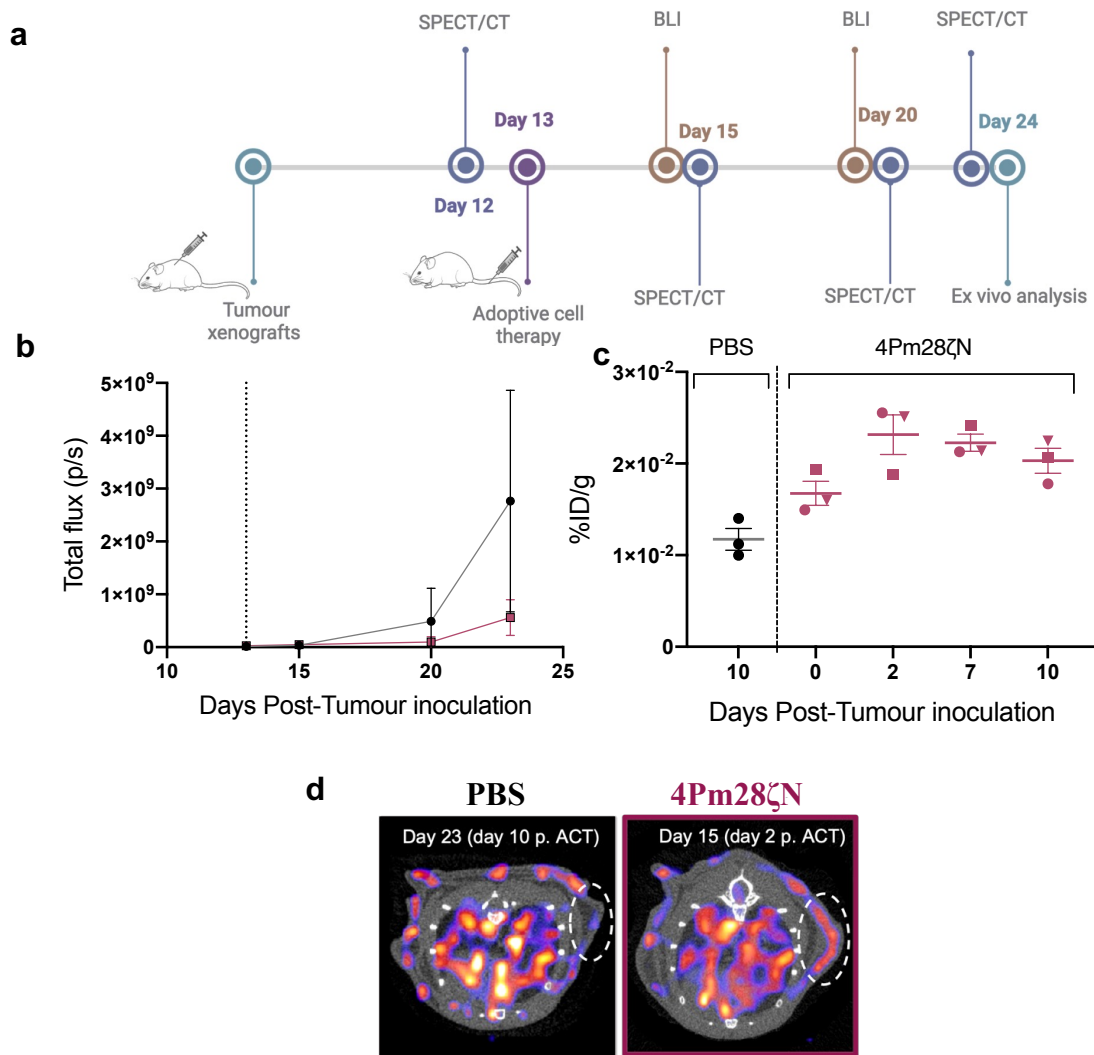
Figure 5.2: Tracking 4Pm28ζN T cells in shoulder xenografts. a) Experimental timeline. b) Average tumour burden measured by bioluminescence. c) SPECT/CT image derived quantitation of $^{99m}TcO_4^-$ uptake from tumours on day 0, 2, 7, and 10 post treatment after administration of 10 MBq of $^{99m}TcO_4^-$. d) Representative SPECT/CT images showing intra-tumoural accumulation of CAR T cells in a treated tumour (magenta frame) or non-specific uptake in a PBS injected control tumour (black frame). n=3 animals/group. Graphs represent mean ± SD.

Analysis of the dynamic SPECT images showed similar time-activity curves for the heart (as a surrogate for blood) not only between animals, but also throughout time (Figure 5.3 a), suggesting that this protocol provides robust and reproducible quantitation. Ten days post treatment, tumours and organs were collected and subjected to gamma counting to

assess radioactivity levels. Tumours that received 4Pm28ζN T cells showed slightly higher radioactivity levels than tumours from control animals. Normal physiological $^{99m}TcO_4^-$ uptake was observed in the salivary glands and stomach for all animals (Figure 5.3 b).
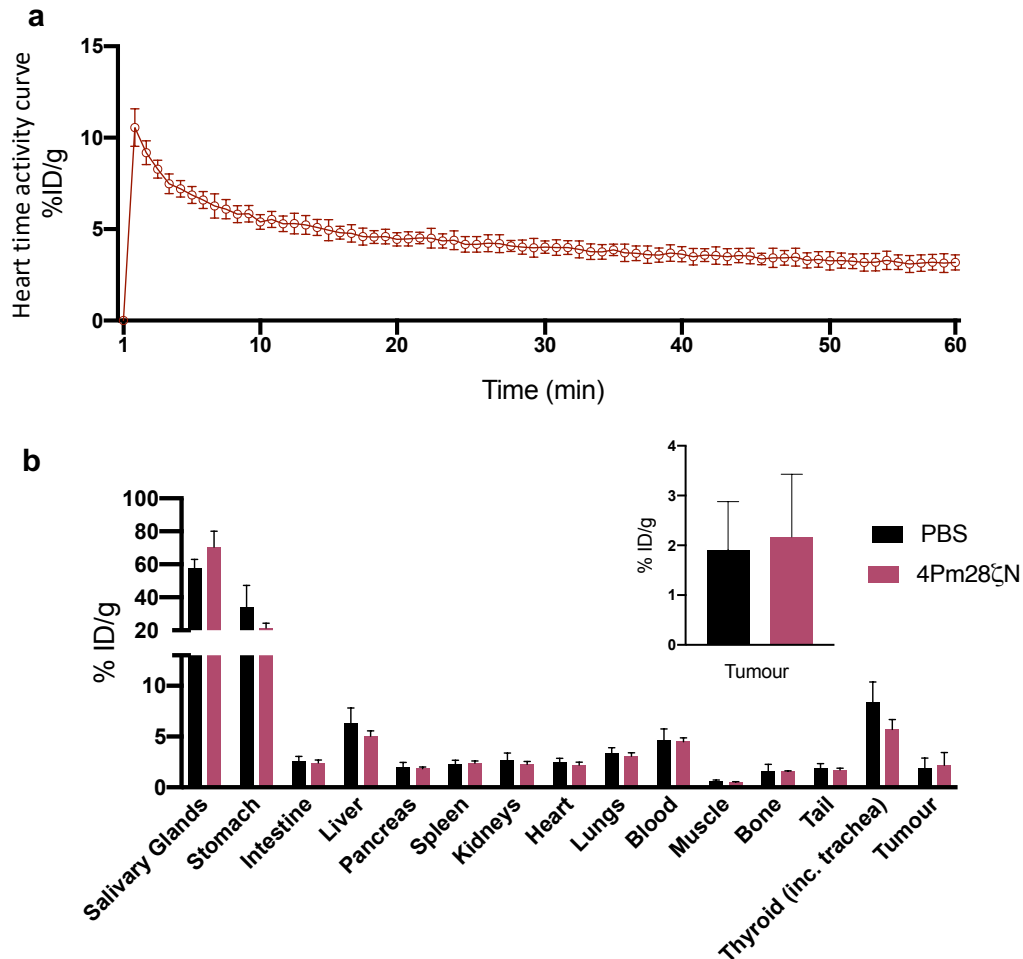
Figure 5.3: *In vivo* **and** *ex vivo* **tracer biodistribution.** a) Average heart (blood surrogate) time-activity curve. Six animals were image at day 0, day 2, day 7 and day 10 post CAR T cell injection assessed by SPECT/CT. n=24 samples b) *Ex vivo* biodistribution at day 10 post CAR T cell infusion, inset shows zoom-in on tumours. n=3 animals/group. Graphs represent mean ± SD.

Despite, the limited tumour engraftment and slow tumour growth, these preliminary results showed: firstly, that CAR T cells can be detected by dynamic SPECT/CT as early as two days post treatment, and secondly, that concentrations of tracer in blood, as measured *in vivo* in the heart, after $^{99m}TcO_4^-$ injection is comparable between animals and across time.

Due to the lack of tumour engraftment observed in this study, the experiment was repeated allowing the tumours to engraft and reach a size of over 100 mm^3 before treatment. This tumour size would facilitate delineating the ROI over the entire tumour using the CT anatomical data.

Subcutaneous injections of 0.25x10^5 PLP-LT cells were administered above the right shoulder in each animal. Fourteen days later established tumours were treated with 4Pm28ζN T cells or PBS. BLI and $^{99m}TcO_4^-$ SPECT/CT imaging were employed to assess tumour burden and intra-tumoural accumulation of CAR T cells, respectively, at the time points depicted in Figure 5.4 a. CAR T cell transduction was determined 24 hours prior to i.v. injection by flow cytometry and the control group received 200 µl of PBS. On the day of CAR T cell administration an uptake assay was performed, with the transduced PBMCs being able to internalise 12.5% of the added $^{99m}TcO_4^-$ (Figure 5.4 b).

For all animals, body weight decreased immediately after CAR T cell or PBS administration, but this recovered within six days (Figure 5.4 c). No therapeutic effect was observed in the treated group compared to the PBS control group, however excised tumours from the treated group did weigh significantly less (Figure 5.4 d & e).

Dynamic SPECT/CT imaging was performed before adoptive T cell transfer, 3- and 7-days post administration. ROIs were drawn over the tumours to quantify $^{99m}TcO_4^-$ uptake by the CAR T cells homing to the tumour by following the tumour anatomy in the CT. SPECT images revealed elevated signal in the tumours that received 4Pm28ζN T cells compared to control tumours. The signal also intensified over time accumulating around the tumour perimeter (Figure 5.5 a). SPECT image quantitation demonstrated an increase in the amount of $^{99m}TcO_4^-$ present in the treated tumours after CAR T cell administration. Tumour uptake in treated animals increased over time compared to $^{99m}TcO_4^-$ pre-CAR T cell baseline scans at day 0, and to control tumours, confirming CAR T cell infiltration at the tumour site. There was no visible increase in SPECT signal or quantified $^{99m}TcO_4^-$ in
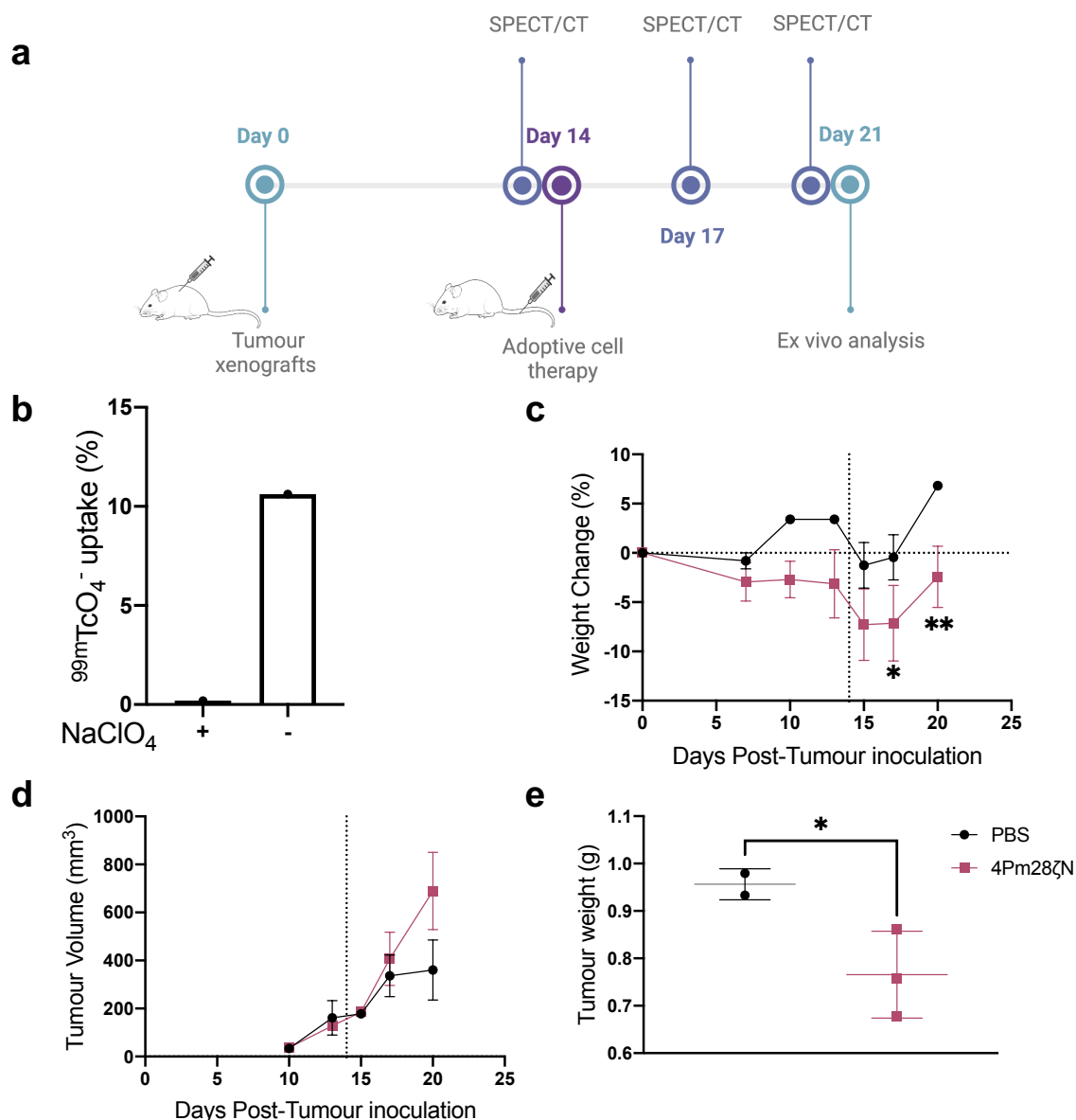
Figure 5.4: Tracking 4Pm28ζN T cells *in vivo*. a) Experimental plan. b) *In vitro* uptake levels of injected CAR T-cells incubated with $^{99m}TcO_4^-$ in the presence or absence of the inhibitor. c) Percentage body weight change. Dashed line represents day of CAR T cell injection. Statistical analysis was performed by Two-way ANOVA. d) Tumour volume was monitored by calliper measurements. e) *Ex vivo* tumour weight measured on day 21 (7 days post ACT). Statistical analysis was performed by Student's T test. n=3/treated groups, n=2/control group. Graphs represent mean ± SD. Statistical analysis was performed by Two-way ANOVA. $^*p \leqslant 0.05$; $^{**}p \leqslant 0.01$. ACT = adoptive cell transfer.
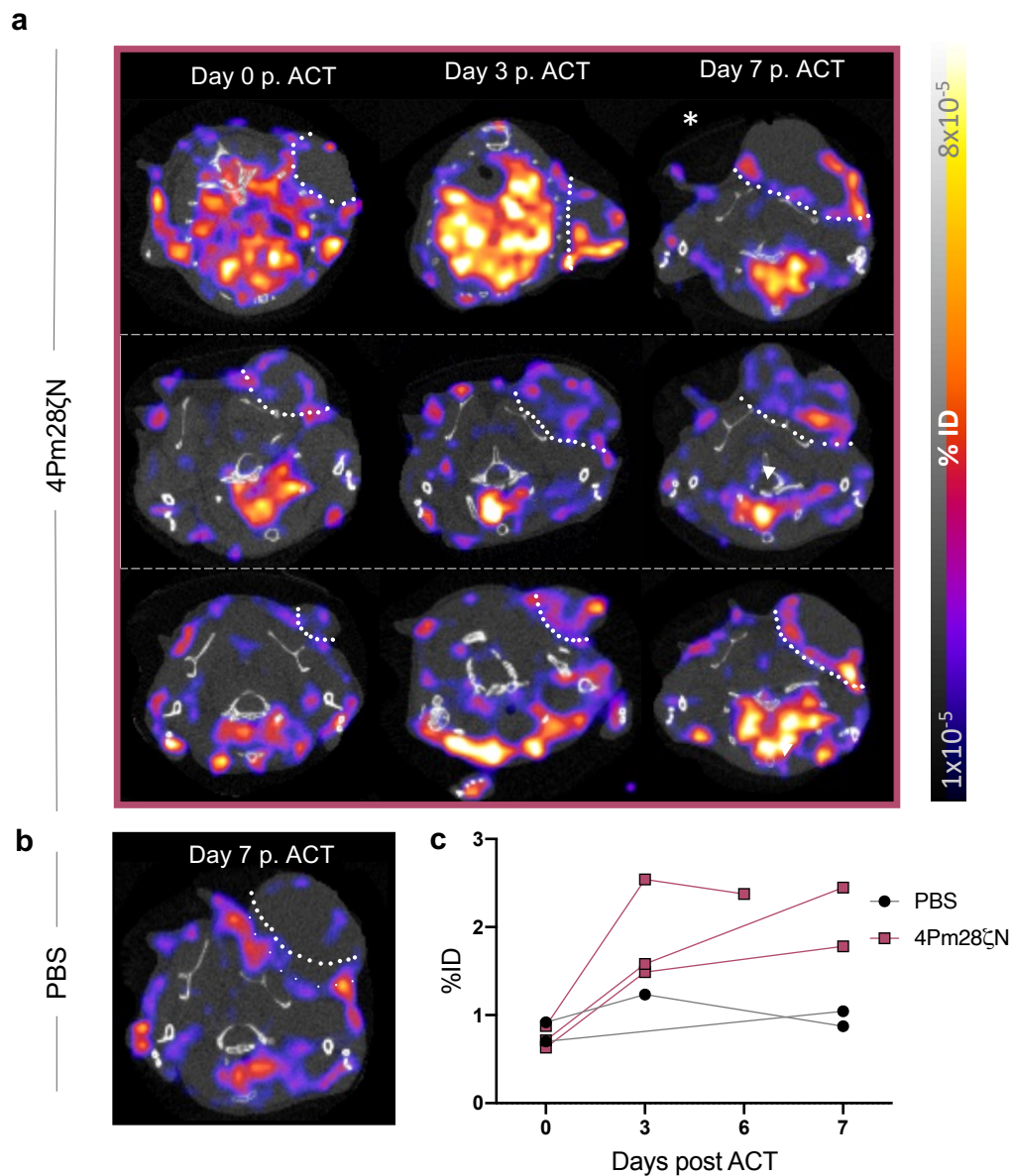
Figure 5.5: Accumulation of CAR T cells in treated tumours by SPECT/CT.
a) SPECT/CT images depicting CAR T cell homing to the tumour in treated animals (a) at different time points and perfusion signal in control animals on day 7 ppost ACT (b) following administration of 10 MBq of $^{99m}TcO_4^-$. Tumour borders are defined by the white dotted line. * Image acquired on day 6 p. ACT. b) $^{99m}TcO_4^-$ uptake was quantified from the SPECT images in a) as percentage of the injected dose (%ID) at the established time points. n=3/treated groups, n=2/control group. p. ACT = post adoptive cell transfer.

the control tumours (Figure 5.5 b). Despite the heterogenous distribution of the SPECT signal between animals, all tumours presented areas with low tracer signal ($<1 \times 10^5$ %ID) at the tumour core (Figure 5.5 a). This lack of signal could be related to disrupted tumour vasculature or the presence of necrotic tissue.

The acquired SPECT data was analysed dynamically. Time-activity curves for heart and tumour were plotted for each animal at the different imaging timepoints (Figure 5.7). If the vein was missed during i.v. injection of the tracer, causing part of the solution to be injected s.c., available tracer concentration in blood was severely affected thus directly impacting tumour uptake (Figure 5.6). These data points were discarded during the data analysis (3 out of 14 timepoints).
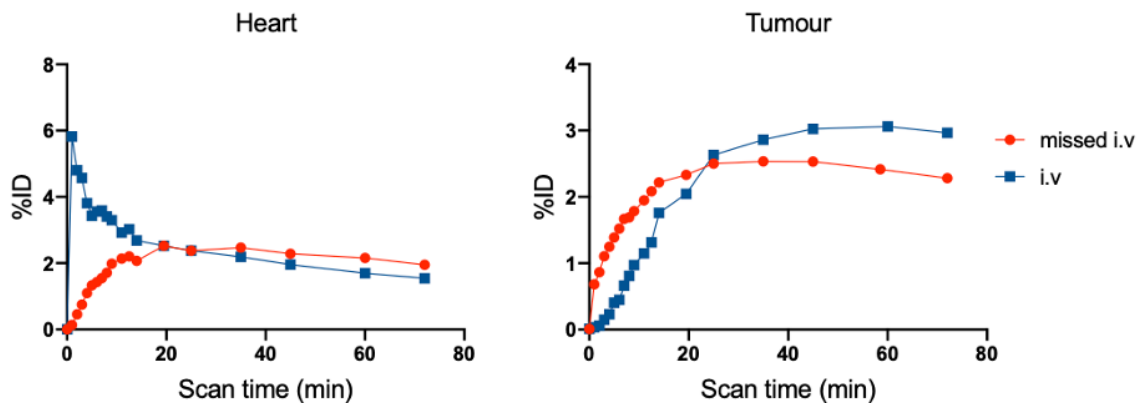
Figure 5.6: Tracer biodistribution after i.v. injection. Biodistribution of tracer in blood and subsequent tumour uptake after a missed (red) and precise (blue) i.v. injection of 10 MBq of $^{99m}TcO_4^-$.

There was rapid increase of tracer circulating in blood following the i.v. injection of $^{99m}TcO_4^-$. Maximum concentration was reached at 1 min post injection followed by an exponential decay phase. Radioactivity amount in blood was comparable between treated and control animals at baseline and day 3 post ACT. However, at day 7 post ACT, circulating tracer in treated animals was consistently higher than for control animals (Figure 5.7). It was

hypothesised that CAR T cells in circulation could be responsible for this difference in the amount of tracer quantified in blood.

There were no differences in the tumour uptake between the groups at baseline, but treated tumours showed accumulation of tracer above background levels at day 3 and 7 post treatment (Figure 5.7). Although the extent of tumour uptake varied within the treated group (Figure 5.7 b), maximum uptake was reached after 20 minutes post tracer injection before reaching steady state, in line with the results yielded during the *in vitro* assays (Figure 3.8).

Imaging quantitation is directly affected by the ROI volume, which may differ between subjects if tumour sizes are not comparable. The data was reanalysed and presented as percentage of injected dose per gram of tumour (%ID/g), to normalise the data to the volume of the drawn ROI. Differences in tracer concentration in blood at day 7 post ACT were still evident. However, differences in tumour uptake between control and treated groups at day 3 and day 7 post ACT were less noticeable (Figure 5.8). Variability in the degree of tumour uptake among animals that received 4Pm28ζN T cells decreased (Figure 5.8 b).
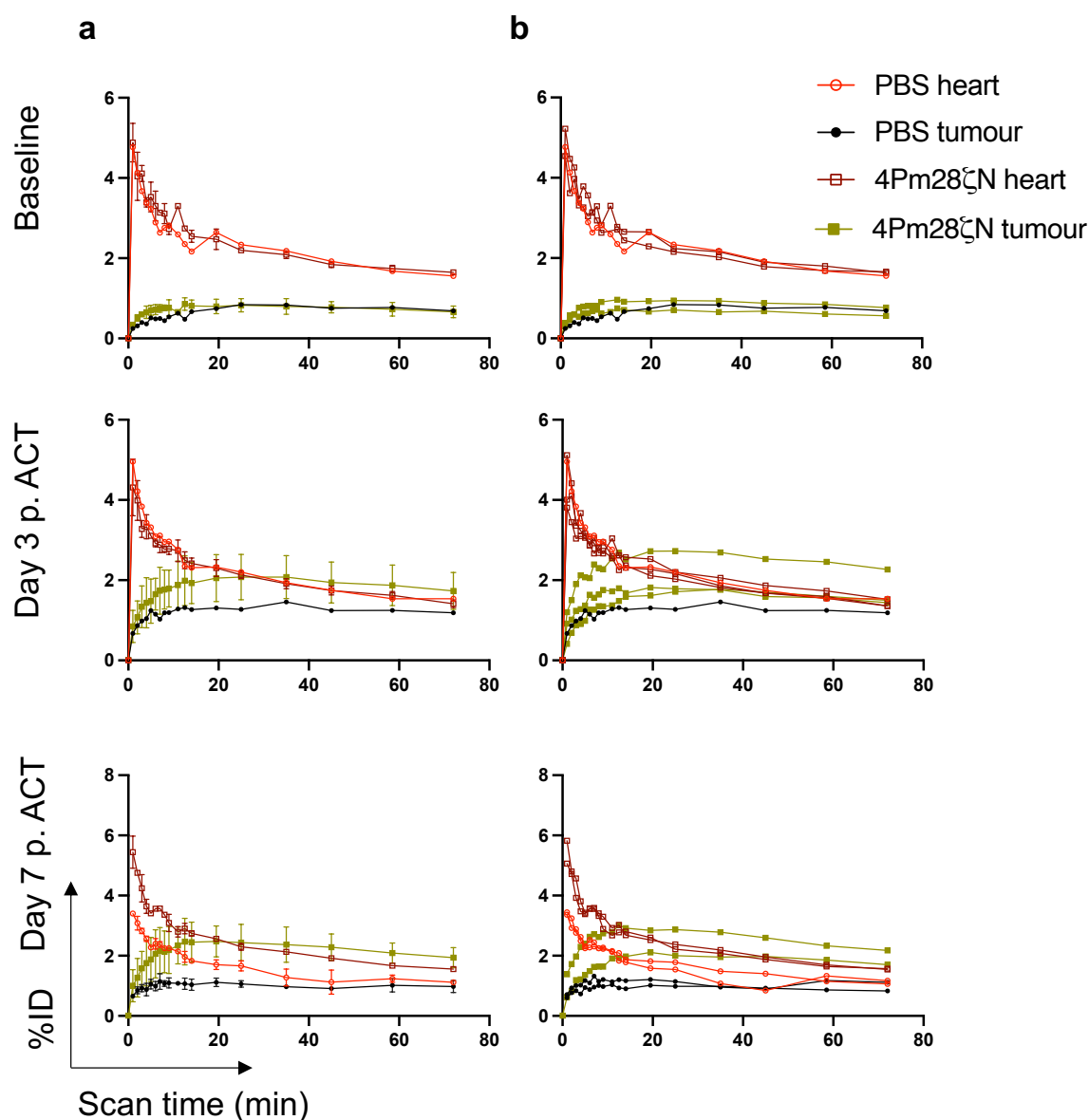
Figure 5.7: $^{99m}TcO_4^-$ **time-activity curves at baseline and at two different time points post ACT.** a) Average and b) individual 70-minute time course of tracer accumulation in heart and tumour of treated (square, n=3) and control (circle, n=2) animals after administration of 10 MBq of $^{99m}TcO_4^-$. Solid shapes represent the activity concentration in the tumour and open shapes represent the activity concentration in the heart. Animals were imaged before administration of immunotherapeutic treatment (baseline) and on day 3 and day 7 after administration of CAR T cells or PBS. Animals with missed i.v. injection of tracer (one trated animal on baseline and one treated animal on day 7 p.ACT) are not included. Uptake is expressed as the percentage of injected dose (%ID) quantified in the entire tumour. Graphs in (a) represent mean ± SD.
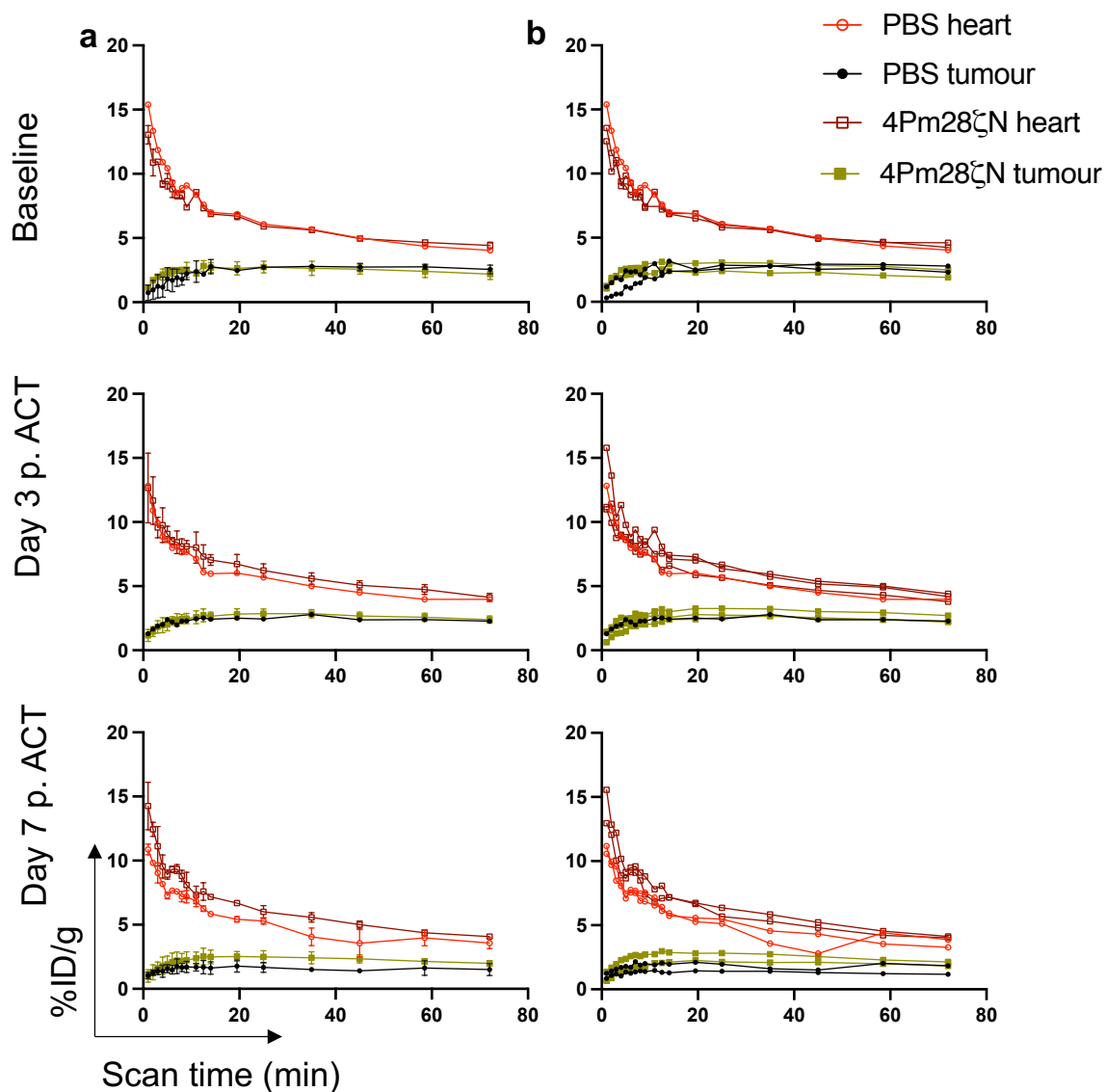
Figure 5.8: $^{99m}TcO_4^-$ **time-activity curves at baseline and at two different time points post ACT.** a) Average and b) individual 70-minute time course of tracer accumulation in heart and tumour of treated (square, n=3) and control (circle, n=2) animals after administration of 10 MBq of $^{99m}TcO_4^-$. Solid shapes represent the activity concentration in the tumour and open shapes represent the activity concentration in the heart. Animals were imaged before administration of immunotherapeutic treatment (baseline) and on day 3 and day 7 after administration of CAR T cells or PBS. Animals with missed i.v. injection of tracer (one control animal on day 3 p.ACT and one treated animal on day 7 post ACT) are not included. Uptake is expressed as the percentage of injected dose per gram (%ID/g) of tumour tissue. Graphs in (a) represent mean ± SD.
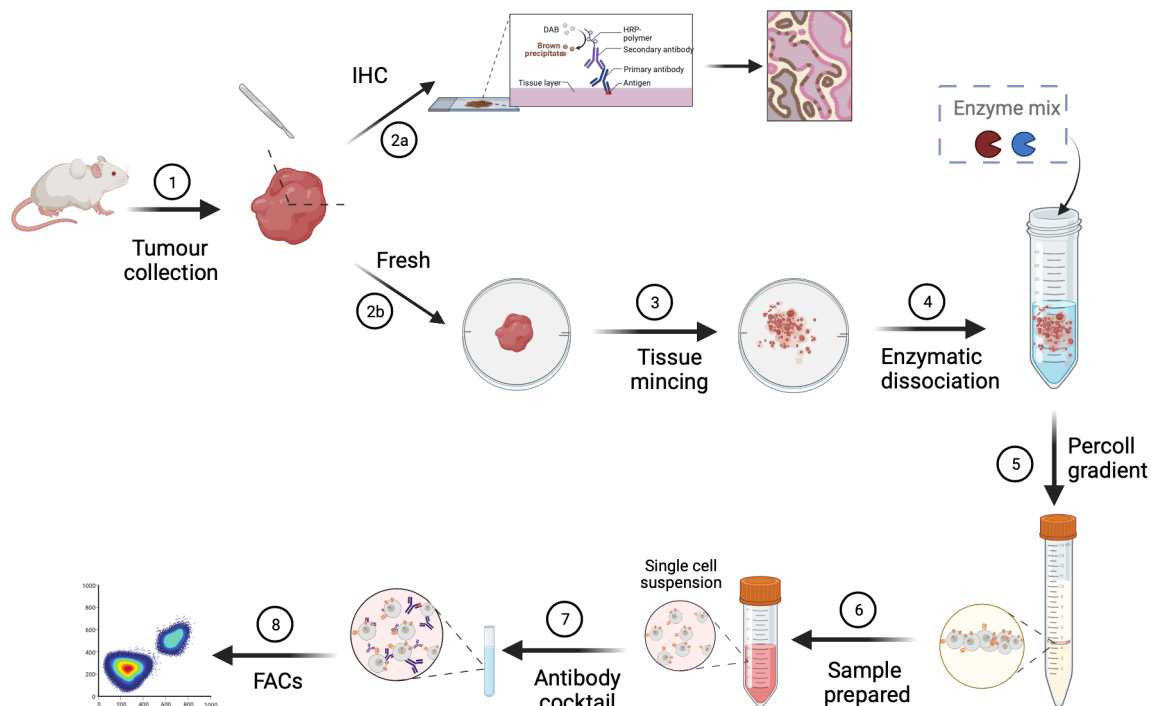
Figure 5.9: Schematic of the *ex vivo* analysis of tumours after *in vivo* SPECT/CT imaging. a) Excised tumours were divided into two parts for (a) immunohistochemistry or (b) FACS staining of human CD3 T cells in the excised tumours.

Following SPECT imaging on day 7 post CAR T cell treatment, tumours were excised and sectioned in two to study the degree of CAR T cell infiltration by flow cytometry and immunohistochemistry (Figure 5.9). CD3$^+$ cells were detected in two of the three tumours that received 4Pm28ζN T cells (Figure 5.10 a & b). Quantified CD3 positive cells by flow cytometry ranged from 40,000 to 120,000 cells/gram of tissue processed (Figure 5.10 c).

Immunohistochemistry staining corroborated the flow cytometry data, revealing different infiltration patterns between tumours that received 4Pm28ζN T cells, with no apparent staining in PBS treated group. Small clusters of CD3 positive cells were observed around the tumour borders in sections from two of the three treated tumours, which corresponded with better staining in the flow cytometry samples (Figure 5.10 a & b). Immunohistochemistry slices were quantified using QuPath software and average numbers from three slices per
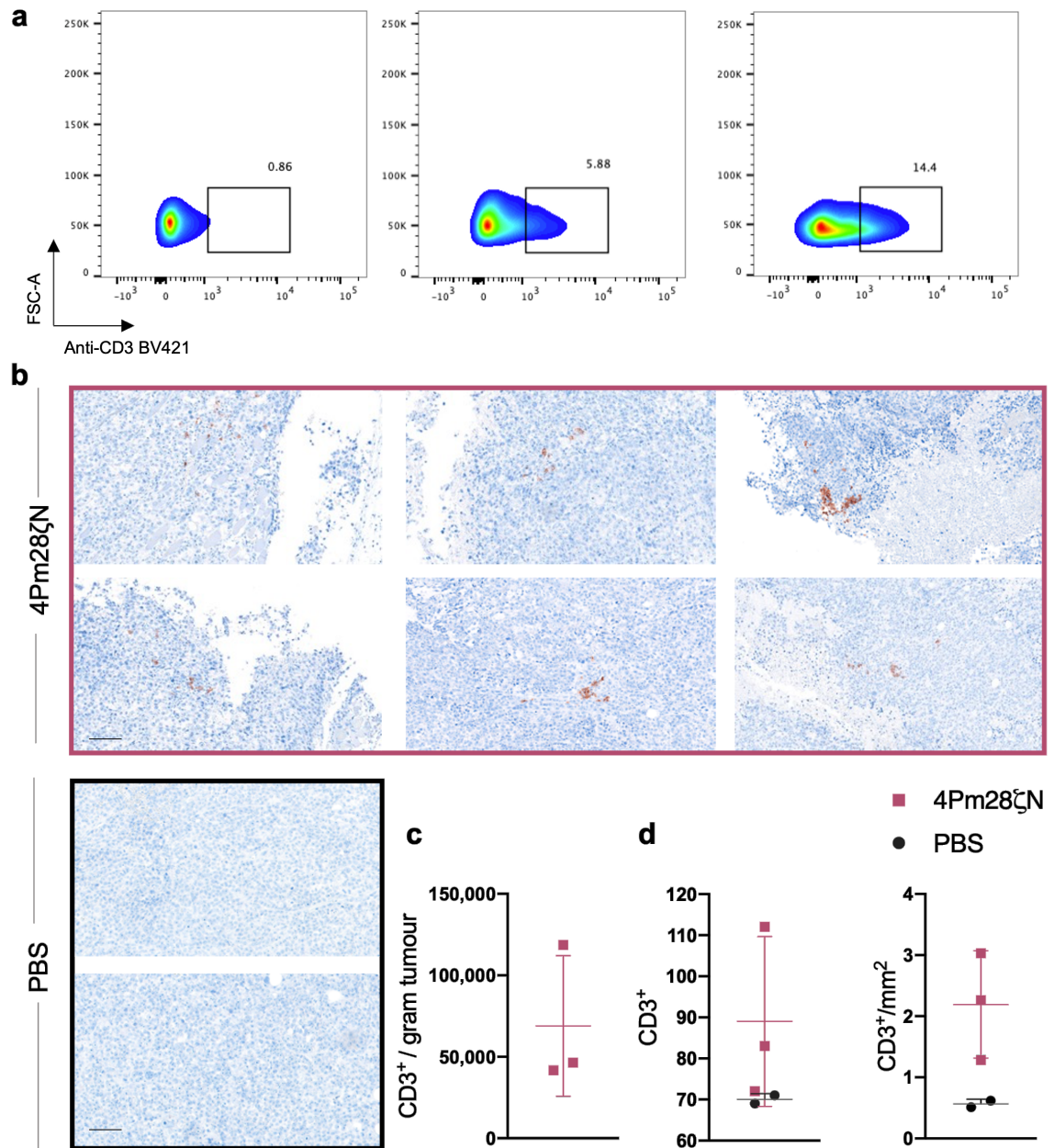
Figure 5.10: *Ex vivo* **analysis of tumours 7 days post ACT.** a) Flow cytometry plots depicting Single/live/CD3 positive cells in tumours that received 4Pm28ζN T cells and were harvested 7 days post ACT. Gating strategy shown in Figure S 8.3. b) Representative IHC images from xenografts harvested 7 days post injection of 4Pm28ζN T cells (n=3) or PBS (n=2). Sections were stained for human-CD3. Two different areas are shown for 4Pm28ζN tumour sections (n=3) and are paired with the flow cytometry plots in a). Scale bar: 100 μm. c) Quantified number of CD3 positive cells per gram of tissue from flow cytometry plots in a). d) Average number of CD3 positive cells quantified in tumour sections using QuPath software (Figure S 8.4). Graphs represent mean ± SD.

tumour are shown in Figure 5.10 d. The total number of CD3 positive cells quantified in two of the treated tumours ranged from 80 to 110 cells, the third treated tumour did not rate above background. Infiltration was overall limited, with an average of only one to three $CD3^+$ cells per mm^2 of tumour tissue. This data demonstrates the heterogenous distribution of $CD3^+$ within the tumours.

In this small case study, tumour engraftment and growth followed the expected course, allowing for the non-invasive monitoring of CAR T cell infiltration followed by *ex vivo* quantitation of the infiltrated CAR T cells. To facilitate imaged derived analysis of tumour uptake, tumours were allowed to reach 180 mm^3 prior to treatment. While it is easier to identify and draw ROIs over large tumours on a CT scan, these tumours grew aggressively leading to ulcerations shortly after treatment and rapidly reaching the maximum tumour size allowed. This limited the long-term monitoring of the CAR T cells, the last time point imaged being only 7 days post CAR T cell injection. Overall, CAR T cell infiltration was limited at the time points studied in this experiment.

Despite these constraints, SPECT images showed heterogenous infiltration of CAR T cell in the treated tumours. The quantified tumour uptake on the SPECT images was higher than in control tumours and it correlated to the *ex vivo* quantitation of CD3 positive cells through flow cytometry and immunohistochemistry. Interestingly, heart time-activity curves at day 7 post CAR T cell administration were considerably higher for treated animals compared to control groups. It was hypothesised that there were CAR T cells in circulation, which could account for the differences in tracer concentration in the heart.

In order to establish a mathematical model to track and quantify CAR T cells *in vivo*, larger group numbers are needed to be able to assess variability among treated animals and be confident about the conclusions drawn. The protocol used for the described experiments is robust and reproducible, however both the *in vivo* imaging and the *ex vivo* processing of tumours are time-consuming steps, limiting the number of animals that can be imaged and

processed in a day. Thus, the best solution was to divide the protocol over two consecutive days, the first day involving the *in vivo* imaging and biodistribution of animals and preserving the whole tumours in MACS® Tissue Storage Solution overnight. The following day, the protocol can be resumed by processing the tumours, staining the samples, and quantifying the number of infiltrating CAR T cells by flow cytometry.

5.3 Optimising the protocol for the non-invasive quantification of CAR T cells

To be able to increase the sample number per group, a new protocol was tested where *ex vivo* tumour processing was delayed to the following day by preserving the tumour samples overnight in MACS® Tissue Storage Solution. To confirm that storing the tumour overnight did not affect CD3 detection, two independent experiments were performed to compare dissociation of fresh tumour vs preserved tumours (Figure 5.11). Furthermore, to assess the relationship between tumour volume prior to CAR T cell treatment and CAR T cell infiltration patterns, established tumours were treated at different stages; in the first experiment tumours were treated when they reached 88 mm^3 , whereas in the second experiment tumours were treated when they reached 64 mm^3 .

In the previous study, differences in the heart activity curves were noticeable between treated and control groups. Thus, in these experiments, blood samples were collected and stained alongside tumours to detect whether there were circulating CAR T cells that could have taken up the tracer leading to such difference (Figure 5.11).

In a first experiment, PLP-LT cells were inoculated s.c. in the shoulder area. After 16 days, established tumours were treated with 4Pm28ζN T cells or untransduced T cells. The average tumour size for animals that received 4Pm28ζN T cells was 88mm^3 . Tumour burden was monitored by BLI twice per week, and tumour size was measured using callipers three
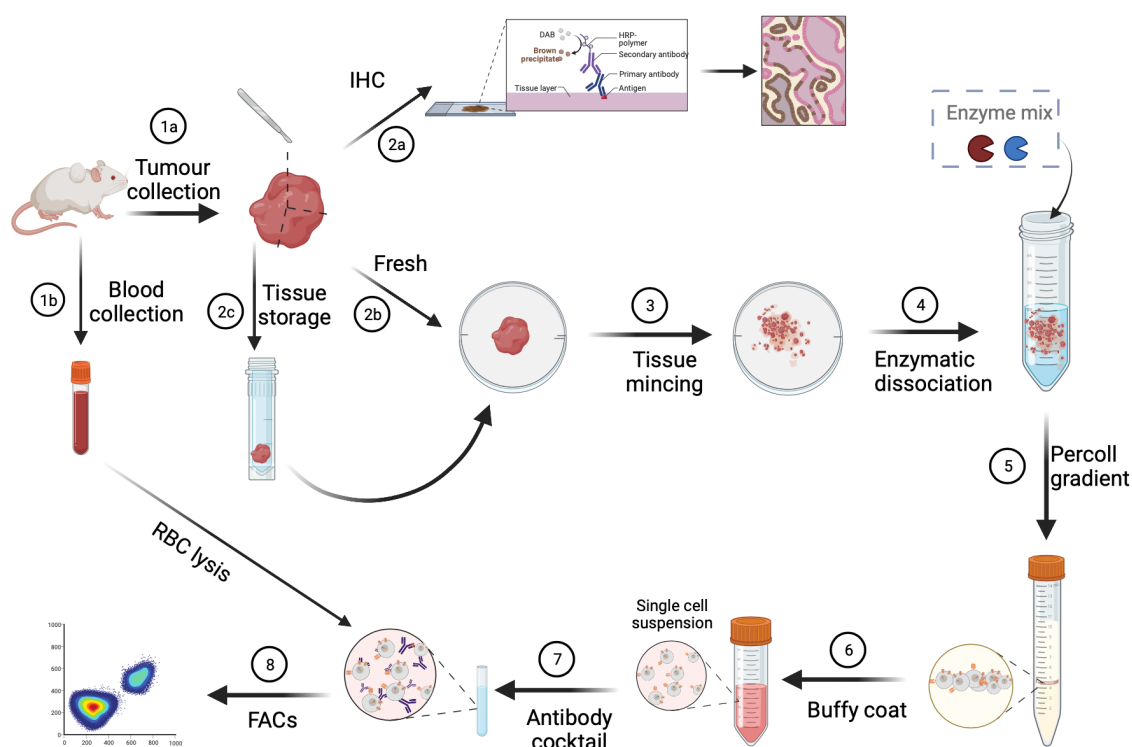
Figure 5.11: Schematic of the *ex vivo* analysis of tumours after *in vivo* SPECT/CT imaging. Excised tumours were divided in three parts for a) immunohistochemistry, b) FACS staining of freshly disassociated tumour, or c) FACS staining of preserved tumours. Blood samples were also stained and analysed by FACS.

times a week. Seven days post treatment, dynamic SPECT/CT images were acquired to study intra-tumoural accumulation of CAR T cells followed by *ex vivo* analysis of the tumours (Figure 5.12 a).

CAR T cell transduction was determined 24 hours prior to i.v. injection by flow cytometry and the control group received the same total number of T cells. On the day of CAR T cell administration an uptake assay was performed, a modest 5% of the added ^{99m}TcO$_4^-$ (0.33 MBq/ml) was internalised by the transduced PBMCs (Figure 5.12 b). After treatment, body weight continuously decreased for all animals (Figure 5.12 c). 4Pm28ζN T cells slowed down
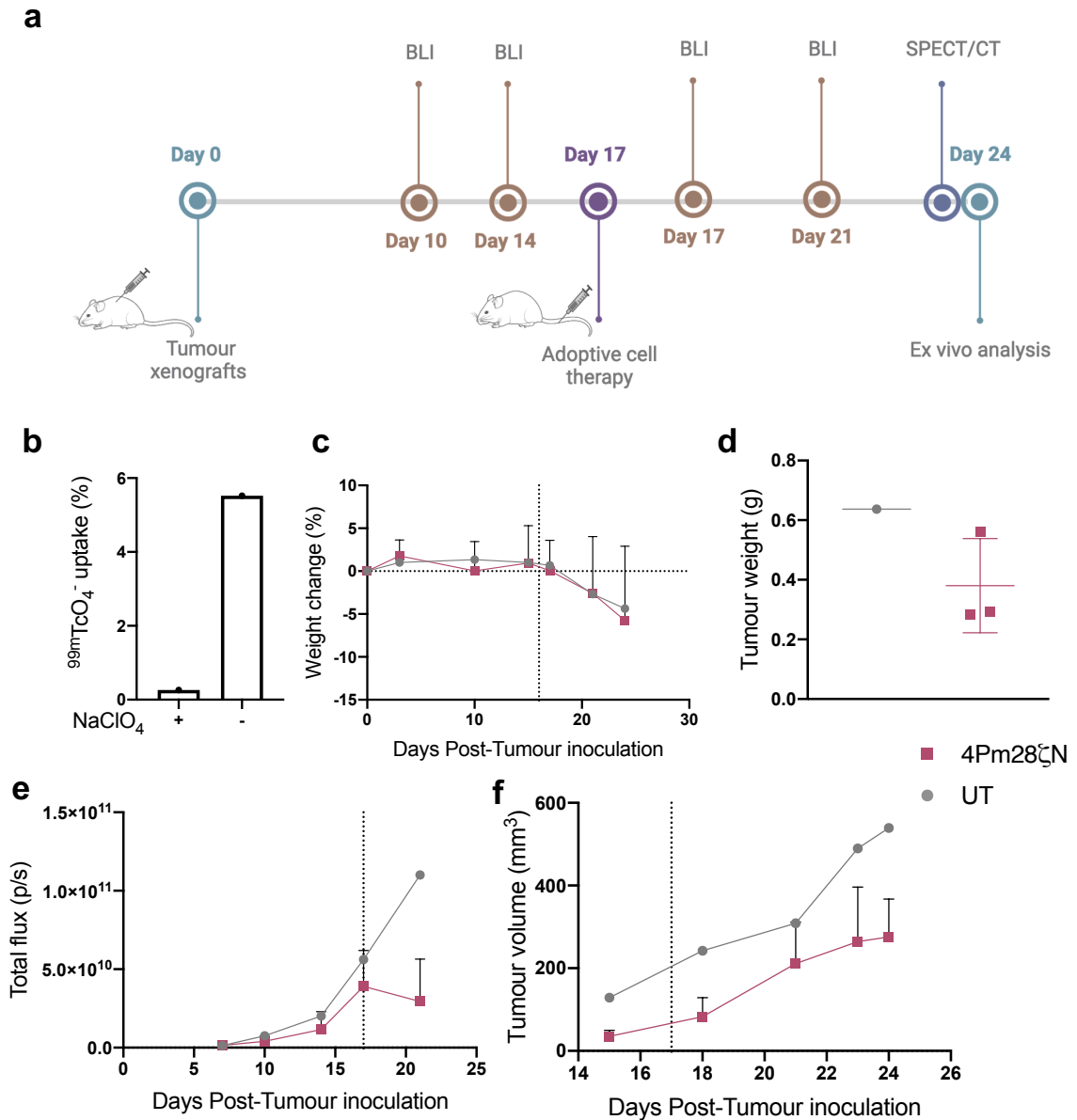
Figure 5.12: Tracking 4Pm28ζN T cells *in vivo*. a) Experimental plan. b) *In vitro* uptake levels of injected CAR T-cells incubated with $^{99m}TcO_4^-$ in the presence or absence of the inhibitor. c) Percentage body weight change. Dashed line represents day of CAR T cell injection. d) *Ex vivo* tumour weight measured on day 24 (7 days post ACT). e) Luciferase burden measured by BLI. f) Tumour volume was determined from calliper measurements. n=3/treated groups, n=1/control group. Graphs represent mean ± SD.

tumour progression compared to the untransduced group, which was reflected in excised tumours from the treated group weighing less than that the control tumour (Figure 5.12 d-f).

Dynamic SPECT/CT imaging was performed seven days post T cell administration and ROIs were drawn over the tumours to quantify $^{99m}TcO_4^-$ uptake by the CAR T cells homing to the tumours. Non-specific signal depicting perfusion was observed in the control animal. In 4Pm28ζN treated animals, tracer signal accumulated around the tumour edges, with no uptake at the tumour core ($<1x10^7$ %ID) (Figure 5.13 a). Tracer uptake in the tumours was quantified from the depicted SPECT images and presented as the percentage of the injected dose accumulated by the entire tumour (%ID) or by gram of tumour (%ID/g). Total uptake was comparable between groups due to the larger size of the control tumour compared to the 4Pm28ζN treated tumours (Figure 5.13 b). In contrast, $^{99m}TcO_4^-$ uptake per gram of tumour in treated tumours was significantly higher than in control animals indicating the presence of infiltrating CAR T cells (Figure 5.13 c).

These observations were corroborated by the dynamic data. Heart time-activity curves revealed similar concentration of tracer circulating in blood for both groups, with a rapid increase of circulating tracer after the i.v. bolus followed by a two-phase decay curve. Tracer concentration in the treated tumours steadily increased after bolus injection reaching maximum tumour uptake at 20 minutes post bolus injection. Uptake quantified for the entire tumours was comparable between groups (Figure 5.14 top) but all tumours that received 4Pm28ζN T cells showed higher uptake per gram of tissue compared to the tumour that received untransduced T cells (Figure 5.14 bottom).
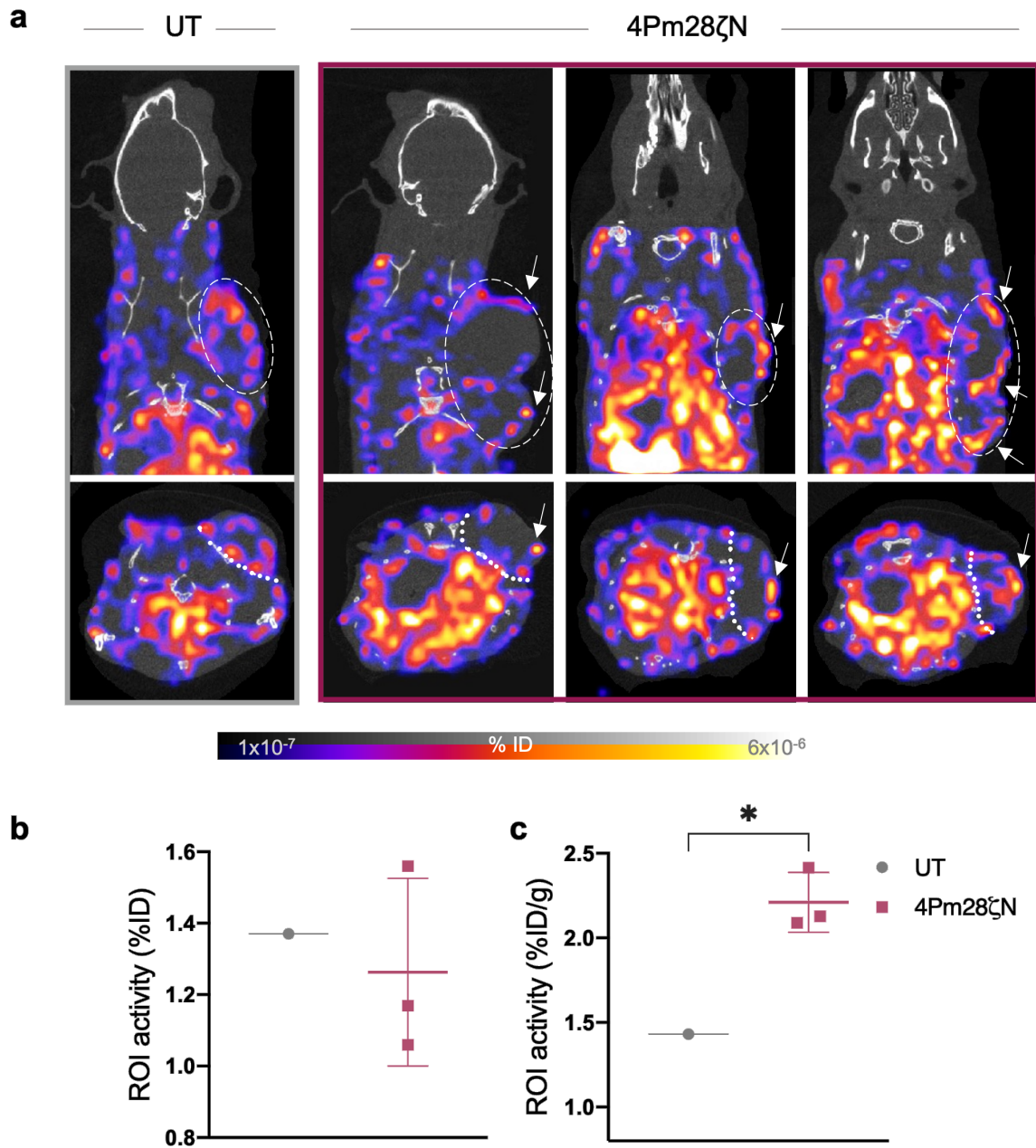
Figure 5.13: Infiltration of CAR T cells in treated tumours is observed through SPECT/CT. a) SPECT/CT images depicting CAR T cell homing to the tumour in control (grey) and treated animals (magenta) on day 7 post ACT after administration of 10 MBq of $^{99m}TcO_4^-$. Tumour borders are defined by the white dotted line. $^{99m}TcO_4^-$ uptake was quantified from the SPECT images as b) percentage of the injected dose or c) normalised to gram of tissue. n=3/treated group, n=1/control group. Statistical analysis was performed by Student's t-test. Graphs represent mean ± SD.
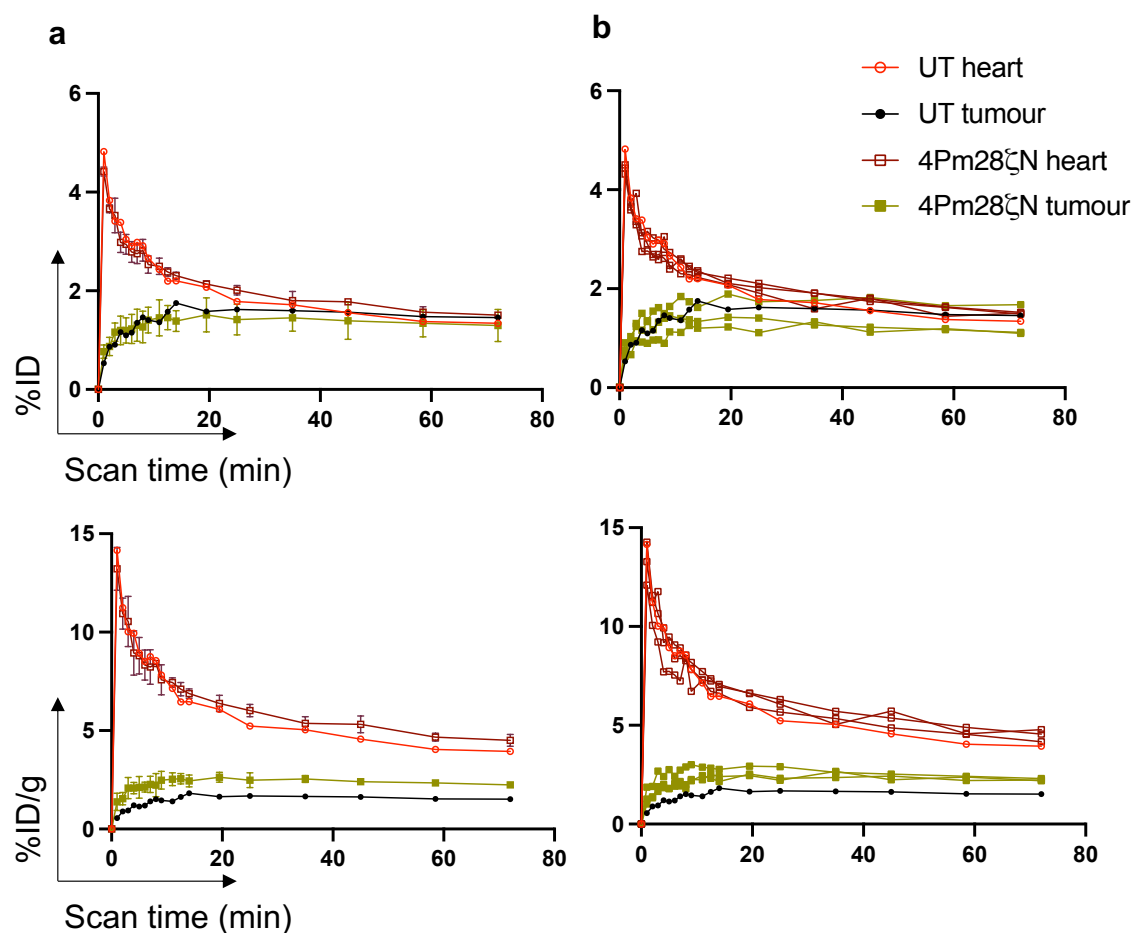
Figure 5.14: $^{99m}TcO_4^-$ **time-activity curves at 7 days post ACT.** a) Average and b) individual 70-minute time course of tracer accumulation in heart and tumour of treated (square, n=3) and control (circle, n=1) animals after administration of 10 MBq of $^{99m}TcO_4^-$, seven days post administration of CAR T cells or PBS. Solid shapes represent the activity concentration in the tumour and open shapes represent the activity concentration in the heart. Uptake is expressed as the percentage of injected dose (%ID) or normalised per gram (%ID/g) of tumour tissue or heart tissue. Graphs on a) represent mean ± SD.

Following the dynamic acquisition, animals were sacrificed and organs, tumours and blood were collected for *ex vivo* analysis. Radioactivity uptake in the samples was measured using a gamma counter. Whole tumours from animals that received 4Pm28ζN T cells showed higher accumulation of tracer compared to tumours from the control animal (inset Figure 5.15). *Ex vivo* biodistribution showed radiotracer accumulation in endogenous
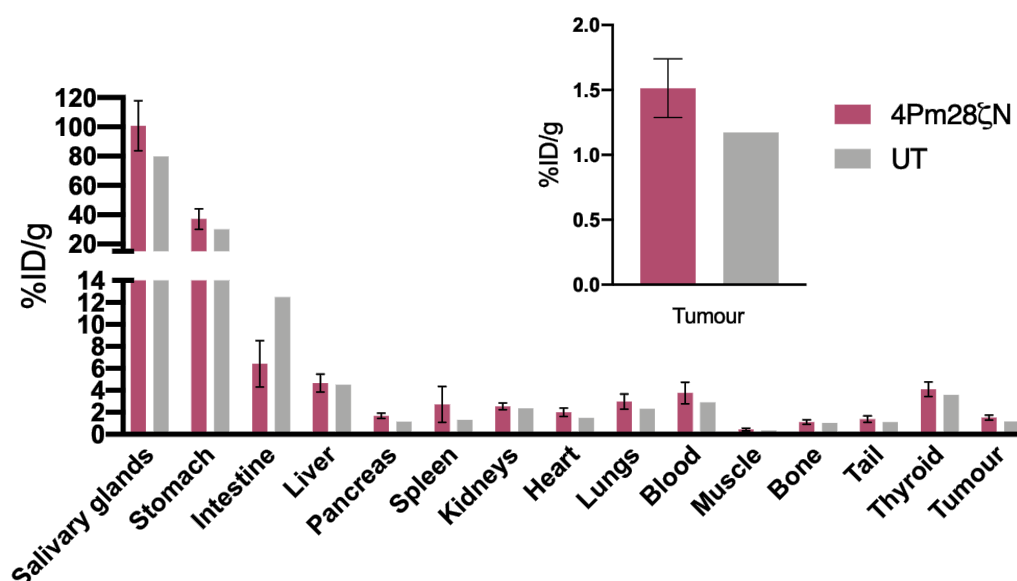
Figure 5.15: *Ex vivo* tracer concentration in organs. Quantified radioactivity uptake of $^{99m}TcO_4^-$ tracer from organs harvested 7 days post ACT. Animals were administered 10 MBq of $^{99m}TcO_4^-$ for SPECT/CT imaging. Following imaging, organs were collected and radioactivity was measured *ex vivo* using a gamma counter. Inset shows zoom-in on tumour uptake. n=3/treated group, n=1/control group. ACT = adoptive cell transfer. Graphs represent mean ± SD.

hNIS expressing organs, i.e., stomach and salivary glands. There was also higher concentration of tracer in the spleen and blood of treated animals (Figure 5.15).

Following gamma counting, tumours were divided in three sections; two sections were used to quantify infiltrating CAR T cells by flow cytometry while comparing differences in CD3 staining between fresh vs preserved tumour tissue in MACS® Tissue Storage Solution; the third section was fixed in formalin for downstream immunohistochemical analysis (Figure 5.11).

The fresh section from the tumour was disassociated and stained for CD3 to quantify infiltrating CAR T cells by flow cytometry. In parallel, blood samples collected by cardiac puncture were stained and analysed alongside the tumours to study whether circulating CAR T cells could take up $^{99m}TcO_4^-$ and contribute to higher concentrations of tracer in blood as observed previously (Figure 5.7 and Figure 5.8).

CD45$^+$CD3$^+$ double positive cells were detected in two of the three tumours that received 4Pm28ζN T cells. All treated animals showed positive CD3 staining, however, background staining was noticeable in the control tumour (Figure 5.16 a). Quantified CD3 positive cells by flow cytometry using counting beads was above background for two of the three treated tumours, ranging from 500,000 to 1,000,000 cells/gram of tissue processed (Figure 5.16 c). Circulating CAR T cells were not detected in the blood samples by flow cytometry (Figure 5.16 b), but higher counts were quantified in blood from treated animals by *ex vivo* gamma counting (Figure 5.15).

The following day, tumour sections preserved in MACS® Tissue Storage Solution were processed, stained for CD3 and analysed by flow cytometry. Unspecific background staining in the control tumour decreased. CD3 staining of 4Pm28ζN treated tumours was not as bright as the previous day (Figure 5.17). The difference in staining could be the result of preserving the tumour tissue or it could reflect the heterogenous infiltration of CAR T cell leading to uneven distribution of CAR T cells within the analysed tumour sections. Results from the second planned experiment would further clarify whether preserving the tissue affects CD3 detection.

As aforementioned, the third and last section of each tumour was used to detect CD3 T cells in paraffin embedded tumour sections. Immunohistochemistry corroborated the presence of infiltrating CAR T cells in all 4Pm28ζN treated tumours, with CAR T cells being detected within the connective tissue or the tumour margins (Figure 5.18), in line with the depicted SPECT/CT images in Figure 5.13. There was no positive CD3 staining in the control tumour (Figure 5.18). Quantitative analysis of the tumour sections using QuPath measured an average of 150 CD3 cells per tumour slice, leading to an average of 10 cells per mm^2 (Figure 5.19).
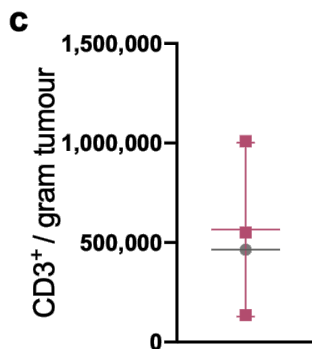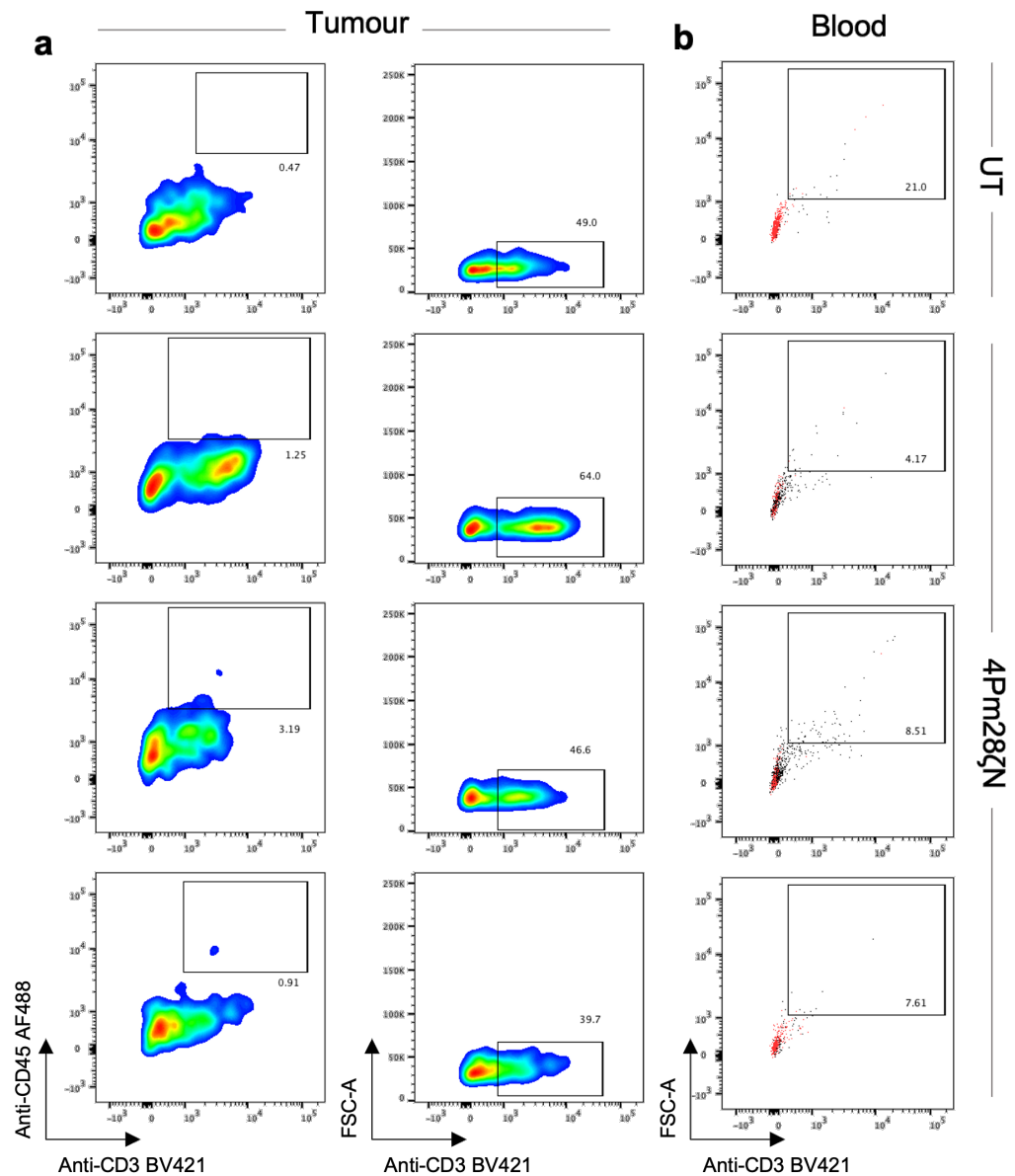
Figure 5.16: *Ex vivo* **quantitation of CAR T cells seven days post adoptive cell transfer.** Tumours were excised and blood samples were collected seven days post ACT for the *ex vivo* quantification of CAR T cells by flow cytometry. a) Flow cytometry plots depicting human $CD45^+CD3^+$ T cells infiltrating the treated xenograft tumours and b) circulating in blood. c) Quantitation of $CD3^+$ T cells from plots in a) using CountiBright beads. n=3/treated group, n=1/control group. Graphs represent mean ± SD.
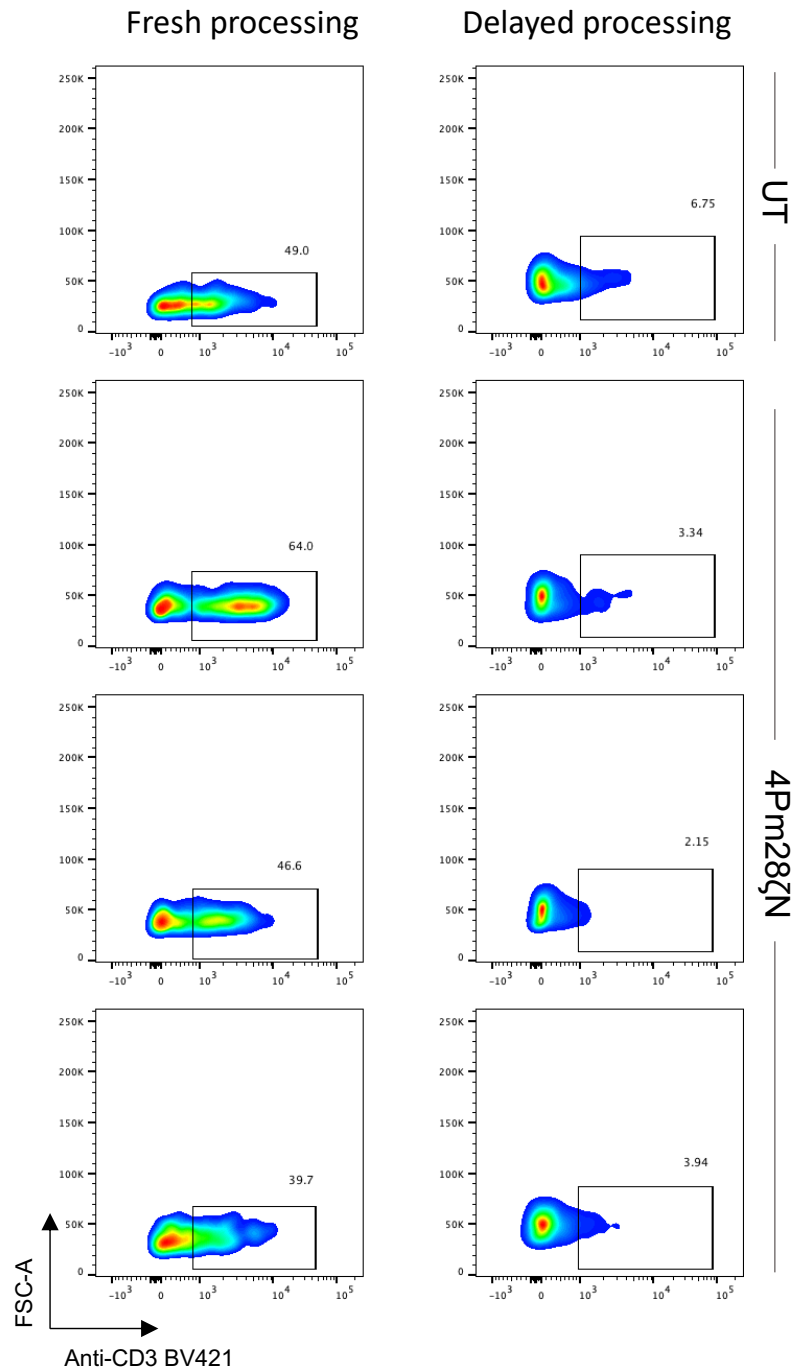
Figure 5.17: Comparison on the *ex vivo* detection of infiltrating CAR T cells from freshly processed tumours vs tumours preserved overnight prior processing. Flow cytometry plots comparing CD3 staining on tumour samples stained fresh on the same day of organ harvesting (left) vs tumour samples preserved overnight in MACS® Tissue Storage Solution and stained one day after organ harvesting (right). n=3/treated group, n=1/control group.
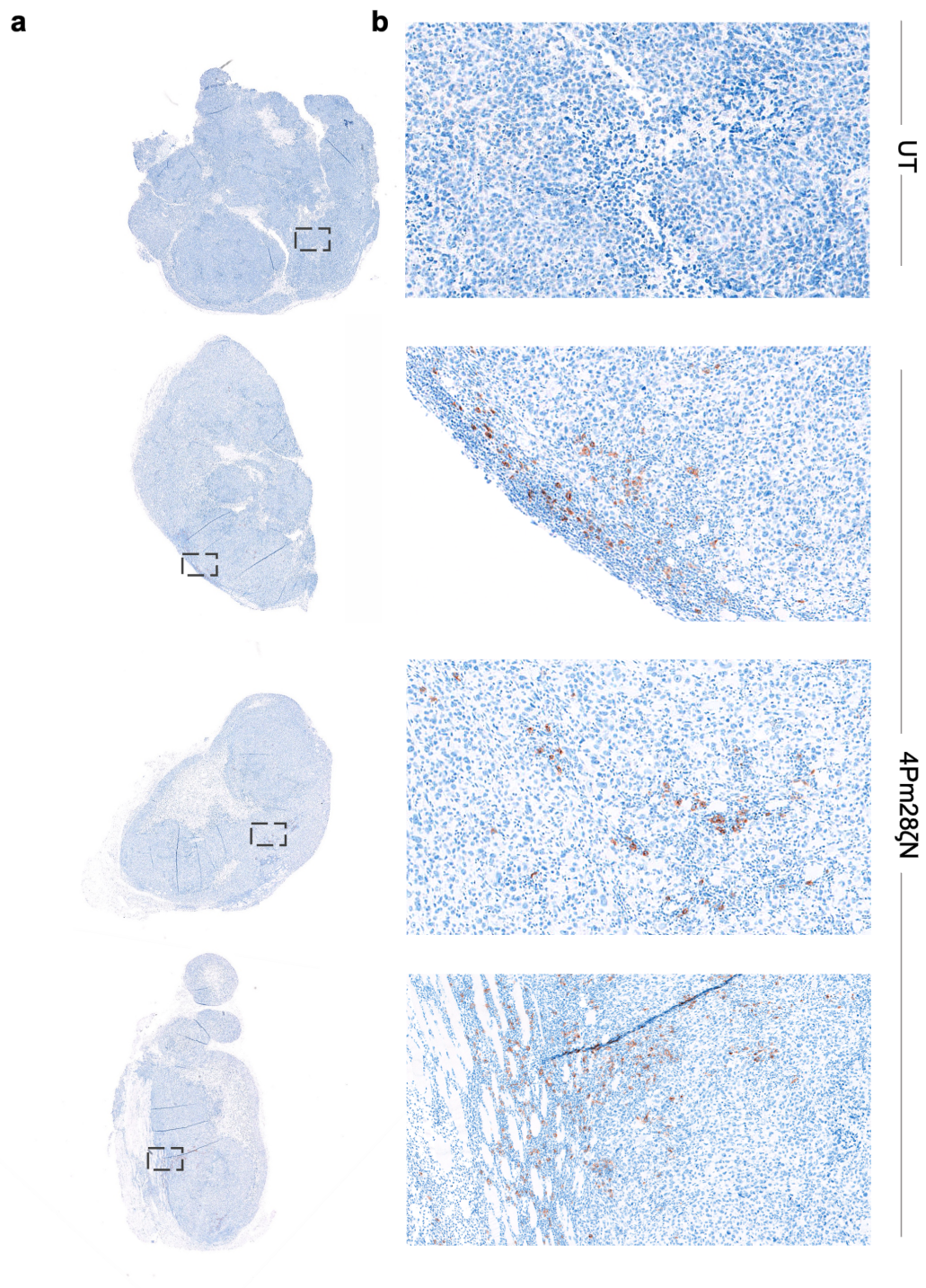
Figure 5.18: *Ex vivo* **analysis of infiltrating CD3 T cells by immunohistochemistry.** a) Paraffin embedded tumour slices were stained for human CD3. Scale bar: 1mm. b) Higher magnification images showing heterogenous infiltration of CD3 T cells in tumour tumours. Location of magnification shown by the black square on a). Scale bar : 0.25mm. n=3/treated group, n=1/control group.
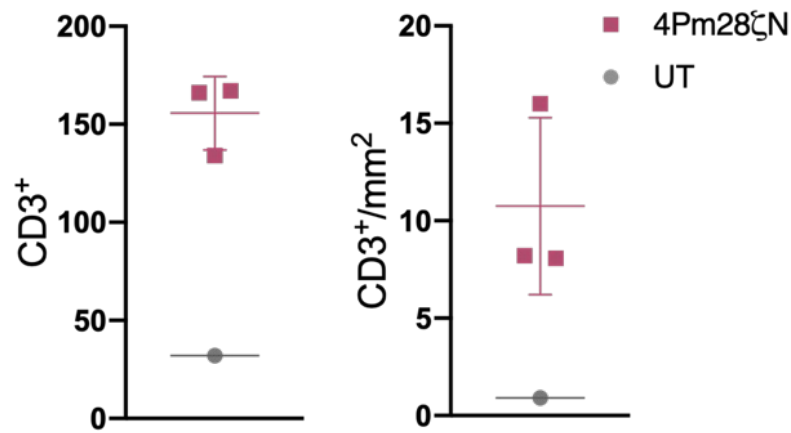
Figure 5.19: *Ex vivo* **quantitation of CD3 cells in tumour sections.** Average number of CD3 positive cells and concentration of $CD3^+$ per mm^2 of tissue quantified using QuPath software (Figure S 8.4). Graphs represent mean ± SD.

To further assess the correlation between tumour size and CAR T cell infiltration patterns, and to confirm the reproducibility of the two-day protocol, a second small study was performed. PLP-LT cells were inoculated s.c. in the shoulder area and after 11 days established tumours were treated with 4Pm28ζN T cells or untransduced cells. The average tumour size for tumours that received 4Pm28ζN T cells was 64 mm^3 (smaller than the 88mm^3 used in the previous study). Tumour growth was monitored through BLI twice per week, and tumour size was measured using a caliper three times a week. Eleven days post treatment, dynamic SPECT/CT images were acquired followed by *ex vivo* analysis of the tumours (Figure 5.20 a).

CAR T cell transduction was measured 24 hours prior to i.v. injection by flow cytometry. On the day of CAR T cell administration an uptake assay was performed, with 3% of the added $^{99m}TcO_4^-$ (0.33 MBq/ml) being internalised by the transduced PBMCs (Figure 5.20 b). All animals maintained their body weight after T cell administration (Figure 5.20 c). The control mouse that received untransduced T cells showed rapid tumour progression and

required sacrificing by day 17. There was no delayed tumour progression in the treated group, and excised treated tumours were heavier than the control (Figure 5.20 d-f).
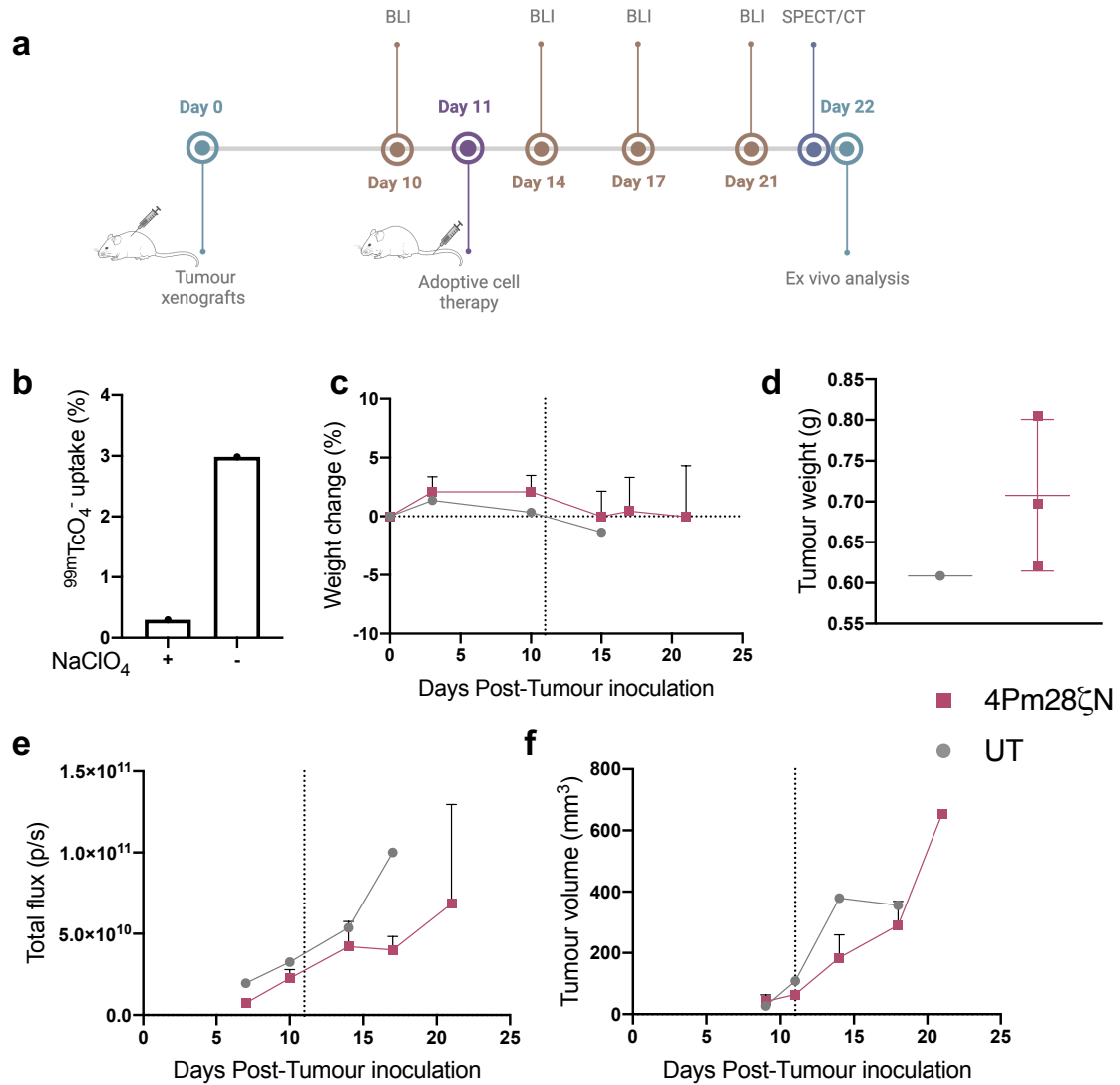
Figure 5.20: Tracking 4Pm28ζN T cells *in vivo*. a) Experimental plan. b) *In vitro* uptake levels of injected CAR T-cells incubated with $^{99m}TcO_4^-$ in the presence or absence of the inhibitor. c) Percentage body weight change. Dashed line represents day of CAR T cell injection. d) *Ex vivo* tumour weight measured on day 22 (11 days post ACT). e) Luciferase burden measured by BLI. f) Tumour volume was monitored by calliper measurements. n=3/treated groups, n=1/control group. Graphs represent mean ± SD.

Dynamic SPECT/CT imaging was performed eleven days post T cell administration and ROIs were drawn over the tumours to quantify $^{99m}TcO_4^-$ uptake by the CAR T cells homing

the tumours. Due to a global shortage of radiotracer and fast progression of the disease, the control mouse could not be imaged before it was sacrificed. Thus, for comparison purposes of the imaging and *ex vivo* data, the control group was taken from the previous experiment.

SPECT images showed accumulation of tracer along the tumour edges for all treated animals (Figure 5.21 a). One treated tumour showed an area of very high uptake, which could correspond to a large number of infiltrating CAR T cells clustering together. Total $^{99m}TcO_4^-$ quantified in the tumours that received 4Pm28ζN T cells was higher than for the control group (Figure 5.21 b). When data was normalised to the tumour size, two animals showed increased uptake over background (Figure 5.21 c).

These observations were corroborated by the dynamic data. Similar concentrations of tracer circulating in blood was observed between groups, with a rapid increase of circulating tracer after the i.v. tracer bolus followed by a two-phase exponential decay curve. Tracer in the treated tumours steadily increased after bolus injection and it reached a plateau after twenty minutes. There was clear accumulation of tracer above background in one of the treated animals, corresponding to the strong signal observed on the SPECT images. Uptake in the other two tumours was comparable to the perfusion levels quantified in the control tumour that received untransduced T cells (Figure 5.22).
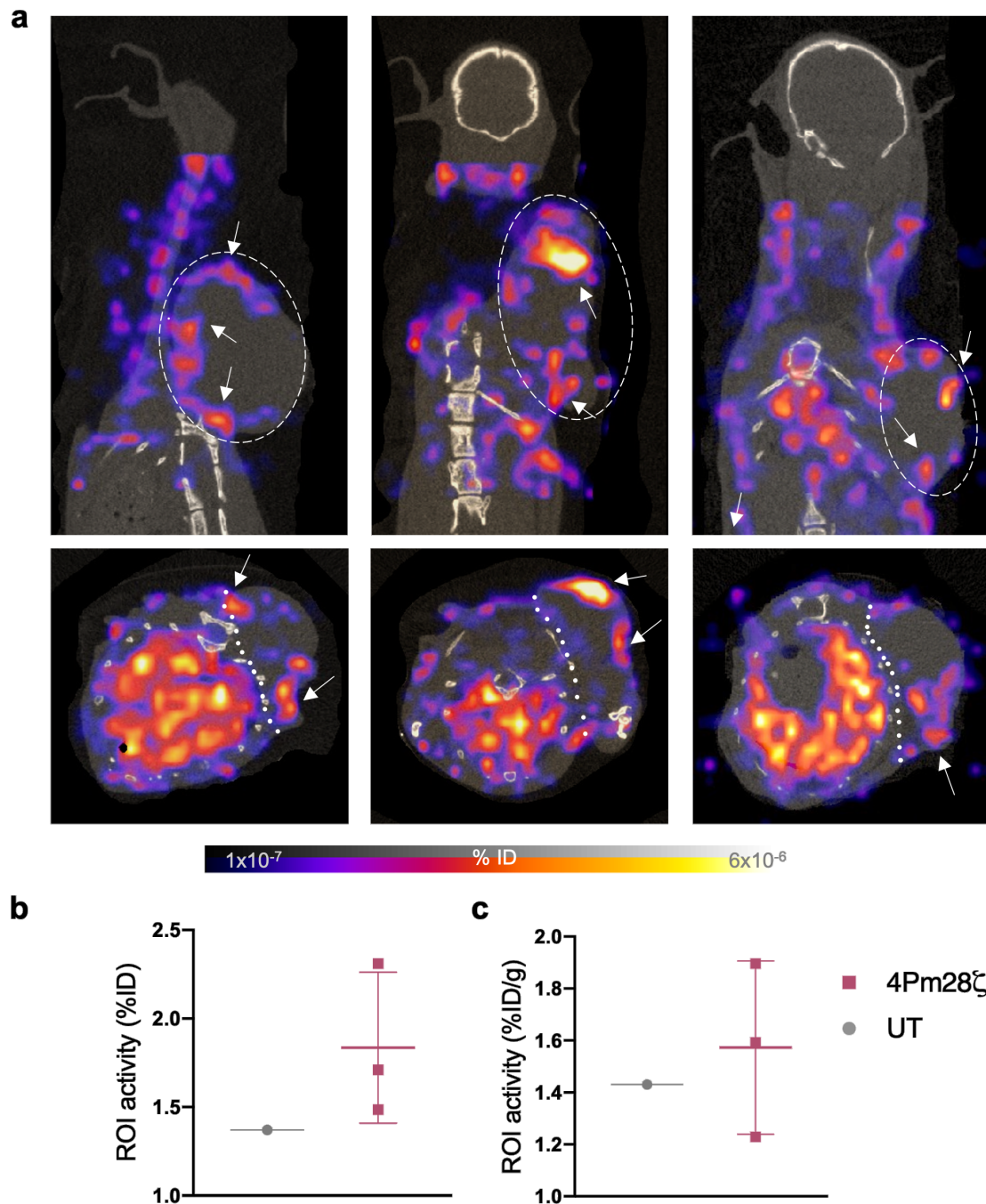
Figure 5.21: Infiltration of CAR T cells in treated tumours is observed through SPECT/CT. SPECT/CT images depicting CAR T cell homing to the tumour in treated animals on day 11 post ACT after administration of 10 MBq of $^{99m}TcO_4^-$. Tumour borders are defined by the white dotted line. Arrows point signal from CAR T cells. $^{99m}TcO_4^-$ uptake was quantified from the SPECT images as percentage of the injected dose (b) or normalised to gram of tissue (c). Injected dose = 10 MBq of $^{99m}TcO_4^-$. n=3/treated group, n=1/control group from previous experiment. Graphs represent mean ± SD.
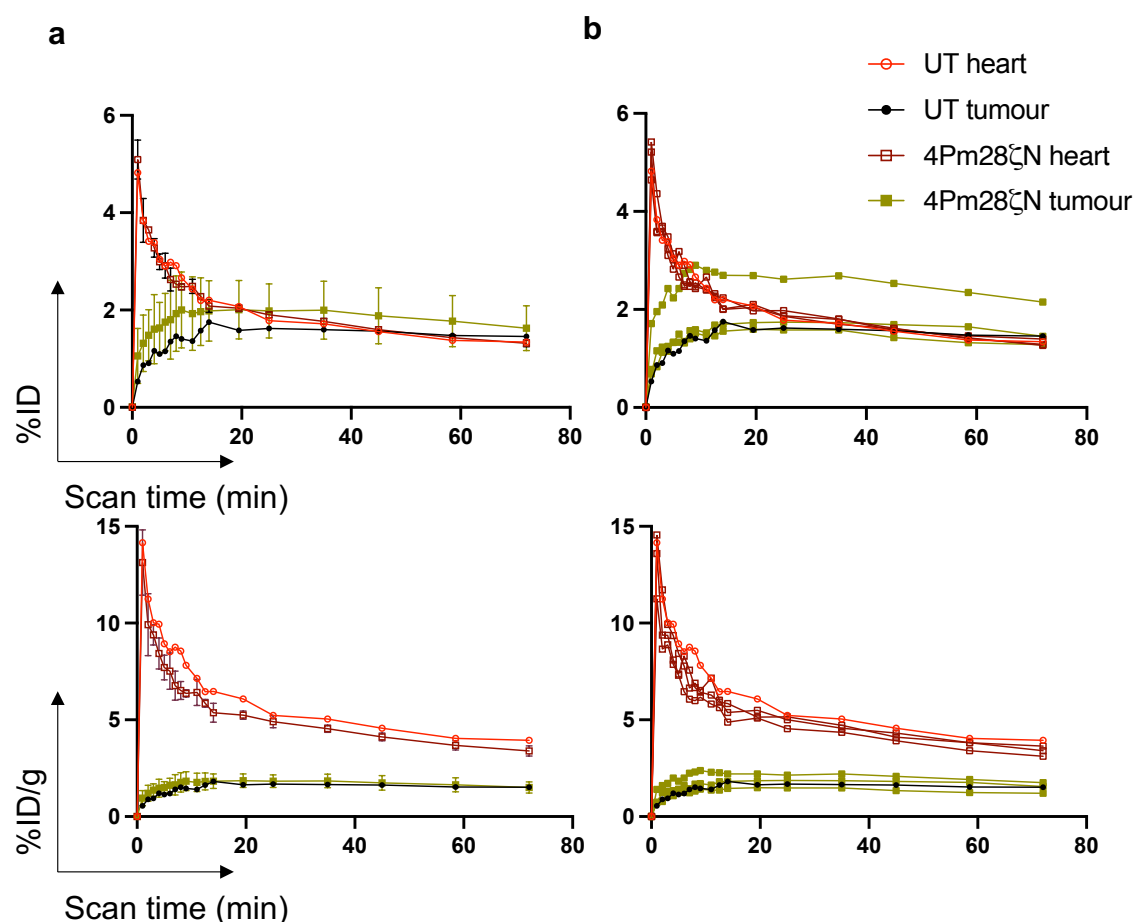
Figure 5.22: Time-activity curves for $^{99m}TcO_4^-$ kinetics on SPECT scans at 11 days post ACT. a) Average and b) individual 70-minute time course of tracer accumulation in heart and tumour of treated (square, n=3) and control (circle, n=1) animals after administration of 10 MBq of $^{99m}TcO_4^-$. Animals were imaged eleven days post administration of CAR T cells or PBS. Solid shapes represent the activity concentration in the tumour and open shapes represent the activity concentration in the heart. Uptake is expressed as the percentage of injected dose (%ID) or normalised per gram (%ID/g) of tumour tissue or heart tissue. Graphs in (a) represent mean ± SD.

Following the dynamic acquisition, animals were sacrificed, and organs and tumours were collected for *ex vivo* analysis. Radioactivity uptake in the samples was measured using a gamma counter. The tumours from animals that received 4Pm28ζN T cells or untransduced T cells showed similar uptake. *Ex vivo* biodistribution showed radiotracer accumulation in endogenous hNIS expressing organs, i.e., stomach and salivary glands (Figure 5.23).
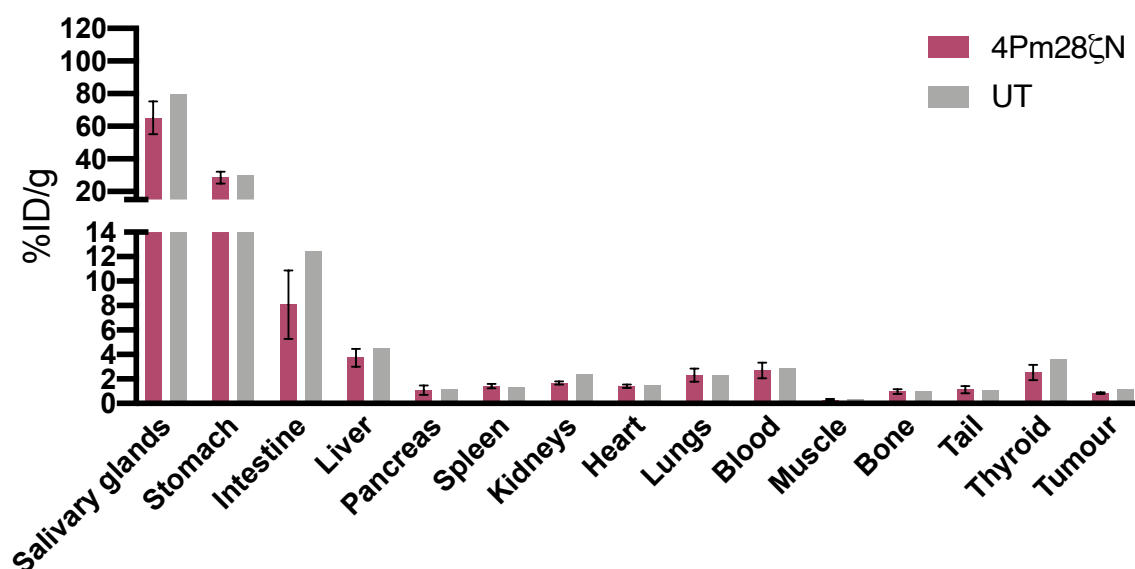
Figure 5.23: *Ex vivo* **tracer concentration in organs.** *Ex vivo* biodistribution of tracer from organs harvested 11 days post ACT after administration of 10 MBq of $^{99m}TcO_4^-$. n=3/treated group, n=1/control group from previous experiment. ACT = adoptive cell transfer. Graphs represent mean ± SD.

Following the same protocol as before, one third of the tumour was fixed in formalin to carry out immunohistochemical analysis, another third of the tumour was stored in MACS® Tissue Storage Solution overnight to delay tumour processing and the last third of the tumour was disassociated and stained for CD3 to quantify infiltrating CAR T cells by flow cytometry (Figure 5.11). $CD45^+CD3^+$ double positive cells were detected in all treated tumours that received 4Pm28ζN T cells, there was also clear accumulation of $CD3^+$ cells within the tumours (Figure 5.24 a). Quantified CD3 positive cells by flow cytometry was above background for two of the three treated tumours, ranging from 5,000 to 18,000 T cells/gram of tissue processed (Figure 5.24 c). A small number of circulating CAR T cells was detected in blood from a treated animal (Figure 5.24 b).

The next day, tumour sections preserved in MACS® Tissue Storage Solution were processed, stained for CD3 and analysed by flow cytometry. Comparable staining patterns
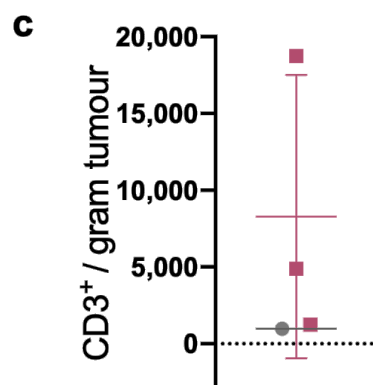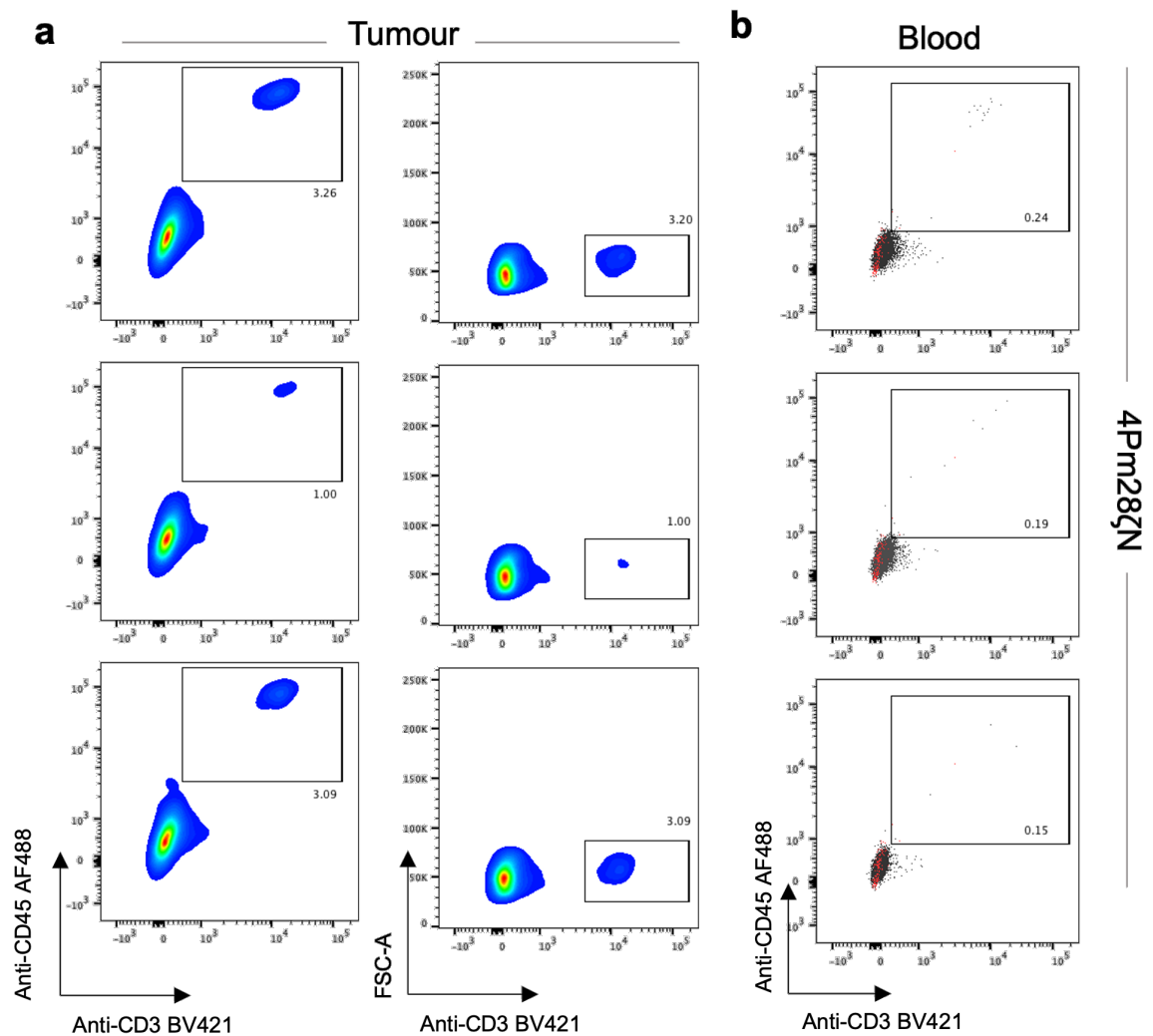
Figure 5.24: *Ex vivo* **quantitation of CAR T cells in tumours and blood.** Flow cytometry plots depicting human CD3 T cells within the harvested xenografts (a) and circulating in blood (b). c) Quantitation of $CD3^+$ T cells from plots in a) using CountiBright beads. n=3/treated group, n=1/control group from previous experiment. Graphs represent mean ± SD.

were observed after processing the tumour section stored overnight in MACS® Tissue Storage Solution (Figure 5.25), suggesting tumour processing can be safely delayed.
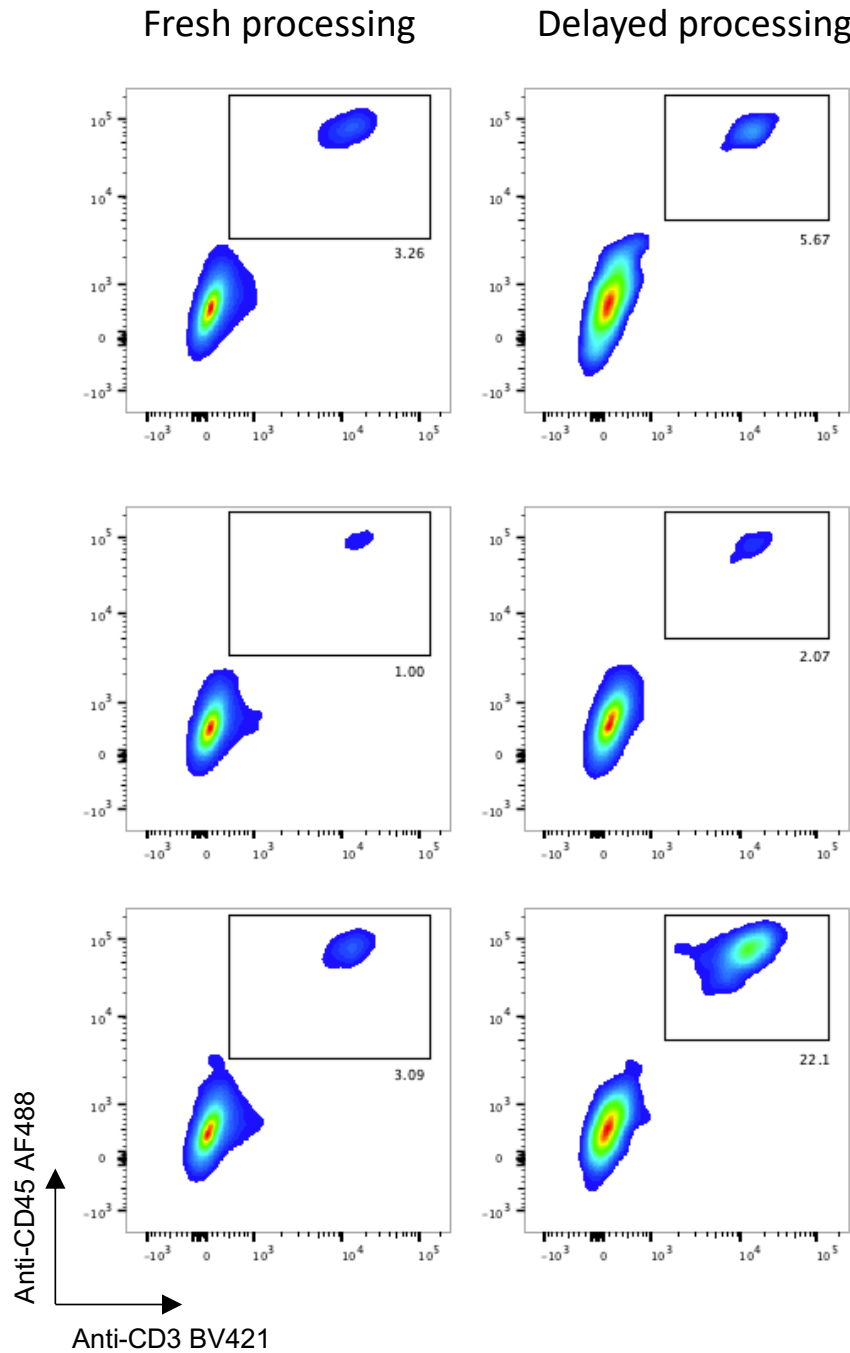
Figure 5.25: CD3 staining on tumours processed after harvesting or preserved overnight. Flow cytometry plots comparing CD3, CD45 double staining on tumour samples stained fresh after harvesting (left) vs delayed processing and staining (right). n=3/treated group.
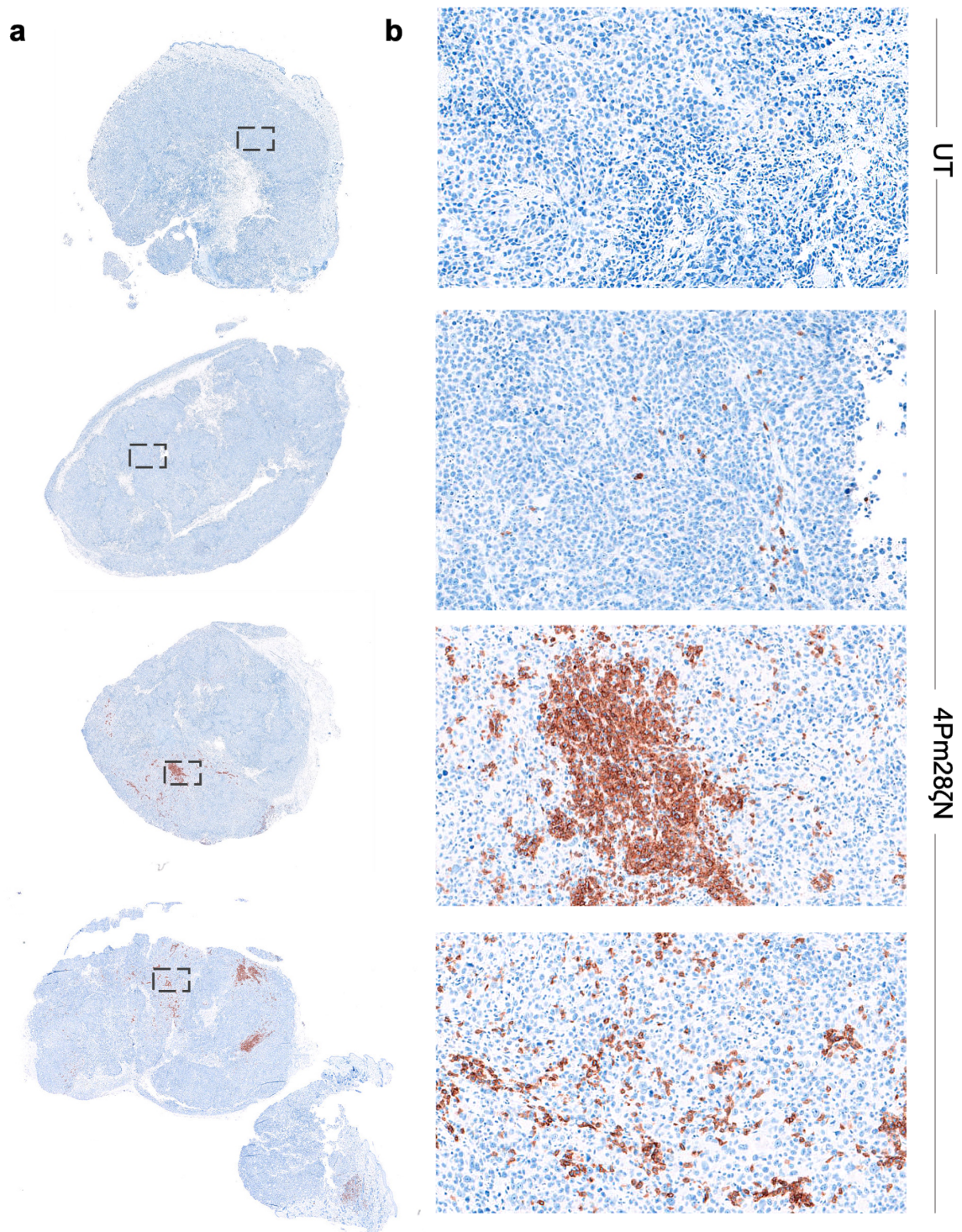
Figure 5.26: *Ex vivo* **analysis of infiltrating CD3 T cells by immunohistochemistry.**
a) Paraffin embedded tumour slices were stained for human CD3. Scale bar: 1mm. b) Higher
magnification images showing heterogenous infiltration of CD3 T cells in tumour tumours.
Location of magnification shown by the black square on a). Scale bar: 0.25mm. n=3/treated
group, n=1/control group.

Immunohistochemistry staining on the remaining tumour tissue corroborated the presence of infiltrating CAR T cells in the 4Pm28ζN treated tumours in line with the tracer distribution pattern observed in the SPECT/CT images (Figure 5.21). There was no positive CD3 staining in the control tumour (Figure 5.26). In contrast to the previous experiments, CD3 positive cells were not only observed around the tumour edge but were also able to penetrate the tumour clustering around the tumour vessels (Figure 5.27).
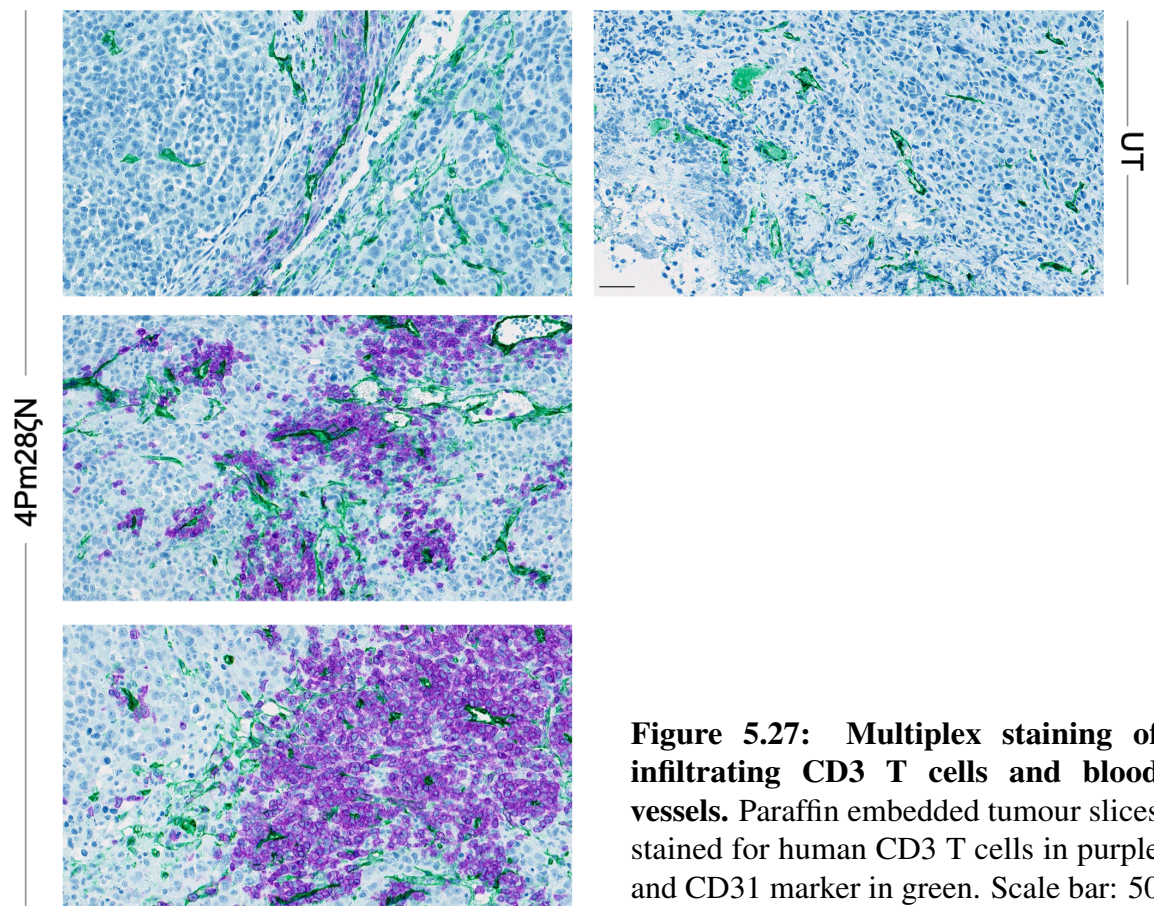
Figure 5.27: Multiplex staining of infiltrating CD3 T cells and blood vessels. Paraffin embedded tumour slices stained for human CD3 T cells in purple and CD31 marker in green. Scale bar: 50 μm. n=3/treated group, n=1/control group.

Quantitative analysis of the tumour sections using QuPath measured an average of 6,000 $CD3^+$ T cells, with an average of 150 cells per mm^2 (Figure 5.28 a). Blood vessel density was slightly higher for the treated group compared to the control tumour (Figure 5.28 b).

There was positive weak correlation (r = 0.6) between the number of infiltrating CAR T cells and blood vessel density (Figure 5.28 c).
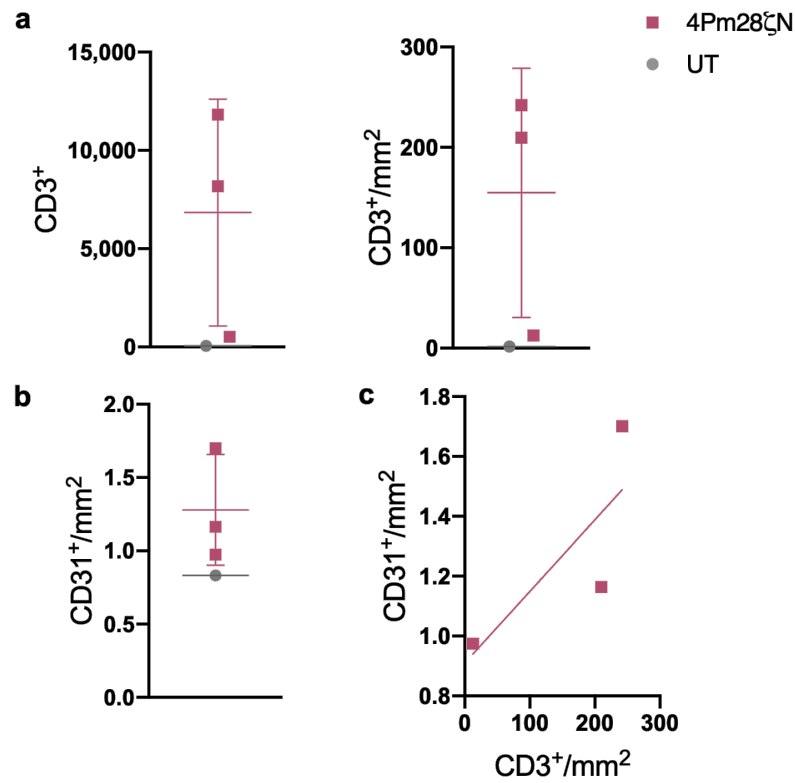
Figure 5.28: *Ex vivo* quantitation of CD3 cells in tumour sections. a) Average number of CD3 positive cells and concentration of CD3 per mm^2 of tumour quantified from sections in Figure 5.26. b) Blood vessel density quantified from sections in Figure 5.27. Quantification was performed in Qupath (Figure S 8.4). c) Correlation between blood vessel density (y-axis) and concentration of infiltrating CD3 T cells (x-axis). r = 0.6. n=3/treated group, n=1/control group. Graphs represent mean ± SD.

5.4 Summary

Taking together, the results from the last three experiments discussed in sections 5.2 and 5.3 demonstrate clear variability in the degree of CAR T cell infiltration between animals, with CAR T cells mainly gathering around the tumour periphery as shown by the SPECT/CT images.

These experiments were named I, II and III corresponding to the experiments described in Figure 5.4, Figure 5.13 and Figure 5.20, respectively. As described in chapter 3, $^{99m}TcO_4^-$ uptake is donor-dependent, thus, to compare the results from these three experiments, quantified SPECT signals were normalised to the uptake level shown by the injected 4Pm28ζN T cells (Figure 5.29).
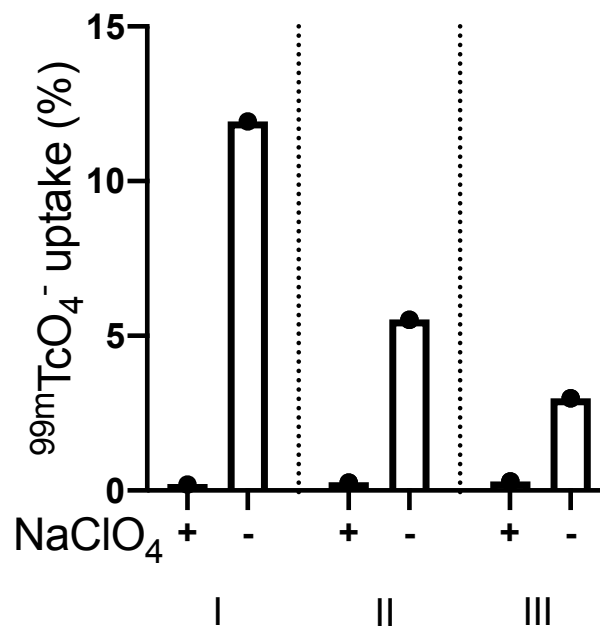
Figure 5.29: ^{99m}**TcO$_4^-$ uptake by the inoculated CAR T cells.** On the day of ACT, PBMCs were incubated with 0.33 MBq/ml ^{99m}TcO$_4^-$ in the presence or absence of the inhibitor. I, II, III = experiments described on Figure 5.4, Figure 5.13 and Figure 5.20, respectively. ACT=adoptive cell transfer

Tumour volume at the time of treatment inversely correlated to the degree of CAR T cell infiltration. Smaller tumour volumes at the time of 4Pm28ζN T cell injection, led to higher

number of CAR T cells infiltrating the tumours. CAR T cell infiltration was assessed by SPECT/CT image derived quantitation of $^{99m}TcO_4^-$ uptake within the tumours and compared to the number of CD3 positive cells present in the tumour slices.

In experiment I, tumours reached 180 mm^3 before treatment. $^{99m}TcO_4^-$ uptake at the tumour site was just above 2% of the injected dose with similar uptake levels observed per gram of tumour tissue. However, if tumours were treated at 85 mm^3 (experiment II), there was a 1.7-fold increase in total tumour uptake and 2.2-fold increase in the uptake quantified per gram of tissue, when compared to experiment I. The inverse correlation between tumour size and tumour uptake was further demonstrated in experiment III, in which tumours were about 65 mm^3 before treatment. There was a higher infiltration of CAR T cells in these tumours leading to a 2.8-fold increase in the total amount of tracer within the tumour and a 2.5-fold increase if uptake was quantified per gram of tissue, when compared to experiment I (Figure 5.30).
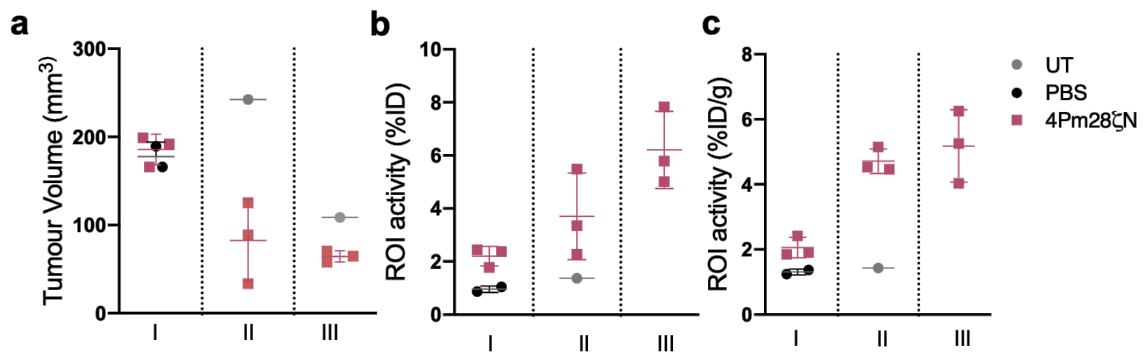
Figure 5.30: Tumour volume at the time of treatment inversely correlated to tumour uptake. a) Tumour volume before treatment. $^{99m}TcO_4^-$ uptake in the entire tumour (b) or per gram of tumour tissue (c) quantified from SPECT images and normalised between donors based on their *in vitro* $^{99m}TcO_4^-$ uptake. I, II, III = experiments described on Figure 5.4, Figure 5.13 and Figure 5.20. Graphs represent mean ± SD.

Likewise, staining of tumour slices using immunohistochemistry also showed a higher accumulation of CD3$^+$ cells if tumours were small before treatment. There was a higher number of infiltrating CD3$^+$ cells in tumours treated in experiments II and III, as demonstrated
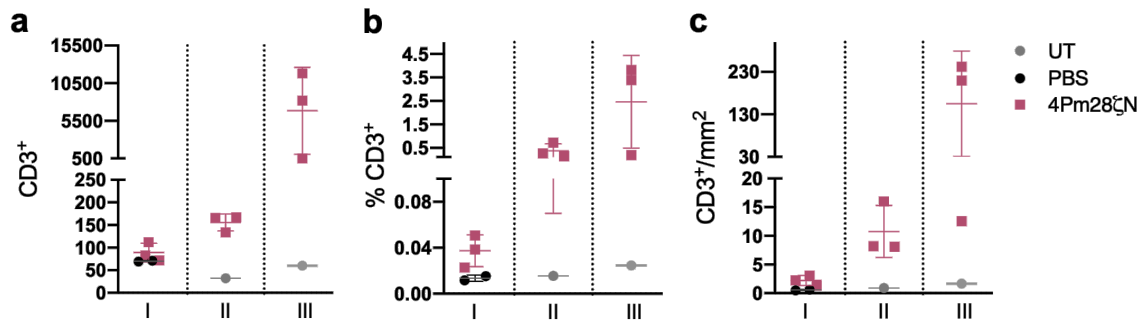
Figure 5.31: Tumour volume at the time of treatment inversely correlated to the number of infiltrating CD3 T cells stained by immunohistochemistry. a) Total number of CD3 positive cells stained per tumour. b) Percentage of CD3 positive over total number of cells detected in the tumour slice. c) Number of CD3 positive cells per tumour area. I, II, III = experiments described on Figure 5.4, Figure 5.13 and Figure 5.20, respectively. Graphs represent mean ± SD.

by the increase in the percentage of $CD3^+$ cells within the total number of cells detected in the tumour slices, the total number of $CD3^+$ cells stained in a tumour slice and the concentration of $CD3^+$ cells per area of tissue (Figure 5.31). The differences where more striking when comparing experiment I (average tumour volume of 180 mm^3) to experiment III (average tumour volume of 64 mm^3).

This data demonstrates that initial tumour burden is a key factor regulating CAR T cell infiltration. Although CAR T cell infiltration showed great intra- and inter-experiment variability, all SPECT/CT images showed heterogenous tracer accumulation, which was further confirmed by immunohistochemistry where the $CD3^+$ T cells were clustering around tumour vessels.

Tumour heterogeneity presents two challenges for the development of a compartmental model. Firstly, it brings the method used to quantify tumour uptake into question. The $^{99m}TcO_4^-$ uptake by the tumours was measured by manually delineating ROIs encompassing the entire tumour based on CT anatomical data. The results were presented as total uptake by the entire tumour (%ID) or the uptake per gram of tissue (%ID/g). Presenting the data as total uptake introduces a bias due to the influence of tumour volume. As the size of

the ROI increases,so does the amount of radioactive tissue being assayed leading different total tumour uptake for different size tumours. Therefore, to normalise for tumour size, it is common practice to express the uptake as a concentration by dividing the quantified radioactivity by gram of tissue or by volume. However, this approach dilutes the true signal due to the heterogeneity of CAR T cell infiltration and the resulting SPECT signal. The total volume of the ROI includes areas with minimal or no uptake, which can mask differences in uptake between control and treated animals, hindering the accurate assessment of CAR T cell infiltration. As an alternative to quantifying uptake in the entire tumour volume, the use of thresholding methods can be employed to quantify only voxels above a certain level of radioactivity, thereby avoiding the dilution of the true signal.
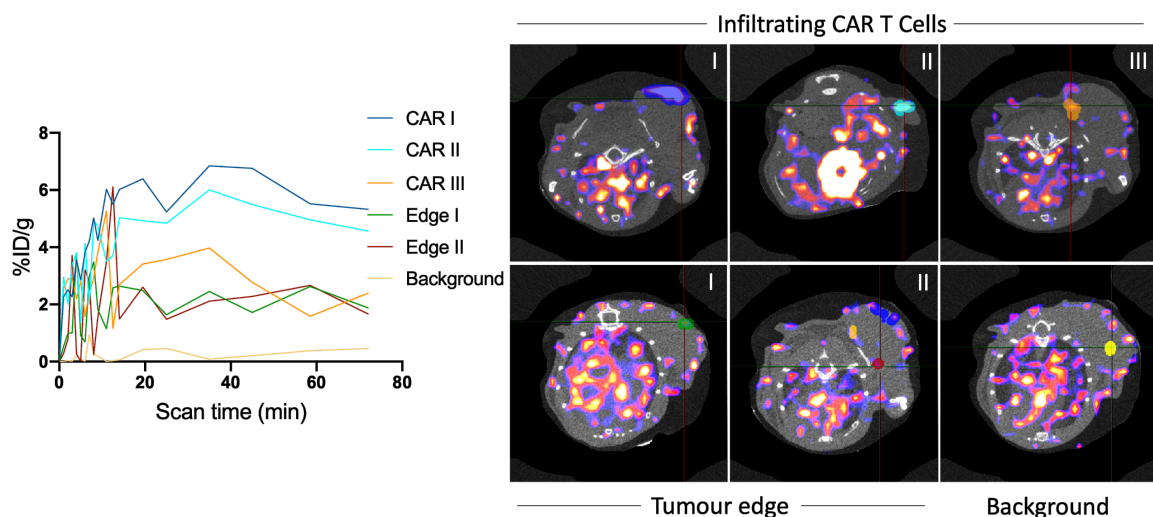
Figure 5.32: Distinct radioactivity uptake patterns within treated tumour. Quantified time-activity curves for different areas of the same treated tumour after administration of 10 MBq of ^{99m}TcO$_4^-$. ROIs were drawn over different areas of a treated tumour measuring signal from infiltration of CAR T cells, signal around the tumour edge or in an area with no visible uptake.

Secondly, compartmental models assume homogeneous uptake within a specific compartment and do not account for concentration gradients. However, as depicted in Figure 5.32, uptake levels can significantly vary between areas of the same tumour, further

emphasising the necessity of employing thresholding approaches to compare uptake levels within homogenous areas inside the tumour.

Despite the challenges associated with heterogenous tumour uptake, these experiments yielded informative results regarding the feasibility of delaying tumour processing. If CAR T cell infiltration is restricted, delaying the processing of tumours may impact detectability. However, with enhanced CAR T cell infiltration, it is possible to safely delay tumour processing without compromising the detection of infiltrating CAR T cells by flow cytometry. Additionally, these experiments proved beneficial in optimising the protocols for *in vivo* $^{99m}TcO_4^-$ SPECT/CT imaging and *ex vivo* analysis.

Chapter 6

Towards the development of a non-invasive quantitation method

After optimising the protocols for the dynamic imaging of CAR T cells *in vivo* and the *ex vivo* analysis of infiltrating CAR T by flow cytometry, an *in vivo* study was performed to study the feasibility of modelling and quantifying CAR T cell infiltration non-invasively through a two-compartment model. The optimised experimental protocol was designed to take place over two consecutive days. On day 1, animals underwent dynamic SPECT/CT imaging followed by organ biodistribution. Radioactivity uptake in the organs was assessed with a gamma counter and treated tumours were then stored in MACS® Tissue Storage Solution overnight while control tumours were fixed in formalin. On day 2, treated tumours were processed to a single cell solution and stained for surface markers to quantify number of infiltrating CAR T cells by flow cytometry. On the other hand, control tumours were embedded in paraffin, sectioned, and stained for immunohistochemical analysis (Figure 6.1). By performing the protocol over two days, more animals could be included per group increasing the study's statistical power.
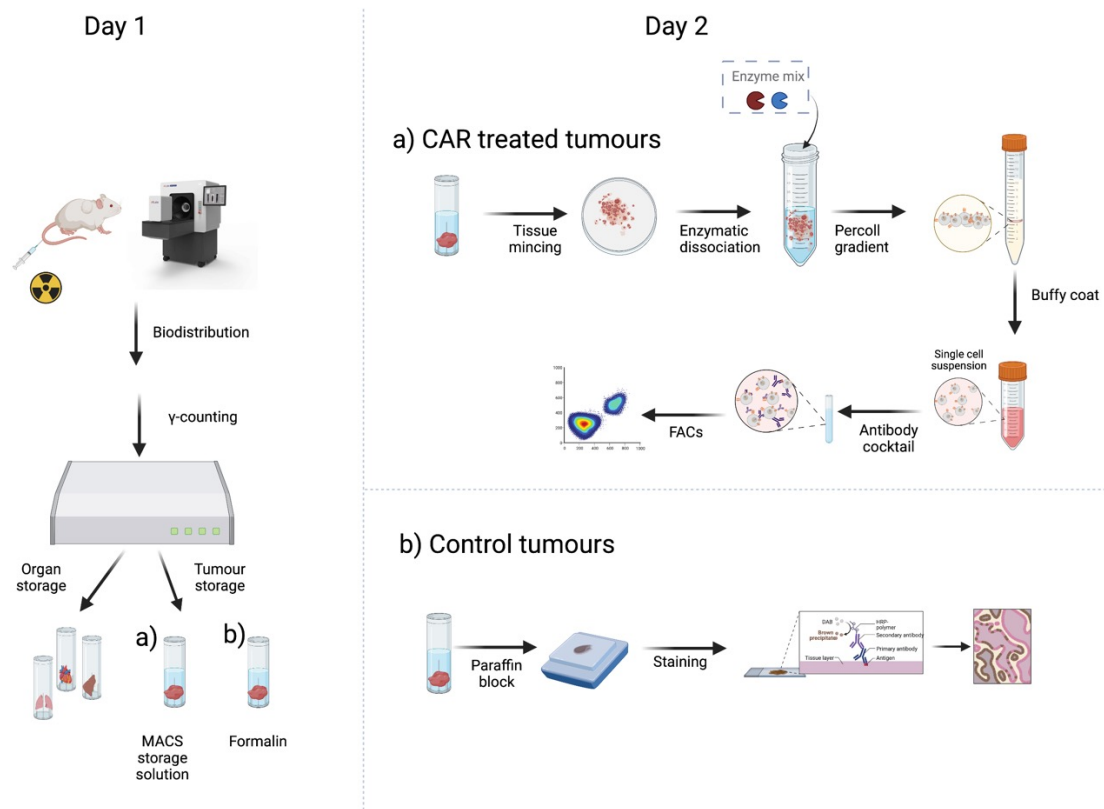
Figure 6.1: Schematic of optimised experimental plan. Dynamic SPECT imaging was performed at the established time point followed by organs and tumour *ex vivo* gamma counting (day 1). a) Tumours from treated animals were stored in MACS® storage solution and the following day (day 2) tumours were processed for staining and detection of CAR T cells by flow cytometry. b) Control tumours were fixed in formalin and the following day (day 2) tumours were embedded in paraffin blocks for downstream sectioning and staining.

6.1 *In vivo* quantitation of CAR T cells

NSG mice were inoculated with PLP-LT tumour cells s.c. in the shoulder area. As shown in the previous chapter, there was an inverse correlation between the initial tumour volume and the number of infiltrating CAR T cells detected at the end of the experiment. Thus, I concluded the optimal timing for ACT was 9 days post tumour inoculation when average tumour size was around 68 mm^3. Animals were randomized into 5 groups, two control groups receiving PBS or untransduced T cells; and three treated groups receiving 4Pm28ζN T cells. Tumour growth was monitored through BLI twice per week, and tumour size was

measured using callipers three times a week (Figure 6.2 a). CAR T cell transduction, based on myc tag and hNIS surface expression, was measured 24 hours prior to i.v. injection by flow cytometry. On the day of CAR T cell administration an uptake assay was performed, with 2.25% of the added $^{99m}TcO_4^-$ being internalised by the transduced PBMCs (Figure 6.2 b). For all animals, body weight was maintained after treatment (Figure 6.2 c). 4Pm28ζN T cells did not exhibit any therapeutic effect when compared to the control groups, as indicated by the higher luciferase burden and tumour volume measured by BLI and calliper, respectively (Figure 6.2 e & f). Additionally, there was a progressive increase in tumour weight (Figure 6.2 d).

Dynamic SPECT/CT imaging was performed at the established time points (Figure 6.2 a). Time frames were binned together after reaching steady state (30 to 70 min post tracer injection) and radioactivity within the tumours was quantified by placing ROIs in the tumour and heart. Non-specific tracer signal around the tumour edges was observed in the tumours of control animals treated with PBS or untransduced cells. Distinct accumulation patterns were observed in treated tumours with the signal intensifying over time. Hot spots within the tumours were hypothesised to be CAR T cells clustering around tumour vessels within the treated tumours (Figure 6.3 a). These observations were further supported by quantitative measurement of radioactivity in the tumour regions. Control tumours that received untransduced cells or PBS showed minimal accumulation of radiotracer (below 1% of the injected dose), indicating tumour perfusion. The average total uptake (%ID) in the treated tumours exceeded the levels of perfusion at the studied time points. Higher tracer accumulation was measured on day 12 and day 14 post CAR T cell, compared to day 9, indicating higher number of CAR T cells in the tumours. To account for the increasing tumour volume over time, tumour uptake was normalised to the ROI volume (%ID/g). Although, differences in uptake between the treated groups decreased, they remain above perfusion levels at all time points (Figure 6.3 b).
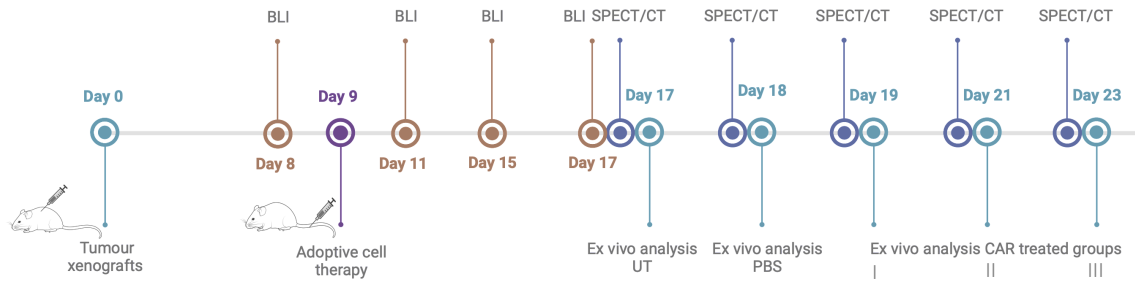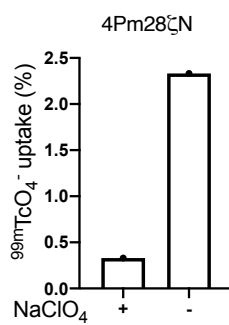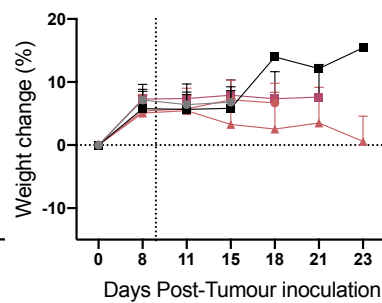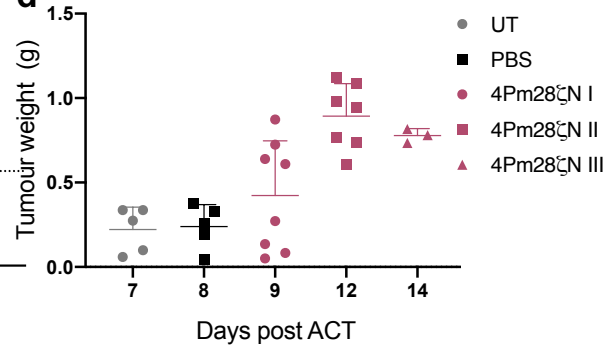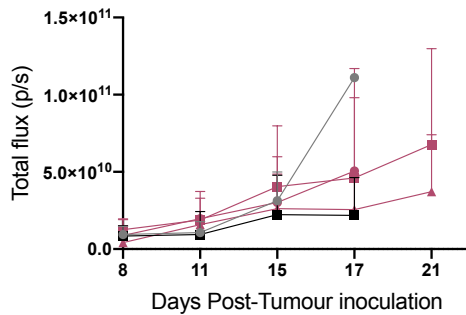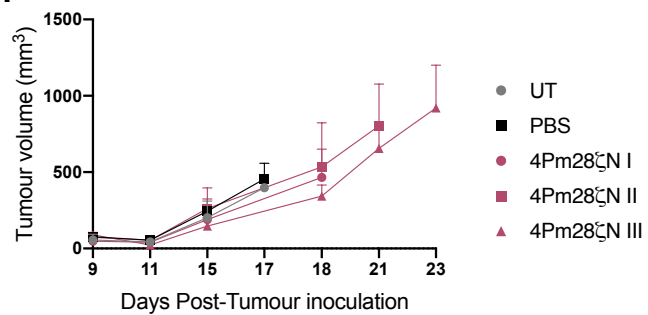
Figure 6.2: Treating tumour xenografts with 4Pm28ζN T cells. a) Experimental plan. b) *In vitro* uptake levels of injected CAR T cells incubated with 0.33 MBq/ml $^{99m}TcO_4^-$ in the presence or absence of the inhibitor. c) Percentage body weight change. Dashed represents ACT day. d) *Ex vivo* tumour weight measured on last time point. e) Tumour burden measured by BLI. f) Tumour volume was monitored by calliper measurements. Animals treated with 4Pm28ζN were culled at different time points (I,II,III) for downstream *ex vivo* analysis. n=3-8/treated groups, n=5/control groups. ACT: adoptive cell transfer. Graphs represent mean ± SD.
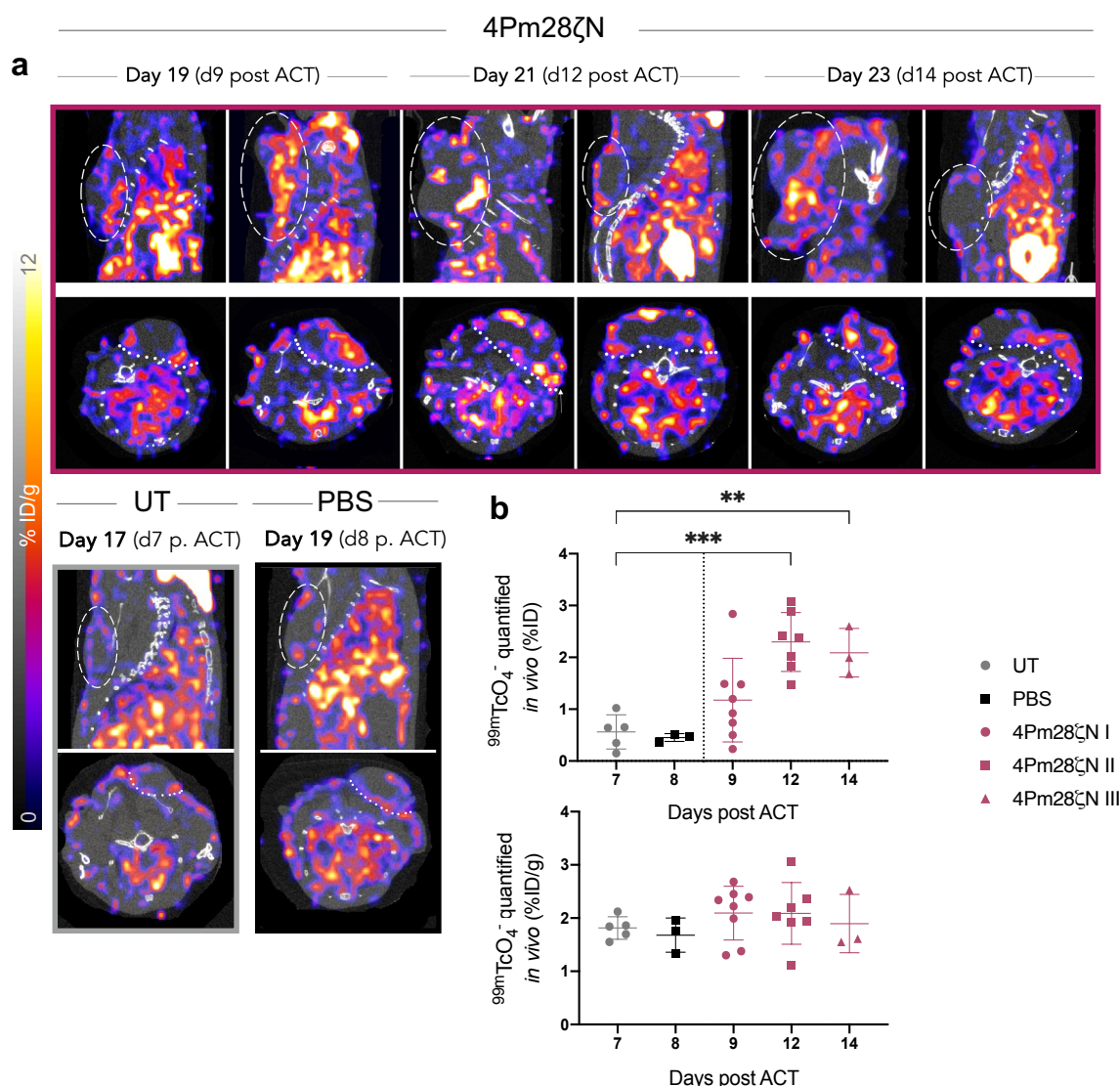
Figure 6.3: Infiltration of CAR T cells in treated tumours observed through SPECT/CT imaging. a) Representative sagittal (top) and transverse (bottom) SPECT/CT images depicting CAR T cell homing to the tumour in treated animals (magenta frame) at different time points after administration of 10 MBq of $^{99m}TcO_4^-$. Perfusion signal in control animals on day 7 (UT, grey frame) or day 9 (PBS, black frame) post ACT after administration of 10 MBq of $^{99m}TcO_4^-$. Tumour borders are defined by the white dotted line. b) $^{99m}TcO_4^-$ uptake was quantified from the SPECT images in a) as percentage of the injected dose (%ID) or normalized to tumour volume (%ID/g). SPECT/CT images from all animals are shown in Figure S 8.5, 8.6 & 8.7. PBS (n=3), UT = untransduced T cells (n=5), 4Pm28ζN I = day 9 post ACT (n=7), 4Pm28ζN II = day 12 post ACT (n=7) and 4Pm28ζN III = day 14 post ACT (n=3). p. ACT = post adoptive cell transfer. Graphs represent mean ± SD.

To quantify tracer concentration concurrently in heart and tumour, the data was quantified by placing ROIs in the tumour and heart to extract the time-activity curves. For this purpose, the three different CAR T treated groups were pooled together. Tracer concentration in blood was similar between groups, achieving maximum concentration shortly after tracer bolus followed by a two-phase decay curve (Figure 6.4 a). Tracer concentration in the tumour steadily increased after tracer bolus, the treated tumours showing concentrations above control tumours, indicating accumulation of tracer by the CAR T cells above perfusion levels. Intra-group variability was large making the difference in uptake between CAR-treated and control groups not significant (Figure 6.4 b).
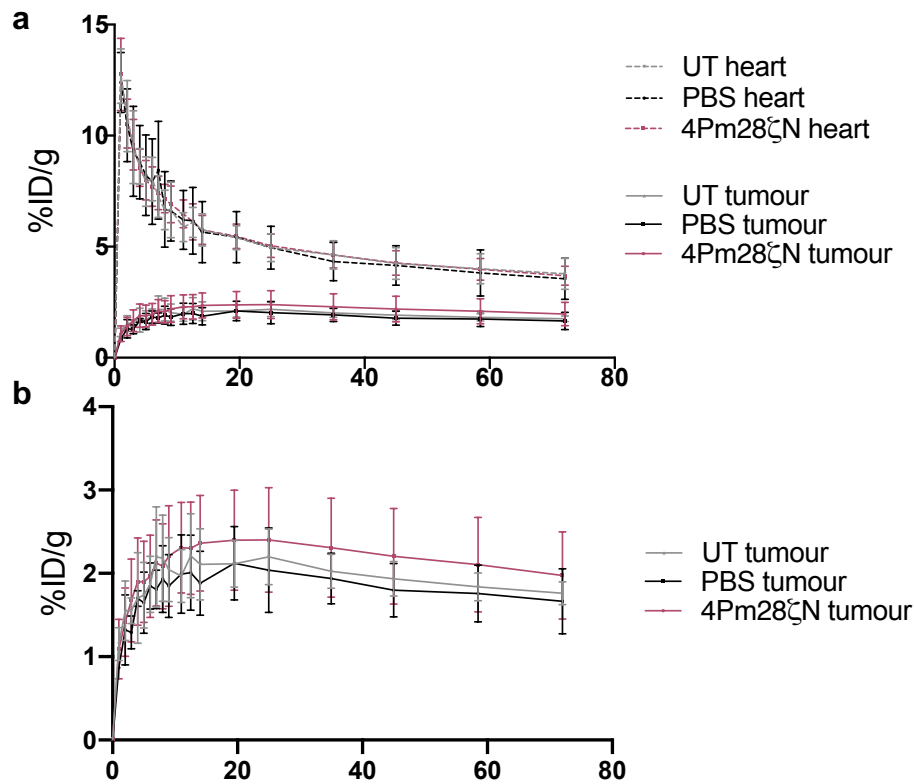
Figure 6.4: Heart and tumour time-activity curves of $^{99m}TcO_4^-$ in control and CAR treated animals. a) Average 70-minute time-activity curves from the hearts (dashed lines) and tumours (solid lines) of animals treated with PBS, UT or 4Pm28ζN CAR T cells following administration of 10 MBq of $^{99m}TcO_4^-$ on the day of imaging. b) Zoom-in of the tumour time-activity curves shown in a). n=18/4Pm28ζN, n=5/ UT and n=3/PBS. Graphs represent mean ± SD.

In order to model the SPECT dynamic data, two models were proposed. The first model was defined as a reversible two-compartment model consisting of a blood compartment and a tumour compartment (Figure 6.5 a). The second model subdivided the tumour compartment into two compartments, representing unbound tracer in the tumour tissue and tracer internalised by the CAR T cells, resulting in a three-compartment irreversible model (Figure 6.5 b).
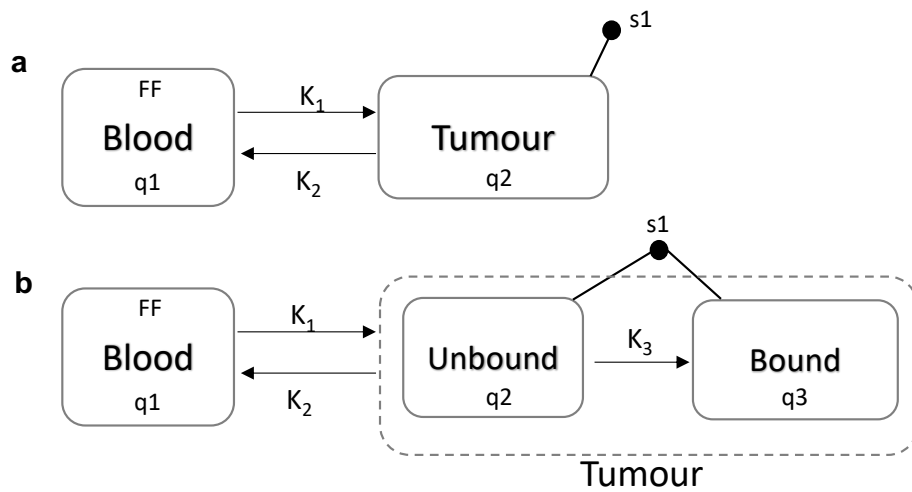
Figure 6.5: Compartmental models built in SAAMII software. a) The blood compartment, q1, exchanges tracer with the tumour compartment, q2, at the rate defined by K_1 and K_2. The blood compartment was fixed with a forcing function (FF) and the quantified tumour signal, s1, was fitted to the model. b) The tumour compartment is formed by two compartments representing the unbound and bound fractions, with the exchange rate defined by K_3.

Control tumours were modelled based on the two-compartment model as there is no specific uptake within the tumours. To determine which of the two models more accurately described the quantification of tracer kinetics in the treated animals, graphical methods were firstly applied to the dynamic data. Graphical methods rely on the transformation of the dynamic data to exploit the status of equilibrium of the tracer. The plots will result in a linear trend after equilibrium if using the appropriate model, allowing extraction of the parameter of interest from the slope. The main graphical methods are the Logan plot and the Patlak plot[144]. The former was originally developed to quantify reversible receptor

binding (i.e, the proposed two-compartment model) and the slope estimates the total volume of distribution (V_T), which equals the ratio of K_1/K_2, and represents the ratio of $^{99m}TcO_4^-$ concentration between the tumour and blood at equilibrium. The latter is used for the modelling of irreversible uptake within a tissue (i.e, the proposed three-compartment model) and the plot estimates the irreversible uptake rate constant K_i, which equals $K_1K_3/(K_2+K_3)$. These plots can be defined as:

$$\frac{\int_0^t C_{\text{tissue}}(T)\, d(T)}{C_{\text{tissue}}(t)} = V_T \frac{\int_0^t C_{\text{blood}}(T)\, d(T)}{C_{\text{tissue}}(t)} + q \tag{6.1}$$

$$\frac{C_{\text{tissue}}(t)}{C_{\text{blood}}(t)} = K_i \frac{\int_0^t C_{\text{blood}}(T)\, d(T)}{C_{\text{blood}}(t)} + V \tag{6.2}$$

Where C_{tissue} represents the concentration of tracer in the tissue and C_{blood} is the input curve. The average dynamic data from 4Pm28ζN T cell treated animals were transformed and plotted. A linear trend was only observed for the Logan plot, suggesting that the dynamic data from treated animals is better represented by the two-compartment model (Figure 6.6 a). Similarly, a linear trend was also observed for the control group using a Logan Plot (Figure 6.6 b & c). The V_T values obtained from the treated and control groups were comparable, suggesting limited infiltration of CAR T cells in the treated tumours.
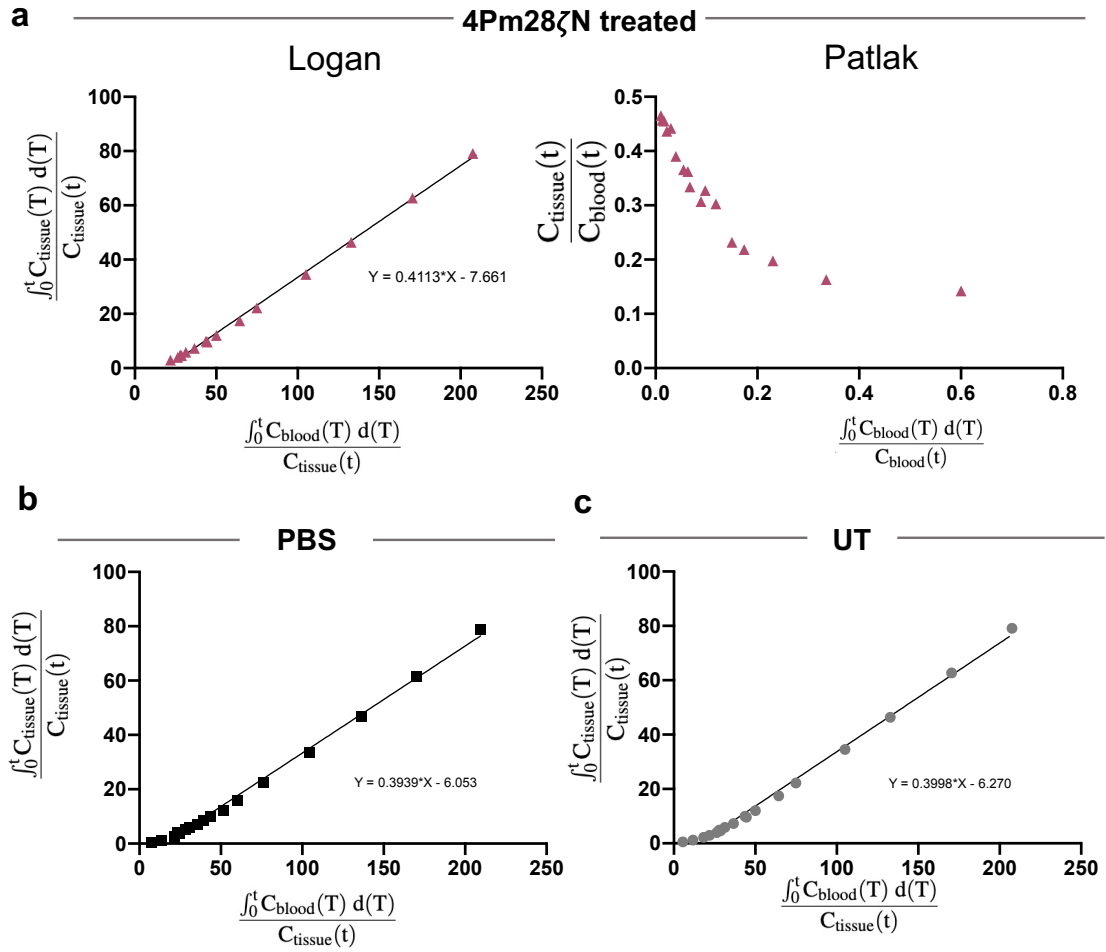
Figure 6.6: Logan and Patlak plots for graphical analysis of SPECT dynamic data.
a) Logan and Patlak plots for the graphical analysis of dynamic data from 4Pm28ζN T cell treated animals. b) & c) Logan plots fitted to the dynamic data from PBS and UT, respectively. The data in the Logan plots showed a linear trend after the tracer has reached equilibrium and the slope corresponds to the V_T.

These graphical methods are simpler quantitative methods based on a compartmental description of the tracer kinetics. To corroborate the results from the graphical methods and attempt to gain a better understanding of the kinetics of the tracer internalisation by the CAR T cells, the described compartmental models were built in SAAMII. Compartmental models offer further information into how the system functions. As above, the two-compartment model was fitted to the dynamic data from the UT and PBS control groups. Both two- and three-compartment models were fitted to the dynamic data from 4Pm28ζN treated group. In

both models, the blood compartment, representing the image-derived input function, was fixed using a forcing function extracted from the two-phase exponential decay equation derived from the heart imaging data. This accounts for missing data for excretion and tracer distribution to other organs. Within these models, several rate constants were defined. K_1 represents the rate of $^{99m}TcO_4^-$ delivery from plasma to tumour tissue; K_2 is the rate constant of tracer efflux from the tumour, and K_3 represents the rate of $^{99m}TcO_4^-$ internalised by the CAR T cells within the tumour (Figure 6.5). Values obtained for these rate constants are summarized in Table 6.1 and Table 6.2.

Table 6.1: **Rate constant values estimated by three- and two-compartment models fitted with data from 4Pm28ζN treated animals.**

Rate constant	4Pm28ζN (three-compartment)		4Pm28ζN (two-compartment)	
	Value (SD)	95% confidence interval	Value (SD)	95% confidence interval
K_1	0.081 (2.67)	-5.594 to 5.766	0.058 (1.24)	-2.567 to 2.682
K_2	0.38 (18.8)	-39.670 to 40.444	0.15 (5.14)	-10.700 to 11.005
K_3	0.0001 (0.92)	-1.952 to 1.952		
AIC	5.47		5.42	

Table 6.2: **Rate constant values by two-compartment model fitted with data from control animals**.

Rate constant	PBS		UT	
	Value (SD)	95% confidence interval	Value (SD)	95% confidence interval
K_1	0.069 (-0.17)	-0.295 to 0.434	0.0578 (1.71)	-3.553 to 3.669
K_2	0.22 (2.75)	-5.583 to 6.032	0.15 (5.75)	-11.990 to 12.219

The fitted curves displayed similar shapes for both the treated and control groups (Figure 6.7). The values for the rate constants were comparable between the treated group and the control groups in the two-compartment model, consistent with the outcomes of the graphical analysis. Using a three-compartment compartment model did not improve the fitting for the treated group; rather, it led to over-fitting, as demonstrated by the similar Akaike information criterion (AIC) values (Table 6.1).
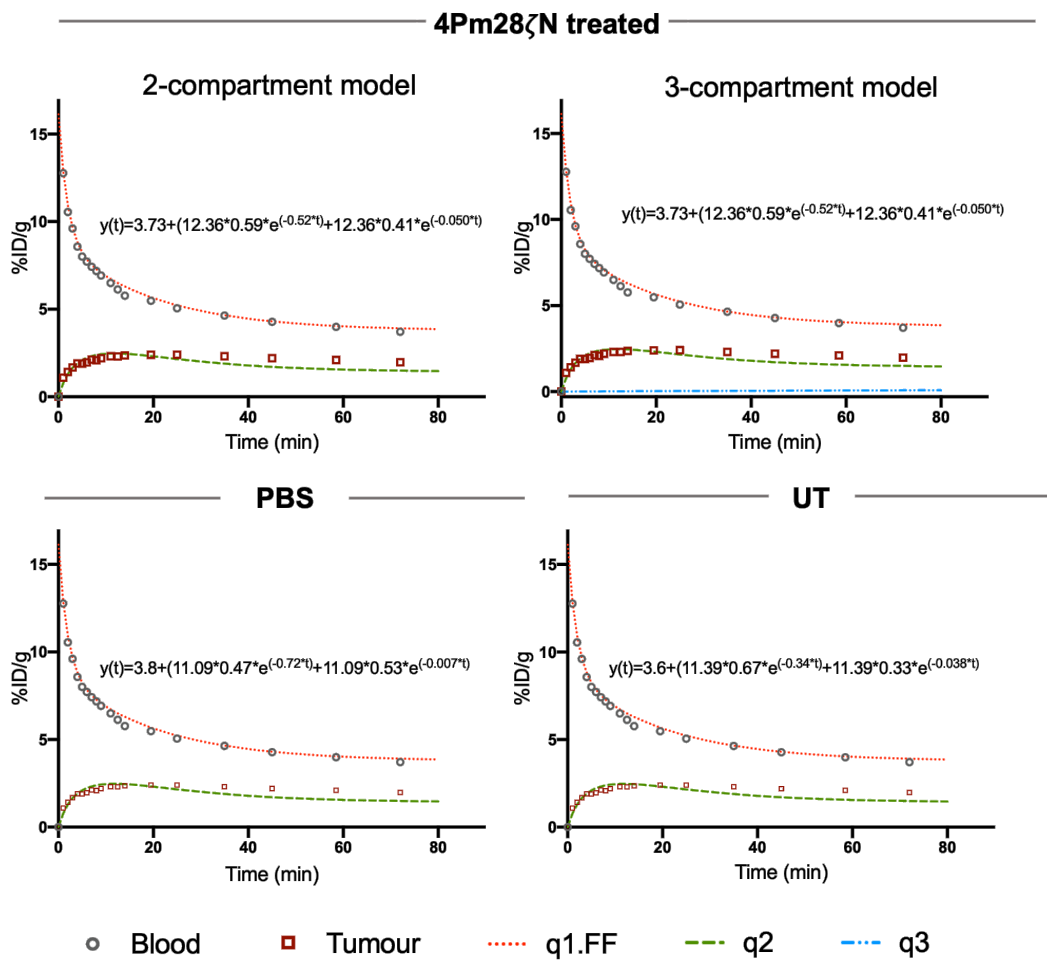
Figure 6.7: Mean heart and tumour time activity curves and fitted models. A two-phase exponential decay equation was used to fix the blood compartment (q1.FF). q2 and q3 are derived from fitting the model to the data following the two-compartment and three-compartment compartment models described on Figure 6.5.

Considering the combined results from graphical and compartment modelling analyses, a two-compartment model was considered suitable for describing the system. Nevertheless, there were notable uncertainties in the fit, as evidenced by the wide confidence intervals. These results emphasise the complexities involved in modelling the heterogeneous tracer uptake by CAR T cells.

6.2 *Ex vivo* quantitation of CAR T cells

Following the dynamic acquisition, animals were sacrificed, and organs and tumours were collected for *ex vivo* analysis. Radioactivity uptake in the samples was measured using a gamma counter. *Ex vivo* biodistribution showed radiotracer accumulation in endogenous hNIS expressing organs, i.e., stomach and salivary glands. There was also higher concentration of tracer circulating in blood at day 9 post ACT (4Pm28ζN I) possibly due to circulating CAR T cells (Figure 6.8).
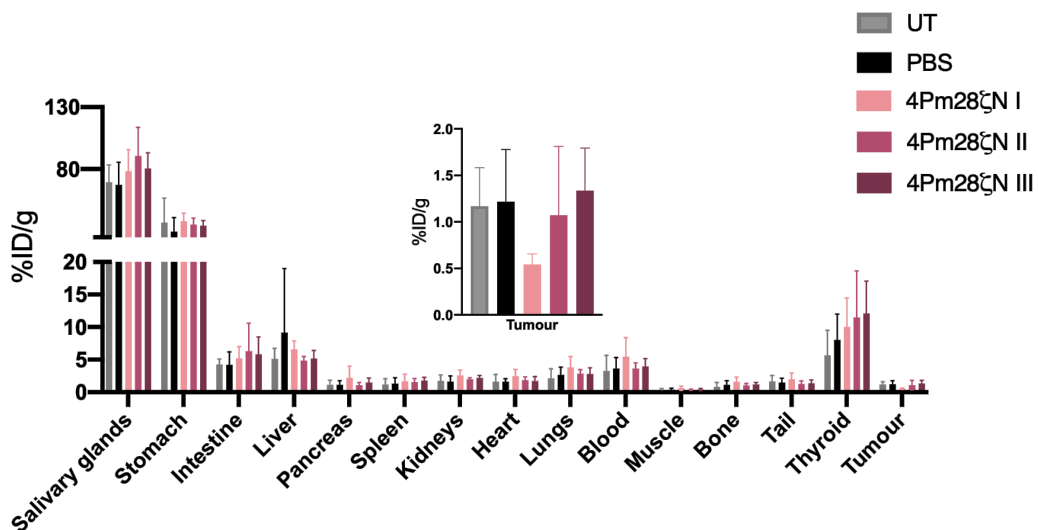
Figure 6.8: *Ex vivo* **tracer concentration in organs.** *Ex vivo* biodistribution of tracer from organs harvested following administration of 10 MBq of $^{99m}TcO_4^-$ prior SPECT/CT dynamic imaging. Inset shows zoom-in on tumour uptake. PBS (n=5), UT = untransduced T cells (n=5), 4Pm28ζN I = day 9 post ACT (n=7), 4Pm28ζN II = day 12 post ACT (n=7) and 4Pm28ζN III = day 14 post ACT (n=3). ACT = adoptive cell transfer. Graphs represent mean ± SD.

The total amount of tracer accumulated in the excised tumours highly correlated (r= 0.83) with the image derived quantitation from the SPECT images in Figure 6.3 (Figure 6.9 a). Moderate correlation (r = 0.5) was observed when comparing concentration of tracer per gram of tissue (Figure 6.9 b), due to volume difference between the excised tumour and the ROI drawn on the SPECT images. The use of CT contrast could enhance the delineation of the ROI on the SPECT images by providing better contrast between the tumour and the surrounding tissues.
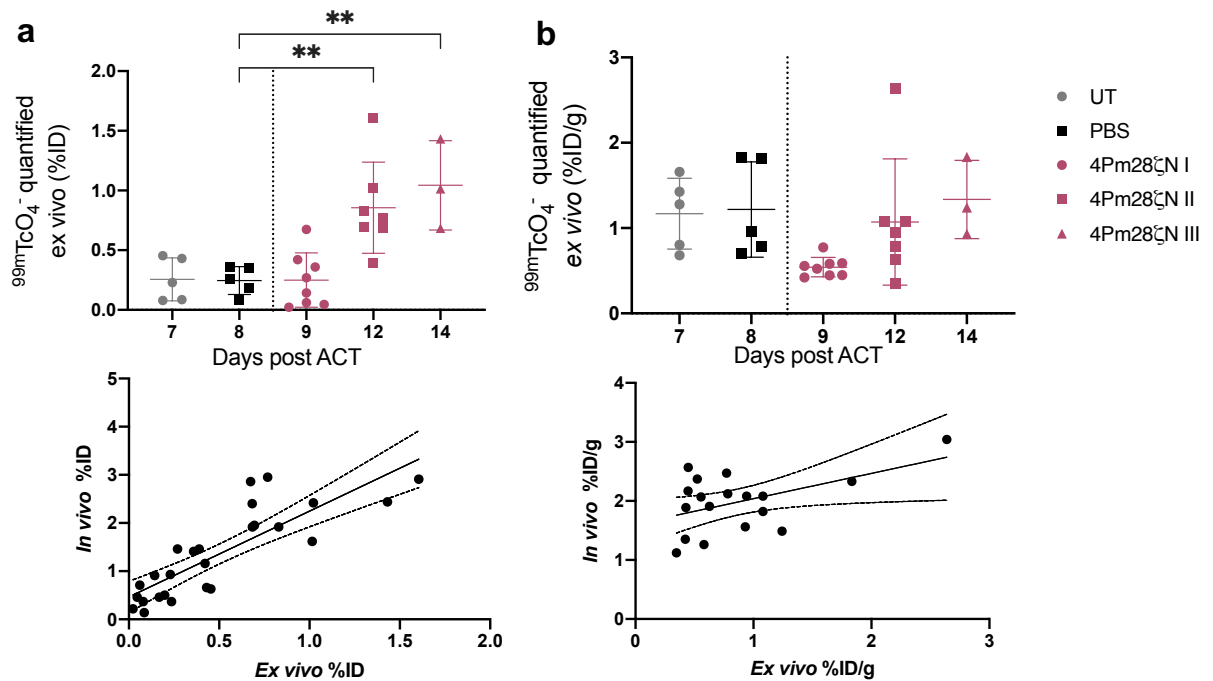
Figure 6.9: *Ex vivo* **tracer concentration in organs.** a) $^{99m}TcO_4^-$ uptake quantified from harvested tumours by gamma counting and plotted as percentage of the injected dose (%ID) and the correlation to the SPECT derived quantitation of tumour uptake. b) $^{99m}TcO_4^-$ uptake quantified from harvested tumours normalized to tumour volume (%ID/g) and its correlation to the SPECT derived quantitation of tumour uptake. PBS (n=3), UT = untransduced T cells (n=5), 4Pm28ζN I = day 9 post ACT (n=7), 4Pm28ζN II = day 12 post ACT (n=7) and 4Pm28ζN III = day 14 post ACT (n=3). ACT = adoptive cell transfer. Graphs represent mean ± SD.

Following gamma counting, control tumours were fixed in formalin for downstream immunohistochemical analysis, while the treated tumours were stored overnight in MACS®

Tissue Storage Solution (Figure 6.1 left). Immunohistochemical analysis of the control tumours revealed no positive staining for CD3 in tumours from animals that received PBS or untransduced cells (Figure 6.10).
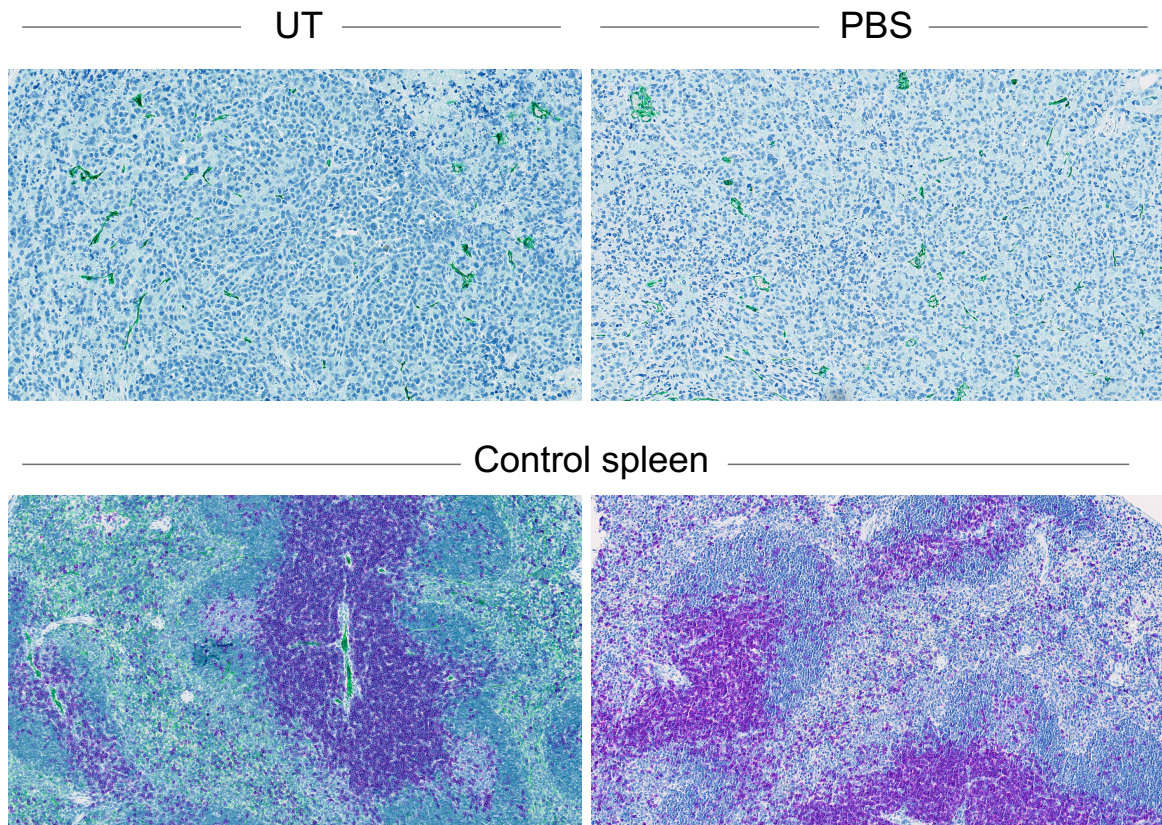
Figure 6.10: *Ex vivo* **analysis of infiltrating CD3 T cells by immunohistochemistry.** Representative tumour sections stained for human CD3 (purple) and CD31 (green) from tumours treated with untransduced cells (UT), PBS or spleen used as a positive control for the staining. Scale bar: 0.25 mm. n=5/PBS group, n=5/untransduced group.

Following the overnight preservation, treated tumours were processed at the established time points to quantify infiltrating CAR T cells by flow cytometry (Figure 6.2 a). The number of infiltrating CD3$^+$ T cells substantially increased between day 9 and day 12 post ACT, and these numbers were maintained on day 14 post treatment (Figure 6.11 b).

These flow cytometry results (Figure 6.11 b) were consistent with the *in vivo* quantitation of tracer uptake (Figure 6.3 b), indicating that the higher the number of infiltrating T cells,

the greater the quantified amount of $^{99m}TcO_4^-$ at the tumour site. To establish the correlation between the *in vivo* and *ex vivo* quantitation, data points falling under the limit of detection for the XXUHS-M collimator, set to 5,000 CAR T cells (Figure 4.9 a), were excluded. Eleven out of the eighteen processed tumours fell under the sensitivity limit.
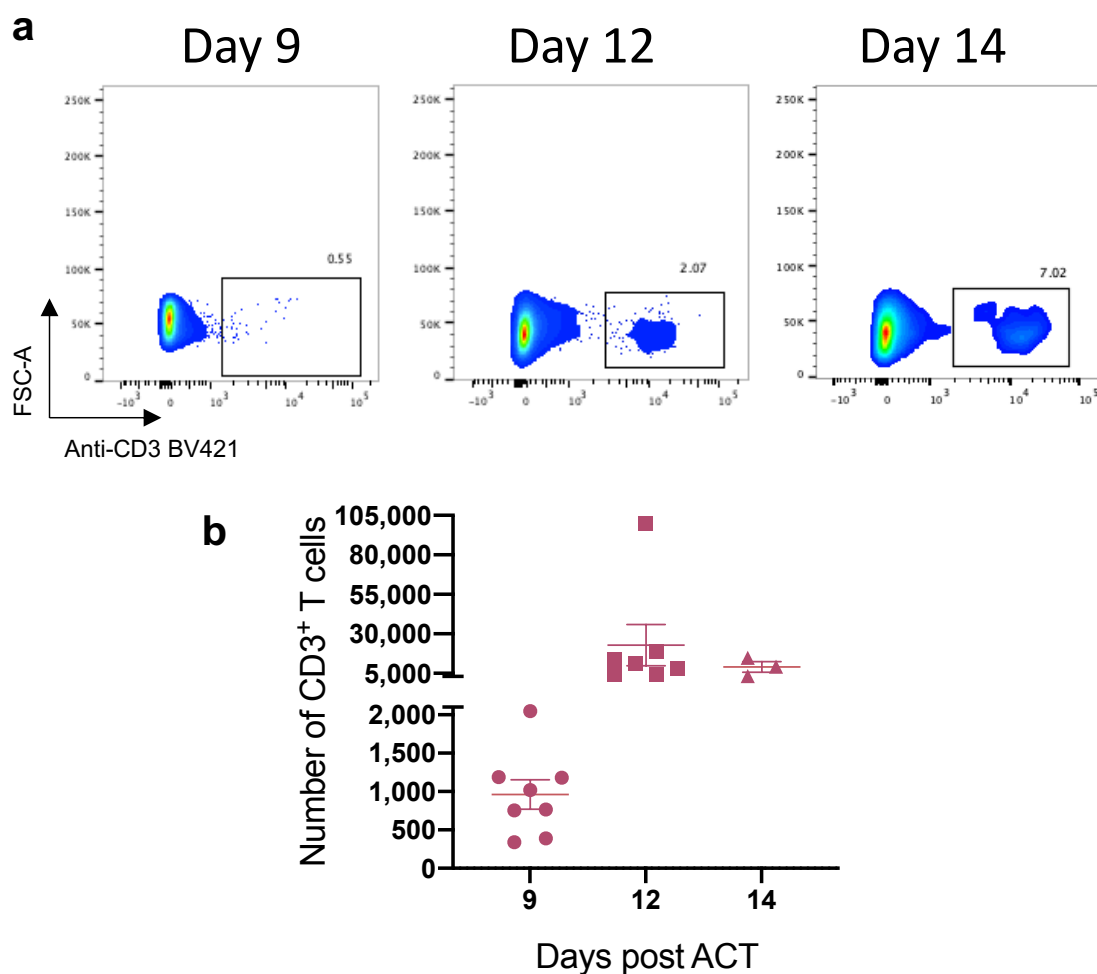
Figure 6.11: *Ex vivo* quantitation of CAR T cells in treated tumours. a) Representative flow cytometry plots depicting the human CD3$^+$ T cells within the harvested xenografts at different time points post adoptive cell transfer. Flow cytometry plots from individuals animals are shown in Figure S 8.5, 8.6 & 8.7. b) Quantitation of infiltrating CD3$^+$ T cells using CountiBright beads. n=8/day 9, n=7/ day 12 and n=3/ day 14. Graphs represent mean $\pm$ SEM.

A moderate positive correlation was observed between the number of infiltrating CD3$^+$ T cells and the total $^{99m}TcO_4^-$ uptake in the tumours (Figure 6.12 a). However, when tumour

uptake was normalized to gram of tissue, the correlation was lost (Figure 6.12 b), due to the differences in tumour volume among treated mice.
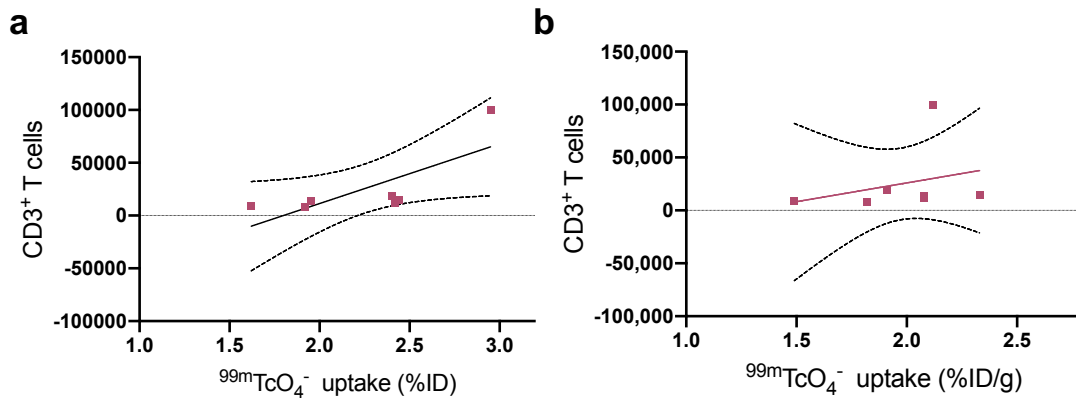
Figure 6.12: *In vivo* **and** *ex vivo* **CAR T cell quantitation.** Correlation between the *ex vivo* quantitation of infiltrating CAR T cells by flow cytometry and the image derived $^{99m}TcO_4^-$ quantitation in SPECT images as a) % injected dose (r = 0.75) or b) %injected dose/gram (r = 0.29). Dotted lines represent the 95% confidence interval.

6.3   Improving the modelling CAR T cell infiltration

The primary limitation encountered during the development of the mathematical model was the lack of tumour homogeneity. Within the tumour, CAR T cell infiltration exhibited significant heterogeneity, resulting in an uneven distribution of $^{99m}TcO_4^-$. This heterogeneity is characterised by the formation of hot spots represented by exceptionally high tracer uptake, corresponding to clusters of CAR T cells, surrounded by areas with minimal uptake. Thus, the standard approach of quantifying tracer concentration in the entire tumour and reporting it as %ID/g leads to dilution of the true uptake signal coming from the infiltrating CAR T cells .

To address this limitation and focus on quantifying areas of the tumour showing accumulation of tracer, a thresholding method was applied to the placed ROIs to include in the quantitation only those voxels with a signal exceeding 2.5% ID/g, thus excluding areas

196

with minimal uptake and fitting to the assumption of homogenous tracer distribution within the compartment (Figure 6.13).
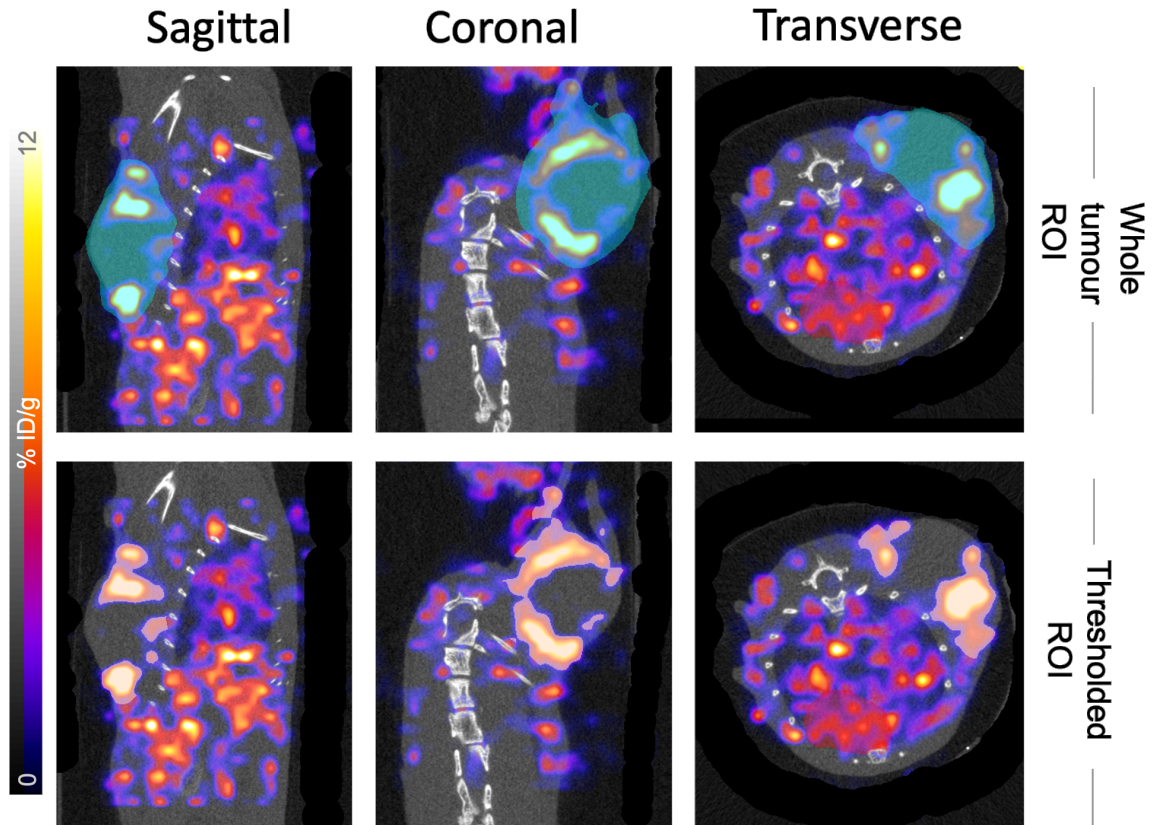
Figure 6.13: ^{99m}TcO$_4^-$ **quantitation of hot spot areas in the tumour using a thresholding method.** Top) ROIs were placed over the entire tumours to quantify radioactivity concentration in the tumours after administration of 10 MBq of ^{99m}TcO$_4^-$. Bottom) A thresholding method was applied to include only those voxels with over 2.5 %ID/g signal within the ROI. Images represent sagittal, coronal, and transverse views from the same animal.

This approach decreased the inter-group variability; however, it did not yield a significant difference in the quantified uptake between the treated and control groups (Figure 6.14 a). A marginal improvement on the correlation between the thresholded tracer uptake *in vivo* and the number of CAR T cells detected in the tumours by flow cytometry was observed (Figure 6.14 b).
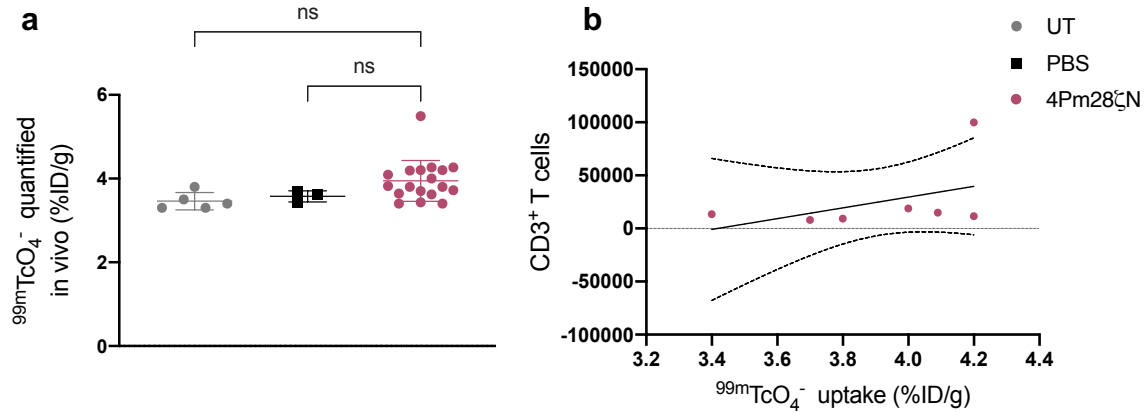
Figure 6.14: ^{99m}**TcO$_4$$^-$ uptake quantification after thresholding ROI.** a) ^{99m}TcO$_4$$^-$ uptake quantified from voxels with a signal over 2.5 %ID/g. Graphs represent mean ± SD. Statistical significance calculated by Student's t-test. b) Correlation between the *ex vivo* quantitation of infiltrating CAR T cells by flow cytometry and the image derived ^{99m}TcO$_4$$^-$ from thresholded SPECT images (r = 0.45). Dotted lines represent the 95% confidence interval.

As an alternative, a second thresholding method was applied to the data to quantify the region with maximal uptake defined as the concentration of the 3x3x3 cube of voxels centred around the voxel with the highest uptake within the ROI (Figure 6.15 a). This drastic approach yielded a homogenous distribution of the tracer within the ROI, as all voxels included in the ROI presented high uptake, and it did result in significant uptake differences between the treated and control groups (Figure 6.15 b). Applying this thresholding method to the dynamic SPECT data increased the noise in the time-activity curves. Faster kinetics were observed, the peak uptake occurred approximately 10 minutes post tracer infusion, followed by a steady state around 20 minutes post-infusion. This time activity curve closely resembled the shape fitted by the model during the proof-of-concept experiment (Figure 4.16 c). Nevertheless, similar uptake patterns were observed for all groups with only significant differences in uptake between treated and untransduced controls during the first 10 minutes of the scan.
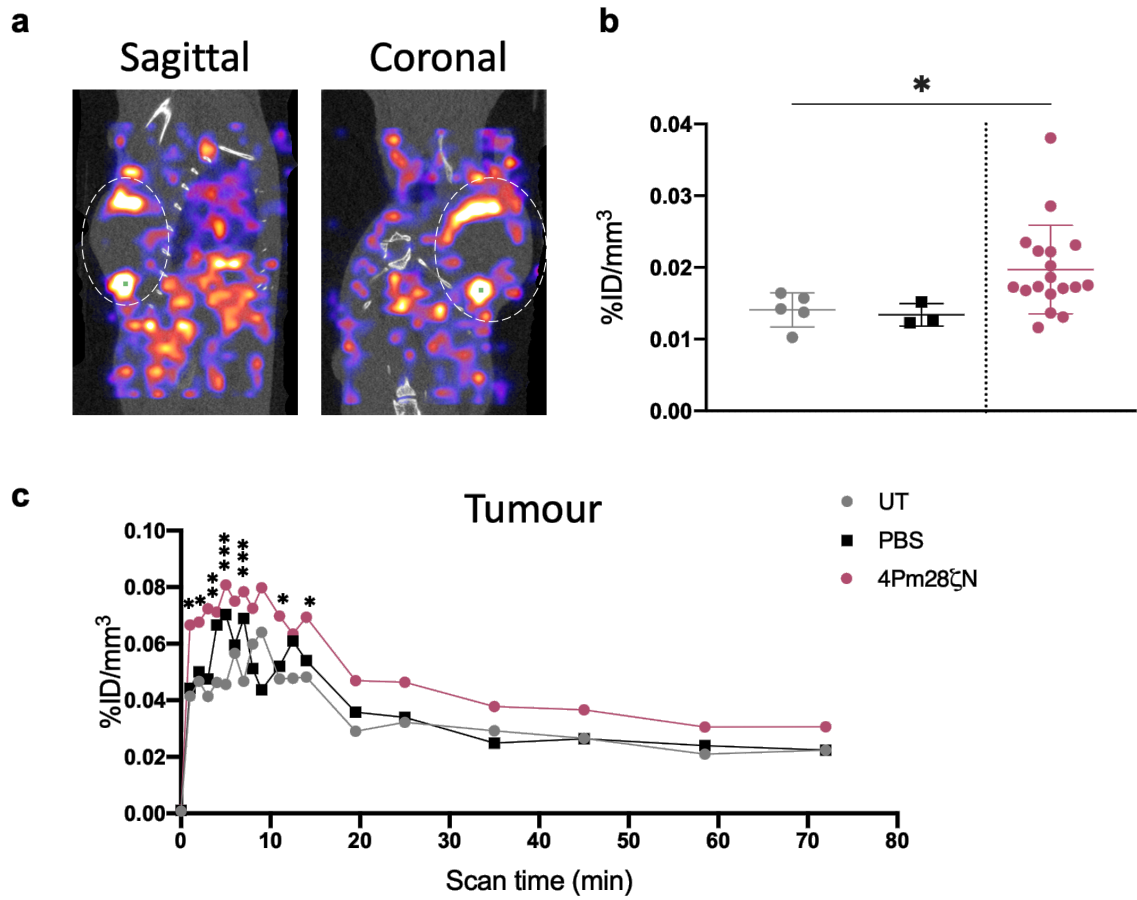
Figure 6.15: $^{99m}\text{TcO}_4^-$ **quantitation of the highest uptake voxels within the ROI.**a) 3x3x3 cube of voxels ROI in green. Dotted lines depicted tumour area. b) Quantified $^{99m}\text{TcO}_4^-$ uptake using thresholding method in a). SPECT data reconstructed as a single frame after steady stated is reached. Graphs represent mean ± SD c) Tumour time-activity curve. Statistical significance comparing 4Pm28ζN to untransduced using a Student's t-test. $^*\text{p} \leqslant 0.05$, $^{**}\text{p} \leqslant 0.01$, $^{***}\text{p} \leqslant 0.001$.

Similarly, when fitting the two-compartment model to the data (Figure 6.16 a), both treated and control groups shared a similar time-activity curve shape for the tumour (Figure 6.16 b & c). The rate constants extracted from the fitted model were comparable between all groups suggesting a similar exchange of tracer between the bloodstream and the tumour, irrespective of the presence of CAR T cells within the tumour. The uncertainties in the fitting persisted, with wide 95% confidence intervals (Table 6.3 & 6.4).
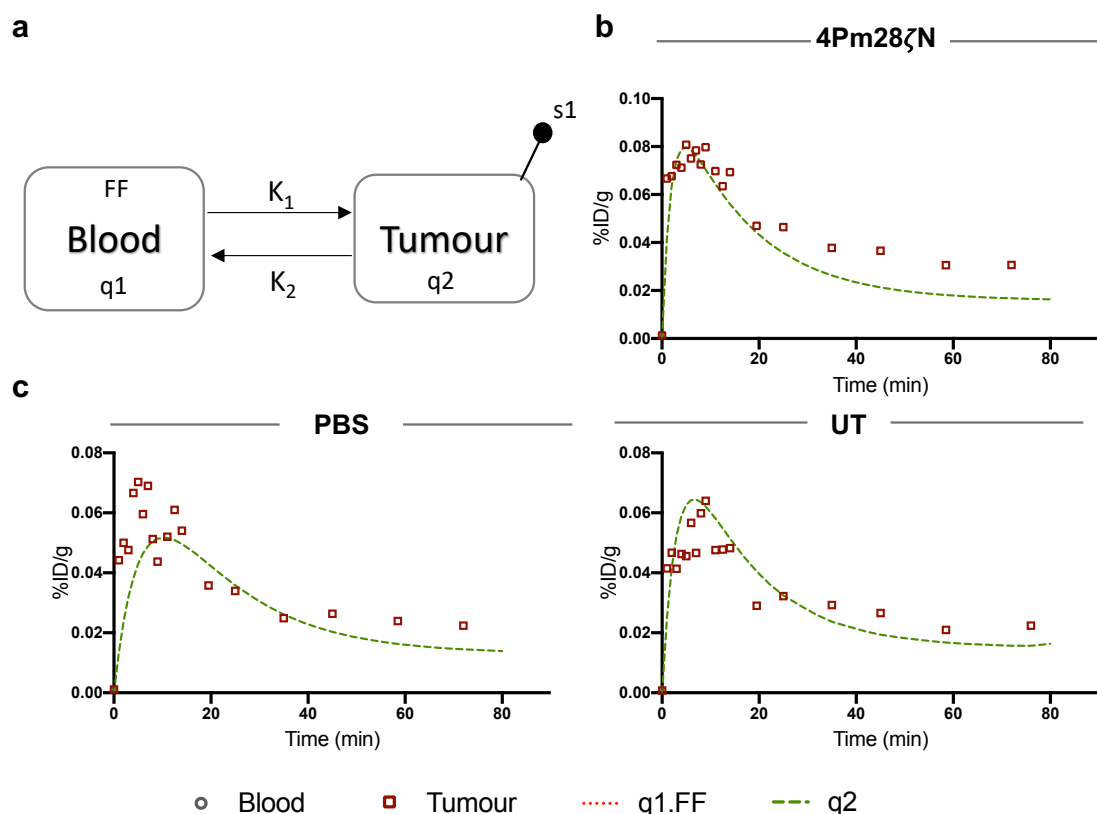
Figure 6.16: Two-compartment model. a) Schematic of the two-compartment model built in SAAMII software. Square dots represent the mean uptake in the tumour at different time points. Dashed line represents the fitted model for treated b) and control groups c).

Table 6.3: **Rate constant values estimated by two-compartment models fitted with data thresholded to the highest uptake cube of voxels in control animals.**

	PBS		UT	
Rate constant	Value (SD)	95% confidence interval	Value (SD)	95% confidence interval
K_1	0.095 (0.4)	-0.928 to 1.11	0.16 (0.08)	-1.529 to 1.852
K_2	0.174 (0.8)	-1.587 to 1.937	0.222 (1.69)	-3.262 to 3.906

Table 6.4: **Rate constant values estimated from two-compartment models fitted to data thresholded to the highest uptake cube of voxels in 4Pm28ζN T cell treated animals.**

Rate constant	Value (SD)	95% confidence interval
K_1	0.194 (1.36)	-2.691 to 3.080
K_2	0.249 (1.7)	-3.351 to 3.850

6.4 Summary

Successful CAR T *in vivo* tracking and *ex vivo* quantitation was achieved in this experiment. The use of MACS® Storage solution allowed for larger sample number per group, increasing the study's statistical power. Non-invasive SPECT imaging demonstrated homing and infiltration of CAR T cells to the tumour site in treated animals. As time progressed, more CAR T cells were present in the tumour, resulting in an increase in the *in vivo* SPECT signal. The *in vivo* data was validated by the *ex vivo* flow cytometry analysis of treated tumours. Higher numbers of $CD3^+$ T cells quantified by flow cytometry corresponded to higher uptake in the tumours, showing a moderate correlation between these measurements.

However, the number of infiltrating CAR T cells was modest, and a significant portion of samples fell below the detection limit of our imaging system. Out of 18 treated animals, only 7 showed more than 5,000 infiltrating CAR T cells, limiting the power of the study.

Furthermore, although distinct clusters of CAR T cells were observed in treated tumours compared to the non-specific signal in control tumours, the time-activity curves displayed similar uptake patterns for all groups, with no significant differences in overall $^{99m}TcO_4^-$ quantitation. Additionally, the heterogeneous infiltration of CAR T cells posed challenges for *in vivo* quantitation using compartmental modelling leading to large uncertainties in the fitting and the possibility of multiple solutions. Improvements in the modelling fit were achieved by thresholding the data to only quantify the hottest voxels within the ROI, however

the high levels of uncertainty in the fits persisted. Considering these factors collectively, further optimisation was required to enable quantitation of CAR T cell infiltration.

Chapter 7

Proof of concept for the non-invasive quantitation of CAR T cells

As described in previous chapters, tumour control by the CAR T cells was limited, as was CAR T cell infiltration in tumoured mice bearing shoulder xenografts. To assess the cytotoxic effect of the CAR T cells, and investigate a possible effect of the injection of $^{99m}TcO_4^-$ for tracking the CAR T cells on their functionality *in vivo*, tumour xenografts were injected s.c. in the right flank.

NSG mice were inoculated with 0.25×10^6 PLP-LT tumour cells s.c. in the right flank. Tumour growth was monitored using callipers three times a week. After 12 days, animals were randomised into six groups with an average tumour size of 46 mm^3. Controls included PBS, UT and 4PmTrN groups to assess the anti-tumoral cytotoxicity of the CAR T cells. Two groups received 4Pm28ζN T cells, but only one was exposed every three days to $^{99m}TcO_4^-$ to investigate the radiation-induced impact on CAR T cell cytotoxicity. A baseline SPECT/CT scan for monitoring CAR T cell infiltration was conducted on three animals from this group. The last group received 4Pm28ζ T cells, which only express the PSMA-targeting CAR, to study the effect of co-expressing the hNIS with the CAR (Figure 7.1 a). CAR T cell transduction, based on myc and hNIS surface expression, was measured 24 hours prior
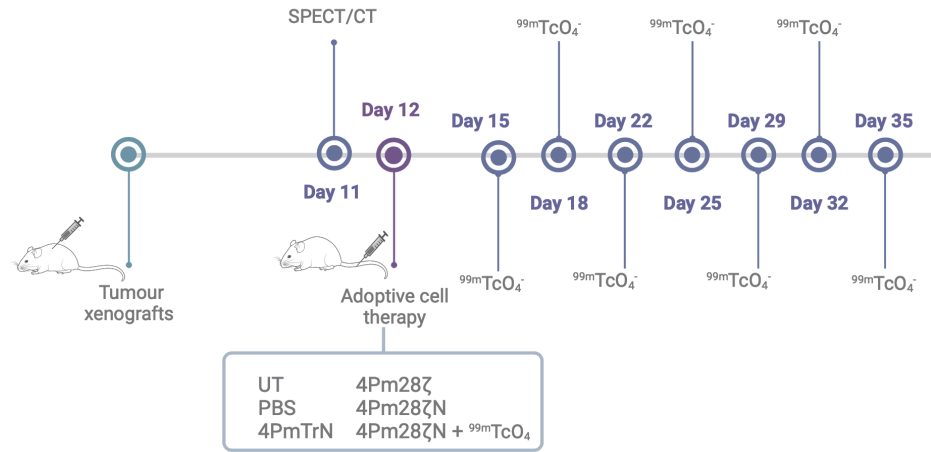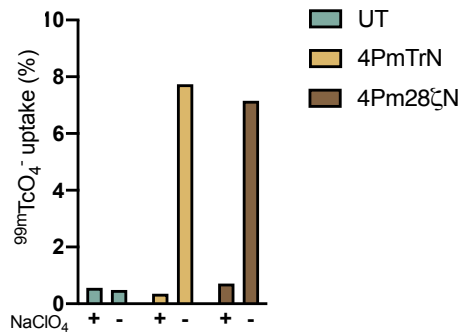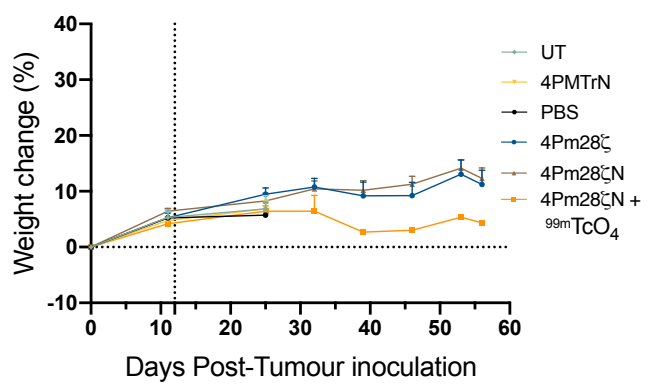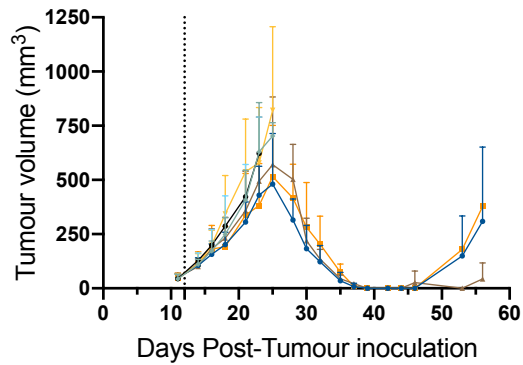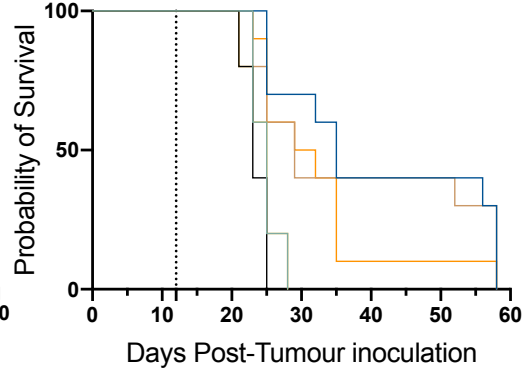
Figure 7.1: Assessing the cytotoxicity of 4Pm28ζN *in vivo* a) Experimental plan. b) *In vitro* uptake levels of injected CAR T cells incubated with $^{99m}TcO_4^-$ in the presence or absence of the inhibitor. c) Percentage body weight change. Dashed line represents ACT day. d) Tumour volume was monitored by calliper measurements. e) Survival curve. n=10/treated groups, n=5/control groups. ACT: adoptive cell transfer. Graphs represent mean ± SD.
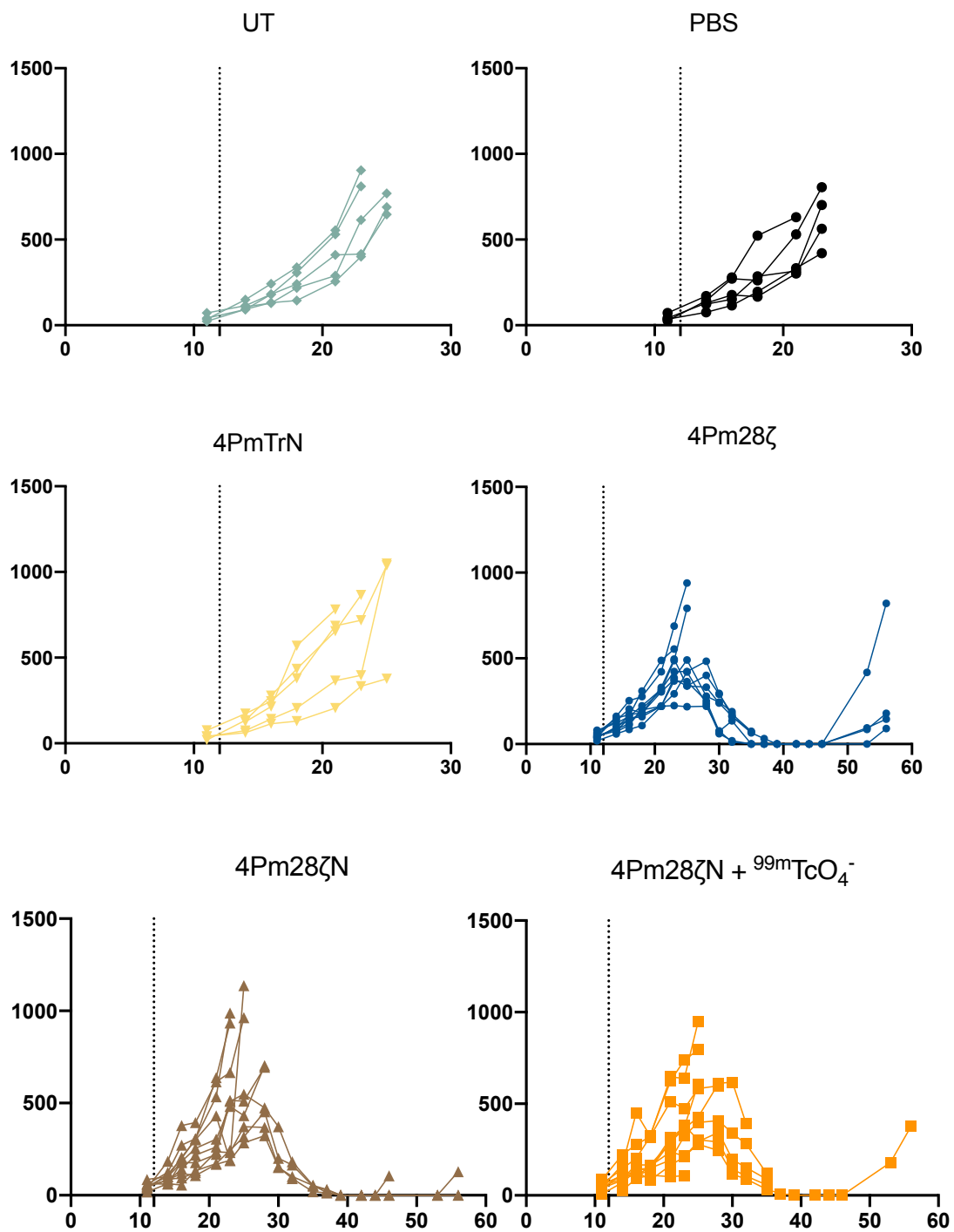
Figure 7.2: CAR T cells show enhanced tumour control. Caliper measurements of tumor volumes for individuals animals. Dashed line represents day of adoptive cell transfer (ACT). n=10/treated groups, n=5/control groups. Graphs represent mean ± SD.

to i.v. injection by flow cytometry. On the day of CAR T cell administration, an uptake assay demonstrated 7.7% internalisation by 4Pm28ζN T cells and 7.1% by 4PmTrN T cells (Figure 7.1 b). Throughout the study, animals maintained stable body weights with reduced body weight gain in the group administered with $^{99m}TcO_4^-$(Figure 7.1 c).

Rapid disease progression was observed, leading to the sacrifice of control mice by day 25 post-tumour inoculation. Both 4Pm28ζN and control 4Pm28ζ T cells exhibited robust anti-tumoural activity, with no differences between groups, demonstrating no detrimental effect from the co-expression of the hNIS or the injection of $^{99m}TcO_4^-$. Complete tumour eradication occurred in animals from all three treated groups, maintaining a tumour-free state for fifteen days before relapse (Figure 7.1 d). Individual tumour growth curves are illustrated in Figure 7.2. All treated animals showed prolonged survival compared to control animals (Figure 7.1 e).

Encouraged by the impressive control of tumour growth by CAR T cells, CAR T cell infiltration was visualised and quantified by SPECT/CT imaging in three animals from the 4Pm28ζN $+^{99m}TcO_4^-$ group. Initially, there was no discernible uptake signal at the tumour baseline, but following ACT, there was clear tumour uptake with the signal intensifying over time (Figure 7.3 a). These visual observations were corroborated by quantitative measurement of radioactivity in the tumours, confirming the increasing infiltration and proliferation of CAR T cells within the treated tumours (Figure 7.3 b).

For the remaining animals, $^{99m}TcO_4^-$ was administered on the day they were scheduled for sacrifice due to substantial tumour burden. An hour later, tumours were excised, and radioactivity uptake was measured using a gamma counter. As anticipated, radioactivity uptake was exclusively observed in hNIS-expressing CAR T cells (4Pm28ζN) (Figure 7.4 a). The amount of the internalised tracer varied among tumours but generally increased over time, reflecting the escalating infiltration of CAR T cells as days progressed (Figure 7.4 b). Immohistochemistry was performed on some of these tumours to visualise the CAR T cell
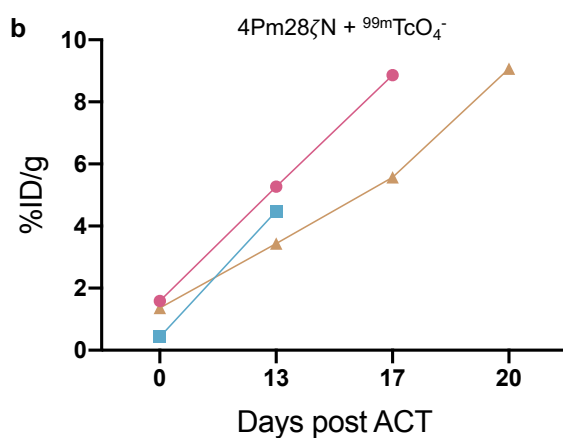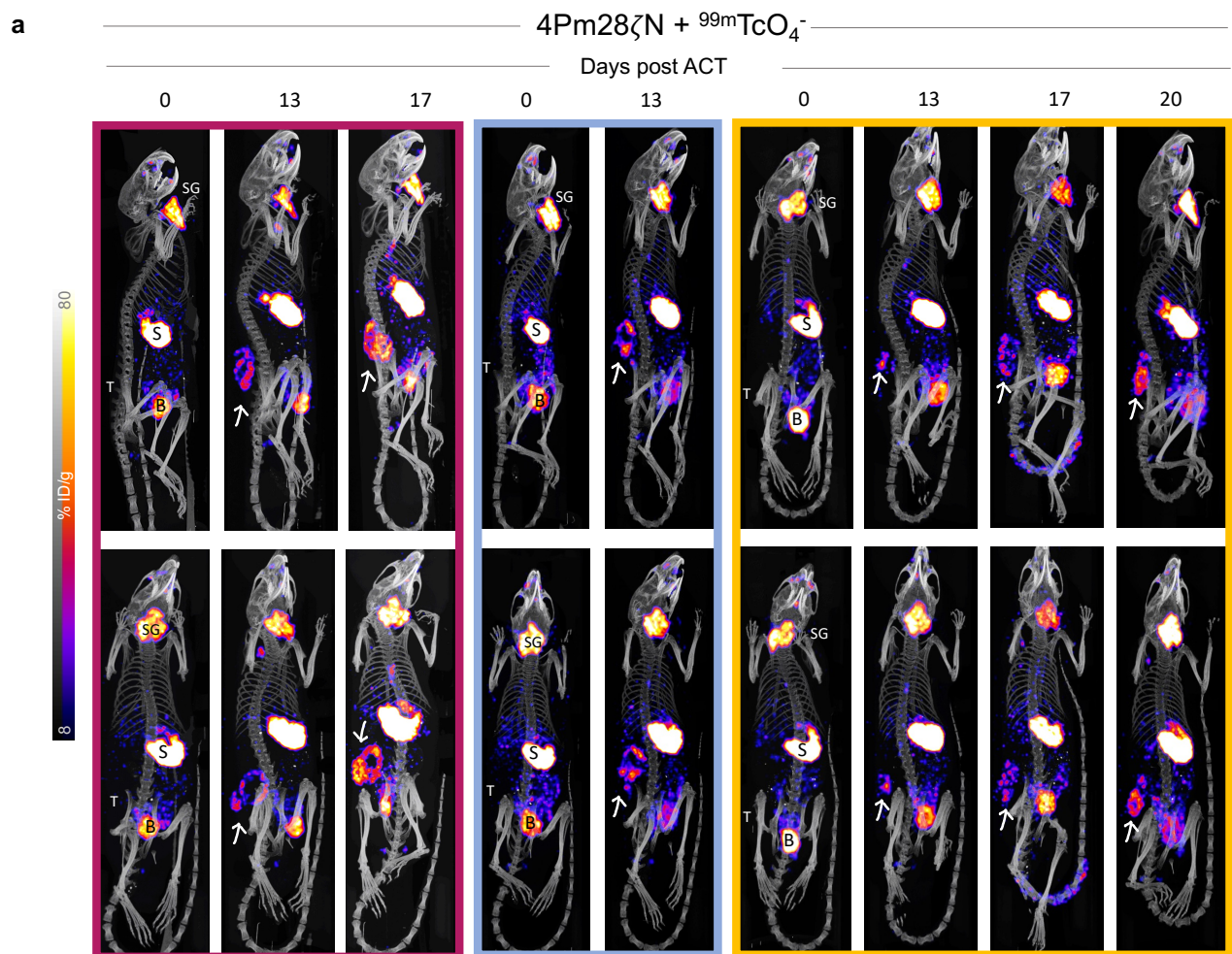
Figure 7.3: High infiltration of CAR T cells in treated tumours is observed through SPECT/CT. a) MIP SPECT images depicting specific $^{99m}TcO_4^-$ uptake by 4Pm28ζN CAR T cells homing to the tumour at different time points after administration of 10 MBq of $^{99m}TcO_4^-$. Two MIP views per animal, n=3 animals from 4Pm28ζN +$^{99m}TcO_4^-$ group. White arrows point signal from CAR T cells. SG=salivary glands, S=stomach, B=bladder, T=tumour. b) $^{99m}TcO_4^-$ uptake quantified from the SPECT images in a) as percentage of the injected dose per gram (%ID/g).
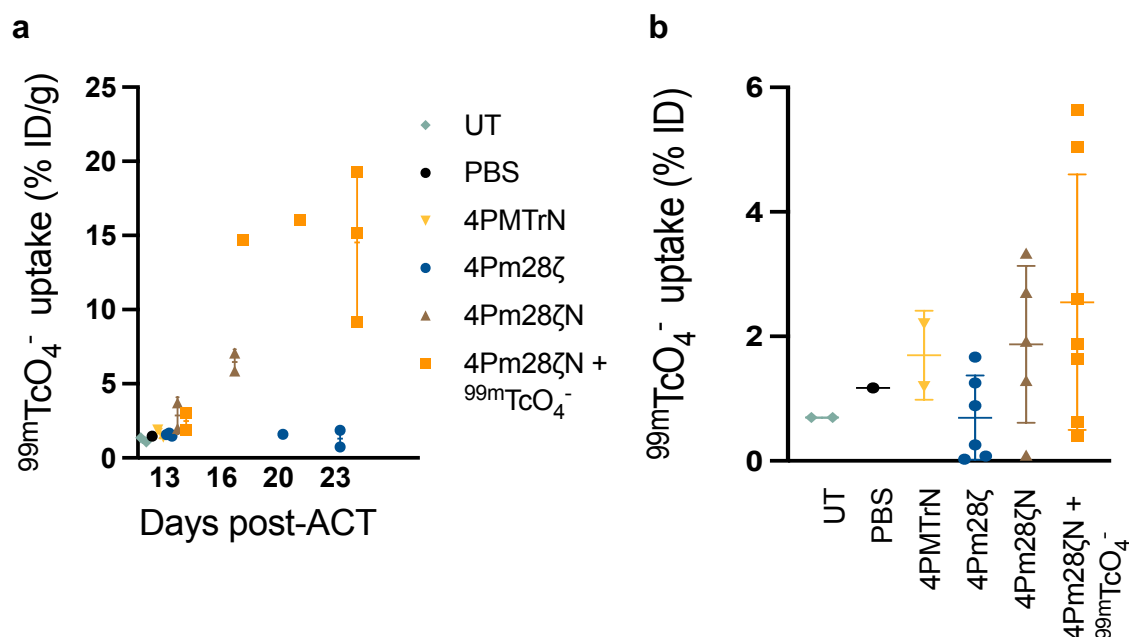
Figure 7.4: *Ex vivo* **quantitation of** $^{99m}TcO_4^-$ **uptake in excised tumours by gamma counting.** a) *Ex vivo* $^{99m}TcO_4^-$ uptake levels in tumours from different treatment groups at the indicated time points post ACT. b) *Ex vivo* $^{99m}TcO_4^-$ uptake levels by treatment group represented as percentage of the injected dose. Graphs represent mean ± SD.

infiltration pattern (Figure 7.5). CD3 T cells were not visible in control animals (Figure 7.5 a), while the extent of CAR T cell infiltration varied among treated animals (Figure 7.5 b). In general, vasculature and CAR T cell infiltration at the core was absent ((Figure 7.5 b) i), accompanied by loss of nuclei staining (Figure 7.5 b) ii), pointing to the presence of necrotic tissue. This aligns with the absence of $^{99m}TcO_4^-$ signal at the core of the tumours in the SPECT/CT signals. Quantification of CD3$^+$ cells from the tumour slices yielded similar results consistent with the gamma counter data. CD3 infiltration was only observed in treated tumours, not in control (Figure 7.6 a). A larger number of CD3$^+$ cells were quantified on day 16 post ACT compared to day 13 (Figure 7.6 b). A strong positive correlation emerged between the uptake quantified at the tumour by gamma counting and the percentage of CD3$^+$ cells quantified from the immunohistochemical staining (Figure 7.6 c).
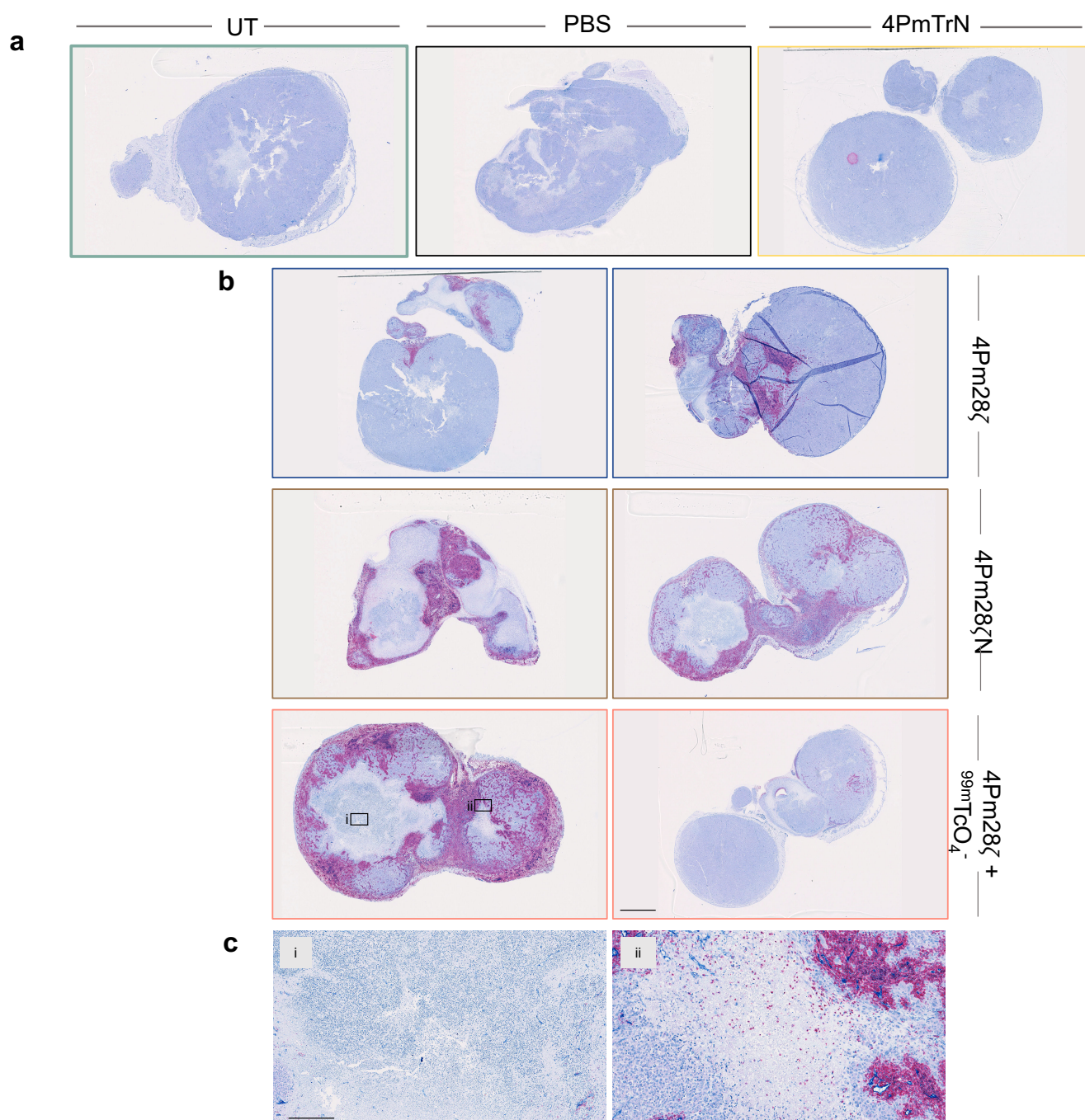
Figure 7.5: *Ex vivo* **analysis of infiltrating CD3$^+$ T cells by immunohistochemistry.** Paraffin embedded tumour slices from control (a) and treated (b) animals were stained for human CD3. Scale bar: 2.5mm. c) Higher magnification images showing the lack of blood vessels at the tumour core (i) and the loss of nuclei staining (ii). Location of magnification shown by the black squares on b). Scale bar : 0.5 μm. n=2/treated group, n=1/control group.
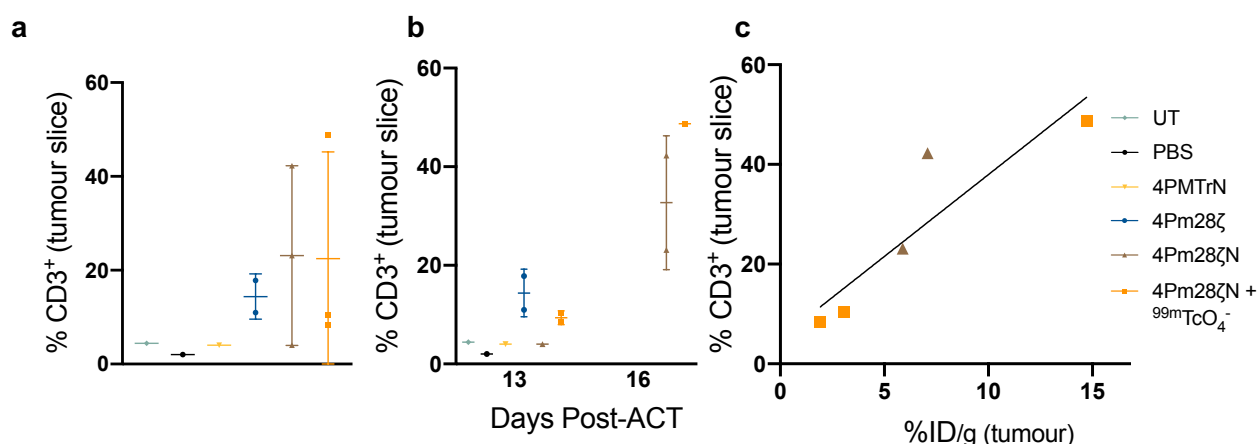
Figure 7.6: *Ex vivo* **quantitation of infiltrating CD3 T cells by immunohistochemistry.** Percentage of CD3 positive cells quantified using QuPath software grouped by treatment (a) or by day of tumour harvesting (b). c) Correlation between the tumour uptake and the percentage of CD3$^+$ cells quantified after immunohistochemistry staining. r = 0.88. Graphs represent mean ± SD.

Increased CAR T cell infiltration was evident in this mouse model, contributing to an enhanced signal-to-background ratio. Mice administered with 4Pm28ζN and 4Pm28ζ T cells were imaged dynamically using the GP-RM collimator in an attempt to establish the mathematical model. Following dynamic acquisition, time frames were binned together after reaching steady state (30 to 60 min post-tracer injection) and the MIP views are displayed in Figure 7.7 a. High tracer uptake was observed in the 4Pm28ζN treated animals, with no visible accumulation in the 4Pm28ζ group. *Ex vivo* immunohistochemical staining of tumour sections clearly illustrated the accumulation of CAR T cells in both groups as expected (Figure 7.7 b).

Quantitative analysis of these SPECT images from 4Pm28ζ treated animals established the perfusion levels around 2% ID/g, while 4Pm28ζN treated animals exhibited clear CAR T cell accumulation, reaching an average tumour uptake of 23% ID/g (Figure 7.8 a). Quantitation of CD3 positive T cells in these tumour slices indicated comparable levels of CAR T cell infiltration between both groups(Figure 7.8 b). This data demonstrated the specific internalisation of ^{99m}TcO$_4^-$ by the hNIS in 4Pm28ζN treated animals.
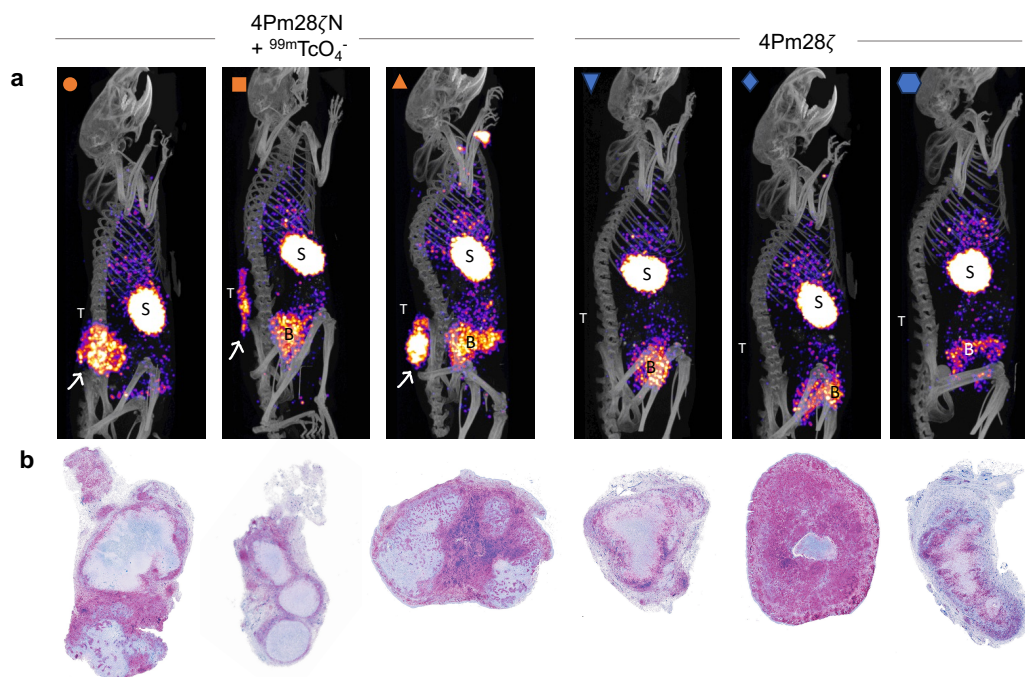
Figure 7.7: High infiltration of CAR T cells was observed in flank xenografts. a) MIP SPECT images depicting specific uptake by 4Pm28ζN T cells homing to the tumour following administration of 10 MBq of $^{99m}TcO_4^-$. White arrows point to signal from CAR T cells. S=stomach, B=bladder, T=tumour. b) Paraffin embedded tumour slices were stained for human CD3 (pink). Higher magnification images are presented in Figure S 8.8 and Figure S 8.9. n=3/group.
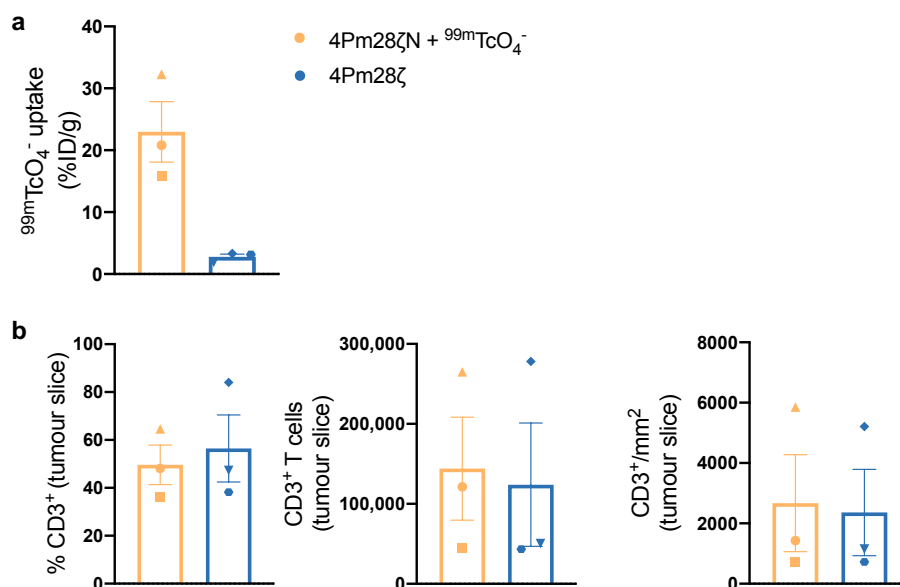
Figure 7.8: Quantitation of CAR T cell infiltration. a) Image-derived *in vivo* quantitation of $^{99m}TcO_4^-$ uptake in tumours. b) *Ex vivo* quantitation of CD3 positive T cells in tumours. n=3/group. Graphs represent mean ± SD.

To quantify tracer concentration concurrently in the heart and tumour from the dynamic data, ROIs were delineated on the tumour and heart of each animal to extract the time-activity curves. Tracer concentration in blood was similar between groups, reaching peak concentration shortly after tracer infusion, followed by a two-phase decay curve. In 4Pm28ζ treated animals, tracer concentration in tumours rapidly reached a plateau showcasing tumour perfusion with no specific uptake by 4Pm28ζ T cells. However, in tumours treated with the hNIS expressing CAR T cells (4Pm28ζN), tracer concentration steadily increased over time, surpassing perfusion levels (Figure 7.9). This data indicates specific uptake of the tracer by the hNIS-expressing CAR T cells and further supports the presence of infiltrating CAR T cells in the tumours treated with 4Pm28ζN T cells.
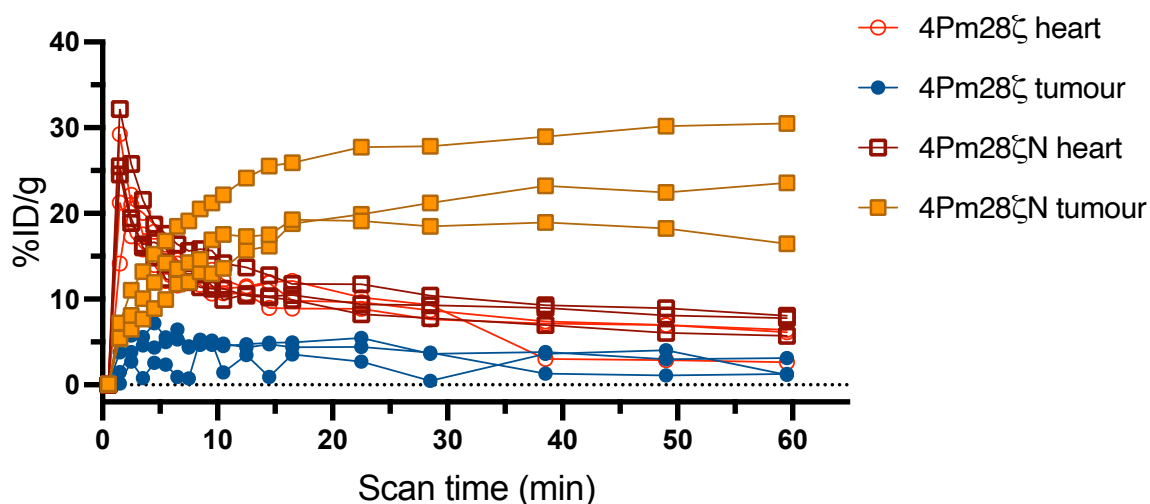
Figure 7.9: Accumulation of ^{99m}TcO$_4^-$ in treated tumours indicates infiltration of CAR T cells. Time-activity curves for ^{99m}TcO$_4^-$ tracer kinetics in hearts and tumours of animals treated with hNIS-expressing CAR T cells (4Pm28ζN) or control CAR T cells (4Pm28ζ) following administration of 10 MBq of ^{99m}TcO$_4^-$. Uptake is expressed as the percentage of injected dose per gram of tissue (%ID/g). n=3/group.

Based on previous results, a two-compartment reversible model, consisting of a blood compartment and a tumour compartment, was deemed appropriate for our system. As previously described (section 1.6), the dynamic data was transformed and plotted to determine

the total volume of distribution (V_T) from the slope of the linear trend, representing the ratio of $^{99m}TcO_4^-$ concentration between the tumour and blood at equilibrium.
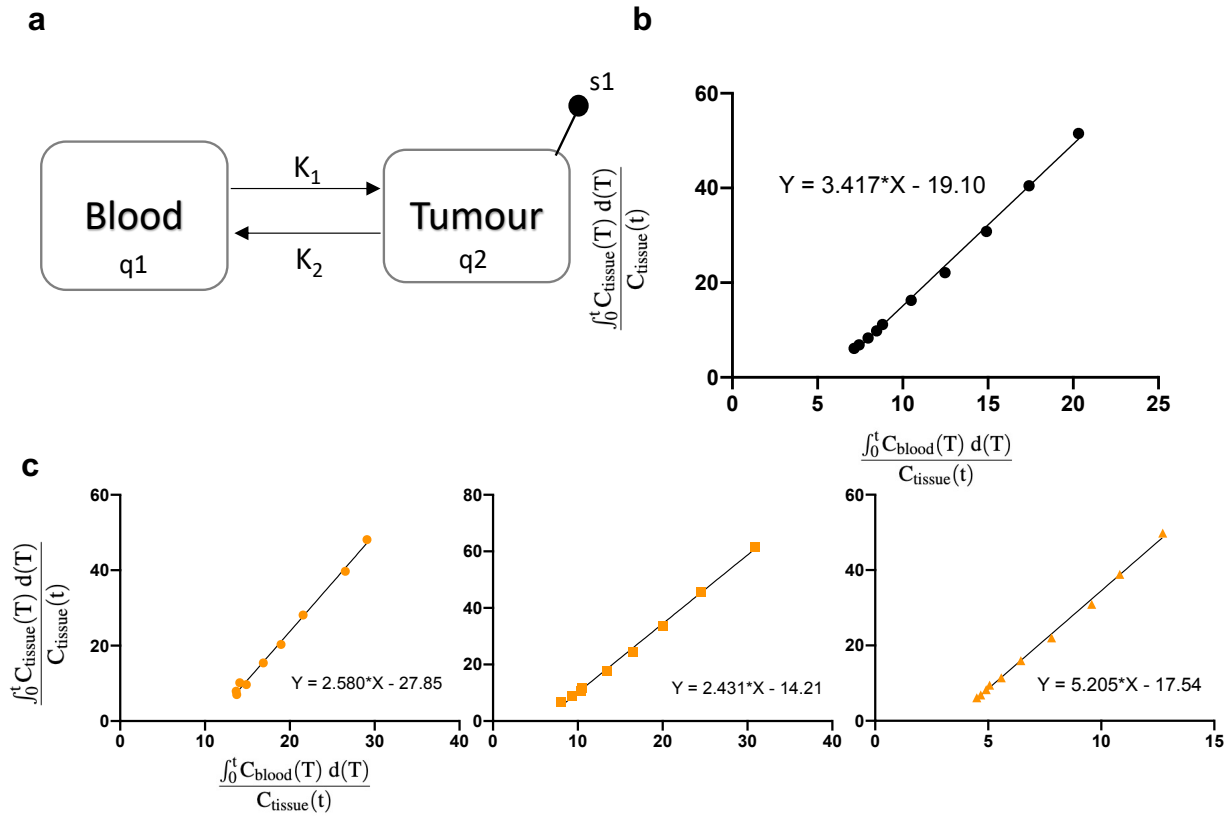
Figure 7.10: Logan plots for graphical analysis of SPECT dynamic data. a) Schematic of the two-compartment model. The blood compartment, q1, exchanges tracer with the tumour compartment, q2, at the rate defined by K_1 and K_2. b) Logan plots for the graphical analysis of the average dynamic data from 4Pm28ζN treated animals. c) Logan plots fitted to the dynamic data of individual animals. The data in the Logan plots shows a linear trend after the tracer reaches equilibrium and the slope corresponds to the V_T.

Additionally, the two-compartment model was also built in SAAMII, and the corresponding rate constants are summarized in Table 7.1. The fitted curves exhibited a good fit of the model, revealing distinctive shapes between the 4Pm28ζ and 4Pm28ζN treated groups (Figure 7.11), which was reflected in the values of the rate constants. The exchange rate of tracer from blood to tumour (K_1) was higher for the 4Pm28ζN group compared to the 4Pm28ζ group. Simultaneously, there was less efflux from tumour to blood (K_2), as the

tracer was internalised by CAR T cells rather than freely diffusing in and out of the tumour (Table 7.1).
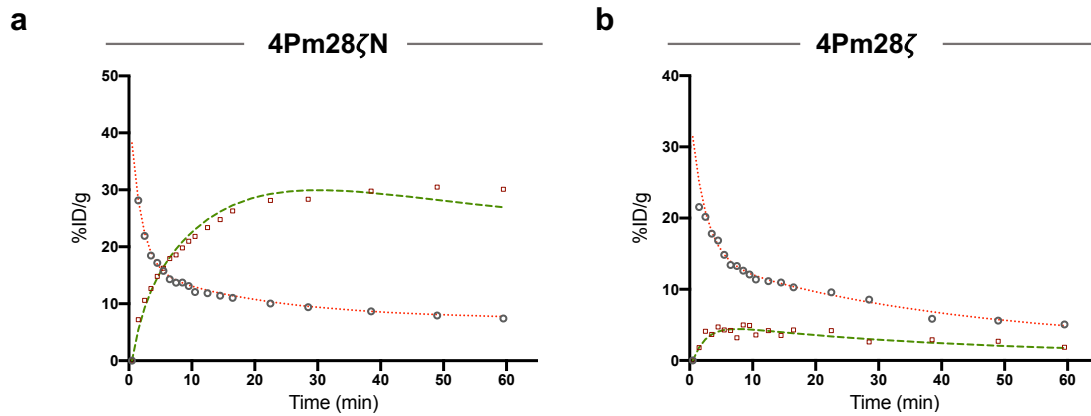
Figure 7.11: Two-compartment model fits the dynamic data. A forcing function (red dotted line) was applied to the blood measurements (grey circles). The average tumour uptake is represented by the square dots and the green dotted line represents the fitted model for 4Pm28ζN a) and 4Pm28ζ (hNIS control) b) groups .

Table 7.1: **Rate constant values estimated by two-compartment models fitted with data from 4Pm28ζN and 4Pm28ζ T cell treated animals.**

Rate constant	4Pm28ζN		4Pm28ζ	
	Value (SD)	95% confidence interval	Value (SD)	95% confidence interval
K_1	0.19 (0.030)	0.12 to 0.25	0.07 (0.01)	0.04 to 0.10
K_2	0.09 (0.044)	-0.002 to 0.18	0.21 (0.05)	0.11 to 0.32

The accumulation of $^{99m}TcO_4^-$ varied across 4Pm28ζN treated animals, as shown in Figure 7.9. This variability was mirrored in the different values of the rate constants extracted from applying the two-compartment model to each individual animal (Table 7.2) and in the V_T values obtained from the Logan plots (Table 7.3). The higher the infiltration of 4Pm28ζN T cells at the tumour site, the more $^{99m}TcO_4^-$ is transferred from the blood to the tumour, resulting in larger K_1 values and less efflux of $^{99m}TcO_4^-$ from the tumour (K_2). As previously

described, V_T equals K_1/K_2 in the case of two-compartment models. In fact, the ratio of K_1/K_2 obtained from the compartmental modelling showed similar results to the V_T obtained from the Logan plot (Table 7.3), further confirming the robust fit of the two-compartment model.

Table 7.2: **Rate constant values estimated by two-compartment models fitted with individual data from 4Pm28ζNCAR T cell treated animals.**

Rate constant	4Pm28ζN (•)		4Pm28ζN (■)	
	Value (SD)	95% confidence interval	Value (SD)	95% confidence interval
K_1	0.0891 (0.008)	0.07 to 0.10	0.1604 (0.017)	0.04 to 0.10
K_2	0.0363 (0.009)	0.01 to 0.05	0.0723 (0.013)	0.12 to 0.19

	4Pm28ζN (▲)	
Rate constant	Value (SD)	95% confidence interval
K_1	0.2206 (0.024)	0.17 to 0.26
K_2	0.0394 (0.009)	0.02 to 0.06

Table 7.3: **V_T and rate constant values estimated by the Logan plot and two-compartment model fitted with individual data from 4Pm28ζN treated animals.**

4Pm28ζN (•)		4Pm28ζN (■)		4Pm28ζN (▲)	
V_T	Ratio K_1/K_2	V_T	Ratio K_1/K_2	V_T	Ratio K_1/K_2
2.58	2.45	2.43	2.41	5.20	5.60

Ultimately, to non-invasively quantify CAR T cell infiltration at the tumour site from SPECT images, these values were correlated with the number of CD3$^+$ cells quantified from the tumour slices after immunohistochemical staining. There was a robust correlation

between the *ex vivo* quantitation of the CD3$^+$ cells in the tumour slices and the V_T values obtained from the graphical modelling (Figure 7.12 a). A similar correlation was also observed comparing the K_1/K_2 obtained from the compartment model (Figure 7.12 b).
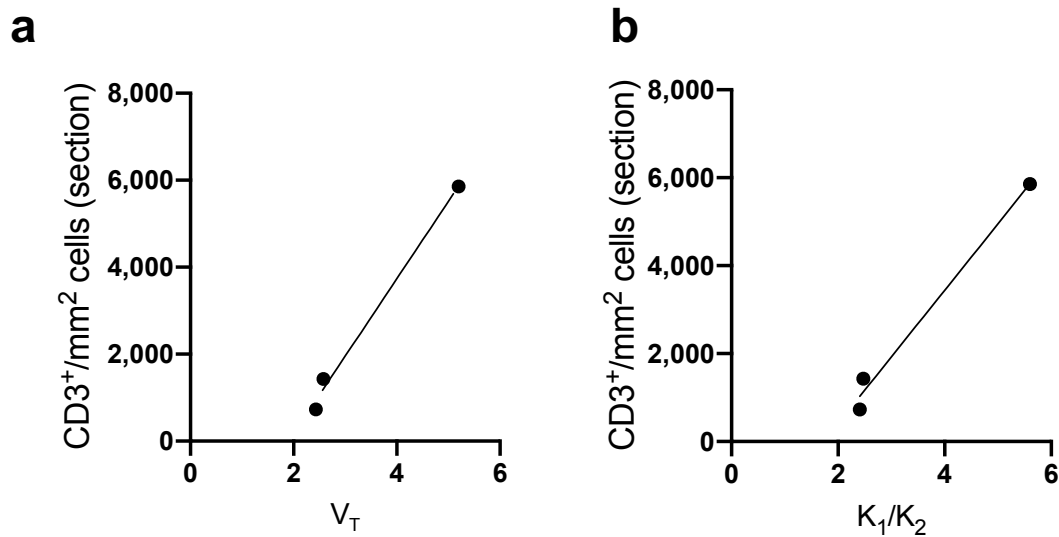
Figure 7.12: Correlation between the rate constants from the modelling and the quantified CD3$^+$ T cells in 4Pm28ζN treated tumours. Robust correlation between the *ex vivo* quantitation of the CD3$^+$ cells in the tumour slices and a) the V_T value obtained from the Logan Plot (r = 0.9969) or b) the K_1/K_2 ratio from the two-compartment model (r = 0.9940).

7.1 Summary

This data established the proof of concept for the *in vivo* non-invasive quantitation of infiltrating CAR T cells through the application of mathematical models. The placement of tumour xenografts in the flank resulted in heightened CAR T cell infiltration compared to previous experiments where tumours were implanted in the shoulder/neck area. This appeared to foster a more homogeneous infiltration pattern and substantial tumour uptake surpassing perfusion levels in comparison to previous experiments. The augmented signal-to-background

ratio facilitated the development of a two-tissue compartment model, incorporating blood and tumour compartments.

The fitting of Logan plots and two-compartment models to the dynamic data yielded congruent values for V_T and the K_1/K_2 ratio. Notably, narrow confident intervals were obtained from the two-compartment modelling, demonstrating the robustness of the fit. These values exhibited a compelling correlation with the number of $CD3^+$ in the tumour slices. Although the power of the study was limited by the small sample number, these finding strongly support the feasibility of employing mathematical modelling to non-invasively assess CAR T cell dynamics *in vivo*.

Chapter 8

Discussion

CAR T cell immunotherapy has revolutionised cancer treatment for haematological diseases. However, this remarkable success has yet to be replicated in the treatment of solid tumours, mainly owing to the intricate complexities inherent to the TME. CAR T cells circulating in the bloodstream must reach the tumour site, extravasate from the disrupted vasculature and survive amidst the immunosuppressive microenvironment to trigger a therapeutic response. Tailoring the dosage of CAR T cells required at the tumour site for achieving tumour remission hinges on the ability to monitor CAR T cell infiltration and quantify their numbers effectively.

In this work the non-invasive *in vivo* longitudinal monitoring and *in vivo*/*ex vivo* quantitation of CAR T cells was achieved in a prostate cancer model through the co-expression of the reporter gene hNIS with a PSMA-targeting CAR. The hNIS is a transmembrane transporter responsible for the uptake of iodide within the thyroid, salivary, gastric and mammary glands. It is also able to transport clinically relevant radionuclides, such as $^{99m}TcO_4^-$ and ^{18}F-tetrafluoroborate, allowing the tracking of cells with ectopic hNIS expression through SPECT and PET, respectively. The human origin of the reporter gene renders it non-immunogenic. Furthermore, the hNIS, upon interaction with the tracer, remains on the cell surface preserving its sensitivity. This is an advantage over the use of receptor-like

reporter genes, such as SSTR2, which are susceptible to internalisation. The hNIS is only functional on viable cells as the internalisation of $^{99m}TcO_4^-$ is linked to the transmembrane sodium gradient created by the Na^+/K^+ ATPase pump, providing *in vivo* localisation of live cells exclusively. This presents an advantage compared to direct labelling techniques[86, 87, 90]. These characteristics make the hNIS an excellent reporter gene for cell tracking *in vivo*. In the field of nuclear medicine, mathematical models are used to describe the pharmacokinetics of tracer biodistribution *in vivo*. An example of mathematical modelling is compartmental modelling where the entity, such as a tracer, being quantified exists in multiple compartments at a given time. Tracer concentration in each compartment changes as a function of time (t) and the flow between compartments is described by rate constants K. The use of the hNIS was proposed as an imaging tool to develop a compartmental model aimed at quantifying the exchange of tracer between the bloodstream and the CAR T cells that have infiltrated the tumour. The rate constants obtained from the modelling could be further correlated with the number of infiltrated CAR T cells, quantified *ex vivo* from the excised tumour samples by flow cytometry or immunohistochemistry.

Expression of the reporter gene did not impede cell proliferation during the transduction process, despite the larger vector size, achieving about 18-fold expansion. The predominant phenotype in the resulting CAR T cell product was effector memory, defined as CD45RA$^-$ CCR7$^-$. These CAR T cells exhibited robust and antigen-dependent anti-tumour activity, which was retained when the CAR T cells were labelled with $^{99m}TcO_4^-$. Exposing the CAR T cells to the required tracer concentrations for *in vivo* tracking did not induce apoptosis or radiation-induced DNA damage. Higher concentrations of $^{99m}TcO_4^-$ did induce apoptosis although it was transient and reversible. Furthermore, the CAR T cells were able to take up the tracer multiple times, enabling repetitive and longitudinal imaging of CAR T cell biodistribution *in vivo*.

In vitro assays demonstrated a direct correlation between the number of CAR T cells and the total amount of internalised tracer. However, no such correlation existed between the total tracer uptake and the number of hNIS transporter copies expressed on the cell surface. The uptake of $^{99m}TcO_4^-$ via hNIS relies on the sodium gradient established by the Na^+/K^+ ATPase pump, consequently, extracellular sodium levels may exert a more significant influence on the regulation of tracer uptake compared to the number of gene copies on the cell surface. However, this hypothesis remained unexplored.

In vivo, high sensitivity and resolution were achieved using the 3mm pinhole XXUHS-M collimator. Although the extent of uptake varied among donors, on average, the limit of detection was established at 5,000 CAR T cells. Following i.v. administration in tumoured animals, CAR T cell clusters were clearly visualised as distinct hot spots in the SPECT images. These findings were corroborated by IHC staining, confirming the presence of these clusters surrounding tumour blood vessels. However, infiltration was limited in this prostate cancer model with shoulder xenografts and the majority of the CAR T cells remained around the tumour border unable to penetrate the tumour. This contributed to the challenges faced by the mathematical model, which were addressed when the number of infiltrating CAR T cells greatly exceeded the limit of detection of the collimator, as observed in the mouse model with tumours located on the flank.

The development of the compartmental model faced two significant challenges. Firstly, CAR T cell infiltration was limited in our shoulder xenograft mouse model, resulting in suboptimal signal-to-noise ratio despite using the most sensitive collimator available, the XXUHS-M collimator. Employing this collimator, the limit of detection for the SPECT camera was established at an average of $5x10^3$ CAR T cells. The number of CAR T cells quantified by flow cytometry exhibited considerable variability between day 9 and day 12 post ACT, ranging from $3.4x10^2$ to $9.9x10^5$ T cells. The limited infiltration significantly

undermined the statistical power of the study, as eleven out of eighteen tumour samples fell below the established limit of detection.

Secondly, compartmental models rely on the assumption that tracer concentration remains uniform within a given compartment. However, the experiments presented in this thesis consistently revealed heterogeneous infiltration patterns of CAR T cell in the SPECT images, which were subsequently confirmed through *ex vivo* IHC analysis. CAR T cells tended to accumulate primarily at the periphery of the tumours, forming a distinctive ring-like pattern around the tumour's edge. This observation suggests the presence of a dense tumour stroma acting as a physical barrier or lack of nutrients and oxygen, however, this hypothesis remained unexplored. IHC analysis further illustrated the limited penetration of CAR T cells, which accumulated mainly in the connective tissue. Additionally, these findings indicated that the degree of CAR T cell infiltration was influenced by the timing of tumour treatment. Tumours treated shortly after they were established, with an average tumour size of 65 mm^3, demonstrated significantly higher levels of infiltrating CAR T cells compared to tumours treated when they had grown to an average size of 180 mm^3. This disparity is likely attributed to the minimal variations in vascularisation between the two tumour sizes due to the rapid growth kinetics observed in this model. This difference was apparent both in the increased uptake levels within the treated tumours and the greater number of CD3 positive cells quantified after IHC analysis of tumour slides from tumours treated at early stages.

Tumours treated at early stages not only showed a higher number of infiltrating CAR T cells but the CAR T cells were distributed both around and within the tumour. This distribution was characterised by hot spots of maximum tracer uptake surrounded by areas with minimal uptake. IHC analysis demonstrated the presence of CAR T cells in proximity to blood vessels, suggesting the ability of the circulating CAR T cells to extravasate from the blood vessels at the tumour site, although limited migration within the tumour tissue was

observed. No circulating CAR T cells were detected in the bloodstream by flow cytometry 7 days after ACT.

In order to non-invasively quantify CAR T cell infiltration, ROIs were placed over the entire tumour guided by the CT anatomical data. Typically, the quantified radioactivity from SPECT images is presented in terms of either %ID or %ID/g. However, presenting data as %ID, i.e. total tumour radioactivity uptake as a percentage of the amount of radioactivity administered, has the inherent limitation that it can be heavily influenced by the total volume encompassed within the ROI. Larger ROIs will increase the quantitation levels due to increased non-specific uptake in addition to specific uptake. Consequently, comparing the uptake of tumours of different sizes can be challenging. To address this issue, it is common practice to express the uptake as a concentration, % ID/g. This allows for a fair comparison of tumour uptake regardless of the tumour size. However, it has its drawback in that it may dilute the specific signal if uptake within the tumour is heterogenous. Larger tumours tend to have bigger areas with minimal uptake, potential masking the differences in specific signal when normalised to volume. Given the heterogeneous uptake patterns observed in the presented studies, quantifying tumour uptake as % ID aligned better with the changes in signal visualised in the SPECT images. Moreover, this approach closely followed the pattern seen during the *ex vivo* quantification of CAR T cells using flow cytometry. Thus, although this method carries some inherent bias, the %ID data provided a more accurate representation of CAR T cell infiltration in the shoulder xenograft model.

Similar levels of radiotracer perfusion were quantified in tumours of animals treated with PBS or untransduced cells, indicating comparable vascular density in these tumours. Perfusion was quantified at approximately 0.5% of the injected dose, while signal from treated tumours ranged from 0.3-3% of the injected dose, with an average of 1.76% of the injected dose. To establish the ground truth for the mathematical model, the number of CAR T cells within the tumour was quantified by flow cytometry on excised tumour samples. The

isolation of CAR T cells from the tumours presented challenges due to the limited CAR T cell infiltration, and a percoll gradient centrifugation was an important step during the isolation to clear debris and tumour cells (Figure S 8.2). The number of CAR T cells quantified by flow cytometry greatly varied over time, ranging from 3.4×10^2 to 9.9×10^5 T cells. The *ex vivo* data revealed a gradual increase in the number of T cells infiltrating the tumours, which corresponded with the rising SPECT signal over time, resulting in a moderate positive correlation between *in vivo* and *ex vivo* quantitation.

The existing methods for quantifying infiltrating CAR T cells rely on establishing a standard curve that correlates labelled T cells doses with the SPECT imaging signal, whether in *in vivo* or *in vitro* phantoms studies. During the assessment of the SPECT camera's limit of detection (Figure 4.9 b), a standard curve was established and used to estimated the number of infiltrating CAR T cells based on the quantified SPECT signal. In this experiment, the estimated CAR T cell count significantly deviated from the *ex vivo* quantitation determined flow cytometry. This discrepancy suggests that the simplicity of this approach may not be sufficient for accurate quantitation.

Therefore, to delve deeper into the correlation between tracer uptake by the tumour and the quantity of infiltrating CAR T cells, the dynamic SPECT data was quantified as %ID/g and mathematical models were applied to the data. Presenting the data as %ID/g effectively homogenises the signal across the tumour, aligning with the assumption of uniform tracer distribution within a given compartment. The International Commission on Radiological Protection offers biokinetic models for various tracers[167]. In the case of iodide, the model subdivides the thyroid gland into two compartments to accomodate iodide organification. Our proposed three-compartment model draws parallels with this model, dividing the tumour compartment into two subcompartments to account for free and internalised tracer by the CAR T cells. However, unlike iodide, $^{99m}TcO_4^-$ does not undergo organification. Additionally, there is potential for tracer internalised by the CAR

T cells to re-enter the vasculature if the $^{99m}TcO_4^-$ concentration in blood is insufficient, suggesting that the reversible two-compartment model is more suitable. This choice was further reinforced by the results from the Logan and Patlak methods. These graphical models facilitated the visualisation of a reversible two-compartment model or an irreversible three-compartment model, respectively. The Logan plot demonstrated a linear trend for both treated and control animals, indicating that the reversible two-compartment model describes the system appropriately.

Despite efforts to fit a model to the dynamic SPECT data, challenges arose due to the presence of sizable regions with minimal uptake, typically observed at the tumor core, and the limited extent of infiltration. Consequently, the uptake in treated tumors did not exceed perfusion levels, introducing substantial uncertainties when attempting to extract the rate constants to define the exchange of tracer between the bloodstream and the tumor. In an effort to improve the quantitation and truly represent a homogeneous uptake signal per gram of tissue, a thresholding method was applied. This method incorporated into a new ROI those voxels with a signal exceeding 2.5% ID/g while disregarding voxels with minimal uptake. This approach provided homogeneous concentrations within the tumour compartment without diluting the true signal. When the same thresholding approach was applied to the control groups, no significant differences were observed between the treated and control groups, suggesting that most of the quantified uptake in treated tumours is associated with tumour perfusion rather than specific to CAR T cell uptake.

To further optimise the image-derived quantitation method, the SPECT dynamic data was thresholded to incorporate those voxels with the highest uptake at the centre of a 3x3x3 cube of voxels. This method ensured the quantitation of peak uptake while maintaining uniform signal across all voxels included in the ROI, complying with the assumption of homogeneous distribution within the tumour compartment. All ROIs were placed over hot spots within the treated tumours, guaranteeing that the signal originated from a cluster of infiltrating CAR

T cells. Although this method led to differences between the control and treated groups, indicating the presence of CAR T cells at the tumour site in line with the flow cytometry results, it still yielded notable uncertainties in the modelling fit.

Based on these results it was hypothesised that in order to establish a compartmental model defining CAR T cell dynamics, CAR T cell infiltration needs to be boosted, ensuring that the specific uptake signal surpasses perfusion levels and the detection limit of the SPECT camera. This hypothesis was supported by the data obtained from the flank xenograft mouse model. In this model, 4Pm28ζN T cell infiltration was enhanced, leading to a more homogeneous infiltration pattern and improved signal-to-noise ratio, which ultimately allowed for non-invasive quantitation of CAR T cells through compartmental modelling. In these flank tumours, 4Pm28ζN T cells were distributed throughout the tumour tissue, with a preference for clustering around blood vessels. There was limited infiltration at the tumour core, characterised by the absence of tumour vessels and loss of nuclei staining, suggesting the presence of necrotic tissue. The more homogeneous distribution of CAR T cells within the tumours, demonstrated both by the SPECT and IHC images, aligned with the assumption of no gradients within a given compartment for compartmental modelling, while still accurately representing the extent of CAR T cell infiltration.

Due to the tumour location on the flank, animals were dynamically imaged with the GP-RM collimator, benefiting from its larger field of view to record 1-minute frames. The XXUHS-M was not used as the small field of view would not have permitted dynamic imaging with short frames. The high number of infiltrating 4Pm28ζN T cells mitigated the lower sensitivity of this collimator, achieving excellent signal-to-noise ratio. As described above, a Logan plot and a two-compartment model were fitted to the dynamic data. The volume of distribution (V_T) obtained from the slope of the linear trend in the Logan plot, represented the concentration factor of $^{99m}TcO_4^-$ in the tumour compared to blood at equilibrium. V_T can also be expressed as the ratio of K_1/K_2. This ratio of K_1/K_2 was obtained from fitting

the two-compartment model. The values obtained from the graphical and two-compartment model were comparable, demonstrating the robust fit achieved by the two-compartment model. Both the V_T and the ratio of K_1/K_2 correlated strongly with the number of CD3 positive cells quantified *ex vivo* through immunohistochemistry. This small-scale study illustrated the feasibility of applying mathematical models for non-invasive and *in vivo* quantitation of CAR T cells.

In studies involving mouse models with limited CAR T cell infiltration, such as our shoulder xenograft models, more advanced imaging analysis could provide a solution for the analysis of the dynamic SPECT data, where CAR T cell infiltration is heterogeneous and restricted. This advanced analysis could subsequently be integrated into the described two-compartment model. One example is the application of voxel-wise analysis, which is based on the analysis and modelling of each individual voxel within an ROI. This approach provides greater sensitivity to heterogeneity, capturing small tracer changes in each specific voxel. However, it comes with increased computational complexity and greater sensitivity to noise, rendering the interpretation of the results more challenging. Voxel-wise compartment modelling strategies are already being applied in the clinical setting for the analysis of dynamic PET data, specifically for characterising the heterogeneous tumour uptake of gliomas using ^{18}F-FET[168] and for employing ^{18}F-FDG total-body compartmental modelling[169].

Limited infiltration is a well-recognised obstacle in the treatment of solid tumours, and various strategies are being developed to enhance T cell homing and infiltration. For example, CAR T cells have been designed to target stromal cells or to secret enzymes capable of degrading the tumour matrix to overcome the stroma physical barrier[75]. Expression of favourable CCRs has proven effective in rectifying the mismatch between the chemokines expressed by tumours and the CCRs expressed on the CAR T cell surface[28,77]. To counteract the immunosuppressive TME, armoured CAR T cells have been designed to produce pro-inflammatory cytokines, thereby locally modulating the TME[40–42]. Combination therapies

involving CAR T cells and immune checkpoint blockade inhibitors have also been shown to improve treatment outcomes[15]. However, most of these studies assess the changes in CAR T cell infiltration *ex vivo*, providing insights only at specific end points.

The quantitative imaging approach developed here could provide valuable information on the dynamic process of T cell infiltration by the repetitive monitoring of CAR T cell infiltration and proliferation, assessing the effectiveness of novel CAR T cell designs or combinatory treatments in a non-invasive and longitudinal manner. This would increase the volume of data collected while minimising the need to expose large number of patients to ineffective doses of CAR T cells in clinical trials. Furthermore, this tool also provides valuable insights into T cell proliferation and its relationship to treatment outcomes, aiding in determining optimal dosing and timing for downstream *ex vivo* analysis.

While the described research focused on PSMA-targeting CAR T cells with SPECT-based monitoring, the hNIS reporter gene is a versatile tool. It can be incorporated directly into the CAR-expressing construct, as described in this thesis, or it could be incorporated by co-transducing an already developed CAR-expressing construct with a hNIS-expressing construct to study the biodistribution of existing CAR T cell products. Furthermore, for *in vivo* monitoring in the clinical context, PET imaging can be employed, utilising hNIS compatible tracers, offering fast dynamic imaging and greatly increased sensitivity.

8.1   Conclusion

The present study successfully demonstrated the feasibility of employing a compartmental modelling-based mathematical approach to non-invasively quantify CAR T cell infiltration *in vivo*. Use of the hNIS reporter gene proved to be an effective strategy, not only for non-invasive CAR T cell tracking but also for providing insights into the number of CAR T cells infiltrating the tumor. While the mathematical model was developed using a limited

sample size, it serves as a promising foundation for further research and development in this area.

8.2 Future work

To consolidate the findings presented in this preliminary study, future work should focus on increasing the sample size, a limiting factor in the current study. Larger sample number per groups are needed to confirm the differences observed in uptake curves between hNIS-expressing (4Pm28ζN) and hNIS-control (4Pm28ζ) CAR T cell treated groups, and refine the proposed compartmental model. Validation of the optimised protocol would subsequently involve the acquisition of additional data.

To refine the proposed compartmental model, future work could focus on examining circulating CAR T cells and distribution of $^{99m}TcO_4^-$ to other organs. Although CAR T cells were not detected in circulation at the established time points, a more comprehensive evaluation could provide insights into the contribution of $^{99m}TcO_4^-$ internalised by circulating CAR T cells to the total quantified $^{99m}TcO_4^-$ in the blood. qPCR could be used to increase the detection sensitivity compared to flow cytometry. If there are indeed circulating CAR T cells modifying the $^{99m}TcO_4^-$ concentration in blood, the blood compartment could then be divided in two subcompartments to account for free $^{99m}TcO_4^-$ in plasma and $^{99m}TcO_4^-$ internalised by the circulating CAR T cells. The blood compartment was fixed using a forcing function due to the lack of data related to excretion and biodistribution of $^{99m}TcO_4^-$ to other organs. Whole-body imaging could be incorporated to collect this data, providing also information about the biodistribution of CAR T cells beyond the tumour, potentially requiring additional compartments in the model if significant trafficking and accumulation in other organs is observed.

The integration of autoradiography into the *ex vivo* analysis, could facilitate the correlation of $^{99m}TcO_4^-$ uptake with the distribution of CAR T cells within the tumour. Colocalising

autoradiography slides with CD3 stained IHC slides would enable the study of specific areas, providing more information beyond the whole tumour comparisons presented in this work.

To generalise the use of the compartmental model across different donors, a normalisation factor must be implemented. This factor, could be derived from the *in vitro* $^{99m}TcO_4^-$ uptake assay performed on the day of CAR T cell injection, and could be incorporated into the model to account for donor-dependent variations in SPECT signal.

This thesis pioneers the validation of a mathematical model designed to quantify CAR T cells *in vivo*. It serves as the initial proof of concept for further research to fully unlock the potential of mathematical modelling for the non-invasive quantitation of genetically modified CAR T cell therapies.

Supplementary data
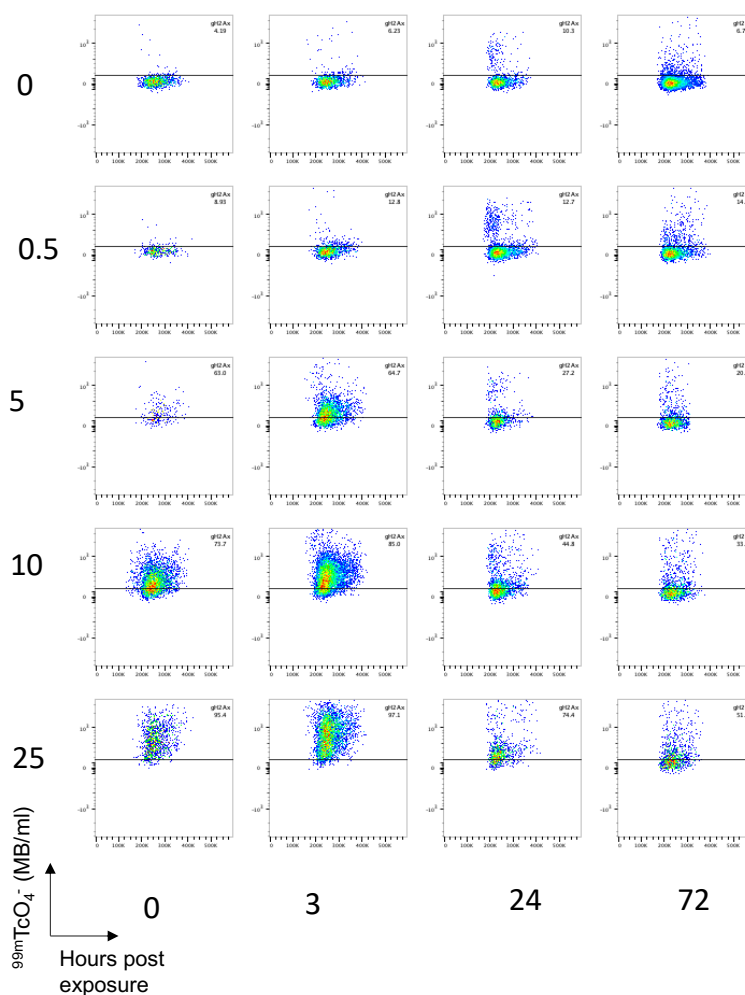
Figure 8.1: Radiation-induced DNA damage. Representative flow cytometry plots from 4Pm28ζN exposed to increasing amounts of $^{99m}TcO_4^-$. DNA damage was assessed by staining for intracellular γH2Ax at the listed time points post exposure.

.
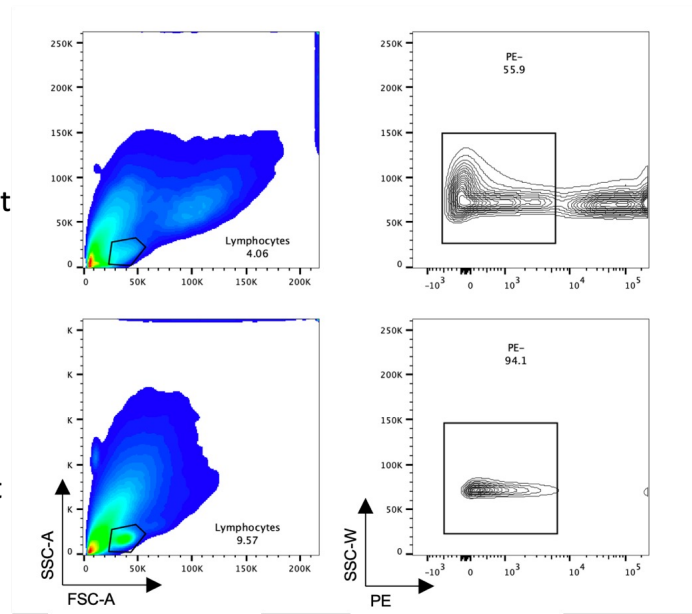
Figure 8.2: Percoll gradient centrifugation essential in the isolation of infiltrating CAR T cells. The use of percoll during the isolation of infiltrating CAR T cells in the excised tumours, minimised the detection of debris and PE^+ tumour cells.

.
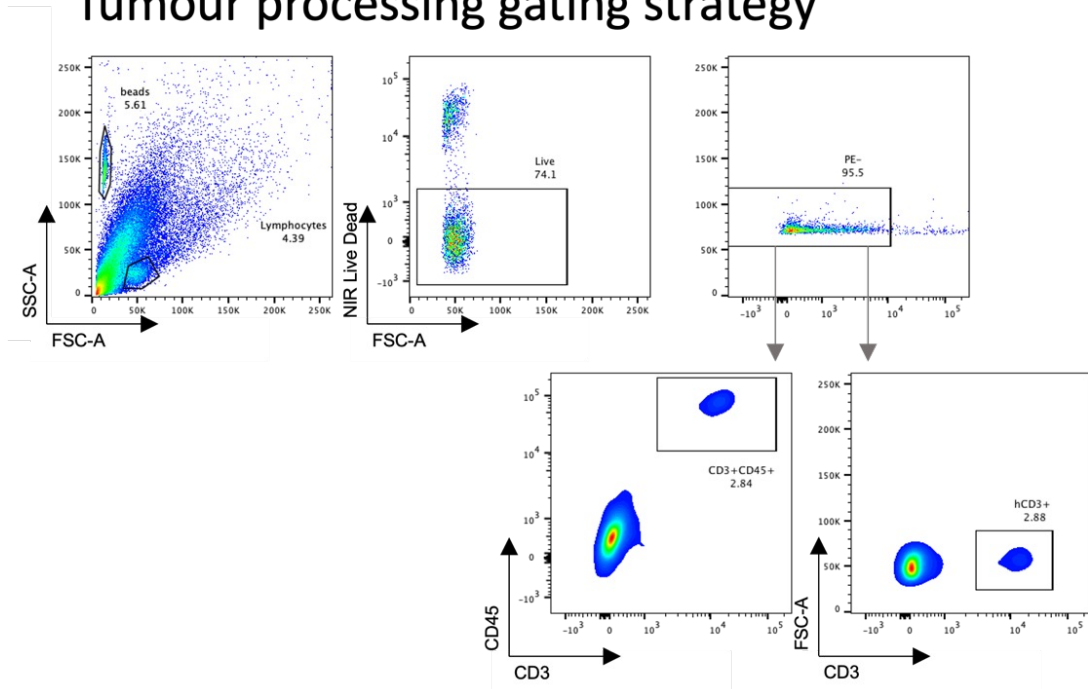
Figure 8.3: Gating strategy for quantifying infiltrating CAR T cells by flow cytometry. Tumours were processed to a single cell dilution as shown in Figure 6.1. The gating strategy begins with the exclusion of debris and dead cells, and the detection of fluorescence beads for quantitation. Tumour cells are excluded using a PE gate. Human T cells are defined as $CD45^+$ and $CD3^+$.
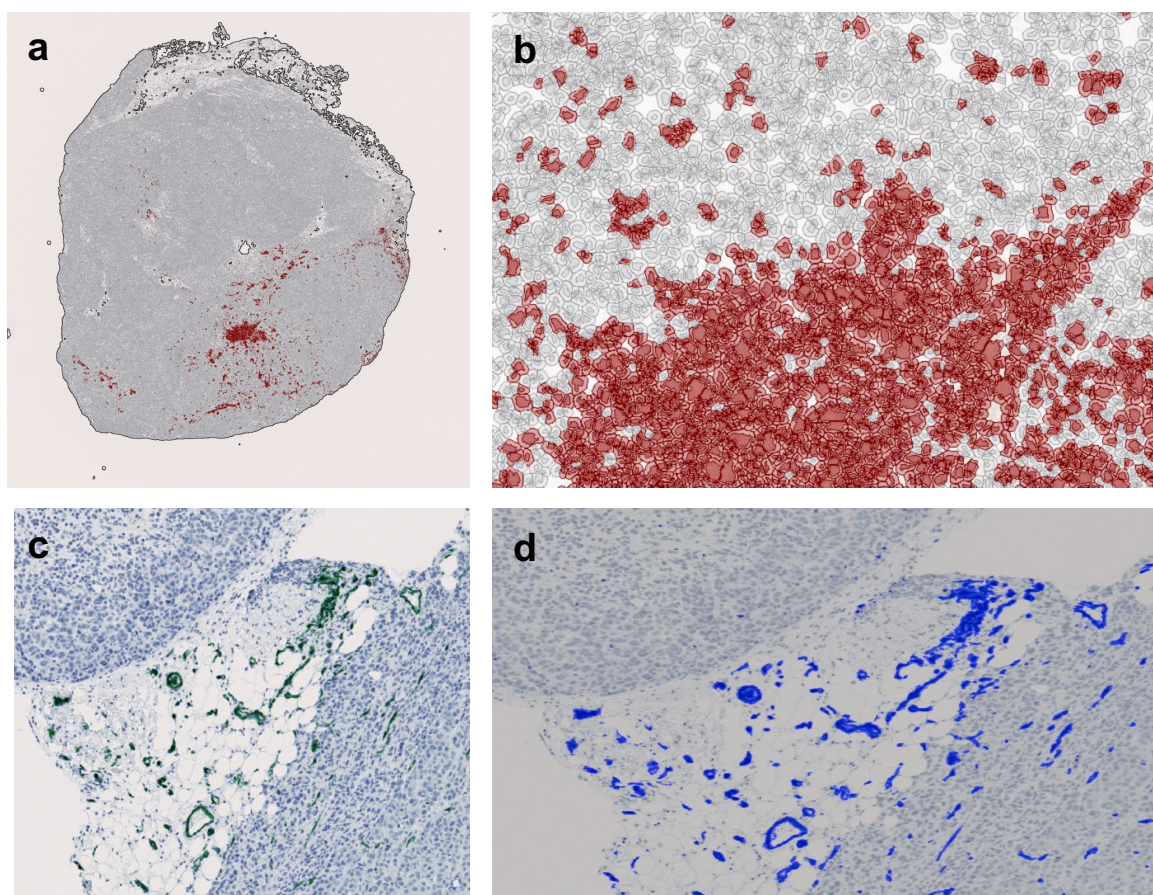
Figure 8.4: Illustration of QuPath's quantitation of CD3 T cells and blood vessels. Representative example of the 'positive cell detection' command used for the quantitation of $CD3^+$ T cells (a & b) or CD31 blood vessel marker (c & d). a) Full tumour sections showing the detection of $CD3^+$ T cells in red. b) Zoom in from a). c) Tumour section showing the presence of blood vessels ($CD31^+$) in green. d) Result of applying the 'positive cell detection' command (blue) on image c) to quantify CD31 expression.

.
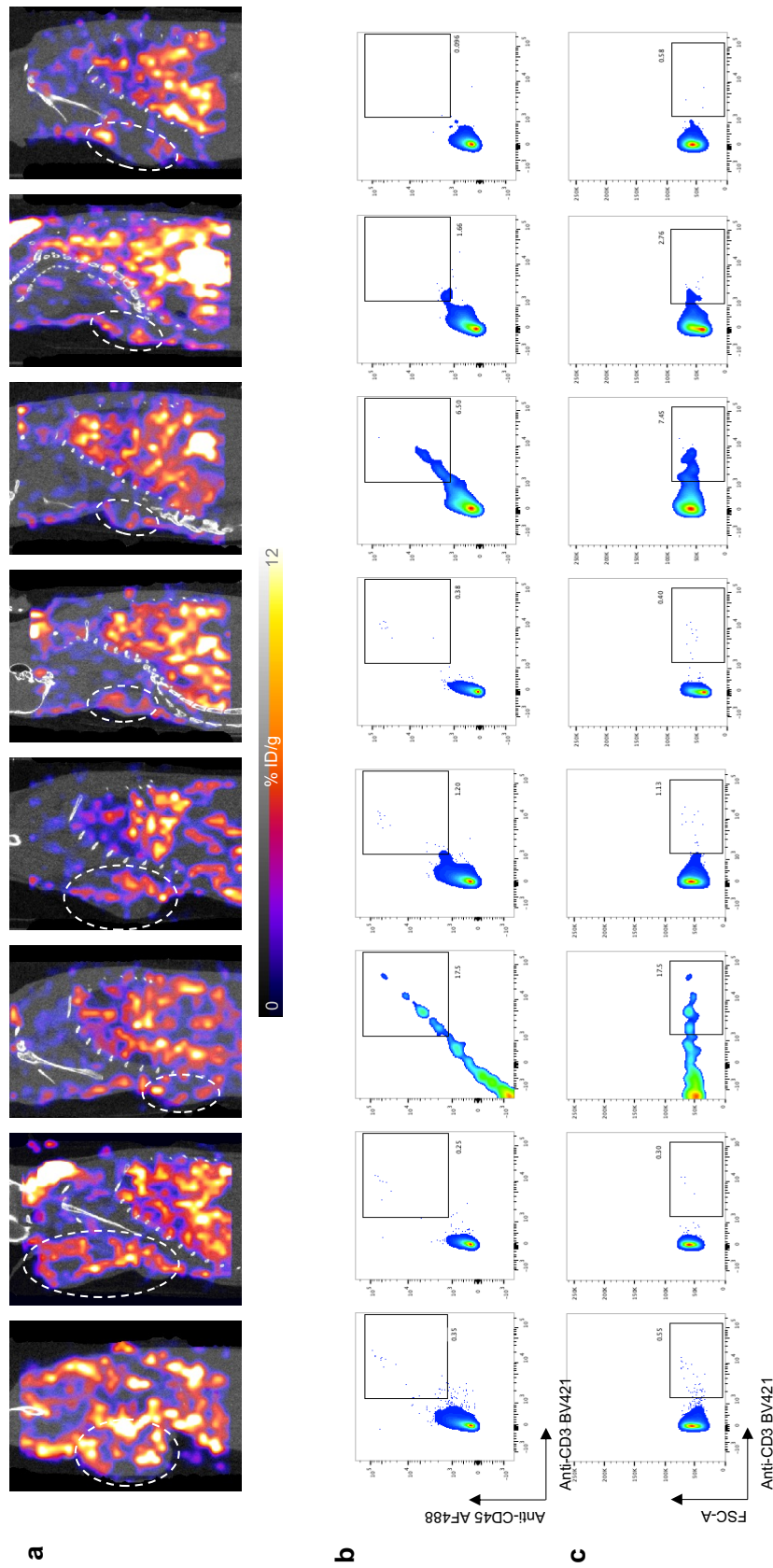
Figure 8.5: *In vivo* and *ex vivo* **detection of CAR T cells in tumour bearing xenografts nine days post ACT.** a) SPECT/CT images showing the infiltration of CAR T cells on tumour xenografts on day 9 post ACT after the administration of 10 MBq of ^{99m}TcO$_4$⁻. Dashed circle represents tumour location. b) Flow cytometry plots detecting the presence of double positive hCD3$^+$hCD45$^+$ T cells or (c) single positive hCD3$^+$ in tumours depicted in a). ACT=adoptive cell transfer. Each image/plot represents a different mouse and flow cytometry plots match SPECT/CT images. n=8 mice.

233
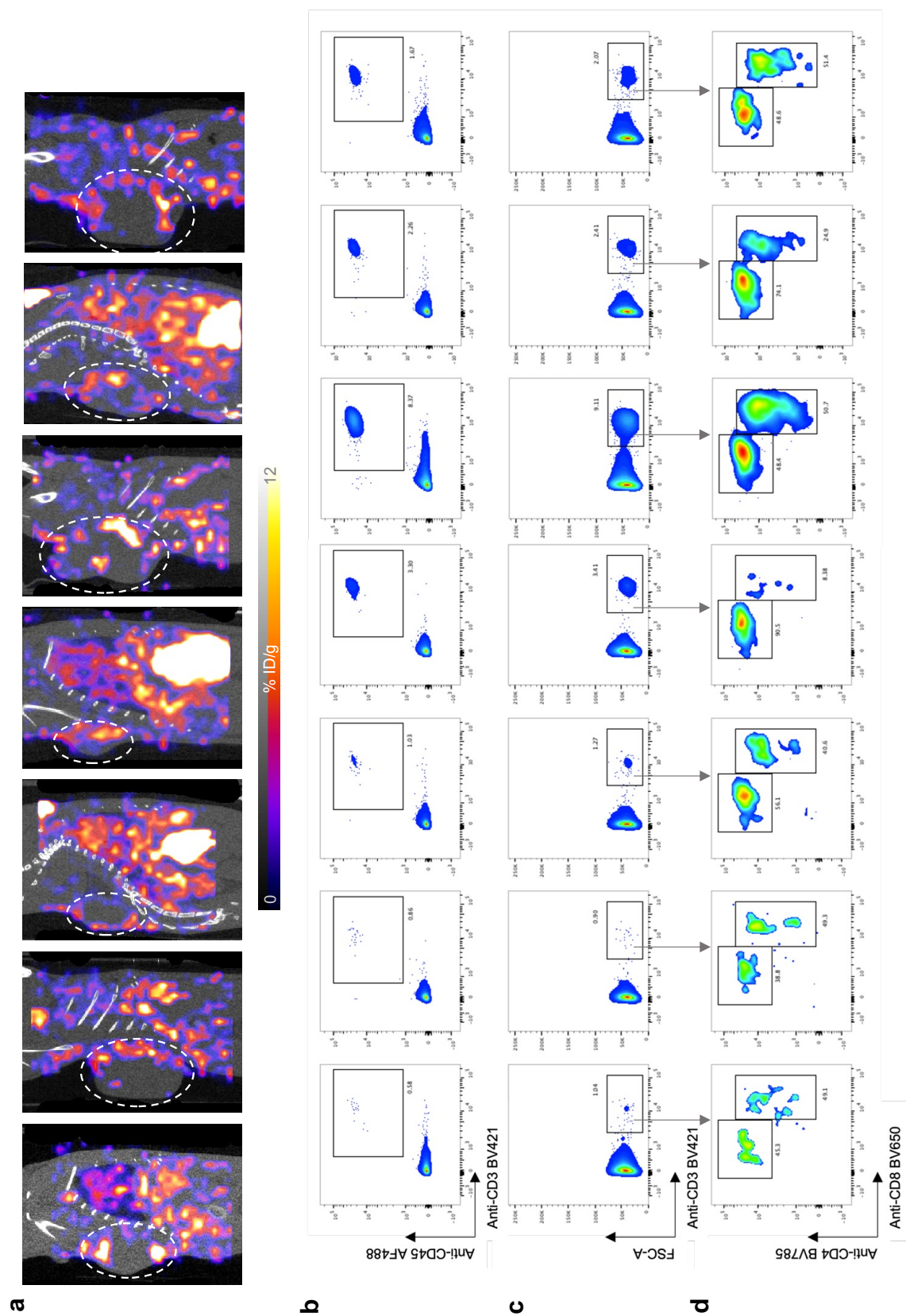
Figure 8.6: *In vivo* and *ex vivo* detection of CAR T cells in tumour bearing xenografts twelve days post ACT. a) SPECT/CT images showing the infiltration of CAR T cells on tumour xenografts on day 12 post ACT after the administration of 10 MBq of $^{99m}TcO_4^-$. Dash circle represents tumour location. b) Flow cytometry plots detecting the presence of double positive hCD3$^+$hCD45$^+$ T cells or (c) single positive hCD3$^+$ in tumours depicted in a). d) Detection of CD8 and CD4 T cells from gating in b). ACT=adoptive cell transfer. Each image/plot represents a different mouse and flow cytometry plots match SPECT/CT images. n=7 mice.

Figure 8.7: *In vivo* **and** *ex vivo* **detection of CAR T cells in tumour bearing xenografts fourteen days post ACT.** a)SPECT/CT images showing the infiltration of CAR T cells on tumour xenografts on day 14 post ACT after the administration of 10 MBq of $^{99m}TcO_4^-$. Dash circle represents tumour location. Each image represents a different mouse. b)Flow cytometry plots detecting the presence of double positive hCD3$^+$hCD45$^+$ T cells or (c) single positive hCD3$^+$ in tumours depicted in a). d) Detection of CD8 and CD4 T cells from gating in b). ACT=adoptive cell transfer. Each image/plot represents a different mouse and flow cytometry plots match SPECT/CT images. n=3 mice.
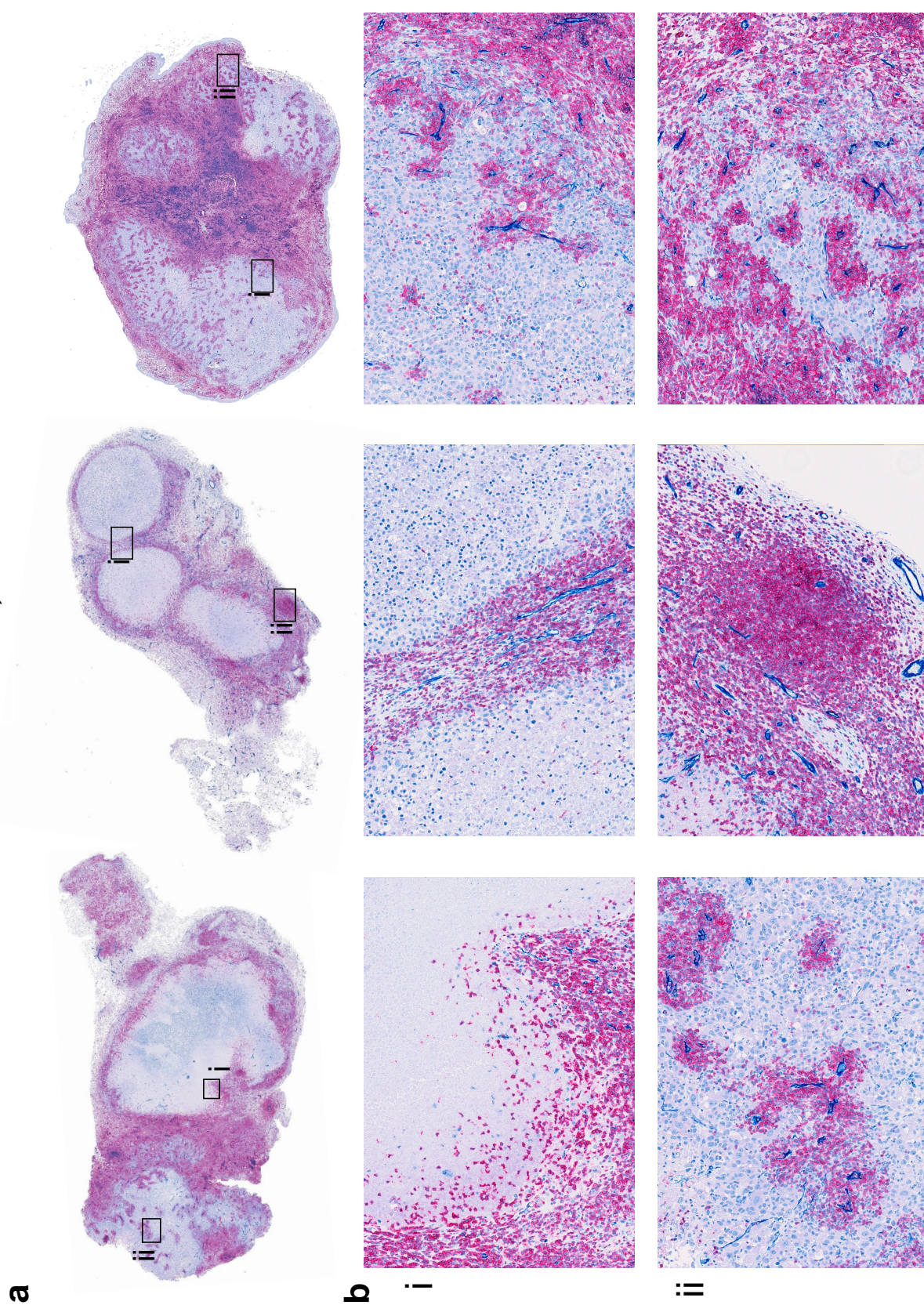
Figure 8.8: *Ex vivo* analysis of infiltrating CD3^{+} T cells by immunohistochemistry. a) Paraffin embedded tumour slices were stained for human CD3 (pink) and CD31 (dark blue). b) Higher magnification images showing the pattern of infiltration. Location of magnification shown by the black squares (i, ii) on a). Scale bar: 0.1 mm. n=3.
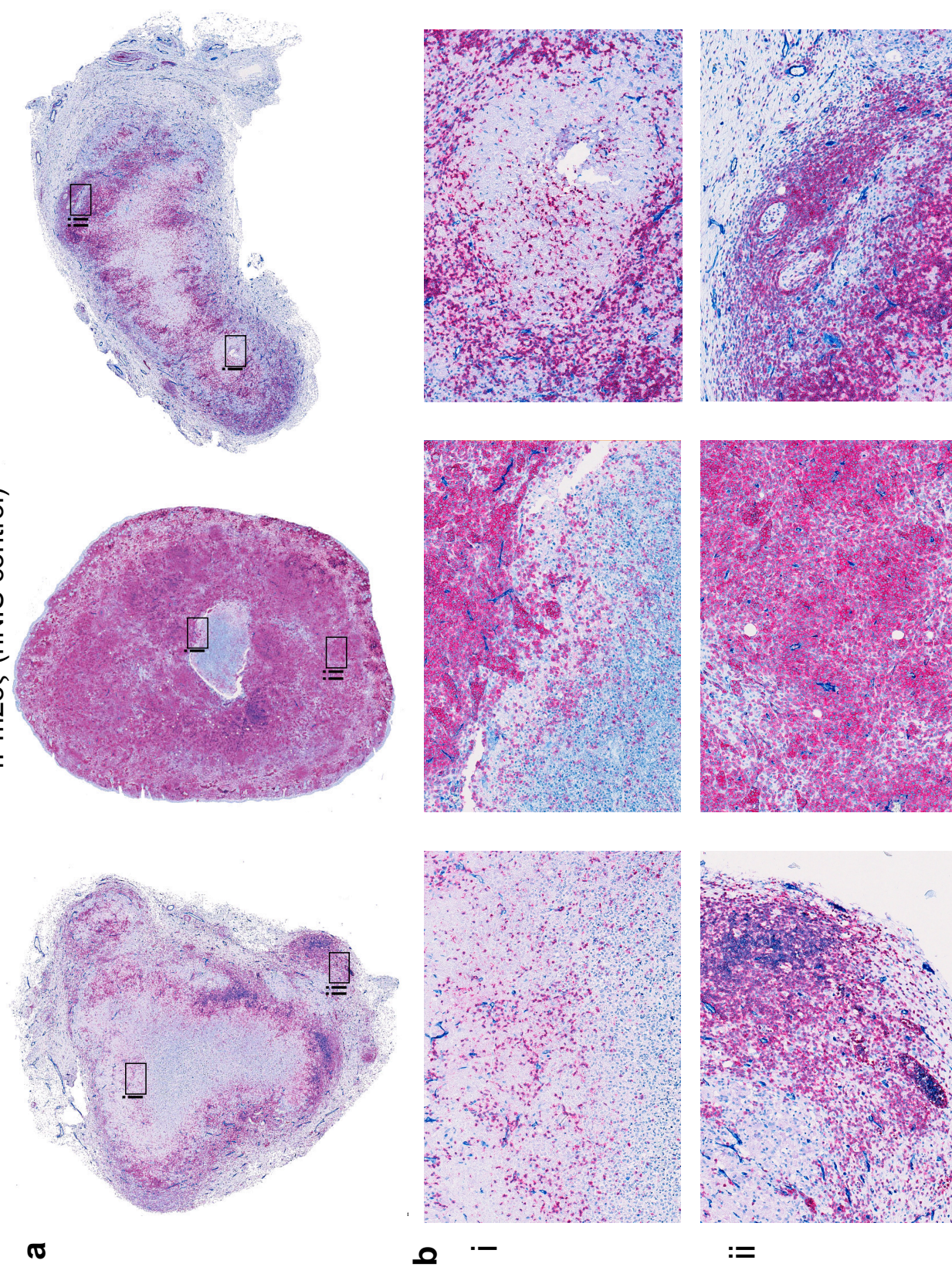
Figure 8.9: *Ex vivo* **analysis of infiltrating CD3$^+$ T cells by immunohistochemistry.** a) Paraffin embedded tumour slices were stained for human CD3 (pink) and CD31 (dark blue). b) Higher magnification images showing the pattern of infiltration. Location of magnification shown by the black squares (i, ii) on a). Scale bar: 0.1 mm. n=3

Bibliography

[1] W B Coley. The treatment of malignant tumors by repeated inoculations of erysipelas. With a report of ten original cases. 1893. *Clinical Orthopaedics and Related Research*, (262):3–11, January 1991.

[2] Meshaal Khan, Ajay V. Maker, and Shikha Jain. The evolution of cancer immunotherapy. *Vaccines*, 9, 2021.

[3] Jacob A. Klapper, Stephanie G. Downey, Franz O. Smith, James C. Yang, Marybeth S. Hughes, Udai S. Kammula, Richard M. Sherry, Richard E. Royal, Seth M. Steinberg, and Steven Rosenberg. High-dose interleukin-2 for the treatment of metastatic renal cell carcinoma: A retrospective analysis of response and survival in patients treated in the Surgery Branch at the National Cancer Institute between 1986 and 2006. *Cancer*, 113:293–301, 2008.

[4] Ken H Young, Benjamin Bonavida, Kristy L Richards, Timothy M Pierpont, and Candice B Limper. Past, Present, and Future of Rituximab-The world's First Oncology Monoclonal Antibody Therapy. *Frontiers in Oncology*, 8:163, 2018.

[5] Thuy Vu and Francois X Claret. Trastuzumab: updated mechanisms of action and resistance in breast cancer. *Frontiers Oncology*, 2:62, 2012.

[6] Elizabeth I. Buchbinder and Anupam Desai. CTLA-4 and PD-1 pathways similarities, differences, and implications of their inhibition. *American Journal of Clinical Oncology: Cancer Clinical Trials*, 39:98–106, 2016.

[7] Sonam Puri and Michael Shafique. Combination checkpoint inhibitors for treatment of non-small-cell lung cancer: an update on dual anti-CTLA-4 and anti-PD-1/PD-L1 therapies. *Drugs Context*, 9:1–11, January 2020.

[8] James Larkin, Vanna Chiarion-Sileni, Rene Gonzalez, Jean Jacques Grob, C. Lance Cowey, Christopher D. Lao, Dirk Schadendorf, Reinhard Dummer, Michael Smylie, Piotr Rutkowski, Pier F. Ferrucci, Andrew Hill, John Wagstaff, Matteo S. Carlino, John B. Haanen, Michele Maio, Ivan Marquez-Rodas, Grant A. McArthur, Paolo A. Ascierto, Georgina V. Long, Margaret K. Callahan, Michael A. Postow, Kenneth Grossmann, Mario Sznol, Brigitte Dreno, Lars Bastholt, Arvin Yang, Linda M. Rollin, Christine Horak, F. Stephen Hodi, and Jedd D. Wolchok. Combined Nivolumab and Ipilimumab or Monotherapy in Untreated Melanoma. *New England Journal of Medicine*, 373:23–34, 7 2015.

[9] S Rosenberg. A new approach to the adoptive immunotherapy of cancer with tumor-infiltrating lymphocytes. *Science*, 233:1318–1321, 1986.

[10] Yueshui Zhao, Jian Deng, Shuangfeng Rao, Sipeng Guo, Jing Shen, Fukuan Du, Xu Wu, Yu Chen, Mingxing Li, Meijuan Chen, Xiaobing Li, Wanping Li, Li Gu, Yuhong Sun, Zhuo Zhang, Qinglian Wen, Zhangang Xiao, and Jing Li. Tumor Infiltrating Lymphocyte (TIL) Therapy for Solid Tumor Treatment: Progressions and Challenges. *Cancers*, 14, 9 2022.

[11] U Dafni, O Michielin, S Martin Lluesma, Z Tsourti, V Polydoropoulou, D Karlis, M J Besser, J Haanen, I m Svane, P S Ohashi, U S Kammula, A Orcurto, S Zimmermann, L Trueb, C A Klebanoff, M T Lotze, L E Kandalaft, and G Coukos. Efficacy of adoptive therapy with tumor-infiltrating lymphocytes and recombinant interleukin-2 in advanced cutaneous melanoma: a systematic review and meta-analysis. *Annals of Oncology*, 30, 2019.

[12] Michal J Besser, Ronnie Shapira-Frommer, Orit Itzhaki, Avraham J Treves, Douglas B Zippel, Daphna Levy, Adva Kubi, Noa Shoshani, Dragoslav Zikich, Yaara Ohayon, Daniel Ohayon, Bruria Shalmon, Gal Markel, Ronit Yerushalmi, Sara Apter, Alon Ben-Nun, Eytan Ben-Ami, Avichai Shimoni, Arnon Nagler, and Jacob Schachter. Cancer Therapy: Clinical Adoptive Transfer of Tumor-Infiltrating Lymphocytes in Patients with Metastatic Melanoma: Intent-to-Treat Analysis and Efficacy after Failure to Prior Immunotherapies. *Clinical Cancer Research*, 19, 2013.

[13] Joost H van den Berg, Bianca Heemskerk, Nienke van Rooij, Raquel Gomez-Eerland, Samira Michels, Maaike van Zon, Renate de Boer, Noor A M Bakker, Annelies Jorritsma-Smit, Marit M van Buuren, Pia Kvistborg, Hergen Spits, Remko Schotte, Henk Mallo, Matthias Karger, Joris A van der Hage, Michel W J M Wouters, Loes M Pronk, Marnix H Geukes Foppen, Christian U Blank, Jos H Beijnen, Bastiaan Nuijen, Ton N Schumacher, and John B A G Haanen. Tumor infiltrating lymphocytes (TIL) therapy in metastatic melanoma: boosting of neoantigen-specific T cell reactivity and long-term follow-up. *Journal for ImmunoTherapy of Cancer*, 8(2), 2020.

[14] Ying Tang, Anne X J Zhang, Guangyu Chen, Yanheng Wu, and Wenyi Gu. Prognostic and therapeutic TILs of cervical cancer-Current advances and future perspectives. *Molecular Therapy. Oncolytics*, 22:410–430, 2021.

[15] Benjamin C Creelan, Chao Wang, Jamie K Teer, Eric M Toloza, Jiqiang Yao, Sungjune Kim, Ana M Landin, John E Mullinax, James J Saller, Andreas N Saltos, David R Noyes, Leighann B Montoya, Wesley Curry, Shari A Pilon-Thomas, Alberto A Chiappori, Tawee Tanvetyanon, Frederic J Kaye, Zachary J Thompson, Sean J Yoder, Bin Fang, John M Koomen, Amod A Sarnaik, Dung-Tsa Chen, Jose R Conejo-Garcia, Eric B Haura, and Scott J Antonia. Tumor-infiltrating lymphocyte treatment for anti-PD-1-resistant metastatic lung cancer: a phase 1 trial. *Nature Medicine*, 27(8):1410–1418, 2021.

[16] Yating Liu, Xin Yan, Fan Zhang, Xiaoxia Zhang, Futian Tang, Zhijian Han, and Yumin Li. TCR-T Immunotherapy: The Challenges and Solutions. *Frontiers in Oncology*, 11, 1 2022.

[17] Theodore S. Nowicki, Beata Berent-Maoz, Gardenia Cheung-Lau, Rong Rong Huang, Xiaoyan Wang, Jennifer Tsoi, Paula Kaplan-Lefko, Paula Cabrera, Justin Tran, Jia Pang, Mignonette Macabali, Ivan Perez Garcilazo, Ignacio Baselga Carretero, Anusha

Kalbasi, Alistair J. Cochran, Catherine S. Grasso, Siwen Hu-Lieskovan, Bartosz Chmielowski, Begoña Comin-Anduix, Arun Singh, and Antoni Ribas. A Pilot Trial of the Combination of Transgenic NY-ESO-1–reactive Adoptive Cellular Therapy with Dendritic Cell Vaccination with or without Ipilimumab. *Clinical Cancer Research*, 25(7):2096–2108, 04 2019.

[18] Indu Ramachandran, Daniel E. Lowther, Rebecca Dryer-Minnerly, Ruoxi Wang, Svetlana Fayngerts, Daniel Nunez, Gareth Betts, Natalie Bath, Alex J. Tipping, Luca Melchiori, Jean-Marc Navenot, John Glod, Crystal L. Mackall, Sandra P. D'Angelo, Dejka M. Araujo, Warren A. Chow, George D. Demetri, Mihaela Druta, Brian A. Van Tine, Stephan A. Grupp, Albiruni R. Abdul Razak, Breelyn Wilky, Malini Iyengar, Trupti Trivedi, Erin Van Winkle, Karen Chagin, Rafael Amado, Gwendolyn K. Binder, and Samik Basu. Systemic and local immunity following adoptive transfer of NY-ESO-1 SPEAR T cells in synovial sarcoma. *Journal for ImmunoTherapy of Cancer*, 7(1), 2019.

[19] Richard A Morgan, Nachimuthu Chinnasamy, Daniel Abate-Daga, Alena Gros, Paul F Robbins, Zhili Zheng, Mark E Dudley, Steven A Feldman, James C Yang, Richard M Sherry, Giao Q Phan, Marybeth S Hughes, Udai S Kammula, Akemi D Miller, Crystal J Hessman, Ashley A Stewart, Nicholas P Restifo, Martha M Quezado, Meghna Alimchandani, Avi Z Rosenberg, Avindra Nath, Tongguang Wang, Bibiana Bielekova, Simone C Wuest, Nirmala Akula, Francis J Mcmahon, Susanne Wilde, Barbara Mosetter, Dolores J Schendel, Carolyn M Laurencot, and Steven A Rosenberg. Cancer Regression and Neurological Toxicity Following Anti-MAGE-A3 TCR Gene Therapy. *Journal of Immunotherapy*, 2013.

[20] Gerald P Linette, Edward A Stadtmauer, Marcela V Maus, Aaron P Rapoport, Bruce L Levine, Lyndsey Emery, Leslie Litzky, Adam Bagg, Beatriz M Carreno, Patrick J Cimino, Gwendolyn K Binder-Scholl, Dominic P Smethurst, Andrew B Gerry, Nick J Pumphrey, Alan D Bennett, Joanna E Brewer, Joseph Dukes, Jane Harper, Helen K Tayton-Martin, Bent K Jakobsen, Namir J Hassan, Michael Kalos, and Carl H June. Cardiovascular toxicity and titin cross-reactivity of affinity-enhanced T cells in myeloma and melanoma. *Blood*, 2013.

[21] Weijun Zhou, Jinyi Yu, Yilu Li, and Kankan Wang. Neoantigen-specific TCR-T cell-based immunotherapy for acute myeloid leukemia. *Experimental Hematology and Oncology*, 11, 12 2022.

[22] Paul Shafer, Lauren M. Kelly, and Valentina Hoyos. Cancer Therapy With TCR-Engineered T Cells: Current Strategies, Challenges, and Prospects. *Frontiers in Immunology*, 13, 3 2022.

[23] Sonia Guedan, Hugo Calderon, Avery D. Posey, and Marcela V. Maus. Engineering and Design of Chimeric Antigen Receptors. *Molecular Therapy - Methods and Clinical Development*, 12:145–156, 2019.

[24] Ting Yan, Lingfeng Zhu, and Jin Chen. Current advances and challenges in CAR T-Cell therapy for solid tumors: tumor-associated antigens and the tumor microenvironment. *Experimental Hematology & Oncology*, 12:14, 2023.

[25] Deep Shah, Brian Soper, and Lindsay Shopland. Cytokine release syndrome and cancer immunotherapies – historical challenges and promising futures. *Frontiers in Immunology*, 14, 2023.

[26] Adam Ajina and John Maher. Strategies to Address Chimeric Antigen Receptor Tonic Signaling. *Molecular Cancer Therarpy*, 17(9):1795–1815, 2018.

[27] Mohamed-Reda Benmebarek, Clara Karches, Bruno Cadilha, Stefanie Lesch, Stefan Endres, and Sebastian Kobold. Killing mechanisms of chimeric antigen receptor (CAR) T cells. *Int. J. Mol. Sci.*, 20(6):1283, March 2019.

[28] Azadeh Sadat Razavi, Angelica Loskog, Sepideh Razi, and Nima Rezaei. The signaling and the metabolic differences of various CAR T cell designs. *International Immunopharmacology*, 114:109593, 2023.

[29] Michael H Kershaw, Jennifer A Westwood, Linda L Parker, Gang Wang, Zelig Eshhar, Sharon A Mavroukakis, Donald E White, John R Wunderlich, Silvana Canevari, Linda Rogers-Freezer, Clara C Chen, James C Yang, Steven A Rosenberg, and Patrick Hwu. A phase I study on adoptive immunotherapy using gene-modified T cells for ovarian cancer. *Clinical Cancer Research*, 12(20 Pt 1):6106–6115, 2006.

[30] Julie R. Park, David L. DiGiusto, Marilyn Slovak, Christine Wright, Araceli Naranjo, Jamie Wagner, Hunsar B. Meechoovet, Cherrilyn Bautista, Wen-Chung Chung Chang, Julie R. Ostberg, and Michael C. Jensen. Adoptive transfer of chimeric antigen receptor re-directed cytolytic T lymphocyte clones in patients with neuroblastoma. *Molecular Therapy*, 15:825–833, 4 2007.

[31] Carlos A. Ramos, Rayne Rouce, Catherine S. Robertson, Amy Reyna, Neeharika Narala, Gayatri Vyas, Birju Mehta, Huimin Zhang, Olga Dakhova, George Carrum, Rammurti T. Kamble, Adrian P. Gee, Zhuyong Mei, Meng Fen Wu, Hao Liu, Bambi Grilley, Cliona M. Rooney, Helen E. Heslop, Malcolm K. Brenner, Barbara Savoldo, and Gianpietro Dotti. In Vivo Fate and Activity of Second- versus Third-Generation CD19-Specific CAR-T Cells in B Cell Non-Hodgkin's Lymphomas. *Molecular Therapy*, 26:2727–2737, 2018.

[32] Sonia Guedan, Xi Chen, Aviv Madar, Carmine Carpenito, Shannon E. McGettigan, Matthew J. Frigault, Jihyun Lee, Avery D. Posey, John Scholler, Nathalie Scholler, Richard Bonneau, and Carl H. June. ICOS-based chimeric antigen receptors program bipolar TH17/ TH1 cells. *Blood*, 124:1070–1080, 2014.

[33] Andreas A. Hombach, Johannes Heiders, Marcel Foppe, Markus Chmielewski, and Hinrich Abken. OX40 costimulation by a chimeric antigen receptor abrogates CD28 and IL-2 induced IL-10 secretion by redirected CD4+ T cells. *OncoImmunology*, 1:458–466, 2012.

[34] Diogo Gomes-Silva, Malini Mukherjee, Madhuwanti Srinivasan, Giedre Krenciute, Olga Dakhova, Yueting Zheng, Joaquim M.S. Cabral, Cliona M. Rooney, Jordan S. Orange, Malcolm K. Brenner, and Maksim Mamonkin. Tonic 4-1BB Costimulation in Chimeric Antigen Receptors Impedes T Cell Survival and Is Vector-Dependent. *Cell Reports*, 21:17–26, 2017.

[35] De Gang Song and Daniel J. Powell. Pro-survival signaling via CD27 costimulation drives effective CAR T-cell therapy. *OncoImmunology*, 1:547–549, 2012.

[36] Anja Krause, Hong-Fen Guo, Jean-Baptiste Latouche, Cuiwen Tan, Nai-Kong V Cheung, and Michel Sadelain. Antigen-dependent CD28 signaling selectively enhances survival and proliferation in genetically modified activated human primary T lymphocytes. *The Journal of experimental medicine*, 188(4):619–626, 1998.

[37] Luciano Castiello, Laura Santodonato, Mariarosaria Napolitano, Davide Carlei, Enrica Montefiore, Domenica Maria Monque, Giuseppina D'Agostino, and Eleonora Aricò. Chimeric Antigen Receptor Immunotherapy for Solid Tumors: Choosing the Right Ingredients for the Perfect Recipe. *Cancers*, 14:1–23, 2022.

[38] Philip George, Nathaniel Dasyam, Giulia Giunti, Brigitta Mester, Evelyn Bauer, Bethany Andrews, Travis Perera, Tess Ostapowicz, Chris Frampton, Peng Li, David Ritchie, Catherine M Bollard, Ian F Hermans, and Robert Weinkove. Third-generation anti-CD19 chimeric antigen receptor T-cells incorporating a TLR2 domain for relapsed or refractory B-cell lymphoma: a phase I clinical trial protocol (ENABLE). *BMJ Open*, 10(2):e034629, 2020.

[39] Maria-Luisa Schubert, Anita Schmitt, Brigitte Neuber, Angela Hückelhoven-Krauss, Alexander Kunz, Lei Wang, Ulrike Gern, Birgit Michels, Leopold Sellner, Susanne Hofmann, Carsten Müller-Tidow, Peter Dreger, and Michael Schmitt. Third-Generation CAR T Cells Targeting CD19 Are Associated with an Excellent Safety Profile and Might Improve Persistence of CAR T Cells in Treated Patients. *Blood*, 2019.

[40] Oladapo O Yeku, Terence J Purdon, Mythili Koneru, David Spriggs, and Renier J Brentjens. Armored CAR T cells enhance antitumor efficacy and overcome the tumor microenvironment. *Scientific Reports.*, 7(1):10541, 2017.

[41] Biliang Hu, Jiangtao Ren, Yanping Luo, John Scholler, Yangbing Zhao, and Carl H June Correspondence. Augmentation of Antitumor Immunity by Human and Mouse CAR T Cells Secreting IL-18. *Cell Reports*, 20:3025–3033, 2017.

[42] V Hoyos, B Savoldo, C Quintarelli, A Mahendravada, M Zhang, J Vera, H E Heslop, C M Rooney, M K Brenner, and G Dotti. Engineering CD19-specific T lymphocytes with interleukin-15 and a suicide gene to enhance their anti-lymphoma/leukemia effects and safety. *Leukemia*, 24(6):1160–1170, 2010.

[43] Michael Hiltensperger and Angela M. Krackhardt. Current and future concepts for the generation and application of genetically engineered CAR-T and TCR-T cells. *Frontiers in Immunology*, 14, 2023.

[44] Adrienne H. Long, Waleed M. Haso, Jack F. Shern, Kelsey M. Wanhainen, Meera Murgai, Maria Ingaramo, Jillian P. Smith, Alec J. Walker, M. Eric Kohler, Vikas R. Venkateshwara, Rosandra N. Kaplan, George H. Patterson, Terry J. Fry, Rimas J. Orentas, and Crystal L. Mackall. 4-1BB costimulation ameliorates T cell exhaustion induced by tonic signaling of chimeric antigen receptors. *Nature Medicine*, 21:581–590, 2015.

[45] Jin-Yuan Ho, Lin Wang, Ying Liu, Min Ba, Junfang Yang, Xian Zhang, Dandan Chen, Peihua Lu, and Jianqiang Li. Promoter usage regulating the surface density of CAR molecules may modulate the kinetics of CAR-T cells in vivo. *Molecular Therapy Methods & Clinical Development*, 2021.

[46] Luca Biasco, Natalia Izotova, Christine Rivat, Sara Ghorashian, Rachel Richardson, Aleks Guvenel, Rachael Hough, Robert Wynn, Bilyana Popova, Andre Lopes, Martin Pule, Adrian J. Thrasher, and Persis J. Amrolia. Clonal expansion of T memory stem cells determines early anti-leukemic responses and long-term CAR T cell persistence in patients. *Nature Cancer*, 2:629–642, 6 2021.

[47] Sarwish Rafiq, Christopher S Hackett, and Renier J Brentjens. Engineering strategies to overcome the current roadblocks in CAR T cell therapy. *Nature Reviews in Clinical Oncology*, 17(3):147–167, 2020.

[48] Shannon L. Maude, Noelle Frey, Pamela A. Shaw, Richard Aplenc, David M. Barrett, Nancy J. Bunin, Anne Chew, Vanessa E. Gonzalez, Zhaohui Zheng, Simon F. Lacey, Yolanda D. Mahnke, Jan J. Melenhorst, Susan R. Rheingold, Angela Shen, David T. Teachey, Bruce L. Levine, Carl H. June, David L. Porter, and Stephan A. Grupp. Chimeric Antigen Receptor T Cells for Sustained Remissions in Leukemia. *New England Journal of Medicine*, 371:1507–1517, 2014.

[49] Stephen J. Schuster, Jakub Svoboda, Elise A. Chong, Sunita D. Nasta, Anthony R. Mato, Özlem Anak, Jennifer L. Brogdon, Iulian Pruteanu-Malinici, Vijay Bhoj, Daniel Landsburg, Mariusz Wasik, Bruce L. Levine, Simon F. Lacey, Jan J. Melenhorst, David L. Porter, and Carl H. June. Chimeric Antigen Receptor T Cells in Refractory B-Cell Lymphomas. *New England Journal of Medicine*, 377:2545–2554, 2017.

[50] Michael Wang, Javier Munoz, Andre Goy, Frederick L. Locke, Caron A. Jacobson, Brian T. Hill, John M. Timmerman, Houston Holmes, Samantha Jaglowski, Ian W. Flinn, Peter A. McSweeney, David B. Miklos, John M. Pagel, Marie-Jose Kersten, Noel Milpied, Henry Fung, Max S. Topp, Roch Houot, Amer Beitinjaneh, Weimin Peng, Lianqing Zheng, John M. Rossi, Rajul K. Jain, Arati V. Rao, and Patrick M. Reagan. KTE-X19 CAR T-Cell Therapy in Relapsed or Refractory Mantle-Cell Lymphoma. *New England Journal of Medicine*, 382:1331–1342, 2020.

[51] Nathan Hale Fowler, Michael Dickinson, Martin Dreyling, Joaquin Martinez-Lopez, Arne Kolstad, Jason Butler, Monalisa Ghosh, Leslie Popplewell, Julio C Chavez, Emmanuel Bachy, Koji Kato, Hideo Harigae, Marie José Kersten, Charalambos Andreadis, Peter A Riedell, P Joy Ho, José Antonio Pérez-Simón, Andy I Chen, Loretta J Nastoupil, Bastian von Tresckow, Andrés José María Ferreri, Takanori Teshima, Piers E M Patten, Joseph P McGuirk, Andreas L Petzer, Fritz Offner, Andreas Viardot, Pier Luigi Zinzani, Ram Malladi, Aiesha Zia, Rakesh Awasthi, Aisha Masood, Oezlem Anak, Stephen J Schuster, and Catherine Thieblemont. Tisagenlecleucel in adult relapsed or refractory follicular lymphoma: the phase 2 ELARA trial. *Nature Medicine.*, 28(2):325–332, 2022.

[52] Natalie F. Uy, Edward Pequignot, Noelle V. Frey, Megan Davis, Elizabeth O. Hexner, Stephen J. Schuster, Saar Gill, Alison W. Loren, Stephan A Grupp, J. Joseph Melenhorst, Simon F Lacey, Joseph A Fraietta, Joan Gilmore, Lester Lledo,

Wei-Ting Hwang, Don L. Siegel, Bruce L Levine, Carl H June, and David L. Porter. Hypogammaglobulinemia and Infection Risk in Chronic Lymphocytic Leukemia (CLL) Patients Treated with CD19-Directed Chimeric Antigen Receptor T (CAR-T) Cells. *Blood*, 136(1):30–32, 2020.

[53] Stephen J. Schuster, Michael R. Bishop, Constantine S. Tam, Edmund K. Waller, Peter Borchmann, Joseph P. McGuirk, Ulrich Jäger, Samantha Jaglowski, Charalambos Andreadis, Jason R. Westin, Isabelle Fleury, Veronika Bachanova, S. Ronan Foley, P. Joy Ho, Stephan Mielke, John M. Magenau, Harald Holte, Serafino Pantano, Lida B. Pacaud, Rakesh Awasthi, Jufen Chu, Özlem Anak, Gilles Salles, and Richard T. Maziarz. Tisagenlecleucel in Adult Relapsed or Refractory Diffuse Large B-Cell Lymphoma. *New England Journal of Medicine*, 380:45–56, 2019.

[54] Sattva S. Neelapu, Frederick L. Locke, Nancy L. Bartlett, Lazaros J. Lekakis, David B. Miklos, Caron A. Jacobson, Ira Braunschweig, Olalekan O. Oluwole, Tanya Siddiqi, Yi Lin, John M. Timmerman, Patrick J. Stiff, Jonathan W. Friedberg, Ian W. Flinn, Andre Goy, Brian T. Hill, Mitchell R. Smith, Abhinav Deol, Umar Farooq, Peter McSweeney, Javier Munoz, Irit Avivi, Januario E. Castro, Jason R. Westin, Julio C. Chavez, Armin Ghobadi, Krishna V. Komanduri, Ronald Levy, Eric D. Jacobsen, Thomas E. Witzig, Patrick Reagan, Adrian Bot, John Rossi, Lynn Navale, Yizhou Jiang, Jeff Aycock, Meg Elias, David Chang, Jeff Wiezorek, and William Y. Go. Axicabtagene Ciloleucel CAR T-Cell Therapy in Refractory Large B-Cell Lymphoma. *New England Journal of Medicine*, 377:2531–2544, 2017.

[55] Bijal D. Shah, Armin Ghobadi, Olalekan O. Oluwole, Aaron C. Logan, Nicolas Boissel, Ryan D. Cassaday, Thibaut Leguay, Michael R. Bishop, Max S. Topp, Dimitrios Tzachanis, Kristen M. O'Dwyer, Martha L. Arellano, Yi Lin, Maria R. Baer, Gary J. Schiller, Jae H. Park, Marion Subklewe, Mehrdad Abedi, Monique C. Minnema, William G. Wierda, Daniel J. DeAngelo, Patrick Stiff, Deepa Jeyakumar, Chaoling Feng, Jinghui Dong, Tong Shen, Francesca Milletti, John M. Rossi, Remus Vezan, Behzad Kharabi Masouleh, and Roch Houot. KTE-X19 for relapsed or refractory adult B-cell acute lymphoblastic leukaemia: phase 2 results of the single-arm, open-label, multicentre ZUMA-3 study. *The Lancet*, 398:491–502, 2021.

[56] Nikhil C. Munshi, Larry D. Anderson, Nina Shah, Deepu Madduri, Jesús Berdeja, Sagar Lonial, Noopur Raje, Yi Lin, David Siegel, Albert Oriol, Philippe Moreau, Ibrahim Yakoub-Agha, Michel Delforge, Michele Cavo, Hermann Einsele, Hartmut Goldschmidt, Katja Weisel, Alessandro Rambaldi, Donna Reece, Fabio Petrocca, Monica Massaro, Jamie N. Connarn, Shari Kaiser, Payal Patel, Liping Huang, Timothy B. Campbell, Kristen Hege, and Jesús San-Miguel. Idecabtagene Vicleucel in Relapsed and Refractory Multiple Myeloma. *New England Journal of Medicine*, 384:705–716, 2021.

[57] Deepu Madduri, Jesus G Berdeja, Saad Z Usmani, Andrzej Jakubowiak, Mounzer Agha, Adam D Cohen, A Keith Stewart, Parameswaran Hari, Nikhil C Munshi, David E Avigan, Abhinav Deol, Alexander M Lesokhin, Indrajeet Singh, Enrique Zudaire, Tzu-Min Yeh, Alicia J Allred, Yunsi Olyslager, Arnob Banerjee, Jenna D Goldberg, Jordan M Schecter, Carolyn C Jackson, William Deraedt, Sen Hong Zhuang, Jeffrey R Infante, Dong Geng, Xiaoling Wu, Marlene J Carrasco, Muhammad Akram, Farah Hossain, Syed Rizvi, Frank Fan, Sundar Jagannath, Yi Lin, and Thomas Martin.

CARTITUDE-1: Phase 1b/2 Study of Ciltacabtagene Autoleucel, a B-Cell Maturation Antigen-Directed Chimeric Antigen Receptor T Cell Therapy, in Relapsed/Refractory Multiple Myeloma. *Blood*, 2020.

[58] Yi-Ju Chen, Bams Abila, and Yasser Mostafa Kamel. CAR-T: What is next? *Cancers*, 15(3):663, 2023.

[59] Nirav N Shah, Bryon D Johnson, Dina Schneider, Fenlu Zhu, Aniko Szabo, Carolyn A Keever-Taylor, Winfried Krueger, Andrew A Worden, Michael J Kadan, Sharon Yim, Ashley Cunningham, Mehdi Hamadani, Timothy S Fenske, Boro Dropulić, Rimas Orentas, and Parameswaran Hari. Bispecific anti-CD20, anti-CD19 CAR T cells for relapsed B cell malignancies: a phase 1 dose escalation and expansion trial. *Nature Medicine*, 26(10):1569–1575, 2020.

[60] Yujie Li, Dengqiang Wu, Xuejia Yang, and Sufang Zhou. Immunotherapeutic potential of T memory stem cells. *Frontiers Oncology*, 11:723888, 2021.

[61] E John Wherry. T cell exhaustion. *Nature Immunology*, 12(6):492–499, 2011.

[62] Olivia C. Finney, Hannah Brakke, Stephanie Rawlings-Rhea, Roxana Hicks, Danielle Doolittle, Marisa Lopez, Ben Futrell, Rimas J. Orentas, Daniel Li, Rebecca Gardner, and Michael C. Jensen. CD19 CAR T cell product and disease attributes predict leukemia remission durability. *Journal of Clinical Investigation*, 129:2123–2132, 2019.

[63] Yang Xu, Ming Zhang, Carlos A Ramos, April Durett, Enli Liu, Olga Dakhova, Hao Liu, Chad J Creighton, Adrian P Gee, Helen E Heslop, Cliona M Rooney, Barbara Savoldo, and Gianpietro Dotti. Closely related T-memory stem cells correlate with in vivo expansion of CAR.CD19-T cells and are preserved by IL-7 and IL-15. *Blood*, 123, 2014.

[64] Judith Feucht, Jie Sun, Justin Eyquem, Yu-Jui Ho, Zeguo Zhao, Josef Leibold, Anton Dobrin, Annalisa Cabriolu, Mohamad Hamieh, and Michel Sadelain. Calibration of CAR activation potential directs alternative T cell fates and therapeutic potency. *Nature Medicine.*, 25(1):82–88, 2019.

[65] Kaichao Feng, Yelei Guo, Hanren Dai, Yao Wang, Xiang Li, Hejin Jia, and Weidong Han. Chimeric antigen receptor-modified T cells for the immunotherapy of patients with EGFR-expressing advanced relapsed/refractory non-small cell lung cancer. *Science China Life Sciences*, 59:468–479, 2016.

[66] Stephanie L Goff, Richard A Morgan, James C Yang, Richard M Sherry, Paul F Robbins, Nicholas P Restifo, Steven A Feldman, Yong-Chen Lu, Lily Lu, Zhili Zheng, Liqiang Xi, Monica Epstein, Lori S Mcintyre, Parisa Malekzadeh, Mark Raffeld, Howard A Fine, and Steven A Rosenberg. Pilot Trial of Adoptive Transfer of Chimeric Antigen Receptor-transduced T Cells Targeting EGFRvIII in Patients With Glioblastoma. *Journal Immunotherapy*, 2019.

[67] Christine E. Brown, Darya Alizadeh, Renate Starr, Lihong Weng, Jamie R. Wagner, Araceli Naranjo, Julie R. Ostberg, M. Suzette Blanchard, Julie Kilpatrick, Jennifer Simpson, Anita Kurien, Saul J. Priceman, Xiuli Wang, Todd L. Harshbarger, Massimo

D'Apuzzo, Julie A. Ressler, Michael C. Jensen, Michael E. Barish, Mike Chen, Jana Portnow, Stephen J. Forman, and Behnam Badie. Regression of Glioblastoma after Chimeric Antigen Receptor T-Cell Therapy. *New England Journal of Medicine*, 375:2561–2569, 2016.

[68] Chrystal U. Louis, Barbara Savoldo, Gianpietro Dotti, Martin Pule, Eric Yvon, G. Doug Myers, Claudia Rossig, Heidi V. Russell, Oumar Diouf, Enli Liu, Hao Liu, Meng-Fen Fen Wu, Adrian P. Gee, Zhuyong Mei, Cliona M. Rooney, Helen E. Heslop, and Malcolm K. Brenner. Antitumor activity and long-term fate of chimeric antigen receptor-positive T cells in patients with neuroblastoma. *Blood*, 118:6050–6056, 12 2011.

[69] Lihua Yu, Lulu Huang, Danna Lin, Xiaorong Lai, Li Wu, Xu Liao, Jiale Liu, Yinghua Zeng, Lichan Liang, Guanmei Zhang, Bin Wang, Zhu Wu, Shaohua Tao, Yuchen Liu, Cheng Jiao, Lung-Ji Chang, and Lihua Yang. GD2-specific chimeric antigen receptor-modified T cells for the treatment of refractory and/or recurrent neuroblastoma in pediatric patients. *Journal of Cancer Research and Clinical Oncology*, 148:2643–2652, 2022.

[70] Nabil Ahmed, Vita S Brawley, Meenakshi Hegde, Catherine Robertson, Alexia Ghazi, Claudia Gerken, Enli Liu, Olga Dakhova, Aidin Ashoori, Amanda Corder, Tara Gray, Meng-Fen Wu, Hao Liu, John Hicks, Nino Rainusso, Gianpietro Dotti, Zhuyong Mei, Bambi Grilley, Adrian Gee, Cliona M Rooney, Malcolm K Brenner, Helen E Heslop, Winfried S Wels, Lisa L Wang, Peter Anderson, and Stephen Gottschalk. Human Epidermal Growth Factor Receptor 2 (HER2)-Specific Chimeric Antigen Receptor-Modified T Cells for the Immunotherapy of HER2-Positive Sarcoma. 2015.

[71] Richard A. Morgan, James C. Yang, Mio Kitano, Mark E. Dudley, Carolyn M. Laurencot, and Steven A. Rosenberg. Case report of a serious adverse event following the administration of T cells transduced with a chimeric antigen receptor recognizing ErbB2. *Molecular Therapy*, 18:843–851, 4 2010.

[72] Donald M O'Rourke, Maclean P Nasrallah, Arati Desai, Jan J Melenhorst, Keith Mansfield, Jennifer J D Morrissette, Maria Martinez-Lage, Steven Brem, Eileen Maloney, Angela Shen, Randi Isaacs, Suyash Mohan, Gabriela Plesa, Simon F Lacey, Jean-Marc Navenot, Zhaohui Zheng, Bruce L Levine, Hideho Okada, Carl H June, Jennifer L Brogdon, and Marcela V Maus. A single dose of peripherally infused EGFRvIII-directed CAR T cells mediates antigen loss and induces adaptive resistance in patients with recurrent glioblastoma. *Science Translational Medicine*, 9(399), 2017.

[73] Evripidis Lanitis, Melita Irving, and George Coukos. Targeting the tumor vasculature to enhance T cell activity. *Current Opinion in Immunology*, 33:55–63, 2015.

[74] Dorota E Kuczek, Anne Mette H Larsen, Marie-Louise Thorseth, Marco Carretta, Adrija Kalvisa, Majken S Siersbæk, Ana Micaela C Simões, Anne Roslind, Lars H Engelholm, Elfriede Noessner, Marco Donia, Inge Marie Svane, Per Thor Straten, Lars Grøntved, and Daniel H Madsen. Collagen density regulates the activity of tumor-infiltrating T cells. *The Journal for ImmunoTherapy of Cancer*, 7(1):68, 2019.

[75] Ignazio Caruana, Barbara Savoldo, Valentina Hoyos, Gerrit Weber, Hao Liu, Eugene S Kim, Michael M Ittmann, Dario Marchetti, and Gianpietro Dotti. Heparanase promotes

tumor infiltration and antitumor activity of CAR-redirected T lymphocytes. *Nature Medicine*, 21(5):524–529, 2015.

[76] Eric Tran, Dhanalakshmi Chinnasamy, Zhiya Yu, Richard A. Morgan, Chyi Chia Richard Lee, Nicholas P. Restifo, and Steven A. Rosenberg. Immune targeting of fibroblast activation protein triggers recognition of multipotent bone marrow stromal cells and cachexia. *Journal of Experimental Medicine*, 210:1125–1135, 2013.

[77] Antonio Di Stasi, Biagio De Angelis, Cliona M. Rooney, Lan Zhang, Aruna Mahendravada, Aaron E. Foster, Helen E. Heslop, Malcolm K. Brenner, Gianpietro Dotti, and Barbara Savoldo. T lymphocytes coexpressing CCR4 and a chimeric antigen receptor targeting CD30 have improved homing and antitumor activity in a Hodgkin tumor model. *Blood*, 113:6392, 2009.

[78] Jade Foeng, Iain Comerford, and Shaun R McColl. Harnessing the chemokine system to home CAR-T cells into solid tumors. *Cell Reports Medicine.*, 3(3):100543, 2022.

[79] Hollie J Pegram, James C Lee, Erik G Hayman, Gavin H Imperato, Thomas F Tedder, Michel Sadelain, and Renier J Brentjens. Tumor-targeted T cells modified to secrete IL-12 eradicate systemic tumors without need for prior conditioning. *Blood*, 2012.

[80] Christopher C Kloss, Jihyun Lee, Aaron Zhang, Fang Chen, Jan Joseph Melenhorst, Simon F Lacey, Marcela V Maus, Joseph A Fraietta, Yangbing Zhao, and Carl H June. Dominant-negative TGF-β receptor enhances PSMA-targeted human CAR T cell proliferation and augments prostate cancer eradication. *Molecular Therapy.*, 26(7):1855–1866, 2018.

[81] Safa Tahmasebi, Reza Elahi, and Abdolreza Esmaeilzadeh. Solid Tumors Challenges and New Insights of CAR T Cell Engineering. *Stem cell reviews and reports*, 2015.

[82] Madeleine Iafrate and Gilbert O. Fruhwirth. How Non-invasive in vivo Cell Tracking Supports the Development and Translation of Cancer Immunotherapies. *Frontiers in Physiology*, 11:1–30, 2020.

[83] Fuqiang Shao, Yu Long, Hao Ji, Dawei Jiang, Ping Lei, and Xiaoli Lan. Radionuclide-based molecular imaging allows CAR-T cellular visualization and therapeutic monitoring. *Issue 14 Theranostics*, 11:6800–6817, 2021.

[84] Mingliang Ren, Bolin Yao, Bing Han, and Cong Li. Nuclear Imaging of CAR T Immunotherapy to Solid Tumors: In Terms of Biodistribution, Viability, and Cytotoxic Effect. *Advanced biology*, 7:e2200293, 2023.

[85] Moritz F. Kircher, Sanjiv S. Gambhir, and Jan Grimm. Noninvasive cell-tracking methods. *Nature Reviews Clinical Oncology*, 8:677–688, 2011.

[86] Filippo Galli, Michela Varani, Chiara Lauri, Guido Gentiloni Silveri, Livia Onofrio, and Alberto Signore. Immune cell labelling and tracking: implications for adoptive cell transfer therapies. *EJNMMI Radiopharmacy and Chemistry*, 6, 2021.

[87] Jung Eun Kim, Senthilkumar Kalimuthu, and Byeong-Cheol Ahn. In vivo cell tracking with bioluminescence imaging. *Nuclear Medicine Molecullar Imaging (2010)*, 49(1):3–10, 2015.

[88] Paris Kosti, James W Opzoomer, Karen I Larios-Martinez, Selvam Thavaraj, John Maher, and James N Arnold. Hypoxia-sensing CAR T cells provide safety and efficacy in treating solid tumors. *Cell Reports Medicine*, 2021.

[89] Matthew S. Skovgard, Hocine R. Hocine, Jasmeen K. Saini, Maxim Moroz, Rebecca Y. Bellis, Srijita Banerjee, Aurore Morello, Vladimir Ponomarev, Jonathan Villena-Vargas, and Prasad S. Adusumilli. Imaging CAR T-Cell Kinetics in Solid Tumors: Translational Implications. *Molecular Therapy - Oncolytics*, 2021.

[90] Peter J. Gawne, Francis Man, Philip J. Blower, and Rafael T.M. De Rosales. Direct Cell Radiolabeling for in Vivo Cell Tracking with PET and SPECT Imaging. *Chemical Reviews*, 122:10266–10318, 6 2022.

[91] Francis Man, Peter J. Gawne, and Rafael T.M. de Rosales. Nuclear imaging of liposomal drug delivery systems: A critical review of radiolabelling methods and applications in nanomedicine. *Advanced Drug Delivery Reviews*, 143:134–160, 2019.

[92] Il Minn, Steven P. Rowe, and Martin G. Pomper. Enhancing CAR T-cell therapy through cellular imaging and radiotherapy. *The Lancet Oncology*, 20:e443–e451, 2019.

[93] Łukasz Kiraga, Paulina Kucharzewska, Stephen Paisey, Łukasz Cheda, Anita Domańska, Zbigniew Rogulski, Tomasz P. Rygiel, Alberto Boffi, and Magdalena Król. Nuclear imaging for immune cell tracking in vivo – Comparison of various cell labeling methods and their application. *Coordination Chemistry Reviews*, 445:214008, 2021.

[94] Il Minn, David J. Huss, Hye Hyun Ahn, Tamara M. Chinn, Andrew Park, Jon Jones, Mary Brummet, Steven P. Rowe, Polina Sysa-Shah, Yong Du, Hyam I. Levitsky, and Martin G. Pomper. Imaging CAR T cell therapy with PSMA-targeted positron emission tomography. *Science Advances*, 5, 2019.

[95] Manel Roca, Erik F.J. De Vries, Francois Jamar, Ora Israel, and Alberto Signore. Guidelines for the labelling of leucocytes with 111In-oxine. *European Journal of Nuclear Medicine and Molecular Imaging*, 37:835–841, 2010.

[96] Flavia Linguanti, Elisabetta Maria Abenavoli, Valentina Berti, and Egesta Lopci. Metabolic Imaging in B-Cell Lymphomas during CAR-T Cell Therapy. *Cancers*, 14, 2022.

[97] B A Pockaj, R M Sherry, J P Wei, J R Yannelli, C S Carter, S F Leitman, J A Carasquillo, S M Steinberg, S A Rosenberg, and J C Yang. Localization of 111indium-labeled tumor infiltrating lymphocytes to tumor in patients receiving adoptive immunotherapy. Augmentation with cyclophosphamide and correlation with response. *Cancer*, 73(6):1731–1737, 1994.

[98] Helga Bernhard, Julia Neudorfer, Kerstin Gebhard, Heinke Conrad, Christine Hermann, Jörg Nährig, Falko Fend, Wolfgang Weber, Dirk H. Busch, and Christian Peschel. Adoptive transfer of autologous, HER2-specific, cytotoxic T lymphocytes for the treatment of HER2-overexpressing breast cancer. *Cancer Immunology, Immunotherapy*, 57:271–280, 2008.

[99] Ana Caterina Parente-Pereira, Jerome Burnet, David Ellison, Julie Foster, David Marc Davies, Sjoukje Van Der Stegen, Sophie Burbridge, Laura Chiapero-Stanke, Scott Wilkie, Stephen Mather, and John Maher. Trafficking of CAR-Engineered human T cells following regional or systemic adoptive transfer in SCID beige mice. *Journal of Clinical Immunology*, 31:710–718, 2011.

[100] Michael R. Weist, Renate Starr, Brenda Aguilar, Junie Chea, Joshua K. Miles, Erasmus Poku, Ethan Gerdts, Xin Yang, Saul J. Priceman, Stephen J. Forman, David Colcher, Christine E. Brown, and John E. Shively. PET of adoptively transferred chimeric antigen receptor T Cells with ^{89}Zr-Oxine. *Journal of Nuclear Medicine*, 59:1531–1537, 10 2018.

[101] Francis Man, Lindsay Lim, Alessia Volpe, Alberto Gabizon, Hilary Shmeeda, Benjamin Draper, Ana C. Parente-Pereira, John Maher, Philip J. Blower, Gilbert O. Fruhwirth, and Rafael T.M. de Rosales. In Vivo PET Tracking of 89 Zr-Labeled Vγ9Vδ2 T Cells to Mouse Xenograft Breast Tumors Activated with Liposomal Alendronate. *Molecular Therapy*, 27:219–229, 1 2019.

[102] Keyvan Kheyrolahzadeh, Mohammad Reza Tohidkia, Ali Tarighatnia, Parviz Shahabi, Nader D Nader, and Ayoob Aghanejad. Theranostic chimeric antigen receptor (CAR)-T cells: Insight into recent trends and challenges in solid tumors. *Life Sciences*, 328:121917, 2023.

[103] Xin yu Wang, Yan Wang, Qiong Wu, Jing jing Liu, Yu Liu, Dong hui Pan, Wei Qi, Li zhen Wang, Jun jie Yan, Yu ping Xu, Guang ji Wang, Li yan Miao, Lei Yu, and Min Yang. Feasibility study of ^{68}Ga-labeled CAR T cells for in vivo tracking using micro-positron emission tomography imaging. *Acta Pharmacologica Sinica*, 42:824–831, 2021.

[104] Aditya Bansal, Mukesh K Pandey, Yunus E Demirhan, Jonathan J Nesbitt, Ruben J Crespo-Diaz, Andre Terzic, Atta Behfar, and Timothy R Degrado. Novel ^{89}Zr cell labeling approach for PET-based cell trafficking studies. *EJNMMI research*, 2011.

[105] Sang-Jin Jin Suk Hyun Sang Ju Lee, Hyunsu Soh, Junho Jin Hwa Chung, Eun Hye Cho, , Ji-Min Min Ju, Joong Hyuk Sheen, Hyori Kim, Seung Jun Oh, , Junho Jin Hwa Chung, Kyungho Choi, Seog-Young Young Kim, Jin-Sook Sook Ryu, and Suk Hyun Leeid and. Feasibility of real-time in vivo ^{89}Zr-DFO-labeled CAR T-cell trafficking using PET imaging. *PLoS ONE*, 15:1–21, 2020.

[106] Parijat Bhatnagar, Zheng Li, Yoonsu Choi, Jianfeng Guo, Feng Li, Daniel Y. Lee, Matthew Figliola, Helen Huls, Dean A. Lee, Tomasz Zal, King C. Li, and Laurence J.N. Cooper. Imaging of Genetically Engineered T Cells by PET using Gold Nanoparticle Complexed to Copper-64. *Integrative biology : quantitative biosciences from nano to macro*, 5:231, 2013.

[107] Yogindra Vedvyas, Enda Shevlin, Marjan Zaman, Irene M. Min, Alejandro Amor-Coarasa, Susan Spencer Park, Susan Spencer Park, Keon-Woo Kwon, Turner Smith, Yonghua Luo, Dohyun Kim, Young Kim, Benedict Law, Richard Ting, John Babich, Moonsoo M. Jin, and South Korea. Longitudinal PET imaging demonstrates biphasic CAR T cell responses in survivors. *JCI Insight*, 1:1–17, 2016.

[108] Konstantin Dobrenkov, Malgorzata Olszewska, Yury Likar, Larissa Shenker, Gertrude Gunset, Shangde Cai, Nagavarakishore Pillarsetty, Hedvig Hricak, Michel Sadelain, and Vladimir Ponomarev. Monitoring the Efficacy of Adoptively Transferred Prostate Cancer–Targeted Human T Lymphocytes with PET and Bioluminescence Imaging. *Journal of Nuclear Medicine*, 49:1162–1170, 2008.

[109] Shahriar S. Yaghoubi, Michael C. Jensen, Nagichettiar Satyamurthy, Shradha Budhiraja, David Paik, Johannes Czernin, and Sanjiv S. Gambhir. Non-Invasive Detection of Therapeutic Cytolytic T Cells with [18F]FHBG Positron Emission Tomography in a Glioma Patient. *Nature clinical practice. Oncology*, 6:53, 2009.

[110] Khun Visith Keu, Timothy H Witney, Shahriar Yaghoubi, Jarrett Rosenberg, Anita Kurien, Rachel Magnusson, John Williams, Frezghi Habte, Jamie R Wagner, Stephen Forman, Christine Brown, Martin Allen-Auerbach, Johannes Czernin, Winson Tang, Michael C Jensen, Behnam Badie, and Sanjiv S Gambhir. Reporter gene imaging of targeted T cell immunotherapy in recurrent glioma. *Science Translational Medicine*, 9(373), 2017.

[111] Surya Murty, Louai Labanieh, Tara Murty, Gayatri Gowrishankar, Tom Haywood, Israt S Alam, Corinne Beinat, Elise Robinson, Amin Aalipour, Dorota D Klysz, Jennifer R Cochran, Robbie G Majzner, Crystal L Mackall, and Sanjiv S Gambhir. PET reporter gene imaging and ganciclovir-mediated ablation of chimeric antigen receptor T cells in solid tumors. *Cancer Research.*, 80(21):4731–4740, 2020.

[112] Hanwen Zhang, Maxim A. Moroz, Inna Serganova, Thomas Ku, Ruimin Huang, Jelena Vider, Helmut R. Maecke, Steven M. Larson, Ronald Blasberg, and Peter M. Smith-Jones. Imaging expression of the human somatostatin receptor subtype-2 reporter gene with ^{68}Ga-DOTATOC. *Journal of Nuclear Medicine*, 52:123–131, 2011.

[113] Mikhail M Doubrovin, Ekaterina S Doubrovina, Pat Zanzonico, Michel Sadelain, Steven M Larson, and Richard J O'reilly. In vivo Imaging and Quantitation of Adoptively Transferred Human Antigen-Specific T Cells Transduced to Express a Human Norepinephrine Transporter Gene. *Cancer research*, 2007.

[114] Maxim A. Moroz, Hanwen Zhang, Jason Lee, Ekaterina Moroz, Juan Zurita, Larissa Shenker, Inna Serganova, Ronald Blasberg, and Vladimir Ponomarev. Comparative analysis of T cell imaging with human nuclear reporter genes. *Journal of Nuclear Medicine*, 56:1055–1060, 2015.

[115] Adam Badar, Louise Kiru, Tammy L. Kalber, Amit Jathoul, Karin Straathof, Erik Årstad, Mark F. Lythgoe, and Martin Pule. Fluorescence-guided development of a tricistronic vector encoding bimodal optical and nuclear genetic reporters for in vivo cellular imaging. *EJNMMI Research*, 5, 2011.

[116] Orlie Levy, Antonio De la Vieja, Christopher S. Ginter, Claudia Riedel, Ge Dai, and Nancy Carrasco. N-linked Glycosylation of the Thyroid Na^+/I^- Symporter (NIS) . *Journal of Biological Chemistry*, 273:22657–22663, 1998.

[117] P. A. Smanik, Q. Liu, T. L. Furminger, K. Ryu, S. Xing, E. L. Mazzaferri, and Sissy M. Jhiang. Cloning of the human sodium iodide symporter. *Biochemical and Biophysical Research Communications*, 226:339–345, 1996.

[118] Silvia Ravera, Andrea Reyna-Neyra, Giuseppe Ferrandino, L Mario Amzel, and Nancy Carrasco. The Sodium/Iodide Symporter (NIS): Molecular Physiology and Preclinical and Clinical Applications. *The Annual Review of Physiology is online at*, 79:261–89, 2017.

[119] Nancy Carrasco. Iodide transport in the thyroid gland. *BBA - Reviews on Biomembranes*, 1154:65–82, 1993.

[120] J. Wolff. Transport of iodide and other anions in the thyroid gland. *Physiological reviews*, 44:45–90, 1964.

[121] Byeong Cheol Ahn. Sodium iodide symporter for nuclear molecular imaging and gene therapy: From bedside to bench and back. *Theranostics*, 2:392–402, 2012.

[122] June Key Chung and Gi Jeong Cheon. Radioiodine therapy in differentiated thyroid cancer: The first targeted therapy in oncology. *Endocrinology and Metabolism*, 29:233–239, 2014.

[123] Sung Hye Kong, Jung Ah Lim, Young Shin Song, Shinje Moon, Ye An Kim, Min Joo Kim, Sun Wook Cho, Jae Hoon Moon, Ka Hee Yi, Do Joon Park, Bo Youn Cho, and Young Joo Park. Star-shaped intense uptake of ^{131}I on whole body scans can reflect good therapeutic effects of low-dose radioactive iodine treatment of 1.1 GBq. *Endocrinology and Metabolism*, 33:228–235, 2018.

[124] Madhura G. Kelkar, Kalimuthu Senthilkumar, Smita Jadhav, Sudeep Gupta, Beyong Cheol Ahn, and Abhijit De. Enhancement of human sodium iodide symporter gene therapy for breast cancer by HDAC inhibitor mediated transcriptional modulation. *Scientific Reports*, 6, 2016.

[125] Kathrin Klutz, Verena Russ, Michael J. Willhauck, Nathalie Wunderlich, Christian Zach, Franz Josef Gildehaus, Burkhard Göke, Ernst Wagner, Manfred Ogris, and Christine Spitzweg. Targeted radioiodine therapy of neuroblastoma tumors following systemic nonviral delivery of the sodium iodide symporter gene. *Clinical Cancer Research*, 15:6079–6086, 2009.

[126] Young Hwa Kim, Hyewon Youn, Juri Na, Kee Jong Hong, Keon Wook Kang, Dong Soo Lee, and June Key Chung. Codon-optimized human sodium iodide symporter (opt-hNIS) as a sensitive reporter and efficient therapeutic gene. *Theranostics*, 5:86–96, 2015.

[127] Jim O'Doherty, Maite Jauregui-Osoro, Teresa Brothwood, Teresa Szyszko, Paul K. Marsden, Michael J. O'Doherty, Gary J.R. Cook, Philip J. Blower, and Val Lewington. 18F-tetrafluoroborate, a PET probe for imaging sodium/iodide symporter expression: Whole-body biodistribution, safety, and radiation dosimetry in thyroid cancer patients. *Journal of Nuclear Medicine*, 58:1666–1671, 2017.

[128] Huailei Jiang and Timothy R. DeGrado. [18F]Tetrafluoroborate ([18F]TFB) and its analogs for PET imaging of the sodium/iodide symporter. *Theranostics*, 8:3918–3931, 2018.

[129] R. Herbert, P. W. Kulke, and R. T H Shepherd. The use of technetium 99m as a clinical tracer element. *Postgraduate Medical Journal*, 41:656–662, 1965.

[130] J. C. Leonidas and D. R. Germann. Technetium 99m pertechnetate imaging in diagnosis of Meckel's diverticulum. *Archives of Disease in Childhood*, 49:21–26, 1974.

[131] Christian Kratzik, Susanne Dorudi, Martina Schatzl, and Helmut Sinzinger. Tc-99m-PSMA imaging allows successful radioguided surgery in recurrent prostate cancer. *Hellenic Journal of Nuclear Medicine*, 21:202–204, 2018.

[132] Richard P. Junghans, Qiangzhong Ma, Ritesh Rathore, Erica M. Gomes, Anthony J. Bais, Agnes S.Y. Lo, Mehrdad Abedi, Robin A. Davies, Howard J. Cabral, A. Samer Al-Homsi, and Stephen I. Cohen. Phase I Trial of Anti-PSMA Designer CAR-T Cells in Prostate Cancer: Possible Role for Interacting Interleukin 2-T Cell Pharmacodynamics as a Determinant of Clinical Response. *Prostate*, 76:1257–1270, 2016.

[133] Nia Emami-Shahri, Julie Foster, Roxana Kashani, Patrycja Gazinska, Celia Cook, Jane Sosabowski, John Maher, and Sophie Papa. Clinically compliant spatial and temporal imaging of chimeric antigen receptor T-cells. *Nature Communications*, 9, 2018.

[134] E. Kurtys, L. Lim, F. Man, A. Volpe, and G. Fruhwirth. In vivo tracking of CAR-T by [^{18}F]BF 4 - PET/CT in human breast cancer xenografts reveals differences in CAR-T tumour retention. *Cytotherapy*, 20:S20, 2018.

[135] Alessia Volpe, Cameron Lang, Lindsay Lim, Francis Man, Ewelina Kurtys, Candice Ashmore-Harris, Preeth Johnson, Elena Skourti, Rafael T.M. de Rosales, and Gilbert O. Fruhwirth. Spatiotemporal PET Imaging Reveals Differences in CAR-T Tumor Retention in Triple-Negative Breast Cancer Models. *Molecular Therapy*, 28:2271–2285, 2020.

[136] Reona Sakemura, Aditya Bansal, Elizabeth L. Siegler, Mehrdad Hefazi, Nan Yang, Roman H. Khadka, Alysha N. Newsom, Michael J. Hansen, Michelle J. Cox, Claudia Manriquez Roman, Kendall J. Schick, Ismail Can, Erin E. Tapper, Wendy K. Nevala, Mohamad M. Adada, Evandro D. Bezerra, Lionel Aurelien Kankeu Fonkoua, Paulina Horvei, Michael W. Ruff, Sameer A. Parikh, Mukesh K. Pandey, Timothy R. Degrado, Lukkana Suksanpaisan, Neil E. Kay, Kah-Whye Whye Peng, Stephen J. Russe, Saad S. Kenderian, Saad S. Kenderian, Lionel Aurelien, Kankeu Fonkoua, Paulina Horvei, Michael W. Ruff, Sameer A. Parikh, Mukesh K. Pandey, Timothy R. Degrado, Lukkana Suksanpaisan, Neil E. Kay, Kah-Whye Whye Peng, Stephen J Russell, Saad S. Kenderian, Lionel Aurelien Kankeu Fonkoua, Paulina Horvei, Michael W. Ruff, Sameer A. Parikh, Mukesh K. Pandey, Timothy R. Degrado, Lukkana Suksanpaisan, Neil E. Kay, Kah-Whye Whye Peng, Stephen J. Russe, Saad S. Kenderian, and Saad S. Kenderian. Development of a clinically relevant reporter for chimeric antigen receptor t-cell expansion, trafficking, and toxicity. *Cancer Immunology Research*, 9:1035–1046, 2021.

[137] Kathryn M. Cappell and James N. Kochenderfer. Long-term outcomes following CAR T cell therapy: what we know so far. *Nature Reviews Clinical Oncology*, 20:359–371, 2023.

[138] David P. Turicek, Victoria M. Giordani, Josquin Moraly, Naomi Taylor, and Nirali N. Shah. CAR T-cell detection scoping review: An essential biomarker in critical need of standardization. *Journal for ImmunoTherapy of Cancer*, 11, 2023.

[139] Luca Gattinoni, Joseph Anthony Fraietta, Jun Huang, and Yifei Hu. The Chimeric Antigen Receptor Detection Toolkit. *Frontiers Immunology*, 11:1770, 2020.

[140] Yarne Klaver, Andre Kunert, Stefan Sleijfer, Reno Debets, and Cor Hj Lamers. Adoptive T-cell therapy: A need for standard immune monitoring. *Immunotherapy*, 7:513–533, 2015.

[141] Ghanashyam Sarikonda, Anil Pahuja, Creton Kalfoglou, Kerri Burns, Kevin Nguyen, Irene L. Ch'en, Reinhold Pollner, Shabnam Tangri, and Naveen Dakappagari. Monitoring CAR-T cell kinetics in clinical trials by multiparametric flow cytometry: Benefits and challenges. *Cytometry Part B - Clinical Cytometry*, 100:72–78, 2021.

[142] Yajing Zhang, Yao Wang, Yang Liu, Chuan Tong, Chunmeng Wang, Yelei Guo, Dongdong Ti, Qingming Yang, Shen Qiao, Zhiqiang Wu, and Weidong Han. Long-term activity of tandem CD19/CD20 CAR therapy in refractory/relapsed B-cell lymphoma: a single-arm, phase 1-2 trial. *Leukemia*, 36(1):189–196, 2022.

[143] Patrick M. Forde, Jamie E. Chaft, Kellie N. Smith, Valsamo Anagnostou, Tricia R. Cottrell, Matthew D. Hellmann, Marianna Zahurak, Stephen C. Yang, David R. Jones, Stephen Broderick, Richard J. Battafarano, Moises J. Velez, Natasha Rekhtman, Zachary Olah, Jarushka Naidoo, Kristen A. Marrone, Franco Verde, Haidan Guo, Jiajia Zhang, Justina X. Caushi, Hok Yee Chan, John-William Sidhom, Robert B. Scharpf, James White, Edward Gabrielson, Hao Wang, Gary L. Rosner, Valerie Rusch, Jedd D. Wolchok, Taha Merghoub, Janis M. Taube, Victor E. Velculescu, Suzanne L. Topalian, Julie R. Brahmer, and Drew M. Pardoll. Neoadjuvant PD-1 Blockade in Resectable Lung Cancer. *New England Journal of Medicine*, 378:1976–1986, 2018.

[144] Alessandra Bertoldo, Gaia Rizzo, and Mattia Veronese. Deriving physiological information from PET images: from SUV to compartmental modelling. *Clinical and Translational Imaging*, 2(3):239–251, 2014.

[145] Raymond M Reilly. The Fundamental Principles of Compartmental Pharmacokinetics Illustrated by Radiopharmaceuticals Commonly Used in Nuclear Medicine Continuing Education for Nuclear Pharmacists And Nuclear Medicine Professionals. *LESSON*, 17, 2013.

[146] Hiroshi Watabe, Yoko Ikoma, Yuichi Kimura, Mika Naganawa, and Miho Shidahara. PET kinetic analysis compartmental model. *Annals of Nuclear Medicine*, 20:583–588, 2006.

[147] Antonia Dimitrakopoulou-Strauss, Leyun Pan, and Christos Sachpekidis. Kinetic modeling and parametric imaging with dynamic PET for oncological applications: general considerations, current clinical applications, and future perspectives. *European Journal of Nuclear Medicine and Molecular Imaging*, 48(1):21–39, 2021.

[148] Evan D Morris, Christopher J Endres, Kathleen C Schmidt, Bradley T Christian, Raymond F Muzic, and Ronald E Fisher. Kinetic modeling in positron emission tomography. *Emission tomography: The fundamentals of PET and SPECT*, 46(1):499–540, 2004.

[149] David Dagan Feng, Kewei Chen, and Lingfeng Wen. Noninvasive Input Function Acquisition and Simultaneous Estimations With Physiological Parameters for PET Quantification: A Brief Review. *IEEE Transactions on Radiation and Plasma Medical Sciences*, 4, 2020.

[150] Alexandra Kamp, Martin Andersson, Sigrid Leide-Svegborn, Dietmar Nobke, Sören Mattsson, and Augusto Giussani. A revised compartmental model for biokinetics and dosimetry of 2-[^{18}F]FDG. *EJNMMI Physics*, 2023.

[151] Jan Taprogge, Iain Murray, Jonathan Gear, Sarah J. Chittenden, Christopher C. Parker, and Glenn D. Flux. Compartmental Model for 223Ra-Dichloride in Patients With Metastatic Bone Disease From Castration-Resistant Prostate Cancer. *International Journal of Radiation Oncology Biology Physics*, 105(4):884–892, 2019.

[152] Glenn Flux, Francesca Leek, Paul Gape, Jonathan Gear, and Jan Taprogge. Iodine-131 and Iodine-131-Meta-iodobenzylguanidine Dosimetry in Cancer Therapy. *Seminars in Nuclear Medicine*, 52:167–177, 2022.

[153] Sara Neira, Araceli Gago-Arias, Isabel Gónzalez-Crespo, Jacobo Guiu-Souto, and Juan Pardo-Montero. Development of a compartmental pharmacokinetic model for molecular radiotherapy with ^{131}I-CLR1404. *Pharmaceutics*, 13, 2021.

[154] Erica Silvestri, Valentina Scolozzi, Gaia Rizzo, Luca Indovina, Marco Castellaro, Maria Vittoria Mattoli, Paolo Graziano, Giuseppe Cardillo, Alessandra Bertoldo, and Maria Lucia Calcagni. The kinetics of 18F-FDG in lung cancer: compartmental models and voxel analysis. *EJNMMI Research*, 8(1), 2018.

[155] Guobao Wang, Lorenzo Nardo, Mamta Parikh, Yasser G Abdelhafez, Elizabeth Li, Benjamin A Spencer, Jinyi Qi, Terry Jones, Simon R Cherry, and Ramsey D Badawi. Total-Body PET Multiparametric Imaging of Cancer Using a Voxelwise Strategy of Compartmental Modeling. *Journal of Nuclear Medicine*, 63:1274–1281, 2022.

[156] Laetitia Vercellino, Dorine de Jong, Roberta di Blasi, Salim Kanoun, Ran Reshef, Lawrence H. Schwartz, and Laurent Dercle. Current and Future Role of Medical Imaging in Guiding the Management of Patients With Relapsed and Refractory Non-Hodgkin Lymphoma Treated With CAR T-Cell Therapy. *Frontiers in Oncology*, 11, 2021.

[157] Jean Logan, Joanna S. Fowler, Nora D. Volkow, Alfred P. Wolf, Stephen L. Dewey, David J. Schlyer, Robert R. MacGregor, Robert Hitzemann, Bernard Bendriem, S. John Gatley, and David R. Christman. Graphical Analysis of Reversible Radioligand Binding from Time—Activity Measurements Applied to [N-11C-Methyl]-Cocaine PET Studies in Human Subjects. *Journal of Cerebral Blood Flow & Metabolism*, 10(5):740–747, 1990.

[158] C S Patlak, R G Blasberg, and J D Fenstermacher. Graphical evaluation of blood-to-brain transfer constants from multiple-time uptake data. *Journal of Cerebral Blood Flow & Metabolism*, 3(1):1–7, 1983.

[159] Aman P Singh, Xirong Zheng, Xiefan Lin-Schmidt, Wenbo Chen, Thomas J Carpenter, Alice Zong, Weirong Wang, and Donald L Heald. Development of a quantitative relationship between CAR-affinity, antigen abundance, tumor cell depletion and CAR-T cell expansion using a multiscale systems PK-PD model. In *MAbs*, volume 12, page 1688616. Taylor & Francis, 2020.

[160] Can Liu, Vivaswath S. Ayyar, Xirong Zheng, Wenbo Chen, Songmao Zheng, Hardik Mody, Weirong Wang, Donald Heald, Aman P. Singh, and Yanguang Cao. Model-Based Cellular Kinetic Analysis of Chimeric Antigen Receptor-T Cells in Humans. *Clinical Pharmacology and Therapeutics*, 109:716–727, 2021.

[161] Timothy Qi, Kyle McGrath, Raghuveer Ranganathan, Gianpietro Dotti, and Yanguang Cao. Cellular kinetics: A clinical and computational review of CAR-T cell pharmacology. *Advanced Drug Delivery Reviews*, 188(114421):114421, 2022.

[162] Deni Hardiansyah and Chee Meng Ng. Quantitative Systems Pharmacology Model of Chimeric Antigen Receptor T-Cell Therapy. *Clinical and Translational Science*, 12:343–349, 2019.

[163] Anne Talkington, Claudia Dantoin, and · Rick Durrett. Ordinary Differential Equation Models for Adoptive Immunotherapy. *Bulletin of Mathematical Biology*, 80:1059–1083, 2018.

[164] Aman P. Singh, Wenbo Chen, Xirong Zheng, Hardik Mody, Thomas J. Carpenter, Alice Zong, and Donald L. Heald. Bench-to-bedside translation of chimeric antigen receptor (CAR) T cells using a multiscale systems pharmacokinetic-pharmacodynamic model: A case study with anti-BCMA CAR-T. *CPT: Pharmacometrics and Systems Pharmacology*, 10:362–376, 2021.

[165] Alec J. Walker, Robbie G. Majzner, Ling Zhang, Kelsey Wanhainen, Adrienne H. Long, Sang M. Nguyen, Paola Lopomo, Marc Vigny, Terry J. Fry, Rimas J. Orentas, and Crystal L. Mackall. Tumor Antigen and Receptor Densities Regulate Efficacy of a Chimeric Antigen Receptor Targeting Anaplastic Lymphoma Kinase. *Molecular Therapy*, 25(9):2189–2201, 2017.

[166] Wentao Li, Shizhen Qiu, Jian Chen, Shutan Jiang, Wendong Chen, Jingwei Jiang, Fei Wang, Wen Si, Yilai Shu, Ping Wei, Gaofeng Fan, Ruijun Tian, Haitao Wu, Chenqi Xu, and Haopeng Wang. Chimeric Antigen Receptor Designed to Prevent Ubiquitination and Downregulation Showed Durable Antitumor Efficacy. *Immunity*, 53:456–470.e6, 2020.

[167] S Mattsson, L Johansson, S Leide Svegborn, J Liniecki, D Noßke, KÅ Riklund, M Stabin, D Taylor, W Bolch, S Carlsson, K Eckerman, A Giussani, L Söderberg, S Valind, and ICRP. Radiation Dose to Patients from Radiopharmaceuticals: a Compendium of Current Information Related to Frequently Used Substances. *Annals of the ICRP*, 44(2 Suppl):7—321, 2015.

[168] Lena Vomacka, Marcus Unterrainer, Adrien Holzgreve, Erik Mille, Astrid Gosewisch, Julia Brosch, Sibylle Ziegler, Bogdana Suchorska, Friedrich-Wilhelm Kreth, Jörg-Christian Tonn, Peter Bartenstein, Nathalie Lisa Albert, and Guido Böning. Voxel-wise analysis of dynamic 18F-FET PET: a novel approach for non-invasive glioma characterisation. *EJNMMI Research*, 8(1), 2018.

[169] Guobao Wang, Lorenzo Nardo, Mamta Parikh, Yasser G Abdelhafez, Elizabeth Li, Benjamin A Spencer, Jinyi Qi, Terry Jones, Simon R Cherry, and Ramsey D Badawi. Total-body PET multiparametric imaging of cancer using a voxelwise strategy of compartmental modeling. *J. Nucl. Med.*, 63(8):1274–1281, 2022.